FABRICATED GERMANIUM-DOPED OPTICAL FIBRES IN COMPUTED TOMOGRAPHY RADIATION DOSIMETRY

By

NUR NADIAH BINTI MOHD RAIS

Thesis Submitted to the School of Graduate Studies, Universiti Putra Malaysia, in Fulfilment of the Requirements for the Degree of Doctor of Philosophy

March 2024

FPSK (p) 2024 10

DEDICATION

This thesis is dedicated to

My late mother:

Nor Rashidah Binti Zainal

Forever will be missed

Abstract of thesis presented to the Senate of Universiti Putra Malaysia in fulfilment of the requirement for the degree of Doctor of Philosophy

FABRICATED GERMANIUM-DOPED OPTICAL FIBRES IN COMPUTED TOMOGRAPHY RADIATION DOSIMETRY

By

NUR NADIAH BINTI MOHD RAIS

March 2024

Chairman : Associate Professor Noramaliza binti Mohd Noor, PhD
Faculty : Medicine and Health Sciences

Newly fabricated germanium (Ge)-doped optical fibres as a potential dosimeter in computed tomography (CT) dosimetry are being investigated due to the several limitations of the current dosimeters and limited study of the optical fibres in the field of diagnostic imaging. As such, the responses of these fibres at radiation quality for CT applications (RQT beam quality) are being compared with gold standard thermoluminescence dosimeter (TLD-100 chip) and optically stimulated luminescence dosimeter (OSLD nanoDot). Four fibre types are studied with different Ge-dopant concentrations in flat fibre (FF) and cylindrical fibre (CF) shapes. These are 2.3 mol% Ge-FF, 6 mol% Ge-FF, 6 mol% Ge-CF, and 2.3 mol% Ge-CF. The first objective is to examine the basic characteristics in terms of dose linearity, RQT beam quality, dose reproducibility, dose sensitivity, minimum detectable dose, and fading. The thermoluminescence (TL) signals of all fibres are discovered to be linear for doses ranging from 2 to 40 milligray (mGy) for all RQT beam quality of 100 kilovoltage (kV) (RQT 8), 120 kV (RQT 9), and 150 kV (RQT 10). However, in the RQT beam quality study, the signal response decreased as the energy increased from 100 kV to

150 kV, exhibiting clear photoelectric dependence. The optical fibres also demonstrated dose reproducibility of better than 4% of the mean, surpassing the performance of the TLD-100 chip. In terms of dose sensitivity, all fibres demonstrated superior sensitivity, with 6 mol% and 2.3 mol% Ge-FF indicating 87 and 84 times more sensitivity than that of the TLD-100 chip. The optical fibres are also able to detect dose levels down to the least delivered dose of 2 mGy used in this study with superior lower dose detection competency of 2.3 mol% Ge-CF to identify doses down to 0.29 mGy. Finally, a higher fading rate of optical fibres ten days post-irradiation is observed due to the shallow electron trappings typical in low-dose radiation. Per the results, the TL response is dependent on the beam quality and fading. Thus, beam quality and fading correction factors are included in the absorbed dose measurement formula. The advanced characteristics in terms of the kinetic parameters of optical fibres have also been investigated prior to establishing absorbed dose methodology with uncertainty analysis. The response for absorbed and entrance skin dose measurements of the radiosensitive organs on CIRS ATOM® dosimetry verification paediatric phantom during head and lung CT scans revealed that the majority of the percentage difference of investigated dosimeters is less than 3% when compared against TLD-100 chips. The dosimetry verification in a real clinical setting for entrance skin dose measurement of the thyroids in paediatric patients undergoing computed tomography pulmonary angiogram (CTPA) examinations is also achieved with a percentage difference of less than 5%. The expanded uncertainties are 5.92%, 3.67%, 2.38%, 1.27%. 2.97% and 4.54% for 6 mol% Ge-FF, 2.3 mol% Ge-FF, 2.3 mol% Ge-CF, 6 mol% Ge-CF, TLD-100 chip and OSLD nanoDot, respectively, after multiplication by a coverage factor k = 2. This uncertainty provided a level of

confidence of approximately 95%. In conclusion, all four fabricated Ge-doped optical fibres are feasible to be potential novel dosimeters in CT dosimetry RQT beam quality.

Keywords: Computed Tomography, Dosimetry, Germanium, Optical Fibre, Radiation

SDG: GOAL 9: Industry, Innovation and Infrastructure

Abstrak tesis yang dikemukakan kepada Senat Universiti Putra Malaysia sebagai memenuhi keperluan untuk ijazah Doktor Falsafah

GENTIAN OPTIK DOP GERMANIUM YANG DIFABRIKASI UNTUK DOSIMETRI RADIASI TOMOGRAFI BERKOMPUTER

Oleh

NUR NADIAH BINTI MOHD RAIS

Mac 2024

Pengerusi : Profesor Madya Noramaliza binti Mohd Noor, PhD
Fakulti : Perubatan dan Sains Kesihatan

Gentian optik yang difabrikasi baru dan didop dengan germanium (Ge) telah diselidiki sebagai dosimeter potensial dalam dosimetri tomografi berkomputer (CT) kerana beberapa batasan dosimeter semasa dan kajian yang terhad pada gentian optik dalam bidang pengimejan diagnostik. Oleh itu, tindak balas gentian ini pada kualiti radiasi untuk aplikasi CT (kualiti sinar RQT) telah dibandingkan dengan dosimeter pendarkilau haba yang merupakan piawaian emas (cip TLD-100) dan dosimeter pendarkilau terangsang optik (OSLD nanoDot). Empat jenis gentian dengan kepekatan dopan Ge yang berbeza dalam bentuk gentian rata (FF) dan gentian silinder (CF) telah dikaji. Jenis-jenis tersebut adalah 2.3 mol% Ge-FF, 6 mol% Ge-FF, 6 mol% Ge-CF, dan 2.3 mol% Ge-CF. Objektif pertama adalah untuk mengkaji ciri-ciri asas termasuk kelinearan dos, kualiti sinar RQT, kebolehulangan dos, sensitiviti dos, dos minimum yang boleh dikesan, dan pemudaran. Isyarat pendarkilau haba (TL) bagi semua gentian didapati linear untuk dos yang berkisar daripada 2 hingga 40 milligray (mGy) untuk semua kualiti sinar RQT 100 kilovolt (kV) (RQT 8), 120 kV (RQT 9), dan 150 kV (RQT 10). Walau bagaimanapun, dalam kajian kualiti sinar RQT, tindak

balas isyarat menurun seiring dengan peningkatan tenaga daripada 100 kV ke 150 kV, menunjukkan ketergantungan fotoelektrik yang jelas. Gentian optik juga menunjukkan kebolehulangan dos yang lebih baik daripada 4% daripada purata, melebihi prestasi cip TLD-100. Daripada segi sensitiviti dos, semua gentian menunjukkan sensitiviti yang lebih unggul, dengan 6 mol% dan 2.3 mol% Ge-FF menunjukkan sensitiviti 87 dan 84 kali lebih tinggi daripada cip TLD-100. Gentian optik juga mampu mengesan tahap dos sehingga dos minimum yang diberikan sebanyak 2 mGy yang digunakan dalam kajian ini dengan keupayaan pengesan dos yang lebih unggul bagi 2.3 mol% Ge-CF untuk mengenal pasti dos minimum sehingga 0.29 mGy. Akhirnya, kadar pemudaran yang lebih tinggi bagi gentian optik sepuluh hari selepas diradiasi telah diperhatikan disebabkan oleh perangkap elektron cetek yang menjadi kebiasaan dalam radiasi dos rendah. Berdasarkan hasil kajian, tindak balas TL bergantung kepada kualiti sinar dan pemudaran. Oleh itu, faktor pembetulan kualiti sinar dan pemudaran telah dimasukkan dalam formula pengukuran dos serapan. Ciri-ciri lanjutan daripada segi parameter kinetik gentian optik juga telah dikaji sebelum penubuhan metodologi dos serapan dengan analisis ketidakpastian. Tindak balas bagi pengukuran dos serapan dan dos kulit masuk organ yang radiosensitif pada phantom pengesahan dosimetri pediatrik CIRS ATOM® semasa imbasan CT kepala dan paru-paru menunjukkan bahawa majoriti perbezaan peratusan dosimeter yang disiasat adalah kurang daripada 3% apabila dibandingkan dengan cip TLD-100. Pengesahan dosimetri dalam tetapan klinikal sebenar untuk pengukuran dos kulit masuk bagi kelenjar tiroid pada pesakit pediatrik yang menjalani pemeriksaan angiogram pulmonari tomografi berkomputer (CTPA) juga dicapai dengan perbezaan peratusan kurang daripada 5%. Ketidakpastian yang diperluaskan adalah 5.92%, 3.67%, 2.38%, 1.27%, 2.97%, dan 4.54% untuk 6 mol% Ge-FF, 2.3 mol% Ge-FF, 2.3

mol% Ge-CF, 6 mol% Ge-CF, cip TLD-100, dan OSLD nanoDot masing-masing, selepas penggandaan dengan faktor liputan k = 2. Ketidakpastian ini menyediakan tahap keyakinan kira-kira 95%. Kesimpulannya, keempat-empat gentian optik yang difabrikasi dan didop dengan Ge boleh dijadikan sebagai dosimeter novel yang berpotensi dalam dosimetri CT kualiti sinar RQT.

Kata Kunci: Dosimetri, Gentian Optik, Germanium, Radiasi, Tomografi Berkomputer

SDG: MATLAMAT 9: Industri, Inovasi dan Infrastruktur

ACKNOWLEDGEMENTS

With the name of Allah the Most Compassionate and Most Merciful

All praise and thanks to Almighty Allah, with His blessing giving me the strength and passion, to finish the research until this thesis is completed.

When I embarked on my PhD journey seven years ago, little did I know the profound experiences that lay ahead. Time appeared to fly by while I pursued my PhD, realising a lifelong desire. Returning to the student environment after several years in the working atmosphere was both daunting and compelling.

I am immensely grateful for the opportunity to be a part of an exceptional research institute. I would like to express my sincere gratitude to my primary supervisor, Assoc Prof. Dr. Noramaliza, for sharing her vast academic expertise and for being instrumental in my professional development within the medical physics community. I am truly thankful for her firm yet compassionate guidance.

I would also like to express my gratitude to my PhD advisors: Assoc Prof. Dr. Hasyma, Dr. Iskasymar, Dr. Noor Diyana, Cik Asmaliza, and Emeritus Prof. David Bradley. I appreciate all of your time, guidance and valuable insights.

To Kak Zaba, Safwan, Faizal, Farid, Lam, Kak Sal, Kak Shai and Su – you guys are the best crew. We have overcome obstacles and celebrated victories together, and I am thankful that I have all of you by my side. To Kak Yati, Adiela and Hafiz – although we did not manage to spend more time together as I was nearing the end of my study, I'd appreciate the constant support and wish all of you the best.

The completion of my dissertation would not have been possible without the support and motivation of my colleagues at UPM, IIUM and Vision College. The existing and new-found friendships that are formed throughout the years are the incidental, beautiful gifts that I will forever cherish.

Finally, I would like to thank my family, especially my husband Nadzreen. Thank you for always being my rock, during all the highs and lows of this PhD journey. Your encouragement and belief in me have given me the courage to never give up. Not forgetting, my loyal and faithful companions, my fur babies, Yuzu and Yuri. I love all of you.

As my seven-year-long PhD adventure draws to an end, I can honestly state that I am incredibly proud of my accomplishments. This life-changing experience has moulded me as a person as well as a researcher, teaching me the priceless lesson that persistence eventually pays off. Those around me have demonstrated unrelenting devotion, determination, and patience to help me be where I am today.

Thank you everyone, from the bottom of my heart.

This thesis was submitted to the Senate of the Universiti Putra Malaysia and has been accepted as fulfilment of the requirement for the degree of Doctor of Philosophy. The members of the Supervisory Committee were as follows:

Noramaliza binti Mohd Noor, PhD
Associate Professor
Faculty of Medicine and Health Sciences
Universiti Putra Malaysia
(Chairman)

Hasyma binti Abu Hassan, MMed
Associate Professor
Faculty of Medicine and Health Sciences
Universiti Putra Malaysia
(Member)

Iskasymar bin Itam @ Ismail, MEmMed
Senior Lecturer
Faculty of Medicine and Health Sciences
Universiti Putra Malaysia
(Member)

Noor Diyana binti Osman, PhD
Senior Lecturer
Advanced Medical and Dental Institute
Universiti Sains Malaysia
(Member)

ZALILAH MOHD SHARIFF, PhD
Professor and Dean
School of Graduate Studies
Universiti Putra Malaysia

Date: 12 September 2024

TABLE OF CONTENTS

LIST OF TABLES

LIST OF FIGURES

LIST OF ABBREVIATIONS

AAPM	American Association of Physicists in Medicine
ALARA	As Low As Reasonably Achievable
ANOVA	Analysis of Variance
AP	Anteroposterior
CF	Cylindrical Fibre
COM	Commercial Fibre
CT	Computed Tomography
CTDI	CT Dose Index
$CTDI_{vol}$	CTDI Volume
$CTDI_{w}$	CTDI Weighted
CTPA	CT Pulmonary Angiogram
CV	Coefficient of Variation
CVD	Chemical Vapour Deposition
DLP	Dose Length Product
E_a	Activation Energy
ED	Effective Dose
EDX	Energy Dispersive X-Ray
ESD	Entrance Skin Dose
ESAK	Entrance Surface Air Kerma
FF	Flat Fibre
FOM	Figure of Merit
GCP	Good Clinical Practice
HPUPM	Hospital Pengajar Universiti Putra Malaysia
HTP	High-Temperature Peak
HVL	Half-Value Layer

IAEA	International Atomic Energy Agency
ICRP	International Commission on Radiological Protection
JKEUPM	Ethics Committee for Research Involving Human Subjects
LED	Light-Emitting Diode
LTP	Low-Temperature Peak
MCP	Midcoronal Plane
MCVD	Modified Chemical Vapour Deposition
MDCT	Multidetector Computed Tomography
MDD	Minimum Detectable Dose
MMU	Multimedia University
MREC	Medical Research Ethics Committee
MSP	Midsagittal Plane
NCICT	National Cancer Institute Computed Tomography
NMRR	National Medical Research Register
OSL	Optically Stimulated Luminescence
OSLD	Optically Stimulated Luminescence Dosimeter
PCF	Photonic Crystal Fibre
PE	Pulmonary Embolisms
PI	Peak Integral
PMMA	Polymethyl Methacrylate
PMT	Photomultiplier Tube
ROI	Region of Interest
RQT	Radiation Quality in CT
SD	Standard Deviation
SEM	Scanning Electron Microscope
SID	Source Image Distance

SSDE	Size-Specific Dose Estimate
SSDL	Secondary Standard Dosimetry Laboratory
TL	Thermoluminescence
TLD	Thermoluminescence Dosimeter
T_{max}	Maximum Peak Temperature
TM R&D	Telekom Research & Development Sdn Bhd
TTP	Time-Temperature Profile
UKM	Universiti Kebangsaan Malaysia
UM	University of Malaya
UMMC	University of Malaya Medical Centre
UPM	Universiti Putra Malaysia
UTM	Universiti Teknologi Malaysia
WinGCF	Windows®-based Glow Curve Fitting
WinREMS	Windows®-based Radiation Evaluation and Management System

CHAPTER 1

INTRODUCTION

1.1 Research Background

Globally, the utilisation of medical radiation is steadily increasing, which aligns with the credible advantages it brings to a health institution. Consequently, it is also acknowledged that medical imaging, particularly diagnostic radiology, delivers the highest radiation dose to society compared to other artificial ionising radiation. Therefore, in principle, the radiation dose has to be ideal to get only the intended imaging particulars without surpassing the threshold of the deterministic effect. However, within the diagnostic dose range, a minimal possibility for malignancy exists, especially for radiosensitive organs such as eyes and thyroids. To minimise the risk whilst attaining the maximum diagnostic outcome consistent with the ALARA (As Low As Reasonably Achievable) principle, recording a precise dose measurement that the patient receives as the earliest step in the dose management chain is significant. Reasonably, an operative, consistent and accurate means of dosimetry is essential to keeping up with these efforts (Dewerd & Wagner, 1999).

Various methods can be used to estimate the radiation dose to the patient, including direct, indirect, and calculational approaches. One of the most straightforward methods is the estimation of the entrance skin dose (ESD), which focuses on the patient's irradiated surface. The thermoluminescence dosimeter (TLD) has been a standard dosimeter used for this purpose (Faulkner et al., 1999). Another passive dosimeter that has gained prominence in recent years is the optically stimulated luminescence dosimeter (OSLD). It's worth noting that the International Atomic

Energy Agency (IAEA) has set guidelines that any new or existing instruments or procedures intended for future applications must be calibrated using the documented methodology to ensure a standardised dosimetry system (IAEA, 2007).

OSLD offers a promising technique for quick and precise dose measurements. It emits distinguished illuminations relative to the absorbed radiation doses once stimulated with a light-emitting diode (LED) during readout. One commercially available OSLD model, the carbon-doped aluminium oxide (Al_2O_3:C) nanoDot (Landauer Inc.), is currently used for dose measurements in medical imaging. Its small size, sturdiness, reusability and sensitivity make it a practical dosimeter, offering a potential solution to the challenges of precise dose measurement in medical imaging without introducing any artefact on the radiograph (Scarboro et al., 2015).

One major setback of OSLD is that although it has been extensively studied in radiotherapy fields (Alvarez et al., 2017; Dunn et al., 2013; Jursinic, 2007), the characterisation and subsequent direct conversion of the light signal to absorbed dose in diagnostic imaging is significantly in question due to the much lesser photon energy and the dose applied. According to Reft (2009), the standard calibration procedure for clinically used OSLD in diagnostic imaging is unsatisfactory due to multiple causes. One of the causes is that the vendor-supplied calibration determines the absorbed dose reading comparatively to 80 kilovoltage (kV) beam quality only. In other words, as the vendor calibration procedure has not considered the disparity in beam quality amongst various scanning specifications, irradiating the nanoDot to a higher or lesser photon energy than 80 kV may present substantial deviation in dose measurement unless a suitable energy correction factor is applied. One of the primary concerns in

using OSLD in the diagnostic field is that its energy response is highly dependent on variations in beam quality (Reft, 2009). Three RQT beam qualities are designated for three different photon energies for computed tomography (CT) dosimetry. These are RQT 8 (100 kV), RQT 9 (120 kV) and RQT 10 (150 kV) (IAEA, 2007). Consequently, a manual methodology for cross-calibration with a standard ionisation chamber is required to determine absorbed dose methodologies and uncertainties for CT dosimetry. Nonetheless, a structured assessment of calibration procedures is needed for optical fibre dose measurements, albeit at a much lesser cost.

Thermoluminescence (TL) is an occurrence of light production once certain elements are heated during readout. The luminescence amount is directly associated with the absorbed dose (Bradley et al., 2012). Harshaw Chemical Company has commercially produced lithium fluoride (LiF) phosphor to be made available as part of the material for vastly used TLD-100, which is LiF doped with magnesium (Mg) and titanium (Ti) (LiF: Mg, Ti). The effective atomic number of LiF is nearly similar to that of tissue, rendering it practically tissue equivalent. Other beneficial characteristics of phosphor-based thermoluminescence dosimeters are small size, reproducibility and precision to within 3%, and relatively low minimum detectable dose, down to the sub milligray (mGy) level (Faulkner et al., 1999).

Even with the benefits mentioned above of TLD-100, it is still liable to several disadvantages. LiF phosphor is a hygroscopic substance that readily absorbs water from its environment but has a relatively poor spatial resolution (Mahdiraji et al., 2015). These characteristics are a challenging concern, particularly for the application in interstitial or intercavitary surroundings and in the radiotherapy field, where a

precise estimation of the patient dose is crucial. TLD-100 also has a complex glow curve owing to its complicated energy traps, making a detailed study of the kinetic parameters taxing. The intrinsic uncertainties in TL dosimetry, especially in its utilisation in diagnostic imaging, are still significant domains that require consistent and continuous study (Mahdiraji et al., 2015). With these limitations in mind, novel TL-based media are presently being investigated in silicon dioxide (SiO_2) optical fibres that propose beneficial features that may widen TLD's practical applicability. Using favourable TL properties of commercially available telecommunication fibres to overcome the numerous limitations as previously mentioned, novel fabricated germanium (Ge)-doped silica fibres are now discovering a niche (Bradley et al., 2012).

A consortium effort between the University of Surrey, United Kingdom and Malaysian counterparts comprising Universiti Putra Malaysia (UPM), Telekom Research & Development Sdn Bhd (TM R&D), Multimedia University (MMU), University of Malaya (UM), Universiti Teknologi Malaysia (UTM) and Malaysian Nuclear Agency (Nuklear Malaysia) focuses on optical fibre fabrication as new dosimetry system, grounded by the principle of thermoluminescence. Theoretically, the electron trapping mechanism of amorphous crystals of the fibres is highly dependent on the optimum existence of defect centres generated by the dopant materials (Yusoff et al., 2005). The consortium group exploits this theory by employing the technique of modified chemical vapour deposition (MCVD) for doping fabricated silicon glass with various dopant materials and concentrations using gas flow rate, reinforced together with fibre-pulling amenities which can accommodate fibre fabrication with different sizes and shapes. The group’s primary objective is to fabricate tailored-made optical fibres characterised according to various beam qualities within the radiation sphere of

radiotherapy and diagnostic imaging for potential clinical use in the near future with a fraction of the price of current commercial dosimeters (Bradley et al., 2014).

Investigations on implementing commercial and fabricated optical fibres in radiotherapy dosimetry have commenced by various research groups, as reviewed by Bradley et al. (2012). Several preliminary findings of these amorphous crystals have positively surpassed that of standard phosphor-based TLDs, such as having high spatial resolution suitable for precise radiotherapy application, water resistant for possible usage in intercavitary and interstitial dose measurements, mechanically sturdy, chemically inactive, biocompatible and reproducible. UPM group alone is currently exploring the dosimetry characteristics of fabricated Ge-doped optical fibres in several radiation fields encompassing high-energy radiotherapy photons (Fadzil et al., 2018), protons (Hassan et al., 2019), small field dosimetry (Lam et al., 2019), and electrons (Zakaria et al., 2020), to name a few. In all such studies, the TL performances of irradiated fibres have shown considerable potential for dosimetric applications in radiotherapy.

Contrariwise, this group of amorphous silica glass are yet to be fully explored in the field of diagnostic imaging and low-energy X-ray photons, with to-date preliminary findings only being issued in four articles by Alyahyawi et al. (2017, 2018), Ramli et al. (2015) and Rozaila et al. (2016). These groups have investigated the response of novel optical fibres in general radiography dosimetry, such as chest and extremities X-rays, mammography, and dental imaging. They have stated, by their experiments, a distinct energy dependency, with the highest TL yield displayed by the fabricated fibres against that of phosphor-based TLD-100. The optical fibres also showed good

dose linearity irrespective of the dopant concentrations, dimensions or fibre shapes. They have also suggested that fabricated optical fibres with Ge as the dopant can provide several potential benefits as opposed to the gold standard TLD-100, predominantly in terms of the higher sensitivity at diagnostic imaging radiation doses. A general issue has been refining the dosimetry characteristics of the optical fibres in other medical imaging modalities, such as fluoroscopy and computed tomography, with the latter being the radiation dosimetry of interest in the present study.

The ever-increasing advancements in modern CT have brought about a surge in clinical utilisation. This has made the CT scan the number one medical imaging modality that gives the maximum radiation dosage compared to other diagnostic imaging examinations, albeit with its enhanced diagnostic competency. Radiation doses from CT scans are 100 to 500 times higher than conventional diagnostic imaging and are within the scale associated with higher malignancy risk (Brenner & Hall, 2007). This associated risk can be three times higher in youngsters than grown-ups, especially in accord with the radiosensitive organs of eyes and thyroids (Pearce et al., 2012). The brain and skin are other organs in which children are highly susceptible to radiation-induced changes. Absorbed doses in youngsters are elevated due to lesser X-ray attenuation in their smaller frames, contributing to the amount of radiation absorbed. Children are also more vulnerable compared to grown-ups due to their fast-dividing cells. Theoretically, they possess many more remaining years left for any malignancy to appear in terms of their expected lifetime risk of cancer (Miglioretti et al., 2013).

The utilisation of CT scan examinations in the paediatric population has rapidly surged in the last twenty years. A 2012 IAEA CT frequency study discovered that the number of examinations done within paediatric age groups in hospitals around Asia, including Malaysia, was 12.2%, with CT brain as the most examination performed, adding up to nearly 75% of all paediatric CT examinations (Vassileva et al., 2012). Yet another 2012 study, this time by Pearce et al. (2012), found that paediatric patients in the United Kingdom who were exposed to CT brain radiation dosage of 50 milligray (mGy) or higher were 2.8 times more predisposed to future risk of brain malignancy and the risk of leukaemia was largest from CT brain examinations for younger patients as opposed to older children. Even though the effective dose for CT brain is comparatively low, the brain and red bone marrow doses are still relatively high, particularly for younger children. Pearce et al. (2012) also stated that most CT brain examinations were performed to rule out traumatic brain injury due to head injury. Therefore, a precise measurement of radiation doses from CT examination to the aforementioned organs in paediatrics is desirable.

According to Ploussi et al. (2017), ESD and organ dose estimations can be done using three methods. The first is through the in vivo dosimetry technique, which is used directly on patients undergoing CT scans. ESD is usually the only feasible to do as the dosimeter is located on the patient's body surface. This technique will accurately read the radiation dose imparted on the patient or superficial organs such as the eyes and thyroid. Unfortunately, it is not easy to execute in a real clinical setting since it has to be ethically considered and approved, with patient consent and cooperation. The second method uses an anthropomorphic phantom via ex vivo dose estimations. It permits a precise absorbed dose estimation in the intended organs or tissues even

though disparities in patient size are not being considered unless the age group for the proposed study is specified. The last method is simple calculation techniques via CT dosimetry software. It is a more straightforward and technologically accessible method, although it doesn't necessarily give an actual estimation of the radiation dose. Hence, independently verifying the measurement with a dosimeter is an essential additional step to validate the precision of the dose delivered.

The primary aim of this research will be centred on the fundamental characterisation of dosimetric properties of a novel fabricated Ge-doped amorphous silica optical fibres irradiated using X-ray photons at energies applied in CT and comparing the responses of these optical fibres with standard TLD (TLD-100 chip) and OSLD (nanoDot). The newly fabricated Ge-doped dosimeters are exposed to RQT beam quality to ensure the utmost thorough X-ray beam specifications from their spectral distributions are being studied. An account and details of radiation qualities in accordance with the X-ray tube voltage and the first and second half-value layers (HVLs) are applied to generate the CT beam spectrometry.

The secondary objective is the implementation of this fabricated optical fibre as the new TL dosimeters in dosimetry verification paediatric anthropomorphic phantom for head and lung CT scans. More specifically, ESD to the eye lens and thyroid, together with absorbed doses to the brain due to scattered and direct radiations generated from head CT scans, are determined. Entrance skin and absorbed doses to the thyroid and lung, respectively, are studied for phantom lung scans due to scattered and direct radiations generated from lung CT scans. Lastly, the potential of applying the fabricated optical fibres in real clinical settings for ESD measurement of the thyroid

in paediatric patients undergoing Computed Tomography Pulmonary Angiogram (CTPA) examinations is also being studied.

1.2 Problem Statement

These group of Ge-doped optical fibres are yet to be fully explored in the field of diagnostic imaging and low-energy X-ray photons, with to-date preliminary findings only being issued in four articles by Alyahyawi et al. (2017, 2018), Ramli et al. (2015) and Rozaila et al. (2016). Ramli et al. (2015) have, for instance, studied the fabricated flat optical fibres of various sizes, all with centrally located dopants based on nominal 6 mol% Ge preform concentrations. The other three studies have investigated Ge-doped fibres in a disc shape, Ge-doped flat fibres co-doped with boron (Ge-B), and photonic crystal fibre (PCF). Concerning the types of radiation dosimetry used to investigate the response of these amorphous crystals, Alyahyawi et al. (2018) have studied the dosimetry response at diagnostic energies for general medical imaging applications, while in yet another study by Alyahyawi et al. (2017) examination was made of at kilovoltage-peak (kVp) potentials common to mammography and dental radiography. In all of these studies, discernible energy-dependent responses are seen, with greater responses and higher sensitivity exhibited by the fibres compared to TLD-100. The optical fibres also showed good dose linearity irrespective of the dopant concentrations, dimensions or fibre shapes. A prevailing issue has been refining the dosimetry characteristics of the optical fibres in other medical imaging modalities, such as fluoroscopy and CT, with the latter being the radiation dosimetry of interest in the present study. Thus, it has been the contention that at diagnostic dose levels, the fibres must benefit from having an established response based on well-defined spectra.

As such, the present study aims to establish the TL yield of the tailor-made fibres using well-defined spectra for standardisation in CT beam quality.

Regarding the increasing CT examination in paediatrics and the growing radiation-induced risk these youngsters are likely to incur, the attentiveness to improve patient management in terms of the radiation dose received is starting to intensify. The initial technique typically done to support the study on patient management is estimating the radiation dose received by the patient. Nevertheless, the current methodology practice in the clinical setting is less than desirable as the task of CT dose documentation and risk approximation is primarily dependent on the CT dose index (CTDI) and dose length product (DLP) displayed on the console panel. These two CT terminologies are based upon a restricted effective dose conversion coefficient simulated through two standard sizes of cylindrical phantoms used in CT (Huda et al., 2008). CTDI volume ($CTDI_{vol}$) is interpreted as the single dose which best approximates the dose distribution provided to a standard cylindrical plastic phantom in a specific CT scanner by particular scan parameters. $CTDI_{vol}$ is, therefore, denoted as a dose index of CT scanner radiation output, not a patient dose index. Since DLP is based on $CTDI_{vol}$, DLP also depicts the total energy transmitted to a cylindrical phantom (Boone et al., 2011). It is best to mention that patient doses acquired with anthropomorphic phantom or CT dosimetry software have not been independently verified with any radiation dose measurements.

1.3 Research Objectives

1.3.1 General Objective

To evaluate fundamental dosimetric properties of fabricated Germanium (Ge)-doped optical fibres irradiated using X-ray photons at energies applied in computed tomography (CT) and to compare the responses of these optical fibres with standard thermoluminescence dosimeter (TLD-100 chip) and optically stimulated luminescence dosimeter (nanoDot).

1.3.2 Specific Objectives

1. To investigate basic dosimetric characteristics of fabricated Ge-doped optical fibres in CT dosimetry, focusing on dose linearity, RQT beam quality, dose reproducibility, dose sensitivity, minimum detectable dose and fading.
2. To study advanced characteristics in terms of the kinetic parameters of fabricated Ge-doped optical fibres using the glow curve analysis, including the maximum peak temperature (Tmax), peak integral (PI) and activation energy (Ea) in the CT radiation dosimetry.
3. To establish absorbed dose methodology, calibration coefficient and correction factors for fabricated Ge-doped optical fibres for CT dosimetry, including uncertainty analysis.
4. To determine the response of the fabricated Ge-doped optical fibres for entrance skin dose (ESD) measurements of the eyes and thyroids together with absorbed dose measurements of the brain and lung on CIRS ATOM® dosimetry verification paediatric phantom during head and lung CT scans.
5. To study the potential of applying the fabricated Ge-doped optical fibres in a real clinical setting for ESD measurement of the thyroids in paediatric patients undergoing Computed Tomography Pulmonary Angiogram (CTPA) examinations.

1.4 Significance of Research

Even though various studies have investigated different types of optical fibres (dopant types, concentrations, sizes, and shapes), primarily in the radiotherapy field, the current study explored the usage of four different types of fabricated Ge-doped optical fibres, specifically in CT radiation dosimetry. The outcomes from this research will hopefully add novel insights regarding the dosimetric response of this fabricated silica glass in the diagnostic imaging sphere, particularly computed tomography RQT beam quality. Every basic dosimetric characterisation, as mentioned in the first specific objective, has yet to be investigated in one dedicated study in any field of diagnostic imaging, let alone CT dosimetry. However, several fundamental properties of these amorphous crystals are studied randomly for different radiation beam qualities. As such, this present study serves as detailed research on the basic dosimetric characterisation response of these fibres to CT radiation dosimetry. This study also presents an in-depth study of the behaviour of fabricated Ge-doped optical fibres by investigating glow curve behaviour. The relative electron populations within the energy level of the silica glass traps may be represented as the relative amplitude of the light emission spectrum in the form of TL energy distribution. In other words, by studying fabricated optical fibres, the possibility of widening the practical applicability of any other TL dosimeters proved beneficial. In addition, converting the initial signal produced by the fibre in nanocoulombs (nC) to milligray (mGy) through the establishment of absorbed dose methodology is the pivotal and final methodology to closing the loop of any fundamental dosimetry study. Therefore, it may serve as a reference, especially regarding the application of correction factors when the optical fibres are used for a future clinical study.

The independent verification to measure the ESD to the radiosensitive lens and thyroid and absorbed doses to the brain and lung during paediatric phantom head and lung CT scans and in paediatric patients undergoing CTPA examinations is unprecedented. Thus, the novel fabricated Ge-doped optical fibre in the present study is hoped to demonstrate an excellent material for dose measurement in CT examination. Desirably, in the long run, implementing evidence-based tools for radiation detection and dose measurement for clinical diagnosis can serve a beneficial purpose and long-lasting benefit in patient care and resource utilisation.

1.5 Thesis Outline

The problem statement, research objectives for the current works and significance of the research are all outlined in Chapter 1's introduction to the topic.

Chapter 2 details a literature review on the theory and background of TL phenomena, which is the principle mechanism of optical fibre. The fundamental concept of thermoluminescence dosimeter (TLD-100 chip) and optically stimulated luminescence dosimeter (nanoDot), the history of the development of silica-based optical fibre and basic knowledge of CT radiation dosimetry are also thoroughly discussed. The comparison of radiosensitive organs and ESD during paediatric head and chest scans and CTPA studies by other research groups are also being reviewed.

Chapter 3 depicts the materials and methodologies concerning the fabrication and preparation of Ge-doped optical fibres and the preparation for the TLD-100 chip in addition to nanoDot. Basic dosimetric characterisations under RQT beam quality, scanning electron microscope (SEM) and energy dispersive X-ray (EDX) analysis,

and TL glow curves using deconvolution software are followed by the establishment of absorbed dose methodology and uncertainty analysis. For clinical application, irradiation set-up for the optical fibre in dosimetry verification paediatric phantom is completed, along with the application of the optical fibre in real clinical settings for paediatric CTPA examinations.

Chapter 4 details all the results of this study. Discussions on general structures of the fabricated Ge-doped optical fibres and the basic dosimetric characterisation of fibres, TLD-100 chip and nanoDot, preluded this chapter. SEM and EDX analysis, glow curve formation, and TL kinetic parameters are also thoroughly discussed. The results on phantom irradiation for ESD of the eyes and thyroids, together with absorbed doses to the brain and lung, and the fibre measurements in the real clinical setting for paediatric CTPA examinations are analysed. Absorbed dose methodology in regards to a calibration curve, correction factors and uncertainty analysis concluded this chapter.

The final chapter, Chapter 5, concludes the outcomes of this dissertation and outlines the limitations and recommendations for future potential research on fabricated Ge-doped optical fibres in CT radiation dosimetry.

CHAPTER 2

LITERATURE REVIEW

2.1 Introduction

There are numerous uses for ionising radiation, including medical treatment and diagnostics as well as industrial and food processing. Radiation monitoring and dosimetry are crucial in ensuring the efficient and reliable delivery of ionising radiation in such applications to achieve the intended goal. Radiation dosimetry has been approached in various ways, including passive methods like thermoluminescence (TL) and active methods using diodes, ion chambers, and scintillators.

Demands for dosimetric devices for dose estimation in radiosensitive organs continue to be driven by the increased number of radiological examinations in relation to technological advancements in medical imaging. It is becoming more difficult for a dosimeter to estimate the radiation dose distribution of such intricate anatomical geometries with the precision and accuracy needed. Due to their relatively large size, current commercially available field dosimeters are impractical in such difficult circumstances. Both passive and active dosimeters have demonstrated this to be true (Zubair et al., 2020).

One of the candidates for closing the gap has emerged as silica glass optical fibre, particularly in the areas of spatial resolution, precision, and broad dynamic range. Initially intended for optical communications, such optical fibres are frequently doped with germanium (Ge) to produce the total internal reflection necessary for communications. Numerous research groups' studies into potential radiation therapy

uses for optical fibres began with TL passive dosimeters dosimeters (Moradi et al., 2017; Noor et al., 2012; Rozaila et al., 2017). At the radiation doses typically used in high-dose radiation-medicine treatments, useful TL emission has been seen. In addition to the standard qualities of optical fibre radiation dosimeters, such as affordability, adequate sensitivity, acceptable fading, response linearity and reproducibility, they also have a few special qualities that make it possible to precisely measure the dose in tissues. However, these manufactured Ge-doped optical fibres have yet to be fully investigated in the areas of diagnostic imaging and low-energy X-ray photons; at the start of this research, only four articles by Alyahyawi et al. (2017, 2018), Ramli et al. (2015), and Rozaila et al. (2016) have published preliminary results. Furthermore, the type of fabricated fibres utilised varies somewhat based on each group's intended custom fibre recipe in terms of forms, diameters, dopant concentrations, and co-doping.

In keeping with the verifiable benefits it offers a healthcare institution, the use of medical radiation is progressively rising globally. As a result, it is also acknowledged that compared to other forms of artificial ionising radiation, diagnostic radiology gives the largest radiation dosage to society. Therefore, in theory, the radiation dose must be perfect in obtaining only the desired imaging details without exceeding the deterministic effect limit. A little chance of cancer does, however, remain within the diagnostic dose range, particularly for radiosensitive organs like the thyroid and eyes. It is crucial to record an accurate dose measurement that the patient receives as the first step in the dose control chain to reduce risk while achieving the highest diagnostic outcome consistent with the ALARA (As Low As Reasonably Achievable) guideline.

In order to maintain these efforts, a practical, reliable, and precise dosimetry method is required (Dewerd & Wagner, 1999).

Direct, indirect, and mathematical methods can all be used to determine the patient's exposure to radiation. Thermoluminescence dosimeters (TLD) are one of the commonly used standard dosimeters for estimating the entrance skin dose (ESD) of the patient's irradiated surface. ESD is the measure of radiation dose absorbed by the skin as it reaches the patient during radiographic imaging. Entrance surface air kerma (ESAK) is a closely similar term as it represents the incident air kerma at the patient entrance reference point. Another passive dosimeter to measure surface dose or air kerma is optically stimulated luminescence dosimeter (OSLD), which has become more common in recent years. New or existing instruments or procedures intended for future applications must be calibrated in accordance with the documented methodology for the fulfilment of a standardised dosimetry system, according to the International Code of Practise on Dosimetry in Diagnostic Radiology published by the International Atomic Energy Agency (IAEA) in 2007 (IAEA, 2007).

This chapter aims to provide a more thorough introduction to the structure of fabricated Ge-doped optical fibres, as well as information on defects, additional impurities, and the theoretical underpinnings of TL in fibres. The concept of TL in the TLD-100 chip, which is lithium fluoride doped with magnesium and titanium (LiF: Mg, Ti), is also briefly introduced, with a comparison with OSLD nanoDot. Computed tomography (CT) dosimetry, in particular within the paediatric realm of head and chest examinations, will then be discussed prior to reviewing the final sub-topic of this thesis in relation to computed tomography pulmonary angiogram (CTPA).

2.2 Thermoluminescence Theory

In the TL dosimetry method, insulators or semiconductors emit thermally stimulated light by absorbing the energy from ionising radiation. The essential ideas of TL are related to the impurities that produce localised energy levels within the forbidden energy band gap in TL material (Bos, 2001). Figure 1 depicts an energy band model for the TL process (Zubair et al., 2020).

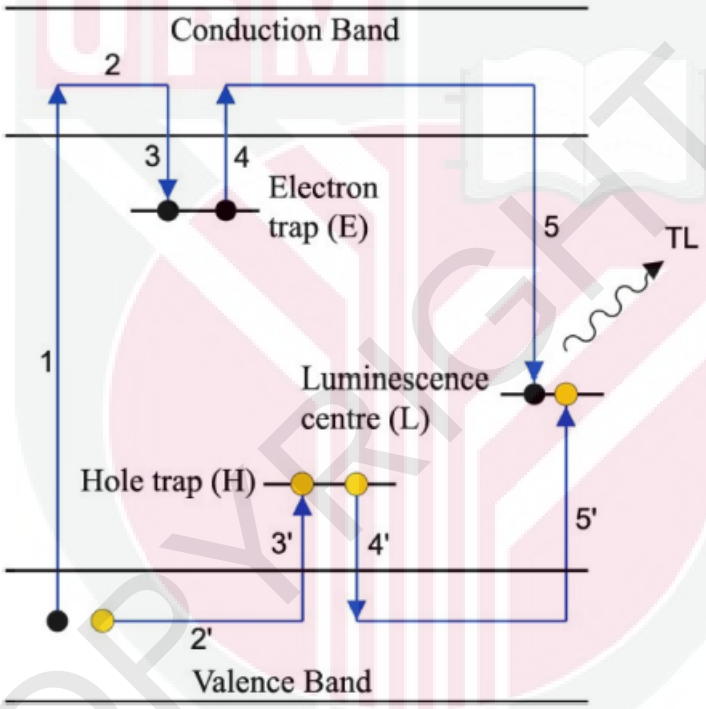

Figure 2.1: Simple energy band model for TL process
(Source: Zubair et al., 2020)

According to the TL theory by Attix (2008), there is a bandgap between the valence and conduction bands in a perfect crystal structure that precludes any possible electron or hole traps from occurring. Whenever the presence of defects affects the structure of such a crystal, one or more extra energy levels can be introduced at the crystal defect within the forbidden gap. The ones immediately above the valence band are hole traps,

while the ones immediately below the conduction band are electron traps. A radiation-induced ionisation event will elevate an electron into the conduction band; as shown in Figure 2.1, it will move to an electron trap (a location in the crystal lattice where a negative ion is absent). The hole that is left behind moves to a hole trap. These traps should be deep enough in terms of potential energy to hold an electron or hole in place for a long time before being intentionally heated to release one or both of them.

In Figure 2.1, the effect of the heating process is also depicted. The electron is released first, presuming that the hole trap in this phosphor is deeper than the depth of the electron trap. The emission of a light photon occurs when the electron reenters the conduction band, migrates to a luminescence centre, and recombines with the hole. Re-trapping of charge carriers at a defect, radiation-less recombination, and luminous recombination are the three primary types of processes that are significant to the TL phenomenon. The light signal required for dosimetry measurement is only produced via the luminescent recombination process.

The process of emptying the trap depends heavily on the two main TL parameters, which are the temperature of the environment and the depth of the trap. While the temperature can be controlled externally, a material's trap depth is determined by inherent defects. If the temperature is increased, the trapped charge carriers may gather enough energy to escape. The quantity of energy absorbed affects how much light the dosimeter emits. In summary, when the dosimeter is heated, the light is detected and transformed into an electrical signal by a photomultiplier tube (PMT), and the resulting signal is integrated and displayed to read the signal of the dosimeter after exposure to ionising radiation (Attix, 2008).

2.3 Thermoluminescence Dosimeter (TLD-100)

Under the brand name TLD-100 (Harshaw Chemical Company, USA), lithium fluoride doped with magnesium and titanium (LiF: Mg, Ti) is currently available for use in TL dosimeters. Since then, TLD-100 has grown in popularity because of their soft-tissue equivalency, minimum signal fading, and high sensitivity for low radiation dose evaluations (Kry et al., 2007). Due to its relatively large size, restrictions on its use in radiotherapy, and perhaps hygroscopic qualities, TLD-100 does not satisfy the standards for dosimetry within soft tissues (Bradley et al., 2014).

In the initial stages of the radiation dosimetry system, TLD is the most dependable and well-established passive radiation detection method. They come in many forms, such as powder, rods, and chips. LiF is nearly tissue-similar because its effective atomic number is roughly identical to tissue. Additional beneficial characteristics of phosphor-based TL dosimeters include reproducibility and precision to within 3%, as well as a comparatively low minimum detectable dosage down to the sub milligray (mGy) level (Kry et al., 2007).

TLD still has a lot of disadvantages despite the benefits described above. According to Mahdiraji et al. (2015), LiF phosphor is a hygroscopic substance with a limited spatial resolution that readily absorbs water from its surroundings. These characteristics present a challenging dilemma, particularly for applications in interstitial or intercavitary environments and radiotherapy, where a precise estimation of the patient dose is crucial. TLD contains complex energy traps and a complicated glow curve, making it challenging to fully examine the kinetic parameters. For a large-scale survey, TLD preparation and readout are less viable due to their time-consuming

nature. The TLD's destructive readout feature, which requires a reset before a new measurement, restricts the ability to reanalyse the absorbed dose. The inherent uncertainties in TL dosimetry remain a crucial topic that necessitates consistent and continuing research (Mahdiraji et al., 2015). This is especially true when employed in diagnostic imaging.

These limitations have led to the investigation of novel TL-based media in the form of silicon dioxide (SiO_2) optical fibres. These media offer beneficial elements that might expand the practical usefulness of TLD. By using the beneficial TL properties of commercially available telecommunication fibres, novel-produced Ge-doped silica fibres are able to overcome the numerous limitations previously described (Bradley et al., 2012).

2.4 Optically Stimulated Luminescence Dosimeter (OSLD)

One commercially available OSLD that is now used for dose measurements in medical imaging is a carbon-doped aluminium oxide Al_2O_3:C nanoDot (Landauer Inc.). When exposed to ionising radiation, energy is deposited in the form of trapped charge carriers. Figure 2.2 depicts the three stages of the basic optically stimulated luminescence (OSL) ionising radiation detection process, which requires three steps. The dosimeter is subjected to ionising radiation in stage (a), and any energy deposited there could result in excitations and ionisations. Stage (b) relates to the time when the dosimeters are kept before measurement and are characterised by a metastable concentration of trapped electrons and holes. By stimulating the electrons by exposure to light of a certain wavelength, the recombination of electrons and holes will happen

prior to luminescence, representing the information stored in the dosimeter (Musa et al., 2017).

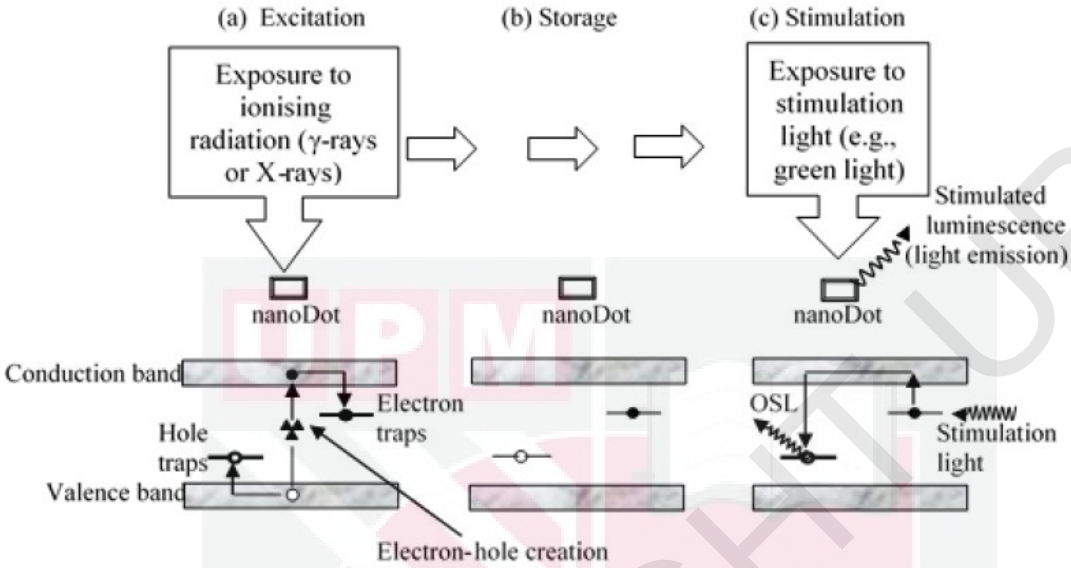

Figure 2.2: Schematic diagram illustrating the stages of the OSL process
(Source: Musa et al., 2017)

Al_2O_3:C OSLDs have been widely employed for radiation dosimetry in clinical radiotherapy because of their good dosimetric characteristics. High sensitivity, the ability to re-analyse, high-speed readout, and the removal of thermal annealing processes are a few of these features (Ponmalar et al., 2017). Due to its small size, robustness, use, and lack of radiography artefacts, it is also known as a practical dosimeter (Scarboro et al., 2015).

The characterisation and subsequent direct conversion of the light signal to absorbed dose in diagnostic imaging is significantly in question because of the much lower photon energy and dose applied, as OSLD have only been majorly studied in radiotherapy fields (Mrčela et al., 2011). Prior research has shown that the Al_2O_3:C's

comparatively high effective atomic number (Z_{eff} = 11.28) compared to tissue's (Z_{eff} = 7.3) results in a strong photoelectric effect in the material for low-energy photons (Al-Senan & Hatab, 2011). They claim that for various reasons, the conventional calibration method for clinically applicable OSLD in diagnostic imaging is insufficient.

One of the causes is that the vendor-supplied calibration only evaluates the 80 kilovoltage (kV) beam quality in relation to the dosage reading. In other words, irradiating the nanoDot to a photon energy greater or less than 80 kV may offer a considerable discrepancy in dose measurement unless a proper energy adjustment factor is implemented. This is a result of the vendor calibration process not accounting for the variation in beam quality between various scanning requirements. One of the primary problems with using OSLD in the diagnostic sector is that its energy response is highly dependent on fluctuations in beam quality. Energy correction factors can be used to reduce these energy dependence-related uncertainties (Musa et al., 2017).

Additionally, the irradiated OSLDs must be kept in light-proof packaging before being read out because Al_2O_3:C is particularly light-sensitive. Three RQT beam qualities are paired with three photon energies for CT dosimetry. These include RQT 8 (100 kV), RQT 9 (120 kV), and RQT 10 (150 kV), according to the IAEA (2007). For CT dosimetry, a manual methodology that includes cross-calibration with a standard ionisation chamber is required to compute absorbed dose methodologies and uncertainties. For TLD and optical fibre dosage measurements, a structured review of calibration methodologies is still necessary for each RQT beam quality.

2.5 Development of Fabricated Ge-doped Optical Fibre

2.5.1 University of Surrey and Malaysian Consortium

A consortium effort between the University of Surrey, United Kingdom and Malaysian counterparts comprising Universiti Putra Malaysia (UPM), Telekom Research & Development Sdn Bhd (TM R&D), Multimedia University (MMU), University of Malaya (UM), Universiti Teknologi Malaysia (UTM) and Malaysian Nuclear Agency (Nuklear Malaysia) focuses on optical fibre fabrication as new dosimetry system, grounded by the principle of TL. Theoretically, the electron trapping mechanism of amorphous crystals of the fibres is highly dependent on the optimum existence of defect centres generated by the dopant materials (Yusoff et al., 2005). The consortium group exploits this theory by employing the technique of modified chemical vapour deposition (MCVD) for doping fabricated silicon glass with various dopant materials and concentrations using gas flow rate, reinforced together with fibre-pulling amenities which can accommodate fibre fabrication with different sizes and shapes. The group's primary objective is to fabricate tailored-made optical fibres characterised according to various beam qualities within the radiation sphere of radiotherapy and diagnostic imaging for potential clinical use in the near future with a fraction of the price of current commercial dosimeters (Bradley et al., 2014).

Investigations on implementing commercial and fabricated optical fibres in radiotherapy dosimetry have commenced by various research groups, as reviewed by Bradley et al. (2012). Several preliminary findings of these amorphous crystals have positively surpassed that of standard phosphor-based TLDs, such as having high spatial resolution suitable for precise radiotherapy application, water resistant for

possible usage in intercavitary and interstitial dose measurements, mechanically sturdy, chemically inactive, biocompatible and reproducible. UPM group alone is currently exploring the dosimetry characteristics of fabricated Ge-doped optical fibres in several radiation fields encompassing high-energy radiotherapy photons (Fadzil et al., 2018), protons (Hassan et al., 2019), small field dosimetry (Lam et al., 2019), and electrons (Zakaria et al., 2020), to name a few. In all such studies, the TL performances of irradiated fibres have shown considerable potential for dosimetric applications in radiotherapy.

Contrariwise, this group of amorphous silica glass are yet to be fully explored in the field of diagnostic imaging and low-energy X-ray photons, with to-date preliminary findings only being issued in four articles by Alyahyawi et al. (2017, 2018), Ramli et al. (2015) and Rozaila et al. (2016). These groups have investigated the response of novel optical fibres in general radiography dosimetry, such as chest and extremities X-rays, mammography, and dental imaging. Through their experiments, they stated a distinct energy dependency, with the highest TL yield displayed by the fabricated fibres against phosphor-based TLD-100. The optical fibres also showed good dose linearity irrespective of the dopant concentrations, dimensions or fibre shapes. They have also suggested that fabricated optical fibres with Ge as the dopant can provide several potential benefits as opposed to the gold standard TLD-100, predominantly in terms of the higher sensitivity at diagnostic imaging radiation doses. A general issue has been refining the dosimetry characteristics of the optical fibres in other medical imaging modalities, such as fluoroscopy and CT, with the latter being the radiation dosimetry of interest in the present study.

2.5.2 Fabrication of Ge-doped Optical Fibre

The optical fibres for dosimetry are primarily fabricated using the MCVD technique (Bradley et al., 2012, 2017). A schematic of an MCVD system is illustrated in Figure 2.3 (Zubair et al., 2020). An MCVD system comprises two major components: the gas and material delivery system and the lathe. The first step in creating an optical fibre using the MCVD process is to fuse two hollow silica tubes, one of which served as an exhaust to catch any leftovers from the vapour deposition. A horizontal lathe that rotates around an axis while being heated by an oxygen-hydrogen flame is used to turn the tubes. A computer-controlled mixture of gases, comprising silicon tetrachloride ($SiCl_4$), germanium tetrachloride ($GeCl_4$), phosphoryl chloride ($POCl_3$), and boron tribromide (BBr_3), is subsequently injected into the tube. These gases are contained in a device known as a "bubbler," which enables the oxygen (O_2) carrier gas to enter the bubbler and transport the gaseous form to the silica tube. To guarantee uniformity of the deposited layer obtained at the tube's inner wall, the lathe turns the tube. For the deposition to occur along the length of the tube, the burner moves transversely along its longitudinal axis. According to the weight gas flow rates, different dopant concentrations for optical fibres are manufactured through this process.

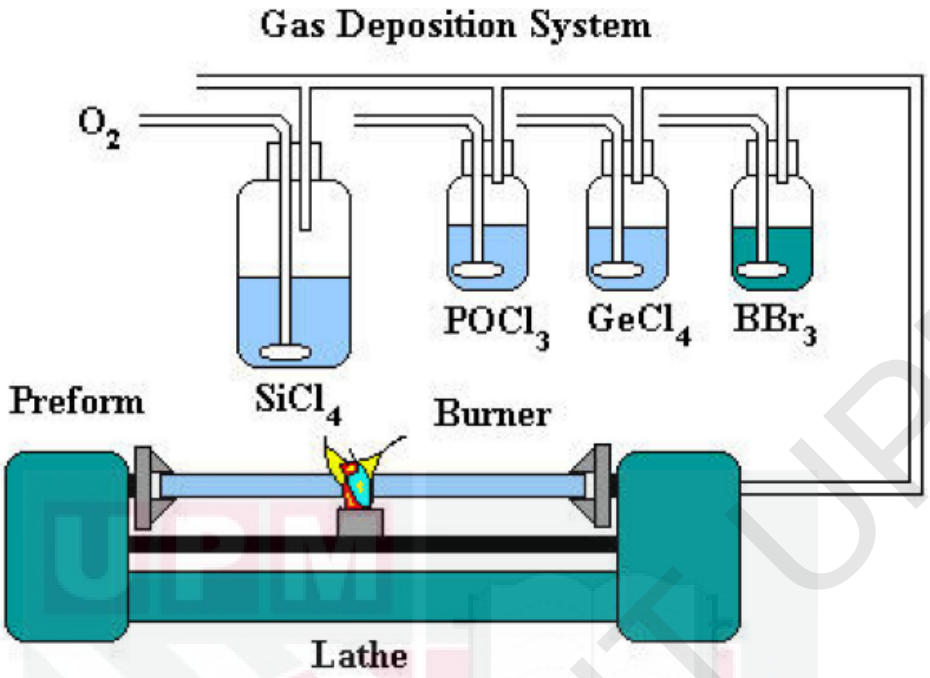

Figure 2.3: A schematic diagram of the MCVD system
(Source: Zubair et al., 2020)

According to Bradley et al. (2012), white soot or other impurity particles are left on the glass tube's interior due to a chemical reaction that takes place when the gases are heated. The glass tube itself would serve as the fibre's covering or cladding while the heat fused the soot to create what would ultimately become the core of the optical fibre. Here, two distinct preforms are made: a fused or collapsed preform for the cylindrical optical fibre's basic shape and an unfused or uncollapsed preform for the optical fibre's eventual flat shape. Next, the thick preform rod is transformed into thin silica glass with desired shapes and sizes using the fibre drawing process, the last stage in fabricating Ge-doped optical fibres. The preform is then inserted vertically into the drawing tower after being detached from the exhaust. The drawing tower's furnace heats one end of the preform, and as the glass melts, gravity helps lower it. The soft glass is stretched until a fine glass fibre is created, using a glass globe as a weight at the other end of the preform. As previously indicated, two distinct preforms are created

separately: a fused or collapsed preform for the cylindrical optical fibre's basic structure and an unfused or uncollapsed preform for the optical fibre's eventual flat shape as shown in Figure 2.4 (Ghomeishi et al., 2015).

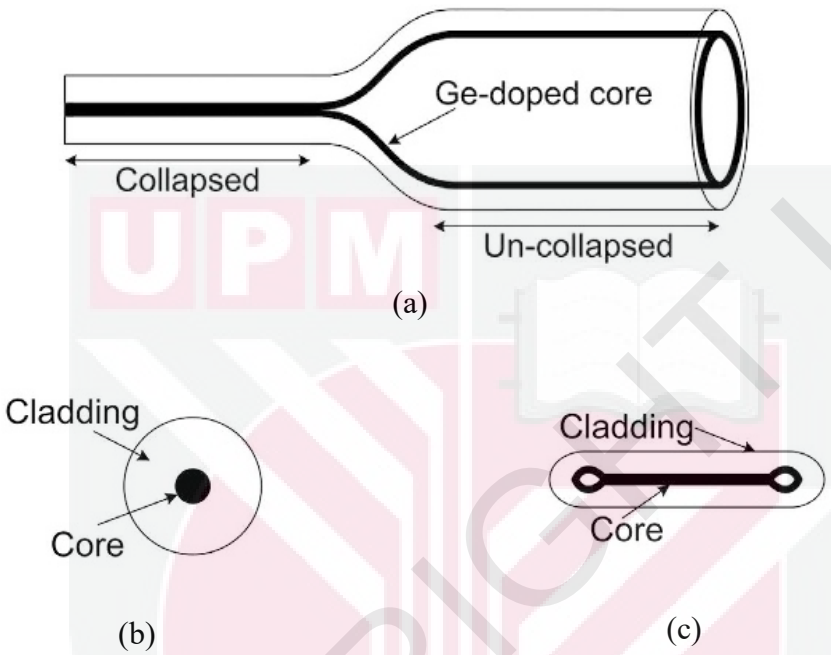

Figure 2.4: A schematic diagram of (a) collapsed and uncollapsed preform for eventual (b) cylindrical and (c) flat shape optical fibre
(Source: Ghomeishi et al., 2015)

Mahdiraji et al. (2015) have demonstrated the TL sensitivity of the fibre when the fibre is collapsed into flat fibre (FF). The findings imply that strain-related defects are produced by collapsing and fusing the tube walls, greatly enhancing the TL yield, and even more so if an impurity or dopant is present in the collapsing surface region. More research has to be done to investigate the impact of fibre structure on fibre dosimeter performance. One of the most important studies has also been done by Mahdiraji et al. (2015), which identifies that the fibre's Ge-doped core produces most of the TL signal while the cladding only contributes a small amount. Figure 2.5 (a) shows a schematic

diagram of the typical geometry of commercial optical fibre and (b) examples of cut fibres (Bradley et al., 2012).

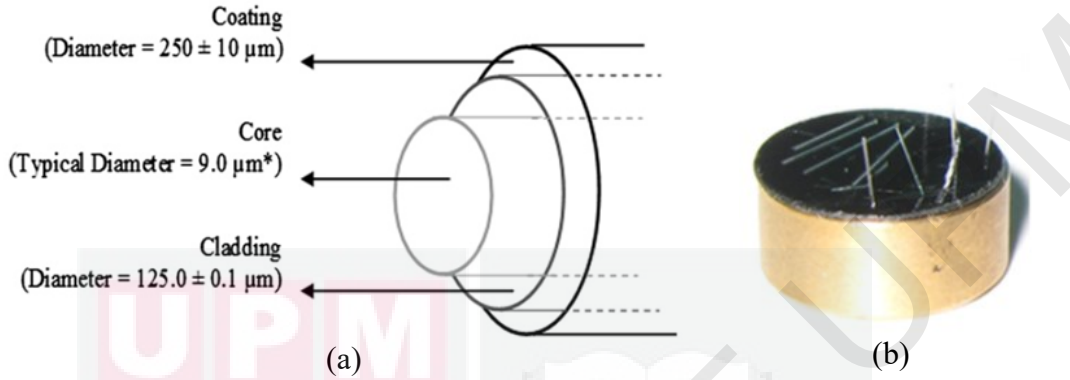

Figure 2.5: A schematic diagram of the typical geometry of commercial optical fibre and (b) examples of cut fibres
(Source: Bradley et al., 2012)

2.5.3 Structures of Ge-Doped Optical Fibres

Molecular structure and composition support the fundamentals of luminescence, with Bradley et al. (2012) reviewing the many related trapping centres and activation energy. SiO_2 is made up of a network of four oxygen atoms around each silicon ion, or amorphous, as shown in Figure 2.6 (a). Meanwhile, the amorphous oxide's tetrahedral structure bonds with silicon by sharing oxygen atoms in a six-membered ring, as in Figure 2.6 (b).

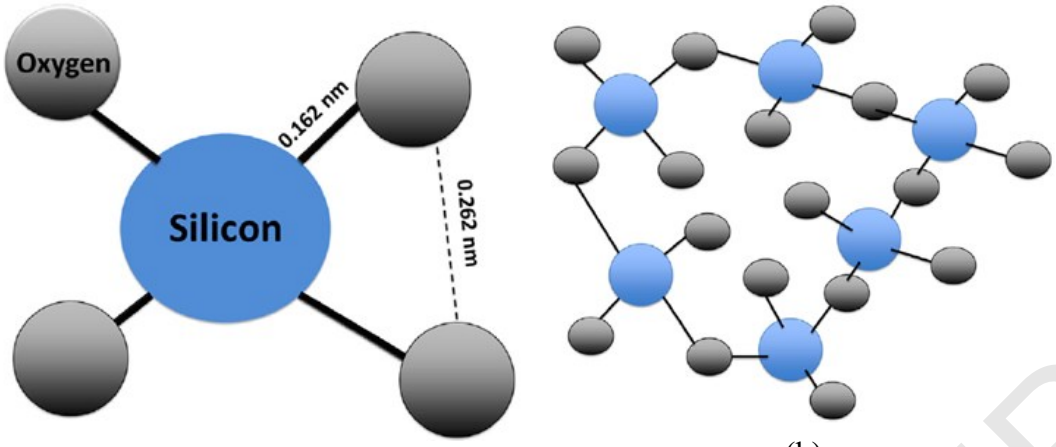

Figure 2.6: (a) Silica molecule and (b) tetrahedral ring lattice of silica molecules
(Source: Bradley et al., 2020)

The production of a refractive profile in fibre optics that causes total internal reflection, which is required for an optical guide, is made possible by doping with particular atoms. As shown in Figure 2.7, oxygen atoms typically bind only to silicon or germanium atoms when used as a dopant (Yaakob et al., 2011). In such TL systems, Ge in SiO_2 performs as a deep electron trap to prevent any possible signal thermal fading. Figure 2.7 illustrates the simplified structures of Ge-doped silica glasses as adapted from Yaakob et al. (2011).

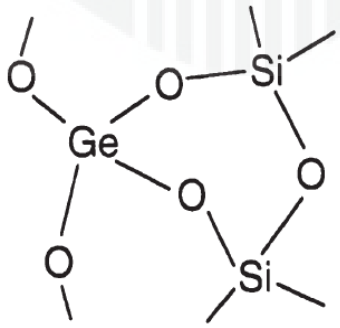

Figure 2.7: Schematic of Ge-doped amorphous silica structural makeup
(Source: Yaakob et al., 2011)

2.5.4 Materials of Ge-Doped Optical Fibres

Different materials have been suggested for radiation dosimetry, including germanium (Benabdesselam et al., 2013; Hashim et al., 2013; Moradi et al., 2017; Zahaimi et al., 2014), boron (Mahdiraji et al., 2015), aluminium (Hashim et al., 2013), phosphorus (Tomashuk et al., 2014) and thulium (Alawiah et al., 2015). In the past ten years, the Ge-doped fibre has received the greatest press attention primarily for medical applications, such as in vivo dosimetry. Ge-doped fibres have been used in most research projects for several reasons, as they have been proven to be an efficient production technique and since the majority of conventional telecommunication optical fibres are composed of this material. Ge-doped fibres also have quite high radiation sensitivity in terms of sensitivity.

Nevertheless, Mahdiraji et al. (2015) have compared the performance of Ge-doped and Ge-Boron (Ge-B) doped fibres. Ge-B-doped fibre is found to have less energy dependency than Ge-doped fibre due to its lower effective atomic number and proximity to human tissue. Compared to Ge-doped, this substance would be a better choice for medical purposes. However, there are just a few publications on this material because of the high production costs caused by boron doping and the limited availability of such fibres. Due to these reasons, the current study concentrates on doping material with germanium.

2.5.5 Effective Atomic Number Ge-Doped Optical Fibres

According to Asni et al. (2010), it is customary to aim for the effective atomic number (Z_{eff}) value that is ideally human soft-tissue equivalent (i.e., 7.42), with Begum et al. (2015) adding that a Z_{eff} value that is human tissue equivalent depends on the incident

photon energy and is directly related to how likely it is that primary photon interactions will occur within the detector's medium. According to Begum et al. (2015), the Z_{eff} values of the optical fibres investigated are within the range of human bones (11.6–13.8). In a study by Noor et al. (2014), the atomic number of fabricated fibres is also found to be bone equivalent in the range of 13.2 to 13.7. The bone equivalency, as opposed to soft tissue, would likely contribute to the energy dependency of the response of the optical fibres. As such, the energy correction factor has to be applied in the absorbed dose methodology during the dose conversion calculation.

2.6 Application of Ge-doped Optical Fibre in Diagnostic Radiology

Diagnostic radiology exposures consist of kilovoltage X-ray pulses that are frequently delivered within a few milliseconds (ms). The optical fibre has the ability to precisely collect dosages in such exposures without compromising the image quality, thanks to its sub-millimetre (mm) size and quick electron-hole dynamics. However, this group of amorphous silica glass is yet to be fully explored in the field of diagnostic imaging and low-energy X-ray photons, with to-date preliminary findings at the start of current research only being issued in four articles by Alyahyawi et al. (2017, 2018), Rozaila et al. (2016) and Ramli et al. (2015).

The basic characteristics studied are similar within the groups mentioned above, such as linearity, energy dependence, dose reproducibility, dose sensitivity and fading. Linearity or dose-response is defined as the functional dependence of the intensity of the measured signal upon the absorbed dose. An ideal radiation dosimeter response should be directly proportional to the radiation dose to ensure the new dosimeter has a linear dose-response over a wide range of doses (Hashim et al., 2013). Ramli et al.

(2015) evaluated new Ge-doped amorphous silicon flat fibres as TLDs in confirming patient ESD in diagnostic exams for doses of 0.02 mGy up to 3 mGy. It has been demonstrated that the flat fibres display linearity between TL yield and dose. Rozaila et al. (2016) demonstrated the linearity of the TL yield for X-ray doses ranging from 0.5 mGy to 10 mGy. The potential for using brand-new, Ge-doped collapsed photonic crystal fibres (PCF-Ge) as efficient dosimeters for diagnostic applications, particularly for chest imaging, has also been evaluated by Alyahyawi et al. (2017). PCF-Ge fibres are produced due to extrinsic doping and flaws caused by strain at the fused inner walls of the collapsed fibres. Alyahyawi et al. (2018) used dental and mammography imaging modalities to investigate the applicability of Ge-B collapsed flat and disc-shaped Ge-doped fibre in a separate study. These fibres made of silica have also demonstrated good linearity across a large dynamic range of dosages.

The energy dependence or beam quality is the variation of the detected TL output for a fixed dose as a function of the energy of the absorbed radiation. As the dosimetry systems are calibrated at a specified radiation beam quality and used over a much wider energy range, the variation of the response of a dosimetry system with energy dependence requires correction. Ideally, the energy response should be flat (the system calibration should be independent of energy over a certain range of radiation qualities). The energy correction must be included in determining the dosimetric quantity for most measurement situations (Hashim et al., 2013). Ramli et al. (2015) found that the Ge-doped flat fibres exhibit a clear energy-dependent response to photons produced at potentials between 40 and 150 kilovoltage-peak (kVp). Rozaila et al. (2016) used X-rays produced at accelerating potentials ranging from 20 kVp to 200 kVp to demonstrate a similar energy response.

The precision of dosimetry measurements specifies the reproducibility of the measurements under similar conditions and can be estimated from the data obtained in repeated measurements. High precision is associated with a small standard deviation of the distribution of the measurement results. Ideally, dosimeters should be reproducible. The reproducibility of each material to a certain dose level can be determined by calculating the standard deviation of a repeated set of measurements under the same exposure and reading condition (Hashim et al., 2013). The reproducibility of the Ge-doped flat fibres examined by Ramli et al. (2015) is better than the 3% standard deviation after repeated testing.

In TL-based dosimetry, sensitivity is defined as TL yield per unit dose per unit mass of the material (Hashim et al., 2013). It is a significant dosimetric characteristic that exhibits material response against any particular dose range. Alyahyawi et al. (2017) have shown a response of 10 times more sensitive fibres than TLD-100, indicating they are an effective tool for the measurement of relatively low doses, while PCF-Ge by Rozaila et al. (2016) fibres producing noticeably greater TL response than that of the phosphor-based dosimeter TLD-100 has been shown by seven times. Ge-doped optical fibres have also proven to have excellent sensitivity in two diagnostic dose ranges for mammography and dental imaging, according to research by Alyahyawi et al. (2018).

One of the last basic characteristics studied is fading, a spontaneous thermal-relaxation signal loss. According to Ramli et al. (2015), the percentage of fading for flat fibres over 14 days was 24%, and Rozaila et al. (2016) observed that the rate of fading for the stored TL signal over 35 days post-irradiation was 20%. According to Alyahyawi

et al. (2017), the rate of fading for PCF-Ge over 30 days post-irradiation was discovered to be 20%. Ge-doped optical fibres have also proven to have a low fading rate, according to research by Alyahyawi et al. (2018). From the present results, it is concluded that Ge-doped fibres represent a viable system for use in diagnostic dosimetry, with corrections being made for the various factors influencing TL yield. In addition, the results show that novel fabrications of doped-silica glass produce TL yields that make them attractive as dosimeters in the diagnosis range of doses, offering high sensitivity for X-ray doses. Table 2.1 shows the energy and dose range used and the characteristics studied by each author within the diagnostic imaging field of Ge-doped optical fibre investigation.

Table 2.1: Application of Ge-doped optical fibre in diagnostic radiology

Author	Exposure	Characteristics Studied
Alyahyawi et al. (2017)	80 kVp to 120 kVp 0.1 mGy to 10 mGy	Linearity Energy dependence Sensitivity Fading
Alyahyawi et al. (2018)	25 kVp to 70 kVp 5 µGy to 1 Gy	Linearity Energy dependence Sensitivity Fading
Ramli et al. (2015)	40 kVp to 150 kVp 2 mGy to 150 mGy	Linearity Energy dependence Reproducibility Fading
Rozaila et al. (2016)	20 kVp to 200 kVp 0.5 mGy to 10 mGy	Linearity Energy dependence Fading

2.7 Computed Tomography Radiation Dosimetry

2.7.1 General Concept

CT scans are essential for diagnosing various illnesses in children, especially in their early years of development (Brody et al., 2007). Radiation dose is overemphasised in youngsters because of their lesser size and higher radiosensitivity (Pearce et al., 2012). There are numerous causes for variation in cancer risk after radiation exposures in youngsters in contrast to grownups for a certain dose. First, tissues and organs that are fully developed are less sensitive to radiation effects than the ones that are currently developing (Hall, 2002). Second, the oncogenic effect of radiation can last for a lengthy, latent period. Hence, an infant or child has a lengthier lifespan expectancy wherein the possible oncogenic effects of radiation are manifested in contrast to adults. Third, for a child's smaller cross-sectional area, the radiation exposure after a predetermined set of CT parameters will lead to a dose that is reasonably higher in contrast to an adult (Mathews et al., 2013). Because of this, their radiation doses from CT examinations must be correctly handled. The radiologists and radiographers cannot efficiently handle the radiation doses of their patients if they do not have valid approximations of the radiation dose being provided. This has led radiologists to solicit a technique to approximate the paediatric patient's doses from CT numerous years earlier (Berdon & Slovis, 2002).

The advantages and disadvantages of the regular terminologies established to approximate CT dose, CT dose index (CTDI), dose length product (DLP) and effective dose (ED) shall be described in this chapter. The dissimilarity between the measured CTDI volume ($CTDI_{vol}$) and the $CTDI_{vol}$ electronically displayed on the CT scanner

depicts a clinical predicament. Displayed $CTDI_{vol}$ signifies the radiation dose provided to a plastic phantom, which varies considerably from the dose provided to the patient, subject to the patient's physical size (Boone et al., 2011). This issue has led to the establishment of uncomplicated techniques to compute effective paediatric doses (Huda et al., 2008). Even though the effective dose is easy to compute, it is not expected to denote the radiation dose for a single patient. The necessity for a straightforward, suitable technique to approximate paediatric patient doses contributes to establishing size-specific dose estimate (SSDE), the latest CT dose index. SSDE is an upgraded approximation of the patient dose to improve the conduct of the patient's radiation dose. However, it still presents several limitations that will be discussed later in this chapter (Boone et al., 2011).

2.7.2 Phantoms for CT Dose Measurement

As referred to in Seeram (2015), to systematise the dose estimation and deliver a clinically representative geometry, the researchers proposed that the ionisation chamber be positioned in one of two cylindrical phantoms throughout the measurement of radiation. The smaller phantom represents a patient's head, while the larger phantom represents a body. Both phantoms' lengths are 15 centimetres (cm). The head phantom diameter is 16 cm, while the body phantom diameter is 32 cm. Both phantoms are solid acrylic with holes at fixed positions on the phantom to house the pencil ionisation chamber (Figure 2.8). Strauss and Goske (2011) stated that occasionally, a 10-cm cylindrical phantom is incorporated with the two typical CTDI phantoms to cover the range of patient sizes from full-term newborns to adult patients.

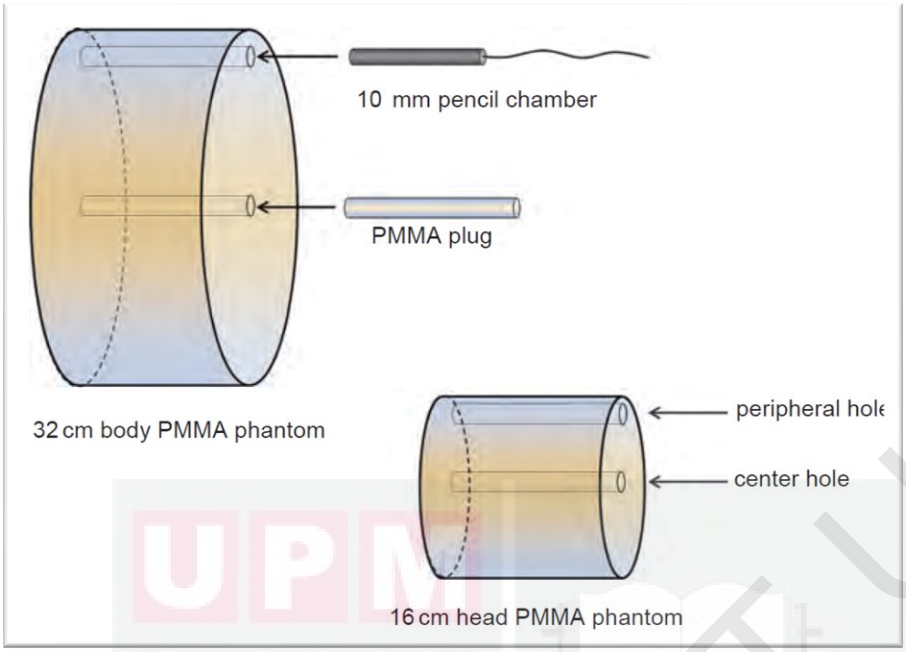

Figure 2.8: Polymethyl methacrylate (PMMA) phantom with a pencil ionisation chamber
(Source: Bushberg et al., 2020)

The measurement method is to position the ionisation chamber in one of the phantom holes, obtain a scan, and document the quantity of electric charge produced by the chamber. Next, the chamber is relocated to the subsequent hole and the process is repeated. Relocating the chamber to another hole permits the dose to be measured at multiple positions inside the phantom. Normally, the dose differs between positions even when a similar method is applied, and thus, it will ultimately contribute to weighted CTDI ($CTDI_w$) (Seeram, 2015). It is to be noted that the CTDI phantom, irrespective of its diameter, does not generate a realistic model of X-ray attenuation inside the patient (Strauss & Goske, 2011).

2.7.3 CT Dose Metrics

Figure 2.9 demonstrates that the usual dose distribution within the transverse plane of a cylindrical 32 cm diameter phantom is not approximately identical in comparison to the 16 cm diameter phantom (relative numerical values shown are just for example). In a 16 cm diameter phantom, the surface or periphery dose is nearly equivalent to the measured dose in the centre. On the other hand, in a 32 cm diameter phantom, the surface or periphery dose is almost twice the centre-measured dose (Strauss & Goske, 2011). Since the X-ray beam revolves 360 degrees around the patient's body, the entrance skin dose is higher than the exit skin dose. It is more evident in a 32 cm diameter phantom because of the greater X-ray attenuation by the surface phantom layers (Seeram, 2015).

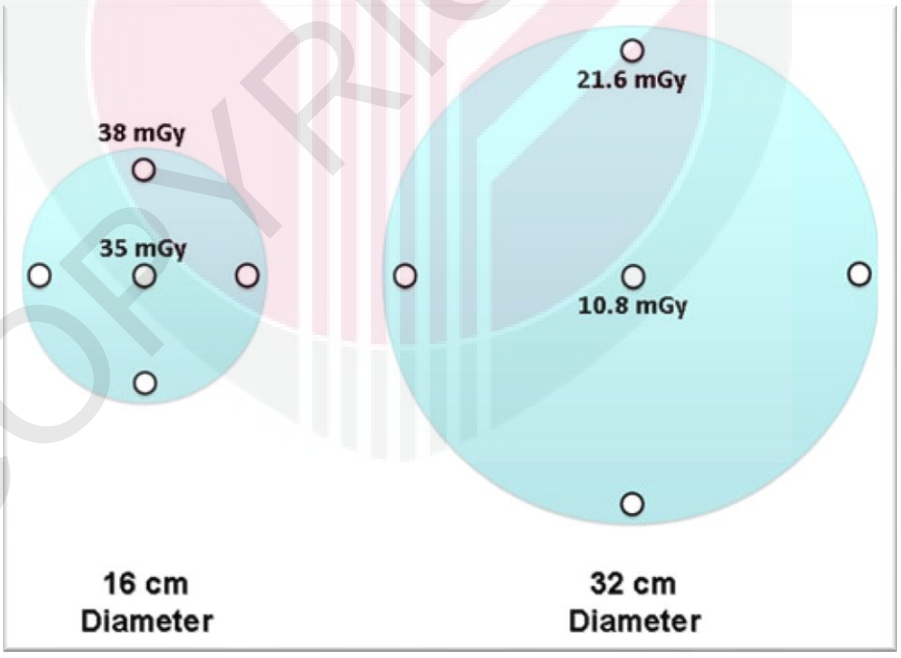

Figure 2.9: Typical results of CTDI dose measurements
(Source: Strauss & Goske, 2011)

2.7.4 Weighted CTDI ($CTDI_w$)

Weighted CTDI ($CTDI_w$) is a single dose established as the average dose within the cross-sectional area of Figure 2.9, whereas $CTDI_{100}$ is radiation measured along a 100-mm pencil chamber length.

$$CTDI_w \text{ (mGy)} = 1/3\ CTDI_{100\ centre} + 2/3\ CTDI_{100\ surface} \qquad \text{Equation 2.1}$$

$CTDI_w$ denotes the average dose in the patient's x-y axis compared to the z-axis. Adding the centre and surface measurements using a 1/3 and 2/3 weighting factor delivers a decent approximation of the phantom average dose, giving rise to the weighted CTDI (Seeram, 2015). Nevertheless, this method only approximates the average dose over the x and y phantom transverse planes throughout a continuous axial or helical scanning with a pitch of 1 (Strauss & Goske, 2011).

2.7.5 Volume CTDI ($CTDI_{vol}$)

The distance the CT table translates throughout one X-ray tube rotation is defined as pitch, while the pitch to the slice thickness or beam collimation ratio is called a pitch ratio. Once the distance the table translates throughout one whole X-ray tube rotation is equivalent to the slice thickness or beam collimation, the pitch ratio is 1:1 or 1 (Seeram, 2015). In other words, relative to the X-ray beam width, the distance the patient couch travels throughout the whole helical scanning will generate an additional variable that influences the delivered dose (Strauss & Goske, 2011). Volume CTDI ($CTDI_{vol}$) deals with variations in the speed of patient translation over the gantry to approximate the average dose in the cross-sectional area of the cylinder phantom.

$$CTDI_{vol}\ (mGy) = n * T * CTDI_w / I = CTDI_w / pitch \qquad \text{Equation 2.2}$$

Where n and T are interpreted as detector elements used (n) and the measurement of each detector element (T), I is the gantry couch speed, and pitch = I / (n ∗ T). $CTDI_w$ and $CTDI_{vol}$ doses are usually stated in units of milliGray (mGy).

2.7.6 Dose Length Product (DLP)

Since $CTDI_{vol}$ delivers an approximation of exposure per slice of a tissue, the dose length product (DLP) contributes to calculating the entire quantity of exposure for a sequence of scans (Seeram, 2015). DLP similarly indicates the radiation energy transmitted to the CTDI phantom. DLP is calculated by:

$$DLP\ (mGy\text{-}cm) = CTDI_{vol} * scan\ length \qquad \text{Equation 2.3}$$

The scan length is the phantom length in the z direction exposed by the radiation scan. The units of DLP are mGy-cm, which is directly proportional to the scan length. It is interesting to note that radiation dose and the volume of the patient's tissues irradiated by the primary beam will influence the patient's risk from ionising radiation related to a CT examination. Therefore, the longer the patient's scanned length (along the z-axis), with every other aspect staying constant, the greater the patient's radiation risk. Thus, though DLP signifies a dose index to a phantom and not to a patient, bigger DLP values may propose a higher risk to the patient (Strauss & Goske, 2011).

Most CT scanners electronically display two dose indices, CTDIvol and DLP. The CTDIvol is displayed in mGy units for every accomplished scan. Each displayed CTDIvol is accompanied by DLP, as stated in mGy-cm units, which depends on the

scan length along the z-axis. For both indices, the object of the displayed doses is based on a cylindrical clear plastic phantom, either 16 cm or 32 cm in diameter.

2.7.7 Estimated Paediatric Radiation Dose during CT

As mentioned previously, $CTDI_{vol}$ is not a practical estimation of paediatric patient dose. To diagnose and treat a child, this turns out to be a much bigger problem clinically for the radiologist to balance the risk after radiation exposure alongside the clinical info to be achieved. The radiologist and radiographer are having difficulty measuring CT radiation dose obtained by paediatric patients and subsequently approximating their patients' risk due to the lack of an effective technique to measure paediatric patient dose from the displayed $CTDI_{vol}$ (Strauss & Goske, 2011).

Patients from neonates to large adults have an extensive disparity of attenuating path lengths for the X-rays travelling from the focal spot to the CT scanner detector. $CTDI_{vol}$ is interpreted as the single dose that best approximates the dose distribution provided to a standard plastic phantom in a specific CT scanner by particular scan parameters. $CTDI_{vol}$ delivers a generalised technique to approximate and relate the radiation yield of different CT scanners. $CTDI_{vol}$ is, therefore, denoted as a dose index of CT scanner radiation output and not a patient dose index. Since DLP is based on $CTDI_{vol}$, it depicts the entire energy transmitted to a phantom, not to a patient. $CTDI_{vol}$ is also not envisioned as a suggestion for the patient's dose. It does not signify the patient's dose and thus must not be documented in the patient's medical record as the patient's dose (Boone et al., 2011).

The American Association of Physicists in Medicine (AAPM) Report No. 204 (Boone et al., 2011), accessible on the AAPM website entitled "Size-Specific Dose Estimates (SSDE) in Paediatric and Adult Body CT Examinations," is documented to permit radiographers and radiologists to approximate independent patient dose from displayed $CTDI_{vol}$ values. These correction factors may be used to approximate patient doses designed for various patient sizes, from the smallest to the largest. However, it should not be concluded that this dose approximation is the best, although the SSDE is a far better approximation for patient dose than $CTDI_{vol}$. Once the size of the CTDI phantom used by the scanner to display the $CTDI_{vol}$ is correctly determined, the precision of SSDE is supposed to be within 20% (Boone et al., 2011). It is to be noted that since SSDE is not error-free, it must only be designated as an approximation of the patient dose and not the actual patient dose.

Since tissue heterogeneity and precise patient anatomy are not considered, SSDE still has difficulties accurately predicting the effective dose. The exposure in low-dose CT procedures can increase by up to 38% of the total patient dose when two CT radiographs are needed to estimate the anteroposterior (AP) and lateral diameters to compute the SSDE of each patient (Schmidt et al., 2013). With stylised adult reference models and Monte Carlo simulations, Shrimpton et al. (1998) first presented the effective dosage per DLP conversion factors, or k-factors (mSv mGy^{-1} cm^{-1}), to assist physicians in calculating doses. For several frequently used CT procedures, updated k-factors were created by different organisations and later extended for paediatric patients (Huda et al., 2008). Deak et al. (2010) then created new conversion factors for various scanning scenarios that were sex- and age-specific. However, in the case of underweight and obese patients, the current k-factors, which are based on reference

phantoms, contribute a considerable over- or underestimation of the effective dose. The effective dosage is directly calculated either by Monte Carlo simulations using mathematical or voxelised models (Geleijns et al., 2015) or experimental measurements on real anthropomorphic phantoms (Zhang et al., 2013).

Accurate ED calculation from a CT scan necessitates a thorough description of the scanner's technical parameters and a sizable number of computational phantoms that consider anatomical variances for various scan acquisition types. Numerous organ dose calculations have also been developed. The first ones, including CTDosimetry, CTDOSE, eXposure, and WinDose, were based on fictitious adult stylised phantoms, with basic geometric shapes used in place of organs, which resulted in significant dosimetry mistakes (up to 21%). In more recent years, the vendor-provided DoseWatchTM application from General Electric Inc. in Milwaukee, USA, based on SSDE, has been able to deliver results after CT scan examinations are completed (Lee et al., 2012). However, it is still based on phantom doses using calculation methods and state-of-the-art software, and they are not independently verified with any radiation dose measurements except with a pencil ionisation chamber in a CTDI phantom (Huda et al., 2008). As a result, confirming the measurement independently using a dosimeter is a crucial additional step to verify the accuracy of the dose administered.

One can use a humanoid phantom made of tissue-equivalent material to obtain dosage readings in areas designated as different organs and run CT scans on it. According to Moore et al. (2014), direct ESD and organ dose measurements can be done using two techniques. The first is through the in vivo dosimetry technique, which is used directly

on patients undergoing CT scans. Since the dosimeter is on the patient's body surface, ESD is typically the only one that can be performed. This method will provide a precise reading of the radiation dosage received by the patient or by superficial organs like the thyroid and eyes. Unfortunately, it is difficult to put into practice in a genuine clinical context because it must be ethically considered and approved with patient agreement and cooperation. The second technique involves estimating ex vivo doses using an anthropomorphic phantom. Even while patient size differences are not considered until the age group for the proposed study is indicated, it allows for precise absorbed dose estimation in the targeted organs or tissues.

These phantoms are frequently built to be anthropomorphic or mimic an average-sized person's shape, size, and anatomy, reducing disparities caused by diverse shapes, sizes, and compositions. Medical dosimetry has frequently employed paediatric anthropomorphic phantoms (Dougeni et al., 2011). Compared to other methods that use straightforward phantoms like cylinders or sets of slabs, experimental direct dose measurements on anthropomorphic phantoms may be more precise (Zhang et al., 2013). The initial step in dose optimisation and comparison with diagnostic reference levels may be determining the effective dose through organ doses related to medical radiation exposure. Furthermore, the degree of radiation danger related to medical exposure can be determined by accurately estimating organ doses. To minimise errors in organ localisation and extent, the proper placement of dosimeters requires knowledge of the precise location and size of each organ in the phantoms. Since the relative positioning of dosimeters in a phantom slice would considerably alter the observed dose, the placement of organs and tissues is crucial in dosimetry to obtain accurate measurements of absorbed radiation. This would reduce the amount of

uncertainty brought on by incorrect organ placement assumptions made during absorbed dose estimations. While large organs like the brain and lung have a non-uniform and occasionally complex organ dose distribution in the body, small radiosensitive organs like the thyroid and eye lenses have a generally uniform organ dose distribution. Due to the significant non-uniformity of dose distributions inside a phantom slice, more dosimeters may be needed for bigger organs (Chapple et al., 2001).

Since organ dose is the primary factor taken into account in radiation risk when a relatively small volume of the patient is exposed to radiation, organ dose may be a better metric for evaluating patient risk than effective dose. Tube output and beam penetrating power may be increased by increasing tube voltage and exposure duration. This indicates that the relationship between the absorbed dosage and the tube voltage and exposure time is essentially linear. Furthermore, as the effective dose is the sum of the weighted equivalent doses in all of the body's tissues and organs, it makes sense that the organ doses must be known in order to estimate the effective dosage. According to the IAEA standard, the ESD is the most suitable metric for determining a patient's dose after a single radiography exposure (IAEA, 2007). The usual procedure for measuring ESD involves placing a dosimeter directly on the patient or phantom surface. For this study, newly fabricated Ge-doped optical fibres will be investigated and compared against TLDs and OSLDs in an attempt to obtain dose maps on radiosensitive organs.

2.8 Paediatric Computed Tomography

Strategies for reducing radiation dose are essential to lowering the chance of developing cancer in the future, particularly in the paediatric population. All CT scans should be subject to a risk-benefit analysis, with a focus on the paediatric population due to its higher risk of radiation-induced illnesses like thyroid cancer, brain cancer, leukaemia, breast cancer, and skin cancer (Almujally et al., 2022). The increased risk of malignancy in children can be attributed to several factors. First, compared to tissues that are mature and in a steady state, growing tissues have a tendency to be more sensitive to ionising radiation. Second, an older adult may die from other causes before the dosage has a clinically meaningful effect, whereas youngsters have a lifetime to display the carcinogenic consequences of ionising radiation. Lastly, the smaller cross-sectional area of a child may result in a dose of radiation that is concentrated in a smaller amount of tissue together with a probability of repeated examinations as they may undergo more than one scan due to the longer follow-up period. Compared to the same scan performed on adults, this may lead to a larger effective dose (Brody et al., 2007).

Tissue absorption influence refers to how different tissues in the human body absorb radiation when exposed. When ionising radiation interacts with biological tissue, it deposits energy along its path, leading to various biological effects. The extent to which different tissues absorb radiation depends on factors such as tissue composition, density, radiation type, energy and dose. For instance, denser tissues, such as bone, attenuate (absorb and scatter) radiation more effectively than less dense tissues, like muscle or fat. Different types of radiation have varying penetration depths and energy deposition characteristics in tissue. Higher-energy radiation can penetrate deeper into

tissues before being absorbed, while lower-energy radiation is absorbed more quickly. Higher doses also result in greater energy deposition and potential biological damage within tissues (Hall & Giaccia, 2006).

In 2007, the International Commission on Radiological Protection (ICRP) published a new set of tissue weighting factors (W_T) for radiosensitive organs such as the lung ($W_T = 0.12$), thyroid ($W_T = 0.04$), brain, and lens ($W_T = 0.01$). The tissue weighting factor is a relative measure of the risk of stochastic effects that might result from irradiation of that specific tissue. It accounts for the variable radiosensitivities of organs and tissues in the body to ionising radiation (ICRP, 2007).

Organs with lower tissue weighting factors are considered to pose a mild risk in terms of radiation exposure. These organs are less sensitive to radiation-induced effects and have lower probabilities of developing radiation-related health issues. Examples include the bones, brain, and skin. Meanwhile, organs with moderate tissue weighting factors are associated with a moderate risk of radiation-induced effects. These organs have a moderate sensitivity to radiation and may have a higher probability of developing radiation-induced health issues than organs with lower weighting factors. Examples include the liver, kidneys, and gastrointestinal tract. Finally, organs with higher tissue weighting factors are considered to pose a severe risk in terms of radiation exposure. These organs are susceptible to radiation-induced effects and have a higher probability of developing radiation-induced cancers and other severe health issues. Examples include the lungs, breast and thyroid gland (ICRP, 2007).

The categorisation of organs into mild, moderate, and severe risk is a simplification. The actual risk associated with radiation exposure depends on various factors, such as the dose received, the type of radiation, and individual susceptibility. However, tissue weighting factors may provide a valuable framework for assessing the relative risks of radiation exposure to different organs and tissues.

For a head CT scan of a 1-year-old, Brenner et al. (2001) found a paediatric fatal cancer risk of 0.06% (about 1 in 1800) for a single slice CT scan. The lifetime attributable risk of cancer incidence for a low-dose chest scan is comparable for 5-year-old children at 0.06% as well. Conversion coefficients for a neonate are roughly 5-fold higher for the head and 3-fold greater for the chest than for a 15-year-old due to higher organ dosages in younger children. The chest coefficients are higher than those for the head at all ages because the chest contains more radiosensitive organs than the head (Feng et al., 2010).

2.8.1 Paediatric Head Scan

An X-ray imaging technique known as a cranial computed tomography scan produces cross-sectional images of the head, including the skull, brain, eye sockets, and sinuses. According to Jibiri and Adewale (2014), a cranial CT scan is used to diagnose or monitor the following conditions: abnormal head or neck development, brain haemorrhage, brain tumours, head injuries, and hydrocephalus. The utilisation of CT scan examinations in the paediatric population has significantly increased during the last thirty years. In hospitals across Asia, including Malaysia, 12.2% of paediatric CT exams were conducted according to an IAEA study on CT frequency (Vassileva et al., 2012). About 75% of all paediatric CT exams were CT brain scans. Another 2012

study by Pearce et al. (2012) found that the risk of leukaemia was higher from CT brain examinations for younger patients than for older children. Paediatric patients in the United Kingdom who were exposed to CT brain radiation dosage of 50 mGy or higher were 2.8 times more predisposed to future risk of brain malignancy. Along with the brain and eye lens, which are exposed directly during head CT, other radio-sensitive organs are not directly exposed, which receive a lesser radiation dose via scatter radiation but are linked to relatively significant lifetime attributable risk such as thyroid (Kiani & Chaparian, 2023).

A single layer of highly active, proliferating epithelial cells makes up the lens, and some of these cells develop into mature lens cells, making them vulnerable to ionising radiation. Ionising radiation may cause cell mutation or death, which may disrupt the layer. This disruption might result in clouding or opacifying the eye's natural clear lens, blocking light from passing through and impairing vision (Abdulhamid et al., 2022). Depending on the device and technique, the radiation exposure to the eye during a brain CT is around 50 mGy. The eye's lens is highly radiosensitive; doses as little as 0.5 to 2 Gray (Gy) can result in observable opacities, while exposures as high as 4 Gy may result in secondary cataract formation and visual impairment. Children's eyes are particularly radiosensitive, with cataracts developing from less than half of this radiation. As such, the skin entrance dose of patients undergoing CT procedures is one of the dose descriptors for determining the level of radiation exposure, knowing fully well that ocular exposure during the CT scan could potentially induce cancer and cataracts (Jibiri & Adewale, 2014).

The thyroid has been identified as an organ with relatively low sensitivity to ionising radiation, as cell damage may occur at a low dose. However, it may take decades or a lifetime for malignancies to manifest in children younger than 12 years old. In other words, thyroid cancer is categorised as a stochastic radiation impact, and it is incredibly uncommon to develop in children, with an annual incidence of fewer than one case per million in most developed nations (Sinnott et al., 2010). However, the thyroid that receives 50–100 mGy of radiation dosage during CT of the head and neck has been linked to a higher risk of thyroid cancer in children (Ghaznavi, 2020).

Table 2.2 compares six investigation groups that implement TLDs to measure entrance skin dose (ESD) to radiosensitive organs of paediatric phantom and actual patients during head CT examinations. Brady et al. (2011) employed TLDs to measure the doses to the brain, lens, and thyroid in an anthropomorphic phantom of a 10-year-old child for a CT brain scan. The brain received the highest average absorbed radiation, 33.6 mGy. Although it was still well below the deterministic threshold of around 1.5 Gy for cataracts (Valentin, 2007), the lens dosage of 19.3 mGy was also quite high. 1.67 mGy of scattered radiation was observed at the thyroid. In another study by Feng et al. (2010), a 5-year-old paediatric phantom was used to evaluate radiosensitive organs during head CT. Compared to the brain, which only received 17.9 mGy, the lens received a considerably greater organ dose of roughly 25.9 mGy. A 2.5 mGy thyroid dosage was also recorded.

In an actual clinical patient study, four study groups were found to investigate the skin doses by using TLDs. Abdulhamid et al. (2022) examined 17 paediatric patients aged six months to 17 between three hospitals. According to measurements made from the

TLD signals, the mean dose to the lens of the eyes and thyroid was 5.87 mGy and 3.42 mGy, respectively. These values were lower than those in Iran by Toossi et al. (2018) in CT brain procedures of 15 paediatric patients between the ages of 1.5 and 15 years old in five different hospitals (16.05 mGy and 5.89 mGy). It was also lower than the lens dosage that Jibiri and Adewale (2014) found during cranial CT treatments on five patients in a Nigerian hospital aged 1.5 to 18 years old, which was 31.14 mGy. The greatest dose was observed by Stathopoulos et al. (2016) when examining paediatric children who underwent head CT scans in Athens, ranging in age from newborns to 15 years old. On the eye lens, the mean surface dosage was 37.01 mGy. Thyroid, however, was only recorded at 1.95 mGy in this investigation. The CT procedures, the acquisition method, and the patient's age between different hospitals contributed to the dose variation.

Table 2.2: Comparison of entrance skin doses in paediatric phantoms and real patients by using TLDs for brain CT

Author	Subject	Measured Dose
Abdulhamid et al. (2022)	6 months to 17 years old (Total of 17 patients)	Lens (5.87 mGy) Thyroid (3.42 mGy)
Brady et al. (2011)	10-year-old phantom	Brain (33.6 mGy) Lens (19.3 mGy) Thyroid (1.67 mGy)
Feng et al. (2010)	5-year-old phantom	Brain (17.9 mGy) Lens (25.9 mGy) Thyroid (2.5 mGy)
Jibiri and Adewale (2014)	1.5 to 18 years old (Total of 5 patients)	Lens (31.14 mGy)
Stathopoulos et al. (2016)	Neonates to 15 years old (Total patients not mentioned)	Lens (37.01 mGy) Thyroid (1.95 mGy)
Toossi et al. (2018)	1.5 to 15 years old (Total of 15 patients)	Lens (16.05 mGy) Thyroid (5.89 mGy)

Patient-specific dosimetry is crucial for paediatric patients despite the many challenges. Therefore, a reliable dosimeter that offers an accurate and efficient way to evaluate skin dose is essential. Additionally, because the thyroid and eyes are superficial organs, the calculated surface dose can provide a reliable estimate of the organ dosage to the thyroid gland and ocular lens (Stathopoulos et al., 2016).

2.8.2 Paediatric Chest Scan

Identifying paediatric diseases such as bronchiectasis, pulmonary metastases and assessing lung volume all require chest CT scans. Despite the advantages, a single chest CT delivers a radiation dose that is roughly 10 times more than a chest radiography examination (Kubo, 2019). The effective dose that paediatric chest CT patients typically receive varies between 1.1 and 7.5 millisieverts (mSv) for each examination (Alkhorayef, 2020). Due to the near proximity of the thyroid to the thorax in children, thyroid exposure during chest CT scans may occasionally be inevitable. According to the ALARA principle, unwanted direct thyroid exposure during paediatric CT scans should be avoided if possible. However, due to the thyroid's proximity to the apices of the lungs and the superior mediastinum, it was typically included in the imaged volume during chest exams. With an incidence rate of 14.4 per 100,000 people and an average annual growth rate of 3.6% due to exposure to ionising radiation and other risk factors, thyroid cancer is the most common endocrine cancer (Kim et al., 2020). The mean dosage administered to the thyroid gland and the age of exposure are the main risk factors for radiation-induced thyroid cancer, with children being at higher risk than adults (Iglesias et al., 2017).

Table 2.3 compares three investigation groups implementing TLDs to measure average doses to radiosensitive organs of paediatric phantom and adult patients during chest CT examinations. Brady et al. (2011) employed TLDs to calculate the organ-absorbed doses for a CT chest scan on an anthropomorphic phantom of a 10-year-old. The thyroid received the highest average absorbed radiation, which was 10.9 mGy, while 9.9 mGy was recorded in the lung. A 5-year-old paediatric phantom was utilised in another investigation by Feng et al. (2010) to measure radiosensitive organs during thorax CT. Organ doses of around 3.40 mGy and 5.41 mGy were recorded for the thyroid and lung, respectively. However, scanning paediatric patients is discovered to be challenging in a real clinical investigation due to various ethical issues. One study by Ramač et al. (2013) assessed and compared ESDs using the standard CT methodology for adult thorax. The average thyroid dose determined by TLD-100 measurements on 60 participants was found to be 4.68 mGy. Despite the many challenges of recruiting paediatric patients for dosimetry study, patient-specific dosimetry is still essential for paediatric patients. Therefore, a reliable dosimeter that accurately and efficiently evaluates skin dose is required (Stathopoulos et al., 2016). According to Tian et al. (2014), there are a variety of organ equivalent doses due to the different anatomical locations and radiosensitivity of each organ in the body. As a result, one of the strongest metrics to distinguish individual radiation burden is the dose exposure on each superficial organ (Tian et al., 2014).

Table 2.3: Comparison of average doses in paediatric phantoms and adult patients by using TLDs for chest CT

Author	Subject	Measured Dose
Brady et al. (2011)	10-year-old phantom	Lung (9.9 mGy) Thyroid (10.9 mGy)
Feng et al. (2010)	5-year-old phantom	Lung (5.41 mGy) Thyroid (3.40 mGy)
Ramač et al. (2013)	22 to 89 years old (Total of 60 patients)	Thyroid (4.68 mGy)

2.8.3 Computed Tomography Pulmonary Angiography

One imaging method to visualise pulmonary arteries to diagnose and treat pulmonary embolisms (PE) is CT pulmonary angiography (CTPA). PE is regarded as a serious health condition with a high death rate that necessitates an early and precise diagnosis, especially in patients at high risk (Harun et al., 2020). The paediatric population has begun to recognise PE more frequently in recent years. Significant factors may be the growing use of central venous catheters and improvements in therapies for people with chronic medical illnesses that predispose them to PE (Hennelly et al., 2016). PE happens when a blood clot lodges in a pulmonary artery and blocks blood flow to a portion of the lung. The widespread use of upper extremity and subclavian central venous catheters, particularly in neonates, is probably the leading cause of the migration of a venous clot starting in the upper extremities, known as deep venous thrombosis, to the lung (Thacker & Lee, 2016).

The current gold standard for diagnosing PE in children is multidetector computed tomography (MDCT) with the CTPA procedure (Thacker & Lee, 2016). To determine the accurate collimation from the level of the thyroid cartilage to the diaphragms,

imaging acquisition begins in the supine position with scout images. Over the main pulmonary artery and the right ventricle, a region of interest (ROI) is then designated. After administering contrast, a series of low-dose scans are taken at the ROI's position to visualise the contrast bolus. The method used the most frequently with children is bolus tracking. Another benefit of CTPA is that it can evaluate alternate diagnoses in children who do not have PE. In a paediatric CTPA study by Lee et al. (2009), they found that alternative diagnoses could be made in 59% of the instances, with pneumonia and atelectasis being the most frequent diagnoses in 77% of the cases, with positive results. Malignancy, congenital cardiac disease, pulmonary hypertension, pericardial effusion, rib fractures, fat embolism, and right atrial thrombus were among the less frequent diagnoses to be found.

However, with the advancement of CT technology, more than 90% of CTPA tests may be performed. The danger of radiation-induced cancer in populations is increased by the fact that a single CTPA examination can provide up to 10 mSv of effective dose (ED) (Sauter et al., 2018). Apart from other interventional radiology methods, it is also one of the sources of radiation exposure with the greatest among all CT techniques due to its complicated acquisition settings and prolonged scanning time. High amounts of radiation exposure can have a negative impact on radiosensitive organs such as the thyroid, breast, skin, and eye lens (Brenner, 2012). According to Frush and Yoshizumi (2006), the effective dose from CTPA (with 80 to 100 kVp) varies typically from 1 to 4 mSv, which is comparable to the range of a standard non-angiographic chest CT and lower than the standard angiography dose (from 5 to 20 mSv) in children. To further lower the amount of radiation exposure associated with CT examinations in children, a reduced-radiation-dose approach based on the patient's age may be helpful (Brody

et al., 2007). To ensure that CTPA is the preferred method to diagnose the clinical condition, it is essential to estimate the radiation exposure a patient receives during CTPA by using appropriate dosimeters.

Limited information is available regarding the current practice of paediatric CTPA procedures in Malaysia, according to Aamry et al. (2020). However, utilising the $CTDI_{vol}$ and DLP metrics, they were able to estimate the dose given to paediatric patients during CTPA. The median $CTDI_{vol}$ and DLP for newborns are 3.6 mGy and 113.9 mGycm, respectively. Meanwhile, the median $CTDI_{vol}$ and DLP for infants under 2 years of age are 5.8 mGy and 205.5 mGycm, respectively. In a different CTPA study by Karim et al. (2019), TLD chips were implanted into slabs of an adult phantom. The thyroid gland received the highest dose, 16.94 mGy, followed by the skin and breast, each receiving 12.95 mGy and 12.61 mGy. The gold standard in applied radiology for assessing absorbed doses using TLD chips was similar to this study or any passive dosimeter.

Assessments made specifically for each patient's exposure to radiation, as opposed to a broad population, may be able to overcome the constraint of radiation dose estimation. Prior to arriving at an evaluation of the risk of cancer, it is crucial to ascertain an organ-absorbed dose (Harun et al., 2020). Usually, the ED is calculated using phantoms or computer models representing the adult human body (Valentin, 2007). This weighted sum of doses absorbed in all exposed organs in the body accounts for variations in organ radiosensitivity. Although it is believed that ED best predicts overall stochastic radiation risk, absorbed dose measurements in the exposed organs are necessary to accurately estimate individual radiation risks (McCollough et

al., 2010). Even when taking into account the age and body size of children, ED still has a substantial margin of error when attempting to predict a person's chance of developing cancer. Studies assessing paediatric CTPA dosage in the past either relied on manufacturer-provided radiation dose estimates of $CTDI_{vol}$ and DLP or were only conducted on phantoms (Huang et al., 2009). To the best of present knowledge, direct measurement of ESD of the thyroid during pediatric CTPA examinations has never been studied. The current study uses newly fabricated Ge-doped optical fibres to measure the ESD of thyroid and compare them with gold standard TLD-100 chips and OSLD nanoDot.

CHAPTER 3

RESEARCH METHODOLOGY

3.1 Study Location

A consortium effort between the University of Surrey, United Kingdom and Malaysian counterparts comprising Universiti Putra Malaysia (UPM), Telekom Research & Development Sdn Bhd (TM R&D), Multimedia University (MMU), University of Malaya (UM), Universiti Teknologi Malaysia (UTM) and Malaysian Nuclear Agency (Nuklear Malaysia) focuses on the development optical fibre fabrication as new dosimetry system, grounded by the principle of thermoluminescence.

The fabricated germanium (Ge)-doped optical fibres were manufactured in two research sites by their respective research groups. The Ge-doped preform was initially fabricated at the Modified Chemical Vapour Deposition (MCVD) laboratory at the Faculty of Engineering, Multimedia University (MMU). Successively, the Ge-doped preform was pulled into fibres with preferred shapes and sizes using the fibre drawing tower located at the Flat Fibre Laboratory, Faculty of Engineering, University of Malaya (UM).

After the fabrication process, the dosimetry characterisation study for selected optical fibre batches would be extensively studied by the UPM research group. For the current research, the optical fibres and other dosimeters were prepared at the Medical Physics Laboratory, Faculty of Medicine and Health Sciences, Universiti Putra Malaysia (UPM).

After the initial screening process, the optical fibres were sent to Quasi-S Technology Sdn. Bhd, Universiti Kebangsaan Malaysia (UKM) for a scanning electron microscopy with energy-dispersive X-ray spectroscopy (SEM/EDX) analysis prior to the commencement of the dosimetry study. The SEM/EDX scanning process was done by the research officers at Quasi-S Technology Sdn. Bhd.

Basic dosimetric characteristics irradiations for all dosimeters were performed at the Secondary Standard Dosimetry Laboratory (SSDL) at the Malaysian Nuclear Agency (Nuklear Malaysia), which is traceable to the primary standard dosimetry laboratory of the International Atomic Energy Agency (IAEA). A dosimetry study using pediatric phantom was accomplished at the Department of Radiology, Hospital Pengajar Universiti Putra Malaysia (HPUPM), while a small clinical study on real pediatric patients was investigated at the Radiology Department, Hospital Serdang. The signals from the dosimeters were read out at HPUPM and Nuklear Malaysia, respectively.

3.2 Study Design

An experimental approach was used to investigate the research objectives prior to the commencement of the final objective in which a small clinical study was done in a real clinical setting with pediatric patients.

3.3 Types of Samples

3.3.1 Fabricated and Commercial Ge-doped Optical Fibres

3.3.1.1 Modified Chemical Vapour Deposition (MCVD)

Chemical vapour deposition (CVD) is a process that employs chemical reactions of gases near substrates to deposit various materials such as coatings and powders. It is widely used in the semiconductor industry while modified chemical vapour deposition (MCVD) is a specialised technique used in the fabrication of optical fibres. It involves depositing thin layers of glass material onto a rotating substrate inside a silica tube. It is specifically employed for producing high-quality glass fibres with specific optical properties for use in telecommunications, sensors, and other optical applications (Doll et al., 2009).

Fabricating an optical fibre via the MCVD method began with fusing an ultra-pure hollow silica tube with another hollow silica tube, which acted as an exhaust to collect any residual from the vapour deposition. This was done at the MCVD laboratory at the Faculty of Engineering, Multimedia University (MMU). Figure 3.1 illustrates the said process. The tubes were placed on a horizontal lathe, which rotated on an axis, and as the tubes spun, they were heated with a hydrogen-oxygen flame. The two tubes were fused near the heating peak temperature of 2000 ºC. Prior to chemical vapour deposition, the now longer hollow silica tube was etched with a flow of sulphur hexafluoride (SF_6) in order to clean its inner part and remove any oily residue, allowing improved chemical bonding between the doping elements and the silica tube. After the etching process was completed, a computer-controlled mixture of gasses such as silicon tetrachloride ($SiCl_4$), germanium tetrachloride ($GeCl_4$), phosphoryl

chloride ($POCl_3$) and oxygen (O_2) was then passed through the inside of the tube as the tube spun. At the same time, a heat source of 1900 ºC from the traversing burner was moved sideways on the outside of the tube to heat everything. For this study, two investigated germanium (Ge) dopant concentrations of 2.3 mol% and 6 mol% were fabricated separately according to the weight gas flow rates.

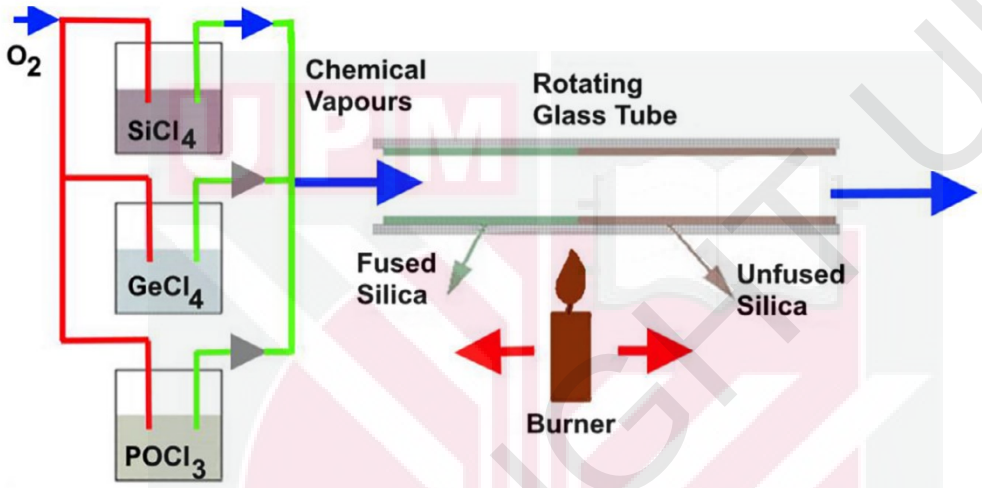

Figure 3.1: Modified chemical vapour deposition (MCVD) process
(Source: Addanki et al., 2018)

As the gases heated up, they underwent a chemical reaction that left white soot or impurity particles on the inside of the glass tube. The heat fused the soot, forming what would eventually become the core of the optical fibre, while the glass tube itself would form the fibre's covering or cladding. When there was enough fused soot, the heat was turned up to 2050 ºC until the soot itself turned into a glass as the movement of the torch within the rapidly spinning preform eventually caused the formation of a glass layer through the sintering process. Herein, two different preforms were separately made: fused or collapsed preform for the basic shape of cylindrical optical fibre and unfused or uncollapsed preform for what would eventually become a flat optical fibre. To fabricate the fused preform, the speed of the rotating tube was

decreased while the temperature flame was increased to 2200 °C to initiate the tube collapsing process into a solid cylindrical preform. The intense heat eventually made the tube collapse to form a solid rod. For unfused preform, the Ge-doped silica tube was left uncollapsed. Figure 3.2 shows (a) the heated Ge-doped preform during the MCVD process and (b) the resulting unfused and fused silica tubes. Finally, a high-temperature flame was placed at the end tip of the solid preform to separate the solid preform from the exhaust and the remaining glass rod. The internal structure of the optical fibre had been achieved, but it was still in the form of a big bulky rod, so the next step was to thin it out. Figure 3.3 shows the essential steps in the MCVD process.

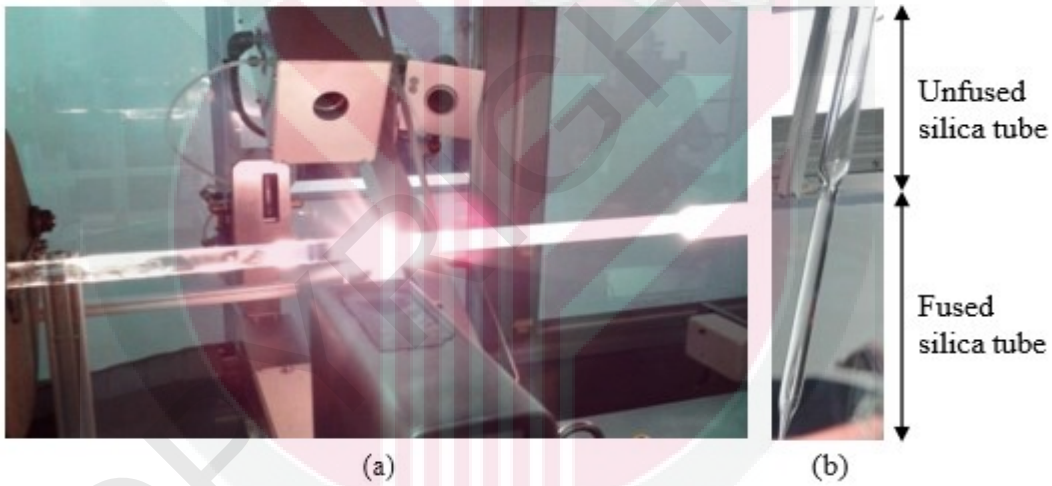

Figure 3.2: (a) Ge-doped preform during MCVD process and (b) unfused and fused silica tubes
(Source: Lam, 2019)

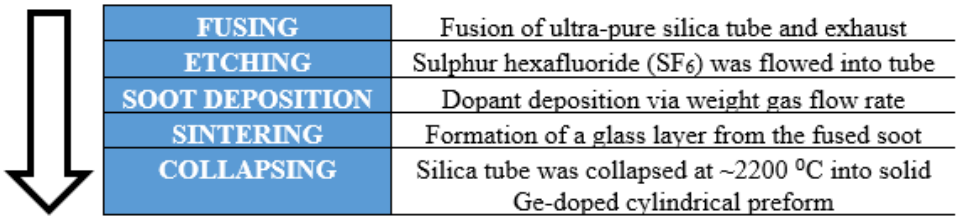

Figure 3.3: Important steps in the MCVD process

3.3.1.2 Fibre Drawing Process

The final step in fabricating Ge-doped optical fibres was to convert the bulky preform rod into thin silica glass with preferred shapes and sizes through the fibre drawing process. Once the preform was separated from the exhaust, it was then installed vertically into the drawing tower, as shown in Figure 3.4 (a) for the upper level and (b) for the lower level of the tower at the Flat Fibre Laboratory in UM. This fibre drawing process was done at the Flat Fibre Laboratory, Faculty of Engineering, University of Malaya (UM). The drawing tower's furnace heated one end of the preform to 2000 ºC, and as the glass softened, gravity helped pull it down. Then, using a glob of glass as a weight at the other end of the preform, the soft glass was stretched until a thin glass fibre was formed. Figure 3.5 (a) displays the thin glass fibre formed as the soft glass was stretched by using a glass drop as a result of the gravity weight at the end of the preform as shown in (b). A series of pullies measured the tension of the fibre as it was being drawn. A special automated dual laser system monitor ensured the fibre was precisely the right diameter by adjusting the feeding and drawing speed with an appropriate furnace temperature (Noor et al., 2014).

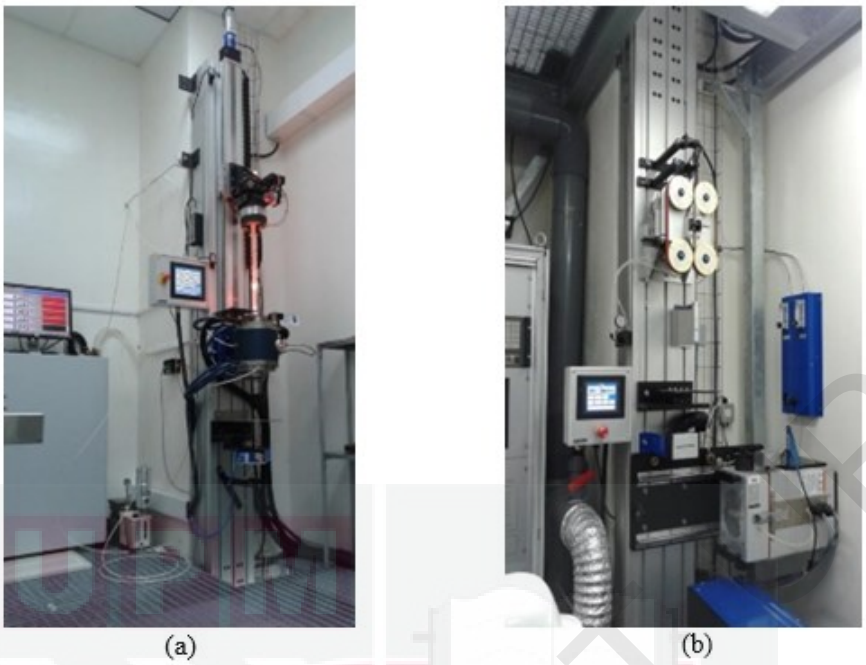

Figure 3.4: Double-storey fibre drawing tower facility comprising of (a) upper level and (b) lower level of the tower at the Flat Fibre Laboratory in UM
(Source: Ahmad Fadzil, 2020)

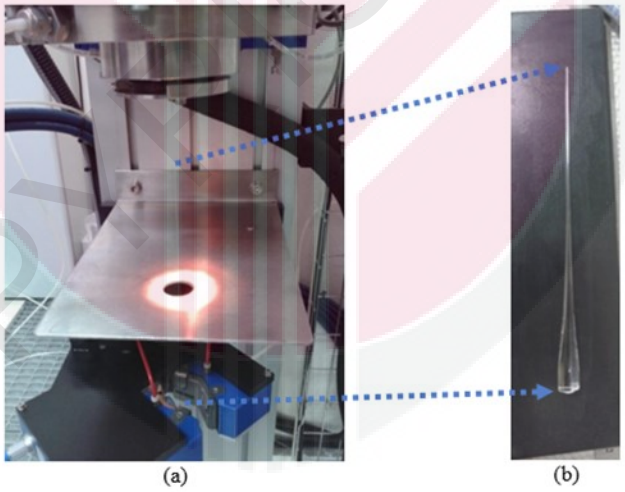

Figure 3.5: (a) Soft glass is stretched by using glass drop as a weight at the end of the preform until (b) thin glass fibre is formed
(Source: Lam, 2019)

As mentioned previously, two different preforms were separately made: fused or collapsed preform for the basis shape of cylindrical optical fibre and unfused or uncollapsed preform for what would eventually become a flat optical fibre. The fused

preform was drawn through the conventional fibre drawing process until cylindrical fibre (CF) with two investigated outer diameters of 475 ± 5 and 615 ± 5 µm were achieved. Once the unfused preform was installed vertically into the drawing tower, one additional step was taken for the drawing process of flat fibre (FF). A vacuum pressure of 25 kiloPascal (kPa) was applied to the internal surface of the hollow silica tube (Figure 3.6) to collapse it into a flat shape as the preform was drawn through the furnace at a temperature around ~2000 °C. The rest of the drawing process was similar to that of CF. Two different outer dimensions of FF were also investigated: (600 x 375) ± 5 and (625 x 170) ± 5 µm². Figure 3.7 displays the grouped blocks for all fabricated fibres used in this study based on different Ge-doped concentrations, shapes, and outer diameter dimensions produced through these comprehensive and detailed processes. These fabricated fibres were also purposely fabricated without polymer coating to be suitable for dosimetry applications, unlike the commercially available optical fibre used in telecommunication.

The fabricated Ge-doped optical fibre was compared with commercially available Ge-doped optical fibre made by CorActive, Canada. This commercial fibre (COM) had a 50 µm core diameter and a 125 µm outside diameter, and it included about 4 mol% of Ge as a dopant (Nawi et al., 2015).

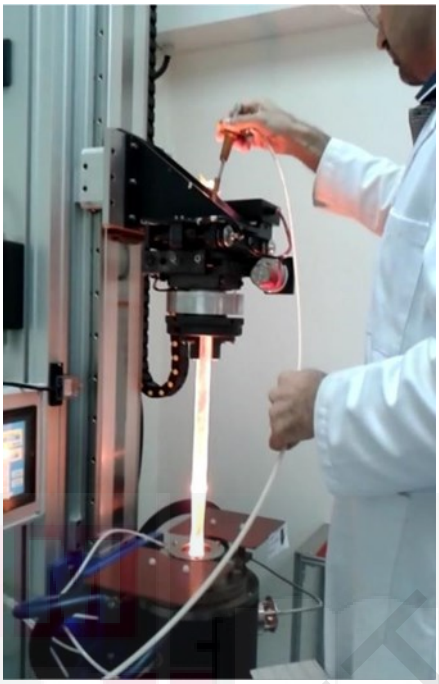

Figure 3.6: Vacuum pressure of 25 kPa was applied to the internal surface of the unfused silica tube to collapse it into a flat shape as the preform was drawn through the furnace at a temperature around ~2000 °C
(Source: Ahmad Fadzil, 2020)

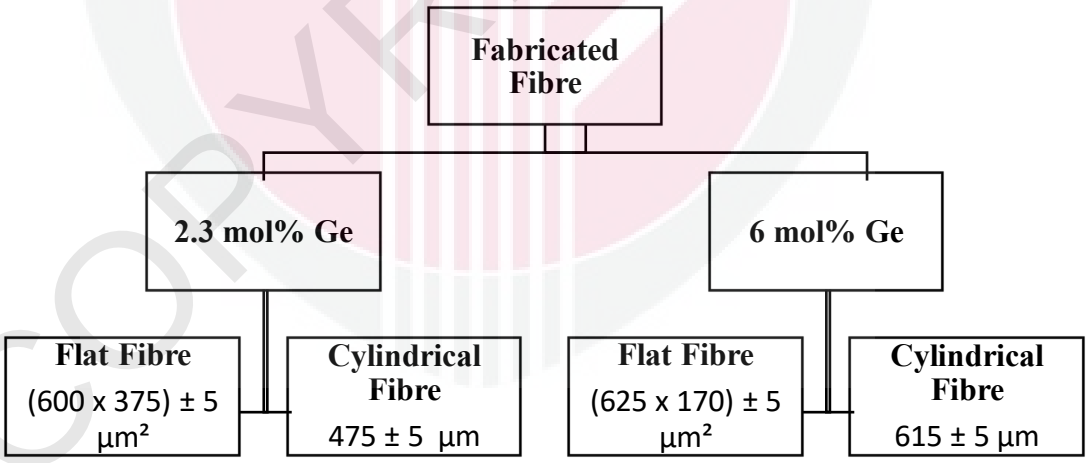

Figure 3.7: Details of the fabricated fibres used in this study

3.3.1.3 Cutting and Cleaning Process

The fabricated Ge-doped optical fibres with different shapes and sizes and commercial fibre were subsequently cut and cleaned at the Medical Physics Laboratory in the Faculty of Medicine and Health Sciences, Universiti Putra Malaysia (UPM). For commercially produced telecommunication fibre, the outer cladding of plastic polymer that came together with the fibre packaging as a protective coating was stripped away using a fibre stripper (Miller, USA). The commercial fibre was wiped with a methyl alcohol moisten-cotton cloth to remove any polymer cladding residue. This cleaning method did not need to be done on fabricated fibres as the fibres were not coated with the outer plastic polymer during the fabrication procedure. The commercial and fabricated fibres were cut into designated lengths of 6.0 ± 1.0 mm using the optical fibre diamond cutter (Thorlabs, USA). The fibre length was chosen to optimally accommodate the planchet size in the thermoluminescence dosimeter (TLD) reader during fibre readout. A vacuum tweezer was used to handle and group the thermoluminescence (TL) materials to minimise the surface abrasion of the fibre and the deposition of dust or finger oil, which might alter emission characteristics during readout. Figure 3.8 (a) shows fabricated Ge-doped optical fibres before cutting, (b) commercial fibres inside CorActive packaging and (c) the apparatus used for fibre preparation.

(a)

(b)

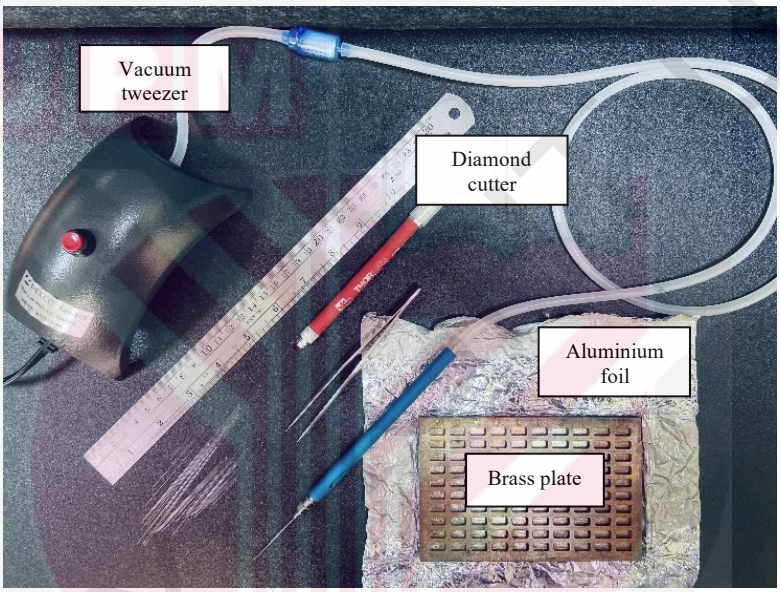

(c)

Figure 3.8: (a) Fabricated Ge-doped optical fibres before cutting, (b) commercial fibre inside CorActive packaging and (c) apparatus used for fibre preparation

3.3.1.4 Annealing Process

The fabricated Ge-doped and commercial fibres were annealed in a Carbolite furnace at the Medical Physics Laboratory (UPM) to normalise their thermal history and sensitivity before any screening, irradiations and subsequent TL measurements were made. This step was essential to eradicate glow peaks produced by low temperatures deemed unstable and eliminate leftover signals, ultimately allowing TL sensitivity reproducibility (Hashim, 2010). With the fibres placed in a brass plate holder wrapped

with aluminium foil, annealing was accomplished by heating the furnace and fibres from room temperature up to 400 °C at a rate of 10 ºC/s and then maintaining the furnace temperature at 400 ºC for 1-hour duration. After that, the fibres were kept inside the furnace to naturally cool down for 24 hours until equilibration at 27 °C room temperature to avoid thermal stress after being heated up (Thermo, 2002). Several optical fibre research groups have commonly used this temperature setting (Bradley et al., 2012; Moradi et al., 2017). They were kept in non-transparent plastic cases before and after irradiation to reduce the fibres to background lights and the environment. Figure 3.9 shows the Carbolite furnace used in this study.

Figure 3.9: Carbolite furnace for the optical fibre annealing process

3.3.2 Thermoluminescence Dosimeters (TLD-100)

Thermo Scientific™ TLD-100, which consisted of lithium fluoride doped with magnesium and titanium (LiF: Mg, Ti), was used in this study to compare the dosimetric responses with the newly fabricated optical fibre and commercial fibre. TLD-100 was chosen as it was one of the reference standards for health and medical physics dosimetry applications with near-tissue human equivalency. LiF crystals were

doped with titanium and magnesium to increase the number of traps and luminescence centres (Sadeghi et al., 2015), and they were usually used in the forms of chips, powders, rods, microcubes, disks and square rods. TLD-100 chips with 3.2 mm × 3.2 mm × 0.89 mm were selected for this study, as shown in Figure 3.10 (a). As TLD-100 chips' light emissions were sensitive to minute scratches, mass loss, and foreign deposits, handling them properly required vacuum tweezers, much like handling optical fibres.

The TLD-100 chips were annealed in a dedicated annealing oven connected to Thermosoft software for temperature setting at the Medical Physics Laboratory (UPM). Using a thin (to assist rapid cooling following annealing) and high-temperature stainless-steel plate, each chip was placed in its slot, as shown in Figure 3.10 (b). Using a dedicated annealing oven reduced the risk of contamination by foreign materials. If there were more than one plate to be annealed simultaneously, the annealing plates were placed on open oven racks with air space to avoid inconsistent heat gradients. The plates should be kept from touching the oven walls. Annealing was accomplished by heating the oven and TLD-100 chips from room temperature to 400 °C within 10 minutes and then maintaining the oven temperature at 400 ºC for one hour. The temperature was then set to go down to 100 ºC within 30 minutes before maintaining the oven temperature at 100 ºC for two hours. Lastly, the temperature was set to decrease to 50 ºC within half an hour before it was left to cool down naturally for 24 hours until equilibration at room temperature. According to Thermo Electron Corporation (2002), the TLD-100 annealing time-temperature profile (TTP) used in this study was within the accepted range recommended by the manufacturer. Figure 3.10 (c) shows the annealing oven used for the TLD-100 annealing process.

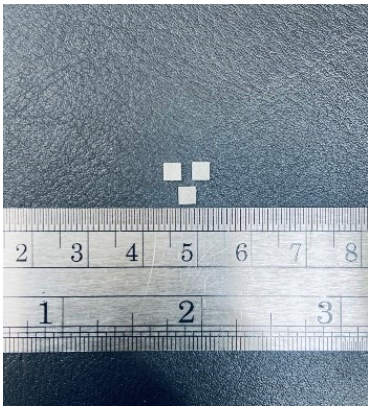

(a)

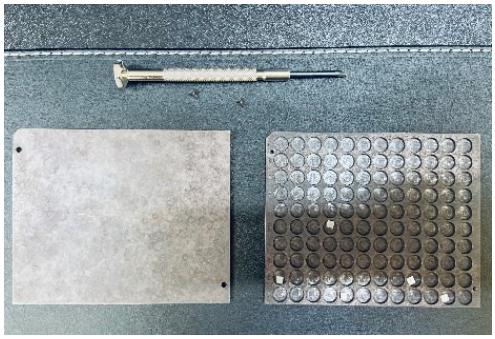

(b)

(c)

Figure 3.10: (a) TLD-100 chips, (b) stainless-steel plate with an individual slot for TLD chips and (c) TLD-100 annealing oven

3.3.3 Optically Stimulated Luminescence Dosimeters (nanoDot)

NanoDot is a flat, 10 mm x 10 mm x 2 mm plastic cassette with a film coated with carbon crystals doped with aluminium oxide (Al_2O_3:C), as illustrated in Figure 3.11 (a). Unlike the more widely used TL dosimetry approach, nanoDot is based on optically stimulated luminescence (OSL) dosimetry. Each nanoDot is given a specific serial number and bar code, and the manufacturer pre-screens each one for variations in crystal sensitivity and adjusts them to be within 2% of one another (Landauer, Inc.,

2019). In addition to having a large operational energy range and the ability to reanalyse doses, the annealing procedure for dosimeter preparation is also required. NanoDot dosimeters are, therefore, intended for use in single-point radiation assessment applications. Handling nanoDot is less tedious than optical fibre or TLD-100, as the plastic cassette can be held directly with bare hands. However, the film-coated Al_2O_3:C is very sensitive to light, so the film inside the plastic covering must not be exposed. They must be kept enclosed in non-transparent plastic cases before and after irradiation.

Due to their high sensitivity to light, nanoDot dosimeters were annealed through light exposure as opposed to optical fibres and TLD-100, which were both annealed under heating conditions. The end tip of a paper clip was carefully used to push out the light-sensitive substance, which was housed in a specially made plastic carrier, exposing it to visible light. Figure 3.11 (b) shows that a customised light-emitting diode (LED) X-ray illuminator model MST-4000 manufactured by Shantou Minston Medical Instruments, China was subsequently used to illuminate the opened nanoDot dosimeters. To provide the best exposure for annealing purposes, the brightness intensity of the LED was regulated. Approximately six hours were utilized with the nanoDot dosimeters inside the LED case with the light on for the complete annealing process (Jursinic, 2007).

(a) (b)

Figure 3.11: (a) NanoDot OSLD with sensitive film pushed out from the plastic casing and (b) OSLD annealer

3.3.4 RQT Radiation Quality Establishment

Prior to radiation, RQT beam quality has to be established in SSDL, Nuklear Malaysia. RQT beam quality is a description of radiation qualities in terms of the X-ray tube voltage and the first and second half-value layers (HVLs). These HVLs are typically used to ensure that there is no ambiguity in the spectrum distribution of X-rays across different X-ray tubes and institutions. While the RQR series simulates the radiation beam originating from a standard X-ray assembly, the RQT series simulates the unattenuated beam utilised in computed tomography (CT) (Table 3.1). Once the radiation qualities of the RQR series have been determined, the radiation qualities of the RQT series can be readily obtained by adding copper (Cu) filtration to the corresponding RQR radiation qualities.

Table 3.1: Radiation qualities for calibration of diagnostic dosimeters (IAEA 2007)

Radiation Quality	Radiation Origin	Material of Additional Filter	Application
RQR	Radiation beam emerging from X-ray assembly	No phantom	General radiography, fluoroscopy and dental applications (free in air)
RQA	Radiation beam with an added filter	Aluminium	Measurements behind the patient (on the image intensifier)
RQT	Radiation beam with an added filter	Copper	CT applications (free in air)
RQR-M	Radiation beam emerging from X-ray assembly	No phantom	Mammography applications (free in air)
RQA-M	Radiation beam with an added filter	Aluminium	Mammography studies

An experimental method was employed at the SSDL in Nuklear Malaysia to establish RQT beam quality. By using a 0.6 cc PTW UNIDOS ionisation chamber cross-calibrated to the International Atomic Energy Agency (IAEA) as the national standard instrument, the copper and aluminium filters with different thicknesses were first slotted in front of Constant Potential Philips Industrial X-Ray machine as added filters in accordance to the previously established RQR beam quality for the investigative radiation quality and X-ray tube voltage in kV (kilovoltage) as shown in Table 3.1. The field size was then set up to be circular with a 7 cm diameter, designed for low scatter contributions. This could be achieved by slotting in a 2 cm diameter circular collimator in front of the added filters and applying 100 cm source image distance (SID). The exposure settings were set as 5 milliamperes (mA) for 50 seconds for each investigative radiation quality RQT 8 (100 kV), RQT 9 (120 kV) and RQT 10 (150

kV), respectively. Temperature, pressure and relative humidity were recorded with a digital barometer and corrected with the correction factors provided.

Table 3.2: Re-establishment of radiation quality series RQT at Malaysian Nuclear Agency for the year 2020

Radiation Quality	X-ray Tube Voltage (kV)	Added Filtration RQR (mm Al)	Added Filtration RQT (mm Cu)	Total Filtration RQR (mm Al) + RQT (mm Cu)	First HVL Filtration (mm Al)	
					Theory	Measured
RQT 8	100	3.7	0.2	3.7 + 0.2	6.9	6.9
RQT 9	120	4.0	0.2	4.0 + 0.2	8.4	8.3
RQT 10	150	4.8	0.2	4.8 + 0.2	10.1	9.9

The first exposure was made without HVL filtration, and the dose reading in milligray (mGy) was recorded. For the second and subsequent exposures, additional aluminium (Al) filters with different thicknesses were slotted in front of the collimator to get the nominal first HVL filtration. Exposures were repeated with the same technical factor settings and different HVL aluminium filter thicknesses to achieve dose readings close to the half value of the first exposure dose without the HVL filtration. A linear graph of the normalised dose against the aluminium thickness was then produced. Finally, the first measured HVL filtration was acquired by interpolating the linear graph. The standard deviation of the dosimeter response for each dose point determined the error bars. This visually represented the spread of data points around the mean. The measured first HVL filtration must not exceed 3% of theoretical first HVL filtration as achieved by Nuklear Malaysia in reference to the last two columns in Table 3.2. If the measured first HVL filtration exceeds 3% of the theoretical value, the copper

filtration needs to be increased or decreased by trial and error before measuring the air kerma with and without the first HVL filtration aluminium thickness as described earlier. The experimental setup for HVL measurements is shown in Figure 3.12 (a) below. Figures 3.12 (b) and (c) show the control panel and filters used for RQT beam re-establishment.

(a)

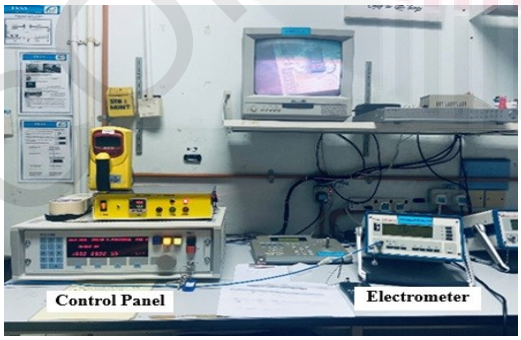

(b)

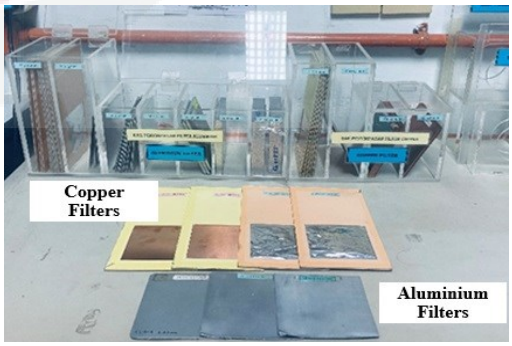

(c)

Figure 3.12: (a) Experimental setup, (b) control panel at SSDL, Nuklear Malaysia and (c) close-up of Al and Cu filters

3.4 Dosimeter Screening

Each group of optical fibres were screened to ensure the fibres chosen possessed more or less similar length and sensitivity before any exposures for basic dosimetric characterisation studies were made, discarding strands that did not conform to the prescribed dimensions or that had sensitivity outside a defined range of the mean. Due to the disparity in dopant concentration throughout the extent of the fibres, a discrepancy in TL yield was to be expected. Hence, the screening was performed for every fresh group of fabricated Ge-doped optical fibres. To carry out the selection process, a 5% coefficient of variation (CV) was implemented (Noor et al., 2014).

The total number of fibres that were screened for 2.3 mol% Ge-FF, 2.3 mol% Ge-CF and 6 mol% Ge-FF were 240 fibres while for 6 mol% Ge-CF, the total was 230 fibres. For commercial fibres, TLD-100 chips and OSLD nanoDots, the total numbers were 90 fibres, 99 chips and 49 nanoDots respectively. The differences in the numbers of dosimeters were due to the pre-determined availability and allocation of the dosimeters at the Medical Physics Laboratory, UPM for this research.

Firstly, to represent independent and separate dosimeters, 10 segmented fibres were assembled within one gelatine capsule and positioned on a square board to a Perspex holder, designed for accurate alignment with the X-ray tube at Nuklear Malaysia as shown in Figures 3.13 (a) and (b). In other words, one capsule would accommodate 10 fibres. The entire sets of Ge-doped fibre capsules were eventually screened to establish individual fibre performance, using Constant Potential Philips Industrial X-Ray Model MG165 as the X-ray source. SSDL at Nuklear Malaysia has previously

established the standard radiation beam quality for CT (RQT) based on the IAEA's Technical Reports Series No.457 (IAEA, 2007).

The entire set was irradiated to a dose of 30 milligray (mGy) with a tube potential of 120 kilovoltage (kV). For dosimeter screening, only one beam quality was chosen as this was an initial process to ensure the fibres chosen possessed similar sensitivity before any exposures for basic dosimetric characterisation studies were made. RQT 9 (120 kV) was selected as it was the middle value between RQT 8 (100 kV) and RQT 10 (150 kV). Only those samples providing a uniform response to within ±5% of the mean TL yield were selected for use in further investigations. For 120 kVp, the radiation quality was RQT 9, and the added filters were as in Table 3.2. After irradiation, the optical fibres were kept in a light-tight box to allow uniform control of thermal fading before the readout of the TL yield. Finally, the distribution of TL yield against the complete set of irradiated optical fibres was produced and analysed. Figure 3.14 (a) shows assembled gelatine capsules positioned on a square board attached to a Perspex holder for irradiation, while Figure 3.14 (b) shows fibre boxes where the screened fibres were slotted in accommodating indentations for subsequent fibres selection and labelling. The same went for the screening of TLD-100 chips and nanoDots, where they were placed on the square board within the collimation field and radiated evenly using the same setting previously mentioned before being kept in their respective screened boxes.

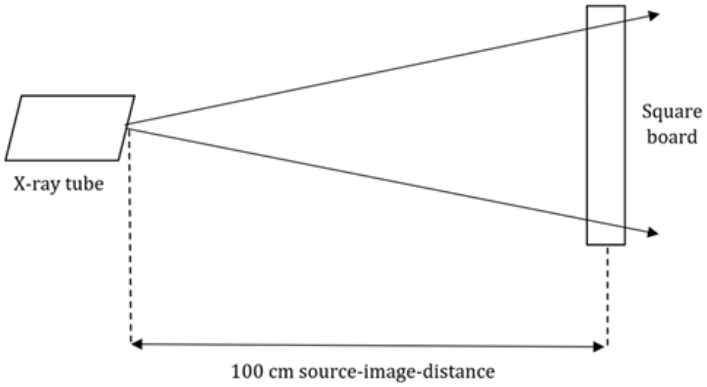

(a)

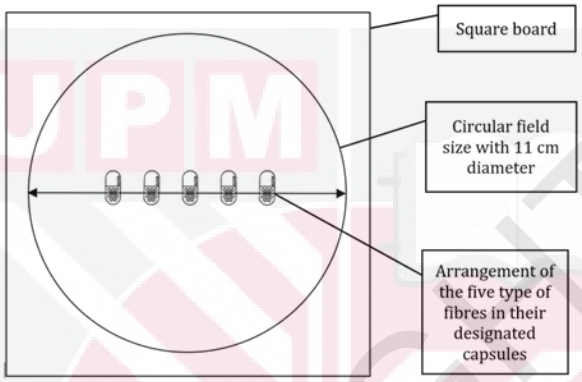

(b)

Figure 3.13: Diagram of the screening set up (a) arrangement of the X-ray tube in relation to the square board and (b) square board with the fibre capsules

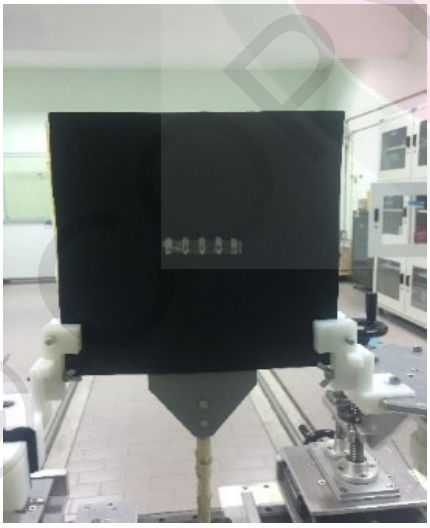

(a)

(b)

Figure 3.14: (a) Square board with fibre capsules attached on a Perspex holder and (b) fibre boxes for subsequent fibre selection and labelling

3.5 Dosimeter Readout

3.5.1 Ge-doped Optical Fibres and TLD-100

A Harshaw TLD™ Model 3500 reader (Thermo Scientific™, USA) located at HPUPM supported with WinREMS software was used to read out the TL signal produced by the optical fibres and TLD-100 chips, as shown in the reader room setup in Figure 3.15. Nitrogen gas at 30 kiloPascal (kPa) was applied to mitigate against specious light signals from triboluminescence and potential oxidation generated from fibre surfaces and the planchet during heating. Prior to the readout process, the performance of the TLD reader was observed to ensure the photomultiplier tube (PMT) noise was within the accepted range of less than 0.3 nanoCoulomb (nC). Time-temperature profiles (TTP) analysis was also done by varying the preheat temperature for each fibre type. The preheat temperature was selected once the peak of the glow curve signal was in the middle of the 200-channel, indicating that the readout parameters were successfully set up to permit maximum data acquisition and thorough removal of any residual signal. The TTP corresponding to the different optical fibres and TLD-100 is shown in Table 3.3. The standard TTP for TLD-100 is recommended in the Harshaw Technical Notice (Thermo Electron Corporation, 2002).

The TL materials were heated to a specific temperature during the preheating phase in order to release shallow traps and remove low-temperature peaks known as unstable peaks. The stable peaks and all TL signals were collected during the acquisition step, which was utilised to gather the data for dosimetry. Nitrogen gas was used throughout to minimise erroneous TL phenomena by minimising heating element oxidation and, therefore, minimising the background signal. The annealing process came after the

heating phase. At this point, a high temperature would be required to remove any residual deeper traps and restore the intrinsic background of the TL materials to their original state. The material should be rapidly chilled with nitrogen gas to guarantee TL materials have good repeatability (McKeever et al., 1995). The measured TL signalsand the glow curves were exported when the read-out procedure was complete to conduct results analysis.

Table 3.3: Time-temperature Profile (TTP) for optical fibres and TLD-100

Sample	Phase	Temperature (°C)	Time (sec)	Rate (°C/sec)
2.3 mol% Ge-FF 6 mol% Ge-CF Commercial	Preheat Acquisition Annealing	95 400 400	10 13.3 10	n/a 30.0 n/a
6 mol% Ge-FF	Preheat Acquisition Annealing	100 400 400	10 13.3 10	n/a 30 n/a
2.3 mol% Ge-CF	Preheat Acquisition Annealing	110 400 400	10 13.3 10	n/a 30.0 n/a
TLD-100	Preheat Acquisition Annealing	50 260 260	0.0 26.7 0.0	n/a 10 n/a

NA: Not applicable

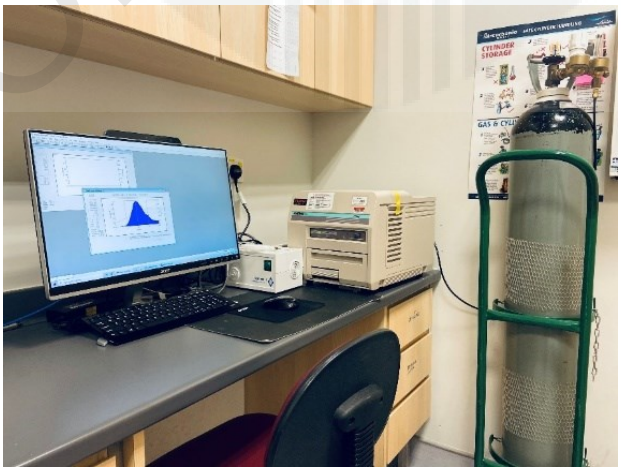

Figure 3.15: Harshaw TLD™ Model 3500 reader room setup

3.5.2 OSLD Nanodot

The microStar InLight® reader (Landauer, Inc., USA) at Nuklear Malaysia was used to read the optically stimulated luminescence (OSL) signals from the irradiated nanoDot. This reader is depicted in Figure 3.16. The irradiated nanoDot was carefully inserted into an adaptor with the bar code pointing forward before being placed in a predetermined location inside the OSL reader for read-out. To get an average reading of the count signals, each nanoDot was read out five times in a row using a rotational knob. The reader was calibrated by the vendor using the industry-standard calibration of 80 kV X-ray photons in order to obtain the absorbed radiation dosage of the measured counts. Based on Equation 3.1, the absorbed radiation dose was obtained through PMT counts, which represented the measured OSL emission, the calibration factor for low radiation dose, and the sensitivity of each particular nanoDot.

$$\text{Absorbed radiation dose} = \frac{\text{Photomultiplier (PMT) counts}}{\text{Calibration factor} \times \text{Sensitivity}} \qquad \text{Equation 3.1}$$

Figure 3.16: MicroStar InLight® reader (Landauer, Inc., USA) located at Malaysian Nuclear Agency

3.6 Scanning Electron Microscope (SEM) with Energy Dispersive X-ray Analysis (EDX)

Subsequent to the screening process, the optical fibres were sent to Quasi-S Technology Sdn. Bhd, Universiti Kebangsaan Malaysia (UKM) for a scanning electron microscopy with energy-dispersive X-ray spectroscopy (SEM/EDX) analysis prior to the commencement of the dosimetry study. The SEM/EDX scanning process was done by the research officers at Quasi-S Technology Sdn. Bhd. As illustrated in Figure 3.17 (a), the individual optical fibres were attached vertically to the surface of a stainless-steel stub using conductive adhesive carbon tape. The sample surface was ensured to be flat and clean to avoid artefacts. Scanning was done over the surface and along the fibres' cross-sectional area to obtain high-resolution images at different magnifications. By selecting the measurement points using a line tool in the calibrated SEM software, an auto-measurement of the dimension was acquired. The ruler size or scale bar was in the unit of micrometres (μm).

For 2.3 mol% Ge-CF, x180 magnification and a scale of 300 μm were applied during the measurements of the core and the cladding diameters while at a magnification of x140, the diameters of 6 mol% Ge-CF were acquired using a 400 μm scale. For flat fibres, the length and width dimensions of both the core and cladding were measured at a magnification of x180 using a 300 μm scale. While SEM analysis was to measure the cross-sectional dimensions of the newly fabricated optical fibres, EDX analysis was carried out to map the elemental distribution and germanium (Ge) concentrations in the cores. The fibres that had the highest yields following irradiation to the RQT beam quality were chosen to most effectively identify the presence of Ge in the fibres.

Characteristic X-rays were produced when high-energy electrons (about 30 kV) interacted with the optical fibres. These interactions also provide information on the relative distribution of the compositional elements. The optical fibres' cross-sectional surfaces were scanned, and a point mapping technique was utilised to focus on element identification in the core area. Cylindrical fibre cross-sections were used for the EDX mapping analysis, whereas the core of flat fibres was covered by four spots. The EDX lines were scanned horizontally across the core for all optical fibres. SEM program identified the core components by detecting peaks in the X-ray spectra. The combined SEM (HITACHI SU1510) and EDX (HORIBA EMAX EX-450) facility at Quasi-S Technology Sdn Bhd (UKM) is depicted in Figure 3.17 (b).

(a) (b)

Figure 3.17: (a) Individual optical fibres attached vertically to the surface of a stainless-steel stub using conductive adhesive carbon tape and (b) a combination of the SEM (HITACHI SU1510) and EDX facility (HORIBA EMAX EX-450) at Quasi-S Technology Sdn Bhd (UKM)

3.7 Basic Dosimetric Characteristics of Optical Fibres, TLD-100 and OSLD nanoDots

Basic dosimetric characteristics of fabricated Ge-doped optical fibres, TLD-100 chips and OSLD nanoDots to photon energy range for CT dosimetry were investigated, focusing on dose linearity, RQT beam quality, dose reproducibility, dose sensitivity, minimum detectable dose and fading. As referred to in Sections 3.3.4 and 3.4, basic dosimetric irradiations were performed after the establishment of RQT radiation quality and dosimeter screening, albeit with a similar radiation set-up with the use being made of Constant Potential Philips Industrial X-Ray Model MG165 located in Secondary Standard Dosimetry Laboratory (SSDL), Malaysian Nuclear Agency as the X-ray source. They have previously established the standard radiation beam quality for CT (RQT) in their laboratory based on the IAEA's Technical Reports Series No.457 (IAEA, 2007).

By using a 0.6 cc PTW UNIDOS ionisation chamber with traced calibration to a reference chamber calibrated at the International Atomic Energy Agency (IAEA) as the national standard instrument, the copper and aluminium filters with different thicknesses were slotted in front of the X-ray machine as added filters with respect to the investigative radiation quality and X-ray tube voltage in kV (kilovoltage) as shown in Table 3.2. The field size was set up to be circular with a 7 cm diameter, designed for low scatter contributions. This could be achieved by slotting in a 2 cm diameter circular collimator in front of the added filters and applying 100 cm source image distance (SID). The dosimeters were positioned on a square board attached to a Perspex holder, which was designed for accurate alignment with the X-ray tube. The exposure settings were set as 5 milliamperes (mA) for each investigative radiation

quality RQT 8 (100 kV), RQT 9 (120 kV) and RQT 10 (150 kV) respectively. To achieve specific doses for each study of basic dosimetry radiations, manual calculations of the seconds (s) in exposure settings were adopted to define X-ray exposure durations. Temperature, pressure, and relative humidity were recorded with a digital barometer and corrected using the correction factors provided. As referred to in the certificate of calibration in Appendix C, the calibration range for temperature was 15 °C to 26 °C with a correction factor of 0.2. For a relative humidity of 40%, the correction factor was -2.2, followed by 50% at -2.4, 60% at -2.3 and 90% at -1.5 correction factors. Finally, for the pressure of 900 hectopascal (hPa), the correction factor was 0.6, followed by 940 hPa at 0.6, 970 hPa at 0.7, 1000 hPa and 1010 hPa at 0.8.

3.7.1 Dose Linearity

Linearity or dose-response is defined as the functional dependence of the intensity of the measured signal upon the absorbed dose. An ideal radiation dosimeter response should be directly proportional to the radiation dose to ensure the new dosimeter has a linear dose response over a wide range of doses used. For the study of TL (for optical fibre and TLD-100) and count signal (nanoDot) versus dose, each RQT radiation quality with designated tube potential was studied. These were RQT 8 (100 kV), RQT 9 (120 kV) and RQT 10 (150 kV). The doses selected were the typical CT doses received by paediatric patients (Jibiri & Adewale, 2014) as referred to in the specific objectives for the subsequent part of the study. The selected doses ranged from 2 mGy to 40 mGy (2-, 4-, 6-, 8-, 10-, 15-, 20-, 25-, 30-, 35- and 40 mGy). Each dose point represented the mean of 10 fibres per capsule, three TLD chips and two OSL nanoDots with the data normalised to sample volume. The error bars were determined by the

standard deviation of the dosimeter response for each dose point. This visually represented the spread of data points around the mean.

3.7.2 RQT Beam Quality

The variation of the observed TL output for a fixed dose as a function of the energy is known as the energy response or beam quality (Hashim, 2010). The fluctuation of energy dependence needs to be corrected because dosimetry systems are calibrated at a specific radiation beam quality and used over a considerably larger energy range. The system calibration should be independent of energy over a range of radiation characteristics, with the energy response ideally being flat. In fact, for most measurement scenarios, the energy correction must be considered when determining the dosimetric quantity. For the study of each RQT beam quality, fixed kilovoltage of RQT 8 (100 kV), RQT 9 (120 kV) and RQT 10 (150 kV) were investigated for selected doses of 20 mGy, 30 mGy and 40 mGy. Each data point represented the mean of 10 fibres per capsule, three TLD chips and two OSL nanoDots with the data normalised to sample volume. The standard deviation of the dosimeter response for each beam quality determined the error bars. This visually represented the spread of data points around the mean.

The percentage of reduction equals the change in the two investigated values divided by the original value, multiplied by 100. It was used to determine the value difference of the dosimeter response and the percent change from the original response of 100 kV to the new response when 120 kV and 150 kV were used. The formula for percentage change is as Equation 3.2.

$$\text{Percentage change} = \left(\frac{\text{Final Value} - \text{Initial Value}}{\text{Initial Value}}\right) \times 100 \qquad \text{Equation 3.2}$$

3.7.3 Dose Reproducibility

The reproducibility of measurements made using similar settings is specified by the precision of dosimetry measurements, which may be approximated using the information gathered from repeated measurements. A low standard deviation (SD) in the distribution of the measurement findings is a sign of high precision. Dosimeters should ideally be reproducible. By measuring the SD of repeated measurements made under the same exposure and reading conditions, it is possible to determine each material's reproducibility to a specific dose level (Hashim, 2010). To investigate dose reproducibility, the dosimeters were irradiated with a reproducible dose of 20 mGy, 30 mGy and 40 mGy and a fixed energy of 120 kV (RQT 9). RQT 9 was selected as it was the middle value between RQT 8 (100 kV) and RQT 10 (150 kV). These irradiations were repeated using the same set of dosimeters subsequent to re-annealing on each occasion. The SD percentage of the dosimeters for each irradiation was then calculated. The coefficient of variation (CV) is a relative measure of variability that indicates the size of SD in relation to its mean. In other words, CV is SD divided by the mean. It was used to compare variability within the group of optical fibres, TLD-100 chips and OSLD nanoDot when irradiated to different doses. The percentage change was also calculated in accordance with Equation 3.2.

3.7.4 Dose Sensitivity

In TL-based dosimetry, sensitivity is defined as TL yield per unit dose per unit mass of the material. It is a significant dosimetric characteristic that exhibits material

response against any particular dose range. Variances in sensitivity may happen even if the dosimeters are produced in a similar group due to several factors (Hashim, 2010). This study calculated average standard deviations for each dosimeter reading within 2 mGy to 40 mGy dose ranges. The dose sensitivity of the TL-typed dosimeters was determined using the following equation:

$$\text{Sensitivity} = \frac{\text{TL (nC)}}{\text{Volume (m}^3\text{) x Radiation Dose (mGy)}} \qquad \text{Equation 3.3}$$

Where TL is the measured signal, the volume was calculated based on the core dimension for optical fibre and outer dimension for TLD-100, and the radiation dose is within the investigated radiation dose range. The results were presented in a graph of normalised TL signals against the radiation dose range from 2 to 40 mGy and expressedin a unit of nC m^{-3} mGy^{-1}. Each dose point represented the mean of 10 fibres per capsule and three TLD chips with the data normalised to sample volume. The error bars were determined by the standard deviation of the dosimeter response for each dose point. This visually represented the spread of data points around the mean.

3.7.5 Minimum Detectable Dose

Identifying the minimum dose boundary for a particular dosimeter is crucial in low-dose applications since several types of research have shown that the signal produced from an irradiated TLD-100 is more or less similar to the background reading. The essential aspects in successfully achieving a low detection limit depend on both dosimeter material with high TL sensitivity and the type of TLD reader used (Hashim, 2010). Here, the minimum detectable dose (MDD), D_0, denotes the minimum dose the dosimeter can detect, over and above that of background, where:

$$D_0 = (B_{mean} + 2\sigma) \times F \quad \text{Equation 3.4}$$

$$F = 1/m \quad \text{Equation 3.5}$$

The MDDs are quantified as deliberated by Furetta et al. (2001) using Equation 3.4, with B_{mean} as the average TL signal measured from the annealed but unirradiated dosimeters and σ the average background's standard deviation. F is the reciprocal of the gradient (m) attained from the dose linearity graph of that particular dosimeter as formulated in Equation 3.5. The dose linearity graphs were previously obtained during the dose linearity measurement, as discussed in Section 3.7.1.

3.7.6 Fading

To investigate the spontaneous thermal-relaxation signal loss, more commonly known as fading, a nominal tube potential for RQT 8 beam quality which was used in the clinical study and a dose of 30 mGy over a 10-day period was observed. In order to get an accurate estimation of the correction factors, X-ray energy used during the characterisation study must be similar to the setting in subsequent clinical studies. RQT 8 beam quality was used in fading characterisation since the subsequent paediatric phantom study would be irradiated with 100 kV. Post-irradiation until measurement of TL yield was carried out, the dosimeters were kept under the same conditions in a light-tight box held at room temperature to avoid thermally or optically stimulated release of the trapped electrons. Each data point represented the mean of 10 fibres per capsule, three TLD chips and two OSL nanoDots, with the data normalised to the 1st-day post-irradiation. The standard deviation of the dosimeter response for each investigated day determined the error bars. This visually represented the spread of data points around the mean.

3.8 Glow Curve Analysis for Fabricated Optical Fibre

The response of a TL material is best described by its glow curve, especially for newly fabricated optical fibres (Alawiah et al., 2015). The amplitude of the peaks depicts the relative population of the electrons in the traps. The absorbed dose in the TL medium can be calculated using the peak height and the area under the glow curve. To study glow curve characteristics within RQT beam qualities, fixed kilovoltages of 100-, 120- and 150 kV were used, with doses of 20-, 30- and 40 mGy delivered. To establish RQT 8, RQT 9 and RQT 10 radiation beam qualities, different thicknesses of aluminium (Al) and copper (Cu) filters were slotted in front of the X-ray tube, as shown in Table 3.2. As a result of the TLD reader heating the TL materials post-readout, the glow curves were extracted from a Windows®-based Radiation Evaluation and Management System (WinREMS) software and analysed using a computerised glow curve deconvolution program known as a Windows®-based Glow Curve Fitting (WinGCF) software. Each data point represented the mean of 10 fibres per capsule, while the standard deviation of the dosimeter response for each channel determined the error bars. This visually represented the spread of data points around the mean. The experimental glow curves were then deconvoluted into five distinct peaks using manual fit mode in order to determine the glow peak kinetic characteristics, such as the maximum peak temperature (T_{max}), peak integral (PI), and activation energy (E_a). The fitted function fits perfectly with the measured data when the figure of merit (FOM) value was less than 5% (Alawiah et al., 2015).

3.9 CIRS ATOM® Dosimetry Verification Paediatric Phantom Irradiation

CIRS ATOM® phantom is an anthropomorphic, cross-sectional dosimetry phantom designed to investigate organ dose. A 1-year-old model of the paediatric phantom was rented for each dosimetry verification irradiation from the Medical Physics Unit, University of Malaya Medical Centre (UMMC). The phantom has a typical sectional design, with a 12 x 14 cm^2 dimension for the thorax, 10 kg in weight, and a total height of 75 cm. There are barely any interfaces between the slabs due to the sectional surfaces' flatness and smoothness. The manufacturer (CIRS, USA) examined and produced accessible anatomical references by referring to ICRU 48 (ICRU, 1992) to determine the size of the paediatric model. This paediatric age-specific phantom enables more accurate determination of effective doses and dose calculations during CT scanning protocols. The ATOM 1-year-old also comes with arms and legs as a standard configuration, as scattering radiation can significantly contribute to the dose delivered to the surrounding tissue.

The phantom holder also features a unique holding mechanism comprising a top and bottom compression plate that can be adjusted using the included wrench, designed to enhance ATOM imaging qualities. Four thin, radiographically opaque Teflon wires are used to connect the plates. There are no solid rods inside the phantom body that could contribute to artefacts. Instead, a little tab at the top of each slab nestles into the corresponding indentation at the bottom of the slab before it. Figure 3.18 (a) and (b) shows the assembled 1-year-old CIRS ATOM® dosimetry verification phantom at the CT scan room, HPUPM, and (c) disassembled phantom in its storage case.

(a)

(b)

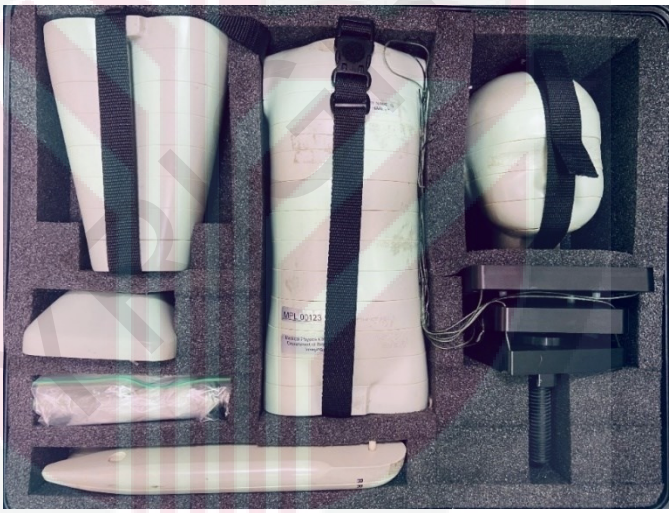

(c)

Figure 3.18: (a) 1-year-old CIRS ATOM® dosimetry phantom at CT scan room, (b) assembled phantom between the holding plates connected with four thin Teflon wires and (c) disassembled phantom in its storage case

Epoxy resin materials that are CIRS tissue equivalents are used to build ATOM phantoms. For soft tissue, bone, and lung, the linear attenuations of the simulated tissues are within 1% of the actual attenuation. Each phantom's lung tissue is standardised using a low-density inhale formulation of 0.2 g/cc. All bones are also

homogeneous and designed to reflect the typical, age-appropriate bone composition. Additionally, the ATOM phantom has tissue simulation, which can accommodate irradiation at various energy levels.

Regarding the dosimetry aspect, this model of ATOM phantom provides a standard 3 cm x 3 cm grid spacing. Optimised dosimetry locations, particularly of the lung and brain used for this study, are possible due to the readily outlined lung and brain organs on the sectional slab offering dose measurements in precise locations, as shown in Figure 3.19 (a) and (b), respectively. In other words, the lung and brain hole locations are optimised for precise average organ dose calculations within a standard grid spacing.

(a) (b)

Figure 3.19: (a) Example of dosimetry holes in standard 3 cm x 3 cm grid patterns for readily outlined lung and (b) brain slices for precise average organ dose measurements

The dosimetry holes are originally filled with 5 mm diameter x 25 mm long, solid plugs of corresponding tissue of soft tissue, bone, lung and brain. For TLD-100 chips dosimetry verification, additional solid tissue equivalent plugs were purchased from the manufacturer (CIRS, USA) and sent to Dellhard Engineering Enterprise (Puchong, Selangor) where they were professionally cut so the TLD-100 chips could be

sandwiched between the cut plug and positioned at the predetermined depth within each section as shown in the measurement diagram of Figure 3.20 (a). Three (3) screened TLD-100 chips with an individual height measurement of 0.89 mm were stacked up to be sandwiched between the cut plugs. The sandwiched method was recommended by the manufacturer as the standard methodology for TLD-100 chips dosimetry in ATOM® dosimetry phantom. For optical fibre dosimetry verification, tissue equivalent plugs were separately purchased to precisely accommodate optical fibres, as referred to in the measurement diagram of Figure 3.20 (b). Five (5) screened fabricated optical fibres with an individual height of ± 6 mm were inserted in the plug holes. These additionally purchased rods and solid tissue equivalent plugs were of brain, lung, bone and soft tissue formulations for precise dosimetry verification paediatric phantom irradiation, as shown in Figure 3.20 (c) and (d). OSLD nanoDot dosimetry, unfortunately, is not available with the majority of ATOM® dosimetry phantoms, including this 1-year-old paediatric model, as these dosimeters require 14 mm diameter drilled thru-holes on the sectional slabs and specialised plugs configuration to receive the OSLD nanoDot dosimeters due to their bigger dimensions. OSLD nanoDot dosimeters, however, could be attached to the surface of the phantom to measure entrance skin dose (ESD) generated from scattered radiations during phantom irradiations of the CT chest and head scans, as detailed in the subsequent sections.

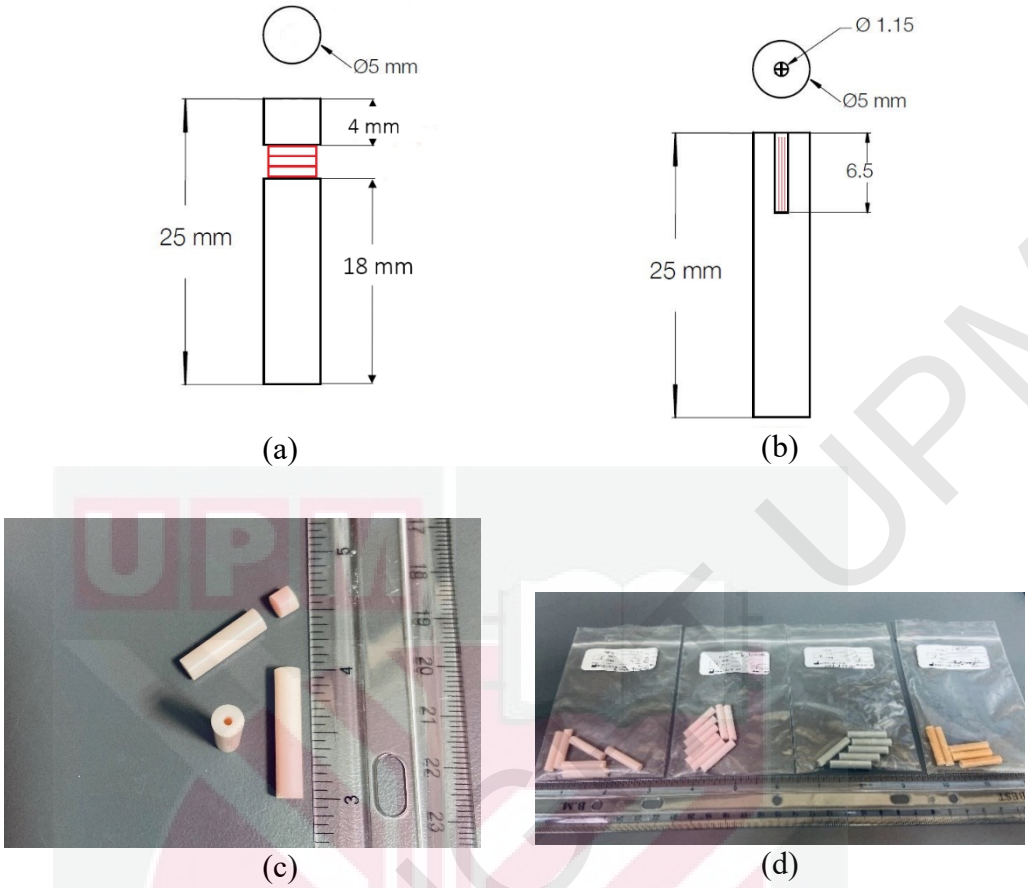

Figure 3.20: (a) Diagram of three (3) stacked TLD chips, sandwiched in between the cut plugs for TLD dosimetry, (b) diagram of optical fibres inside the plug holes for optical fibre dosimetry, (c) example of the cut and fibre hole tissue equivalent plugs and (d) tissue equivalent plugs from left to right (brain, lung, soft tissue and bone)

In summary, a comparative study of three different dosimeters between four types of fabricated optical fibres, TLD-100 chips and OSLD nanoDots on CIRS ATOM® dosimetry paediatric 1-year-old phantom during routine chest and head computed tomography scans was done to estimate organ doses and ESDs generated from direct and scattered radiations to verify the dosimetric capability of the newly fabricated dosimeters against the gold standards dosimeters. Table 3.4 shows the details of the phantom irradiation performed on the chest and head CT scans, the types of measured doses for selected radiosensitive organs and the investigated dosimeters for all dose measurements.

Table 3.4: Details of the scans done on CIRS ATOM® dosimetry paediatric 1-year-old phantom for a comparative study of the investigated dosimeters

CT Scan	Measured Dose	Involved Organ	Studied Dosimeter
Head Routine	Organ Dose	Brain (direct irradiation) Eye (scattered radiation) Thyroid (scattered radiation)	2.3 mol% Ge-FF 2.3 mol% Ge-CF 6 mol% Ge-FF 6 mol% Ge-CF TLD-100 chip
	Entrance Skin Dose	Eye (scattered radiation) Thyroid (scattered radiation)	2.3 mol% Ge-FF 2.3 mol% Ge-CF 6 mol% Ge-FF 6 mol% Ge-CF TLD-100 chip nanoDot
Chest Routine	Organ Dose	Lung (direct irradiation) Thyroid (scattered radiation)	2.3 mol% Ge-FF 2.3 mol% Ge-CF 6 mol% Ge-FF 6 mol% Ge-CF TLD-100 chip
	Entrance Skin Dose	Thyroid (scattered radiation)	2.3 mol% Ge-FF 2.3 mol% Ge-CF 6 mol% Ge-FF 6 mol% Ge-CF TLD-100 chip nanoDot

3.9.1 Head Computed Tomography Scan

The head scan was done by using 100 kV at HPUPM. For the organ dose study of the brain, the four types of screened fabricated optical fibres and TLD-100 chips were inserted interchangeably into the brain equivalent plugs. In contrast, soft tissue equivalent plugs were used for radiosensitive eyes and thyroid organ dose measurements generated from the scattered radiations during the brain scan. The eyes and thyroid were chosen due to the proximity of these organs to the radiation beam during the brain scan. Eyes or lenses were within the field of view on the frontal brain

scan. There was a total of 33 brain dosimetry holes across four sectional slabs (slabs 2 to 5), two (2) lens dosimetry holes and one (1) thyroid dosimetry hole on the 4th and 8th slab, respectively. Figure 3.21 shows the four sectional brain slabs on ATOM® dosimetry paediatric phantom. Due to the high cost of the tissue equivalent plugs, only six (6) brain tissue equivalent plugs could be purchased from the manufacturer (CIRS, USA). As such, the radiations had to be repeated several times for each investigated dosimeter to accommodate each brain dosimetry hole.

The phantom was positioned supine, head first into the gantry. The phantom's midsagittal plane (MSP) was adjusted to be aligned with the central beam and the couch's midline with equal margins between the head. No rotation or tilt of the phantom head was also ensured by placing the midcoronal plane (MCP) parallel to the couch. A routine head CT scan included the region from the base to the vertex of the skull in 5- to 8-mm slices. The technical parameters selected for this examination were the routine parameters used for paediatric head CT scans in HPUPM, shown in Table 3.5. The dose report of the scan showing the Dose Length Product (DLP) and Volume Computed Tomography Dose Index ($CTDI_{vol}$) was retrieved after the examination.

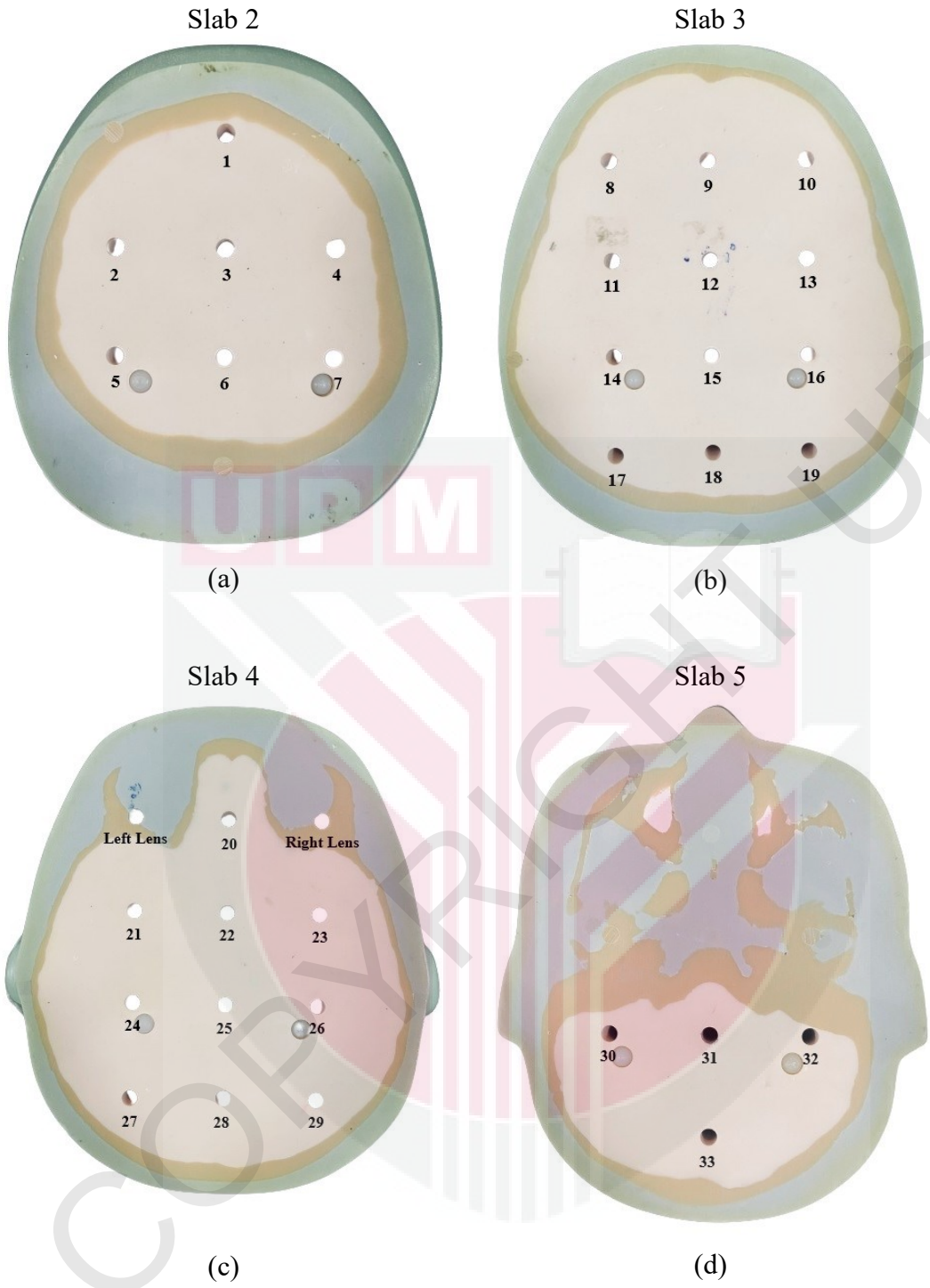

Figure 3.21: (a) to (d) showing 33 brain dosimetry holes across four sectional slabs of 2 to 5. Also (c) shows dosimetry holes for the right and left lenses

Table 3.5: Routine technical parameters used for paediatric head CT scan in HPUPM

Technical Parameters	Parameters
kV	100
Effective mAs	350
Scan time	6.25 s
Rotation time	1 s
Slice thickness	5 mm (Acq 128 x 0.6 mm)
Pitch	0.8
Coverage	Base of skull through vertex
Algorithm	Soft tissue
Scan direction	Caudocranial

The phantom position and technical parameters used for each scan of the investigated dosimeter were constant for an accurate comparison study of 2.3 mol% Ge-FF, 2.3 mol% Ge-CF, 6 mol% Ge-FF, 6 mol% Ge-CF and TLD-100 chips, respectively.

For the entrance skin dose (ESD) study, five (5) screened fabricated optical fibres and three (3) screened TLD-100 chips, which were inserted inside each capsule together with one (1) screened nanoDot, were interchangeably attached on the surface of the eyes and thyroid region on the phantom. Figure 3.22 shows an example of the nanoDots attachments on the eyes and thyroid region to measure ESD generated from scattered radiation of the head CT scan. Per the organ dose study, the scans were repeated with constant positioning and technical parameters for each dosimeter. After the scans, the capsules and nanoDots were removed from the phantom surface to be read out. The nanoDots were read five (5) times for the average dose measurements.

A comparative study between the responses of four types of fabricated optical fibres against the gold standards TLD-100 chips and nanoDots from head CT scans on ATOM® dosimetry paediatric phantom was achieved through the measurements of

the average organ and entrance skin doses on the brain, radiosensitive lenses, and thyroid. The Dose Length Product (DLP) value for this examination was also recorded and discussed in the next chapter.

Figure 3.22: ATOM® dosimetry phantom positioning with nanoDots attachment on the radiosensitive eyes and thyroid region to measure ESD generated from scattered radiation of head CT scan

3.9.2 Chest Computed Tomography Scan

Chest CT scan was done on a CIRS ATOM® Dosimetry Paediatric 1-Year-Old Phantom at the Department of Radiology, Hospital Pengajar Universiti Putra Malaysia (HPUPM), using a Siemens Somatom Definition Flash CT Scanner. The general specifications of the scanner are shown in Table 3.6. 100 kV was employed for routine paediatric chest scans in HPUPM.

Table 3.6: General specifications for Siemens Somatom Definition Flash CT Scanner at HPUPM (Reference: www.siemens.com/healthcare)

Item	Specification
Detector	2 x Stellar Detector
Number of slices	2 x 128
Detector collimator	2 x 1D scatter collimator
Generator	200 kW (2 x 100 kW)
Isotropic resolution	0.33 mm
Cross-plane resolution	0.30 mm
Temporal resolution	75 ms, heart rate independent
Maximum scan speed	458 mm/s with Flash Spiral
Table load	Up to 307 kg
Gantry opening	78 cm

Prior to the first chest scan for organ dose study, five (5) screened 2.3 mol% Ge-FF optical fibres were inserted into the lung equivalent plugs for direct organ dose measurement of the lung. In contrast, a soft tissue equivalent plug was used for thyroid organ dose measurement generated from the scattered radiation during the chest scan. The thyroid was chosen because it was one of the most radiosensitive organs primarily affected during lung scanning. The fibre holes were taped to prevent the fibres from coming out of the plugs during phantom assembly. Due to the high cost of the tissue equivalent plugs, only eight (8) lung tissue equivalent plugs could be purchased from the manufacturer (CIRS, USA). As such, the radiations had to be repeated several times for each investigated dosimeter to accommodate each lung dosimetry hole. There was a total of 19 lung dosimetry holes, which were filled with lung equivalent plugs across four sectional slabs (slab 9 to 12), and one (1) thyroid dosimetry hole, which was filled with soft tissue plug on the 8^{th} slab as referred to in Figure 3.23 and 3.24 respectively. Only dosimetry holes located entirely within the investigative organs were used for dose measurements. As the phantom was drilled with a standard 3 cm x 3 cm grid spacing, there were bound to be dosimetry holes between two

adjacent tissues. These dosimetry holes were not selected for dose measurements as the tissue equivalent plugs provided were only for one type of tissue per hole. This represents a precise measurement of organ dose in terms of electron interactions of the optical fibres or TLD-100 chip within the specific tissue-equivalent dosimetry plugs. Once the plugs were inserted entirely into the dosimetry holes, the sectional slabs were stacked onto each other. The top of each slab has a small tab that fits into the corresponding indentation on the underside of the preceding slab. A total of 29 sectional slabs to represent the whole phantom were stacked between a top and bottom compression plate joined with four thin, radiolucent Teflon wires. The knob at the top of the compression plate was then adjusted with the included wrench to tighten the wires and the stacked sectional slabs against each other. The phantom was then ready to be positioned on the CT scanner.

The phantom was positioned supine, head first into the gantry. The phantom's midsagittal plane (MSP) was adjusted to be aligned with the central beam and the couch's midline with equal margins between the lateral thorax. No rotation of the phantom was also ensured by placing the midcoronal plane (MCP) of the phantom parallel to the couch, as referred in Figure 3.25. A scout image was obtained to determine the range of the scan. A routine chest CT scan protocol included the region from the lung apices through the diaphragm. The technical parameters selected for this examination were the routine parameters used for paediatric chest CT scans in HPUPM and are shown below in Table 3.7. The dose report of the scan showing the Dose Length Product (DLP) and Volume Computed Tomography Dose Index ($CTDI_{vol}$) was retrieved after the examination.

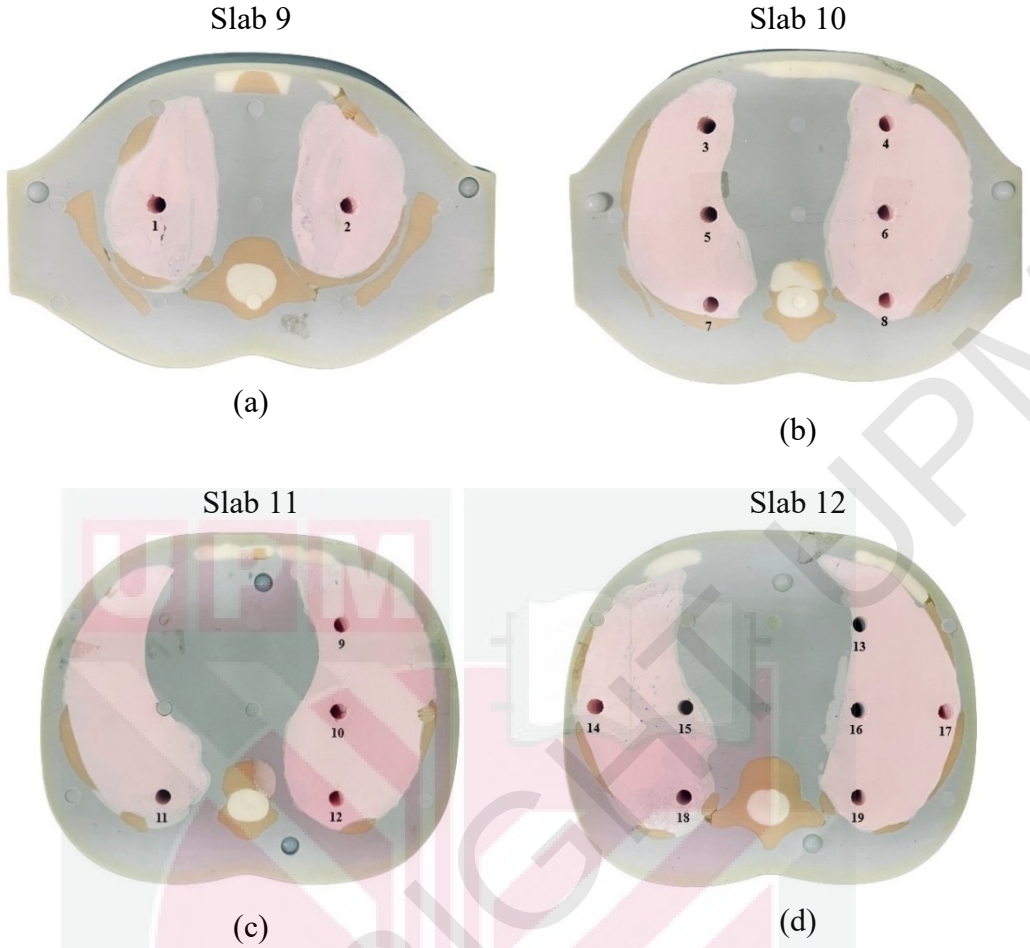

Figure 3.23: (a) to (d) showing 19 lung equivalent plugs across four sectional slabs of 9 to 12

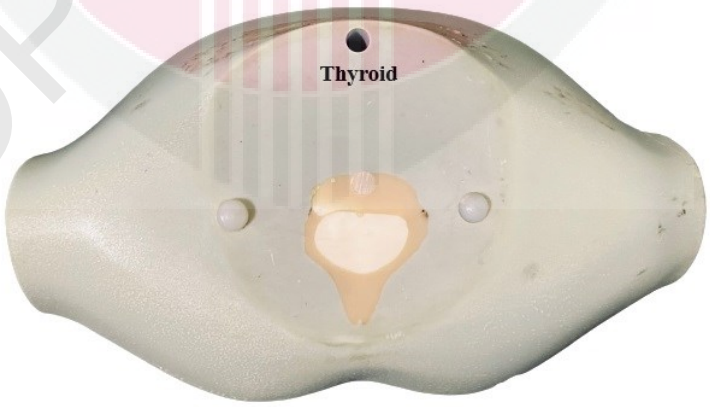

Figure 3.24: Thyroid dosimetry hole filled with soft tissue plug on the 8th slice of ATOM® dosimetry phantom

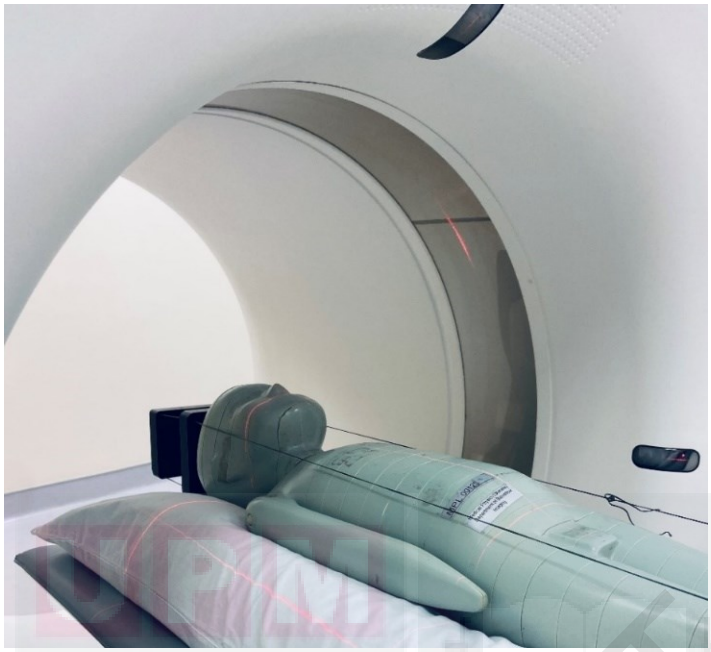

Figure 3.25: ATOM® dosimetry phantom positioning for chest CT scan

Table 3.7: Routine technical parameters used for paediatric chest CT scan in HPUPM

Technical Parameters	Parameters
kV	100
Effective mAs	30
Scan time	2 s
Rotation time	0.5 s
Slice thickness	3 mm (Acq 32 x 1.2 mm)
Pitch	1.4
Coverage	Lung apices through the diaphragm
Algorithm	Soft tissue and lung
Scan direction	Craniocaudal

After the first scan, the phantom was disassembled to remove the dosimetry plugs from the sectional slabs. Using a push rod provided, the dosimetry plugs were carefully pushed out of the holes so that the optical fibres stayed within the plugs and did not accidentally scatter off. Systematic coding of the dosimetry holes and plugs was essential to ensure a correct and smooth process for subsequent scans intended for other investigated dosimeters. The second scan was done by inserting 2.3 mol% Ge-

CF inside the tissue equivalent plugs, and the whole step was repeated. The phantom position and technical parameters used for this scan and the subsequent scans were made constant for an accurate comparison study of the different dosimeters. The third, fourth and fifth scans were done for 6 mol% Ge-FF, 6 mol% Ge-CF and TLD-100 chips, respectively.

For the entrance skin dose (ESD) study, five (5) screened fabricated optical fibres (for all four (4) fibre types) and three (3) screened TLD-100 chips were inserted inside each capsule together with one (1) screened nanoDot were interchangeably attached on the surface of the thyroid region on the phantom. Figure 3.26 (a) shows an example of the fibre / TLD-100 chip capsule, while Figure 3.26 (b) shows the nanoDot attachment on the thyroid region to measure ESD generated from scattered radiation of the chest CT scan. Per the organ dose study, the scans were repeated with constant positioning and technical parameters for each dosimeter. After the scans, the capsules and nanoDot were removed from the phantom surface to be read out. Noted here is the inclusion of a nanoDot dosimeter for the ESD study due to the possibility of it being attached to the phantom surface. The nanoDot was read five (5) times for the average dose measurements.

A comparative study between the responses of four types of fabricated optical fibres against the gold standards TLD-100 chips and nanoDots from chest CT scans on ATOM® dosimetry paediatric phantom was achieved through the measurements of the average organ and entrance skin doses on lung and radiosensitive thyroid. Dose Length Product (DLP) and Volume Computed Tomography Dose Index ($CTDI_{vol}$) values for this examination were also recorded and discussed in the next chapter.

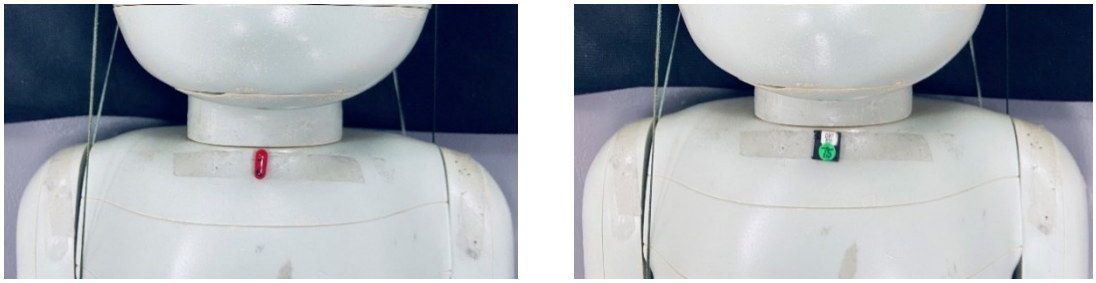

(a) (b)

Figure 3.26: (a) Example of the fibre / TLD capsule and (b) nanoDot attachment on the radiosensitive thyroid region for the measurement of ESD generated from scattered radiation of chest CT scan

3.10 Dosimetry Verification in Real Clinical Setting: CT Pulmonary Angiogram (CTPA)

A comparative study between the investigated dosimeters of four types of fabricated optical fibres, TLD-100 chips and nanoDots was conducted in a real clinical setting at the Radiology Department, Hospital Serdang, from October 2021 to March 2022. The paediatric patients selected were those under two (2) years of age who underwent a CT Pulmonary Angiogram (CTPA). CTPA was chosen as the primary examination for the dosimetry verification study because it was the most frequently requested scan for paediatric patients under two (2) years of age as Hospital Serdang was also a specialised referral centre for paediatric cardiology. A total of 15 patients who satisfied the inclusion criteria were able to be requited in this dosimetry study within a period of six months. Table 3.8 shows the dosimeters studied for the measurements of entrance skin doses on radiosensitive thyroid due to the scattered radiations from the CTPA examination.

Table 3.8: Comparative study of the investigated dosimeters in measuring ESDs of radiosensitive organs during CTPA examination

Examination	Measured Dose	Involved Organ	Studied Dosimeter
Routine CTPA	Entrance Skin Dose	Thyroid (scattered radiation)	2.3 mol% Ge-FF 2.3 mol% Ge-CF 6 mol% Ge-FF 6 mol% Ge-CF TLD-100 chip nanoDot

Five (5) screened fabricated optical fibres and three (3) screened TLD-100 chips, which were inserted inside designated capsules together with one (1) screened nanoDot, were attached to a piece of soft fabric for convenient and constant dosimetry placement on the participating patients. Since this was an actual patient examination, it was impossible to attach each dosimeter interchangeably, as was the case with the ATOM® dosimetry phantom study. As such, a dosimeter strip where all investigated dosimeters could be attached to and placed conveniently on the patient without interfering with the image acquisition was proposed. The soft fabric was chosen for the point of attachment as it was also one of the materials used in attaching the right (R) and left (L) lead markers during medical imaging procedures to mark the patient's anatomical side. Thus, it had been proven that soft fabric would not produce any artefact even if it were incidentally radiated within the field of view. For this clinical dosimetry study, the lead markers at the end of the fabric were removed. The investigated dosimeters were then attached to the middle portion of the fabric, which was then placed on the patient's thyroid region. The position of the dosimeter strip on the area to be studied was maintained for the duration of the CTPA examination. Micropore tape was also used to help maintain the position of the dosimeter strip on the patient. Figure 3.27 shows an example of a dosimeter strip with capsules and

nanoDot attachments on the radiosensitive thyroid or neck region for the measurement of ESD. A preliminary study on the phantom was also done to ensure that the dosimeter strip would not interfere with the acquisition of the image and that the dose measurement for each dosimeter had no significant difference due to the placement of the capsules and nanoDot along the dosimeter strip.

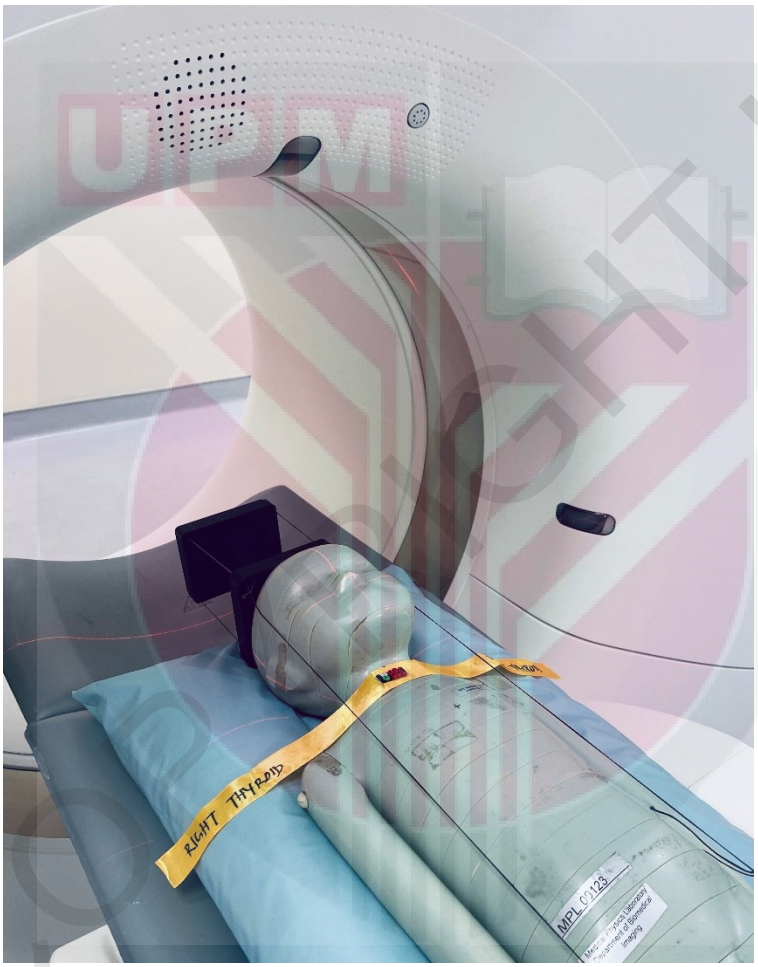

Figure 3.27: Placement of a fabric strip with attached dosimeter capsules and nanoDot on thyroid region of ATOM® dosimetry phantom for a preliminary study

3.10.1 Ethical Approval

In keeping with Malaysian legislation and ethics guidelines, non-opposition to research participation was obtained from legal representatives after oral and written

information was provided. The Medical Research Ethics Committee (MREC) approved and registered the study under the National Medical Research Register (NMRR) with the NMRR-20-570-52577 study identification number. After receiving MREC approval, the Ethics Committee for Research Involving Human Subjects (JKEUPM) was notified. Good Clinical Practice (GCP) certificate was also obtained by the researcher for research involving human subjects.

3.10.2 Participating Patients

Children under two (2) years old who already consented to CTPA examinations that came to the Radiology Department, Hospital Serdang, were approached to participate in this study, subject to their caregivers' approvals. These were also known as the subject's inclusion criteria. The exclusion criteria included if the patient was present with thyroid or neck injury or disease, preventing the dosimeter placement on the region of interest. The other criteria for suspending or terminating the study even after the dosimeter was put in place were when sedation was unsuccessful, when the patient woke up before or during the scan and if the patient developed an allergic reaction to the injected contrast media required for CTPA examination. Subjects were withdrawn from this study when they failed to be fully sedated and developed a contrast media reaction, as CTPA examination would also be abandoned. The caregivers would then be informed, and timely arrangements would be made for their children's future care and follow-up. Table 3.9 summarises the inclusion and exclusion criteria for the subject selection process. A total of 15 patients who satisfied the inclusion criteria were able to be included in this dosimetry study between October 2021 and March 2022.

Table 3.9: Summary of inclusion and exclusion criteria for the subject selection process

Inclusion Criteria	Exclusion Criteria
• Referred to the Radiology Department for CTPA examination • Under two (2) years of age • Caregivers consented	• Thyroid or neck injury or disease which prevented the placement of dosimeter strip • Failed sedation • Allergic reaction to contrast media

3.10.3 Informed Consent and Study Workflow

Patients who had previously been consented for CTPA examination by their primary caregivers and referred to the Radiology Department, Hospital Serdang, were identified. Patients were then pre-selected to be included in the dosimetry study if they satisfied the inclusion criteria of under two (2) years of age. Parental approval and consent for the dosimetry study were done before the patient was brought into the CT scan room. The informed consent form entailed the title of the study, the statements of consent, the dates and signatures, identification card numbers and names of the parents or caregivers and investigators conducting informed consent. An impartial witness was required if the parent or caregiver was illiterate and the contents of the participant information sheet were orally communicated to the parent. Any medications, sedations and contrast media for CTPA scanning itself were separate matters to which the parents (on behalf of their children) had consented with their respective physicians prior to them being invited to participate in this study.

Once patients were inside the CT room, they would initially be monitored to confirm successful sedation. Paediatric patients must be fully sedated before imaging to attain proper images without motion artefacts caused by movements. The scans would have

to wait until the patients were asleep before being performed. When the patients were successfully sedated, dosimeter strip placement was done simultaneously during the patient and part positioning. Patients were excluded from the study if they presented with thyroid or neck injury or disease, which would hinder the proper placement of the dosimeter strip if the sedations were unsuccessful and/or if the patients developed allergic reactions to intravenously injected contrast media. CTPA scan would then proceed with a routine step sequence encompassing a topogram scan, pre-monitoring contrast, monitoring and pulmonary angiogram. Finally, the dosimeter strip would be removed from the patient once the examination was done and kept in a light-tight box to be read out after 24 to 48 hours. Figure 3.28 shows the workflow of the dosimetry study.

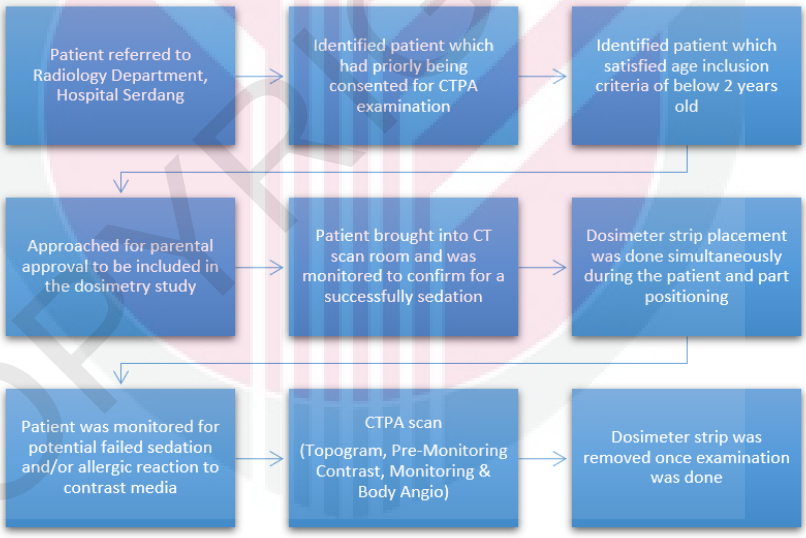

Figure 3.28: Study workflow for CTPA dosimetry study

3.10.4 Means for Protecting Privacy and Confidentiality

Personal information collected from the subjects included patient identification, name, age, gender, and the date and time of presentation to the Radiology Department and subsequent CTPA scan. All personal details were treated as strictly confidential

through officially signed informed consent by both parties. Study subjects were anonymised by assigning separate study codes. All subjects' information obtained in this study was confidential and handled by applicable laws and regulations. The subject's identity would not be revealed without the parent's consent when publishing or presenting the study results or any images.

3.10.5 CT Pulmonary Angiogram on Paediatric Patients Below 2 Years Old

To primarily diagnose pulmonary embolism (PE), CTPA uses CT angiography to obtain a picture of the pulmonary arteries. Due to the patient's minimally invasive nature, as the scan only requires an intravenous line, it is a recommended option for the diagnosis of PE. The gold standard for diagnosing pulmonary embolism is CTPA, which can produce images with appropriate resolution quickly compared to earlier diagnostic methods such as direct pulmonary angiography. An injector pump is used to administer a rapid intravenous injection of contrast agents to the patient. In a typical CTPA scan, the contrast will be seen filling the pulmonary arteries and will appear opaquely white. Mass-filling defects, such as an embolus, will obstruct the area where blood should flow into the lungs and thus appear darker in the CT scan images (Harun et al., 2020).

The routine technical parameters used for paediatric CTPA examinations using a Siemens CT scanner at the Radiology Department, Hospital Serdang, are referred to in Table 3.10. To be noted, 80 kV was a routine exposure factor in Hospital Serdang. As such, a correction factor needed to be done to correct the value of the beam quality. The participating patient was first positioned supine, feet into the gantry. As the intravenous line was usually set on the right hand, it would be more convenient to

position the patient's feet rather than head into the gantry to correspond with the position of the injector pump on the anterior aspect of the CT machine. Similar to the positioning in the chest CT scan, the patient's midsagittal plane (MSP) was adjusted to align with the central beam and the couch's midline with equal margins between the lateral thorax. No patient rotation was also ensured by placing the midcoronal plane (MCP) parallel to the couch. A usual topogram scan was initially done for a scout image of the patient's positioning. The monitoring slice (region of interest, ROI) was then positioned below the carina at the level of the pulmonary trunk with an ROI on the pulmonary artery. A small 'test' quantity of contrast was injected, and sequential axial slices at the set ROI were acquired to calculate the peak contrast enhancement time and determine an optimal scan delay. Figure 3.29 shows examples of patient position for CTPA examination at Hospital Serdang, together with the placement of dosimeter strips on the thyroid region.

Table 3.10: Routine technical parameters used for paediatric CTPA examination in HPUPM

Technical Parameters	Parameters
kV	80
Scan sequence mAs:	
-Topogram	50
-Pre-monitoring contrast	20
-Monitoring	20
-Body Angio	80-90
Average acquisition time	5-6 s
Rotation time	1 s
Slice thickness	3 mm (Acq 128 x 0.6 mm)
Pitch	0.8
Coverage	Lung apices through the diaphragm
Algorithm	Soft tissue and lung
Scan direction	Caudocranial

(a)

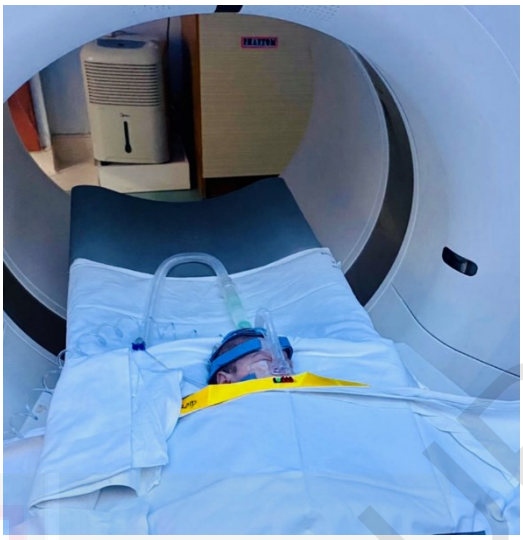

(b)

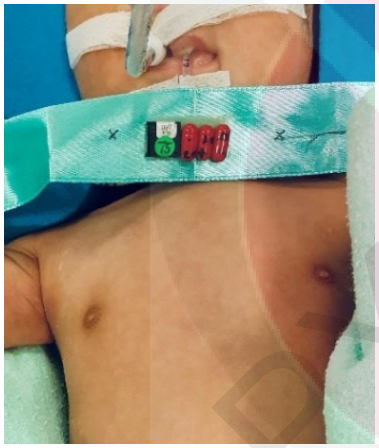

(c)

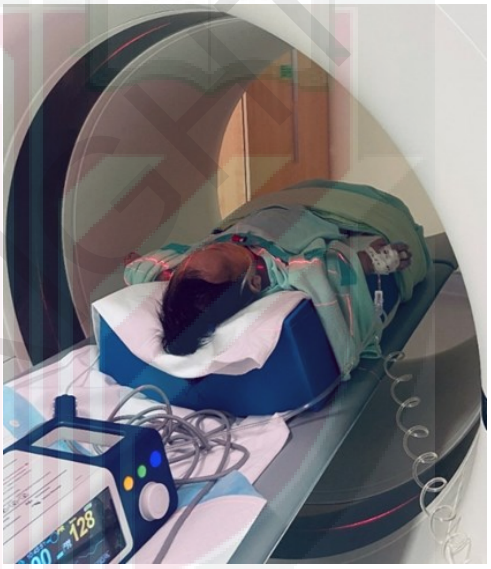

(d)

Figure 3.29: Patients' positions for CTPA examinations at the Radiology Department, Hospital Serdang together with the placements of dosimeter strips on thyroids and gonadal regions for paediatric patients below 2 years old

A comparative study between the responses of four types of fabricated optical fibres against the gold standards TLD-100 chips and nanoDots from CTPA scans on paediatric patients under two years of age was achieved through the measurements of the entrance skin doses on radiosensitive thyroid. Figure 3.30 summarises the

dosimeter verification study for both phantom and real clinical irradiations in terms of the selected organ and entrance skin doses.

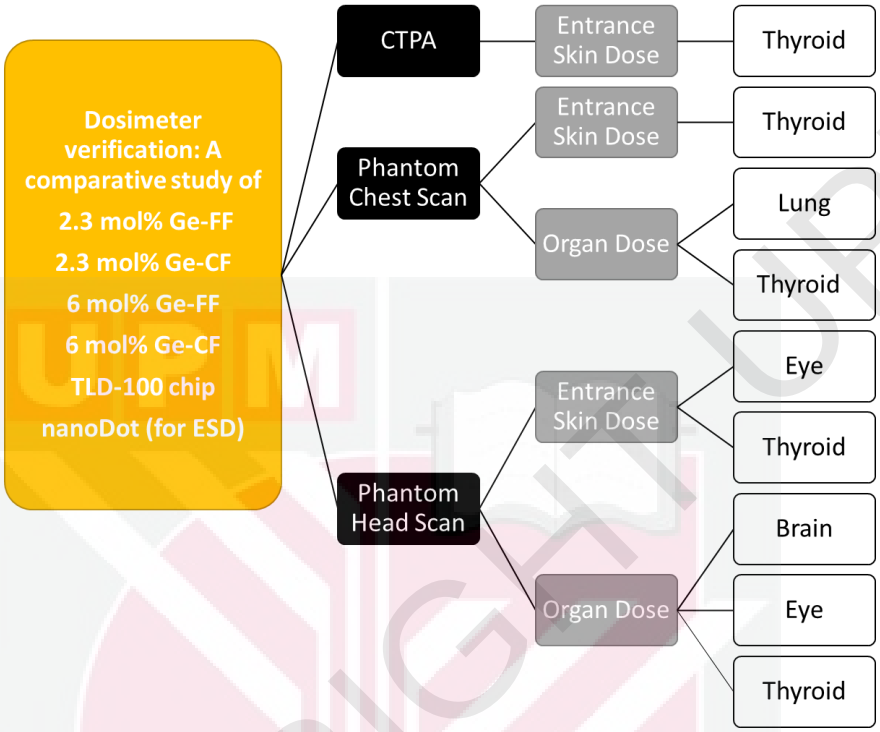

Figure 3.30: Summary of dosimeter verification study for phantom and real clinical irradiations in terms of the selected organ and entrance skin doses

3.11 Calibration Curves of the Investigated Dosimeters

As a relative dosimeter, the Ge-doped fabricated optical fibres, TLD-100 chips and nanoDots must be calibrated against absolute dosimetry systems such as a calibrated ion chamber before they are used (IAEA, 2007). In this study, the investigated dosimeters were calibrated against a 0.6 cc PTW Unidos ionisation chamber. The ionisation chamber was cross-calibrated against another standard ionisation chamber at the Secondary Standard Dosimetry Laboratory (SSDL), Malaysian Nuclear Agency. The latter has been calibrated with the reference standard ionisation chamber in terms of RQT beam quality at the IAEA Dosimetry Laboratory according to procedures

described in the IAEA TRS-457 (IAEA, 2007). The calibrations were performed by the substitution method in which the PTW Unidos ionisation chamber and the investigated dosimeters were positioned one after the other with their reference points on the beam axis at a distance of 100 cm from the focal spot.

Only a calibration curve for RQT 8 (100 kV) was established for this dosimetry study since it was the primary kV used in the comparative dosimetry verification study, as described in previous sections. In reference to Table 3.2 of radiation quality series RQT established at Nuklear Malaysia, 0.2 mm copper filter together with 3.7 mm aluminium filters were first slotted in front of Constant Potential Philips Industrial X-Ray machine as added filters with respect to the RQT 8 radiation quality and 100 kV X-ray tube voltage. The field size was then set up to be circular with a 7 cm diameter, designed for low scatter contributions. This could be achieved by slotting in a 2 cm diameter circular collimator in front of the added filters and applying 100 cm source image distance (SID), also known as the calibration point. In calibration by substitution, the reference 0.6 cc PTW Unidos ionisation chamber was initially placed at the calibration point to determine the reference output of the beam through a set of readings. It was then replaced by the investigated dosimeter to be calibrated, and a similar set of readings was taken. The dosimeters to be calibrated were positioned on a square board attached to a Perspex holder, which was designed for accurate alignment with the X-ray tube. The exposure settings were set as 5 milliamperes (mA). Manual calculations of the seconds (s) in exposure settings were adopted to define X-ray exposure durations to achieve the range of calibrated doses. The selected doses were similar to the dose linearity study in the 2 mGy to 40 mGy range (2-, 4-, 6-, 8-, 10-, 15-, 20-, 25-, 30-, 35- and 40 mGy). Temperature and pressure were recorded

with a digital barometer and corrected with the correction factors provided. As referred to in Equation 3.6, the reading of dosimeter which was already corrected for influence quantities, D, was obtained by multiplying the mean value of the readings taken after the ionisation chamber was settled (M_{RAW}) with the calibration factor of the SSDL reference standard for RQT 8 beam quality (N_{DW}) which was obtained from the calibration certificate, and a factor to correct for the departure of air density from reference conditions in terms of temperature and pressure (k_{TP}).

$$D = M_{RAW} \cdot N_{DW(RQT8)} \cdot k_{TP} \qquad \text{Equation 3.6}$$

The calibration coefficients refer to T=20°C, P=101.325 kPa and 50% relative air humidity. The measured ionisation current was corrected for the reference temperature of 20°C and pressure of 101.325 kPa, as referred to in Equation 3.7. The relative air humidity at the dosimetry laboratory was kept between 30% and 70%. No correction was applied for the humidity.

$$k_{TP} = (273.2\ ^{o}C + T_{REF}\ (^{o}C) / 273.2\ ^{o}C + 20\ ^{o}C) \times (101.325\ kPa / P_{REF}) \qquad \text{Equation 3.7}$$

Figure 3.31 shows the set-up of the Constant Potential Philips Industrial X-ray machine with RQT 8 filters aligned with 0.6 cc PTW Unidos reference chamber with a 100 cm distance from the source to the calibration point. The calibration curve was established by graphing the dosimeter response against the measured dose. Each dose point represented the mean of 10 fibres per capsule, three TLD-100 chips and two OSLD nanoDots. The standard deviation of the dosimeter response for each dose point determined the error bars. This visually represented the spread of data points around the mean.

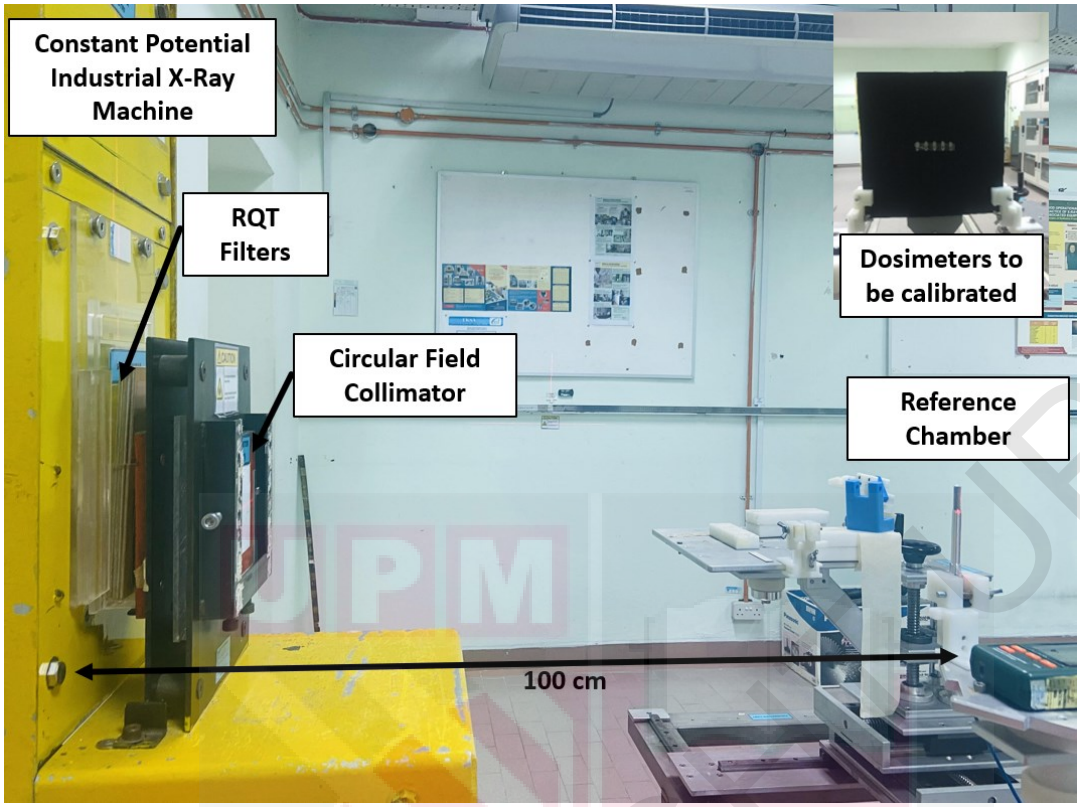

Figure 3.31: Calibration set-up of Constant Potential Philips Industrial X-ray machine with RQT 8 filters

3.12 Absorbed Dose, Calibration Coefficient, Correction Factors

3.12.1 Absorbed Dose Determination

The determination of absorbed dose using the fabricated Ge-doped optical fibres was acquired by comparing the response of the fibres with the readings given by the ion chamber. The absorbed dose from fabricated Ge-doped optical fibre measurement, D_{FIBRE} was calculated using Equation 3.8 adapted from a study by Noor et al. (2014):

$$D_{FIBRE} = R_{FIBRE} \cdot N_{FIBRE} \cdot K_{SI(FIBRE)} \cdot K_{LIN(FIBRE)} \cdot K_{RQT(FIBRE)} \cdot K_{FAD(FIBRE)}$$

Equation 3.8

Where R_{FIBRE} is the average fibre response, and N_{FIBRE} is the calibration coefficient of the Ge-doped optical fibres, respectively. The correction factor for the individual capsule is represented by $K_{SI(FIBRE)}$, while the other correction factors herein were developed from the basic dosimetric characteristics previously studied in section 3.8. These are $K_{LIN(FIBRE)}$, which represents the correction factor for dose linearity, $K_{RQT(FIBRE)}$ for RQT beam quality or energy dependence and $K_{FAD(FIBRE)}$ for TL signal fading post-irradiation.

The equations for determining the absorbed dose by the TLD-100 chip and nanoDot are similar to D_{FIBRE} apart from the name change in the subscript, as shown in Equations 3.9 and 3.10 for the TLD-100 chip and OSLD nanoDot, respectively.

$$D_{TLD} = R_{TLD} \cdot N_{TLD} \cdot K_{CHIP(TLD)} \cdot K_{LIN(TLD)} \cdot K_{RQT(TLD)} \cdot K_{FAD(TLD)}$$

Equation 3.9

$$D_{OSL} = R_{OSL} \cdot N_{OSL} \cdot K_{DOT(OSL)} \cdot K_{LIN(OSL)} \cdot K_{RQT(OSL)} \cdot K_{FAD(OSL)}$$

Equation 3.10

3.12.2 Average Reading

The average reading for Ge-doped fabricated optical fibres for the dosimetry phantom and clinical studies was acquired through the measurements of five (5) fibres in one tissue-equivalent plug or capsule for all four fibre types (2.3 mol% Ge-FF, 2.3 mol% Ge-CF, 6 mol% Ge-FF and 6 mol% Ge-CF). Meanwhile, three (3) chips sandwiched in between tissue-equivalent plugs or inserted inside a capsule were used for the average readings of the TLD-100 chip, and one (1) nanoDot in its respective casing, which was read five (5) times represented the mean reading for OSL dosimeter. The mean readings for optical fibre and TLD-100 chip are in TL signals (nC), while for

nanoDot, the signals are denoted as counts. To calculate the average reading, $\overline{R}$, of the five (5) fibres, three (3) TLD-100 chips and five (5) nanoDot readings, n, the following Equation 3.11 was employed (Noor et al., 2014). R_i is the dosimeter response of the i^{th} capsule, while B is the average background reading also known as the average unirradiated dosimeter reading or control. The control dosimeter is placed in the area of the control panel, outside the X-ray room.

$$\bar{R} = \frac{1}{n}\sum_{i=1}^{n} R_i - B \qquad \text{Equation 3.11}$$

3.12.3 Calibration Coefficient

The average calibration coefficient, N, obtained from the n readings of Ge-doped optical fibres, TLD-100 chips and nanoDots were determined according to Equation 3.12 as adapted from Noor et al. (2014).

$$N = \frac{1}{n}\sum_{i=1}^{n} \frac{D_i}{(R_i - B)} \qquad \text{Equation 3.12}$$

Where D_i and R_i are the doses given to the i^{th} capsule and the average reading in the i^{th} capsule respectively, while B is the average background reading. The calibration coefficients are given in mGy/nC for optical fibre and TLD-100 chip while mGy/count is given for nanoDot.

For calibration irradiations, the absorbed dose given to investigated dosimeters, D, is compared against measurements obtained using a 0.6 cc PTW Unidos ionisation chamber as described in section 3.11 for calibration curve establishment in reference to TRS 457 (IAEA, 2007).

3.12.4 Individual Correction Factor

The value of individual correction factor capsules or casing for fabricated Ge-doped optical fibre, TLD-100 chip and OSLD nanodot, K_{SI} / K_{TLD} / K_{OSL} was determined by applying the relation of Furetta et al. (2001) and adapted in reference to Noor et al. (2014) in Equation 3.13:

$$K_{SI}/K_{TLD}/K_{OSL} = \sum_{i=1}^{n} \frac{\bar{R}_{net}^{ref}}{R_i - R_{oi}} \qquad \text{Equation 3.13}$$

where $\bar{R}_{net}^{ref}$ is the average of the reference irradiated dosimeters, R_i is the reading of the i^{th} capsule, annealed and irradiated at a well-defined dose D, and R_{oi} is the dosimeter's background reading after annealing but without being irradiated. Reference dosimeters are chosen from the group of optical fibres, TLD-100 chips, and nanoDots that demonstrate average dose response or sensitivity in the entire group of screened dosimeters.

3.12.5 Beam Quality Correction Factor

As discussed in section 3.11, the investigated dosimeters were calibrated under RQT 8 (100 kV) beam quality by using a 0.2 mm copper filter together with a 3.7 mm aluminium filter to achieve the first HVL filtration of 6.9 mm Al in accordance with TRS 457 (IAEA, 2007). The beam quality or energy correction factor, K_{RQT8}, is the ratio of the dosimeter response per unit dose (R/D), computed at calibrated RQT 8 (100 kV) beam quality to the dosimeter response per unit dose (R/D) calculated at different beam quality used in clinical settings such as RQT 9 (120 kV) or RQT 10 (150 kV). However, the primary beam quality used in this research is the calibrated

RQT 8 (100 kV); as such, no beam quality or energy correction factor may be applied in such cases. Equation 3.14 shows the beam quality or energy correction factor adapted from Noor et al. (2014).

$$K_{RQT8} = \frac{(R/D)_{RQT8}}{(R/D)_{(RQT9\ or\ RQT10)}} \qquad \text{Equation 3.14}$$

3.12.6 Fading Correction Factor

The fading function, f_{fad}, is defined as the ratio of the dosimeter response, f_t, read on day x, to the dosimeter response, f_o, read on day x_o, as shown in the following Equation 3.15, adapted from Noor et al. (2014):

$$f_{fad} = \frac{f_t}{f_o} = \frac{f_o[(y_o - d)e^{-kx} + d]}{f_o} = (y_o - d)e^{-kx} + d \qquad \text{Equation 3.15}$$

Where y_o is the value of y when x value is zero, d is the value of y at infinite times (known as a plateau), and k is a rate constant. The y_o, d and k values were obtained from the exponential decay equation model using GraphPad Prism software. The fading correction factor, K_{FAD}, is the ratio of the fading function of the dosimeter at a reference day set by the researcher, in which the fading function will be equal to 1, to the fading function of the dosimeter when it is read on x day, as in the following Equation 3.16.

$$K_{FAD} = \frac{f_{fad\ (ref\ day)}}{f_{fad\ (x\ day)}} = \frac{(y_o - d)e^{-kx(ref\ day)} + d}{(y_o - d)e^{-kx(x\ day)} + d} \qquad \text{Equation 3.16}$$

3.12.7 Dose Linearity Correction Factor

Based on the basic dosimetric characteristics study on the four types of fabricated Ge-doped optical fibres, TLD-100 chips and OSLD nanoDots, the dosimeter responses were linear over the dose range studied (2 to 40 mGy). Thus, no correction factor of dose linearity was applied for the measurement of absorbed dose for all investigated dosimeters.

3.13 Uncertainty Analysis

A statement of uncertainty indicates how large the measurement error might be (IAEA, 2008), as simplified in Equation 3.17:

$$T = T_m \pm U_T \qquad \text{Equation 3.17}$$

Where T is the true value, T_m is the measured value and the range $\pm U_T$ is the measurement uncertainty. The analysis of the uncertainty of the experimental results is essential in order to clarify the level of confidence and accuracy that the value lies within the range defined by the uncertainty interval. Apart from that, it also allows users of the results to assess the reliability of the measured data.

The present work uses two types of uncertainty in measurement: Type A (denoted as u_a) and Type B (denoted as u_b). Type A standard uncertainties are evaluated based on a statistical analysis of a series of independent observations or the repeatability of instrument readings towards its calibration uncertainty (IAEA, 2008). Examples of the Type A uncertainties associated with this study are repeated measurement of dosimeter response and several correction factors employed for the determination of absorbed dose by the fabricated Ge-doped optical fibres, TLD-100 chips and nanoDots

such as individual capsule correction factor, fading correction factor, and beam quality correction factor.

When the calibrated instrument is subsequently used to make another measurement, its calibration coefficient makes a Type B contribution to the uncertainty of that subsequent measurement. Type B uncertainties are not based on statistical data analysis and cannot be estimated by repeat measurements (IAEA, 2008). Examples of Type B uncertainties are barometer calibration, barometer resolution, and calibration uncertainty for reference based on instrument calibration reports and previous measurement data.

3.13.1 Uncertainty of an Average Reading

The uncertainties in the average reading of fabricated Ge-doped optical fibres, TLD-100 chips and OSLD nanoDots *u(Ri)* are given by:

$$u(Ri) = \frac{\sum_i \sigma_i}{\sqrt{n} \cdot l} \qquad \text{Equation 3.18}$$

Where σ_i is the standard deviation of the fibres and TLD-100 chips response of the *i*th capsule or the standard deviation of the repeated readings for *i*nanoDot, *l* is the number of capsules and nanoDots used in the investigation, and *n* is the number of fibres or TLD-100 chips per capsule or the number of readings per nanoDot (Izewska et al., 2008).

3.13.2 Uncertainty of the Calibration Coefficient

The uncertainty of the calibration coefficient of fabricated Ge-doped optical fibres, TLD-100 chips and nanoDots was contributed by several factors, including uncertainty in the readings of optical fibres and TLD-100 chips within a capsule or repeated readings per nanoDot $u(R_i)$ and uncertainty during the determination of absorbed dose by the ionisation chamber $u(D_{IC})$. Uncertainty due to the background reading, B is disregarded as its magnitude is smaller than the average reading of a capsule or nanoDot (Izewska et al., 2008). Thus, in order to calculate the uncertainty of a calibration coefficient of investigated dosimeters $u(N)$, the combined relative uncertainty is used, where n is the number of reference capsules and nanoDots given by:

$$u(N) = \sqrt{\frac{u(D_{IC})^2 + u(R_i)^2}{n}} \qquad \text{Equation 3.19}$$

3.13.3 Uncertainty in an Individual Correction Factor

The uncertainty of an individual correction factor is obtained using the combined relative uncertainty provided by Equation 3.20, adapted from Noor et al. (2014):

$$u(K_{SI}\ or\ K_{TLD} or\ K_{OSL}) = \sqrt{u(\overline{R}_{net}^{ref})^2 + u(R_i)^2} \qquad \text{Equation 3.20}$$

Where $u(\bar{R}_{net}^{ref})$ is the relative uncertainty of the average reading of the reference irradiated dosimeters and $u(R_i)$ is the relative uncertainty in the average reading of the dosimeter in the ith capsule or $i$nanoDot.

3.13.4 Uncertainty of the Beam Quality

Uncertainty in the energy correction factor is calculated from least-squares fit as referred in Noor et al. (2014) where $y_{i(measured)}$ is the energy correction measured value, $y_{calculated}$ is the estimation of the y-value from the best-fit line *(y = mx + c)* and *N* represents the number of the investigated dosimeters used in the fit. The response of each beam quality of RQT 8 (100 kV), RQT 9 (120 kV) and RQT 10 (150 kV) was normalised to the response for RQT 8 beam quality since it was used in the phantom study as given by:

$$u(K_{RQT8}) = \sqrt{\frac{I}{N-2}\sum_{i=1}^{N}(y_{i(measured)} - y_{calculated})^2} \quad \text{Equation 3.21}$$

3.13.5 Uncertainty in the Fading Correction Factor

The uncertainty in the fading correction factor of investigated dosimeters due to TL was evaluated from error propagation according to Equation 3.22 developed by Noor et al. (2014):

$$u(K_{FAD}) = \sqrt{\left(\frac{\partial K_{fad}}{\partial y_0}\right)^2 u(y_0)^2 + \left(\frac{\partial K_{fad}}{\partial d}\right)^2 u(d)^2 + \left(\frac{\partial K_{fad}}{\partial k}\right)^2 u(k)^2} \quad \text{Equation 3.22}$$

Where $u(y_0)$, $u(d)$and $u(k)$ are the uncertainties in the coefficient y_0, *d* and *k* obtained from nonlinear regression analysis using GraphPad Prism software.

3.13.6 Combined and Expanded Uncertainty

All the measurable parameters that contributed to the measurement of the absorbed dose are considered independent of each other. Hence, the square root of the sum of

square uncertainties of each measurement parameter is used to calculate the combined uncertainty (denoted as u_c) (IAEA, 2008). The combined uncertainty of absorbed dose determination for fabricated Ge-doped optical fibre, TLD-100 chip and OSLD nanoDot is as Equation 3.23:

$$u_c(D) = \sqrt{u(Ri)^2 + u(N)^2 + u(K_{SI})^2 + u(K_{RQT8})^2 + u(K_{FAD})^2} \quad \text{Equation 3.23}$$

Lastly, the expanded uncertainty (denoted as u_p), was calculated by multiplying the combined uncertainty, with a coverage factor, k_p having a level of confidence, p, as shown in Equation 3.24:

$$u_p(D) = \left[\sqrt{u(Ri)^2 + u(N)^2 + u(K_{SI})^2 + u\left(K_{RQT8}\right)^2 + u(K_{FAD})^2}\right] \times k_p \quad \text{Equation 3.24}$$

The result of a measurement is commonly written as $y \pm u_p$ which has an approximate level of confidence, p. The values of $k_p = 1$, $k_p = 2$, and $k_p = 3$ correspond to confidence limits of approximately 68%, 95% and 99%, respectively.

CHAPTER 4

RESULTS AND DISCUSSION

In this chapter, the results and discussion of this study are described. They are mainly categorised into a basic dosimetric characteristic study, a phantom study and a small clinical study.

4.1 RQT Radiation Quality Establishment

The utmost comprehensive description of an X-ray beam is characterised by its spectral distribution. To establish specific radiation quality, the portrayal of these beam qualities in the form of X-ray tube voltage and the first half value layer (HVL) is usually applied because the spectrometry of X-rays necessitates a substantial amount of in-field competency and it also takes longer duration to be accomplished. A concession amongst the equally varying needs of evading extreme methodology to establish a radiation quality and of warranting any uncertainty in the description of the radiation quality amongst many diagnostic imaging centres has led to the documentation of the standardised International Code of Practice TRS 457 (IAEA, 2007). Specific radiation quality generated by different X-ray tubes at different institutions may still possess non-identical beam spectrometry due to the inconsistency in the X-ray tube's age and construction concerning the anode angle, anode roughening and inherent filtration throughout the years. As such, the Secondary Standard Dosimetry Laboratory (SSDL) in every country must act as the national standard in reference to the secondary standard laboratory in Vienna, Austria for the calibration of dosimeters against the radiation quality to be tested. In Malaysia, SSDL

is under the government-run Malaysian Nuclear Agency (Nuklear Malaysia), where all radiation qualities are established.

As referred to in Table 4.1, radiation qualities implemented in calibrations for diagnostic imaging dosimeters are shown with their probable applications. The additional filtration determination technique for measuring the first HVL can be applied to depict different radiation qualities. This technique is based on the methodology documented in Technical Report Series 457 (IAEA, 2007). For the experimental technique, narrow beam geometry must be applied to define the additional filtration needed for the first HVL using a small collimator. Secondly, the circular radiation beam field incident to the ionisation chamber must be adequate to expose it entirely and consistently for an accurate measurement. This close collimation technique guarantees a lesser amount of scattered radiation, which can eliminate the contribution of significant signals to be recorded by the reference ionisation chamber.

The RQT radiation quality simulates the unattenuated beam applied in computed tomography (CT), while the RQR radiation quality simulates the radiation beam emerging from general X-ray radiography. The RQT beam quality can be conveniently established by determining additional filtration of copper (Cu) to the corresponding RQR beam quality after the prior establishment of RQR beam quality. In other words, RQR radiation quality must be established first before the other radiation qualities are determined. A yearly assessment of the first HVL filtration of the specified radiation quality must be done to validate that probable differences, when compared against the previous years' first HVL values, should not exceed 3% (IAEA, 2007). In subsequent

sections, an establishment for RQT radiation quality at Nuklear Malaysia for the year 2020 is thoroughly described.

4.1.1 RQT 8 Additional Filtration Determination

The determination of additional filtration for characterisation of radiation quality RQT 8 (100 kV) was initiated by slotting in RQR-added filters with 3.7 mm aluminium (Al) thickness and RQT-added filter of 0.2 mm copper (Cu) thickness in front of the X-ray tube. The thickness of the added filters was in accordance with the previously established RQR beam quality for the years 2016-2019. Once the added filters were slotted in, the first measurement was made with the technical factor settings, as mentioned in Chapter 3, section 3.3.4. This measurement was considered as a measurement without an HVL filter, and the average dose recorded was 10.9 mGy, as shown in columns 4 and 5 of Table 4.1. Theoretically, half of the average dose of 10.9 mGy was 5.45 mGy. By the experimental method of adding in an HVL filter of different thicknesses, the HVL filters were later added on until the average dose as close to half of the original dose without an HVL filter was achieved. The nominal first HVL filtration for RQT 8 was 6.9 mm Al in reference to the theoretical value of IAEA (2007). As such, the thickness of HVL filters could be added around this value. For the second exposure, an HVL filter of 5.0 mm Al thickness was slotted in front of the collimator, and the average dose of five readings was recorded as 6.6 mGy. This step was repeated by adding in subsequent 6, 7- and 8-mm Al thickness and average dose readings of 5.9, 5.5- and 4.9-mGy were achieved, respectively. A linear graph of the normalised average dose against the Al thickness was then produced, as shown in Figure 4.1. Finally, a measured first HVL filtration was acquired from the interception of the linear graph at its half value of normalised average doses represented by the

dotted line in Figure 4.1. The Al thickness required could also be calculated by determining the x-value in the linear equation provided through the graph. For this experiment of RQT 8, the first HVL filtration was calculated to be 6.9 mm Al, as shown in column 7 of Table 4.1. This was an exact value to the theoretical first HVL filtration as IAEA (2007) recommended; thus, no further measurement was necessary. RQT 8 radiation quality at Nuklear Malaysia for the year 2020 was successfully established.

Table 4.1: Determination of additional filtration for characterisation of radiation quality RQT 8

Radiation Quality	X-ray Tube Voltage (kV)	Added Filtration RQR (mm Al) + RQT (mm Cu)	HVL Filter (mm Al)	Average Dose (mGy)	First HVL Filtration (mm Al)		Diff (%)
					Theory	Measured	
RQT 8	100	3.7 + 0.2	0	10.9	6.9	6.9	0
			5.0	6.6			
			6.0	5.9			
			7.0	5.5			
			8.0	4.9			

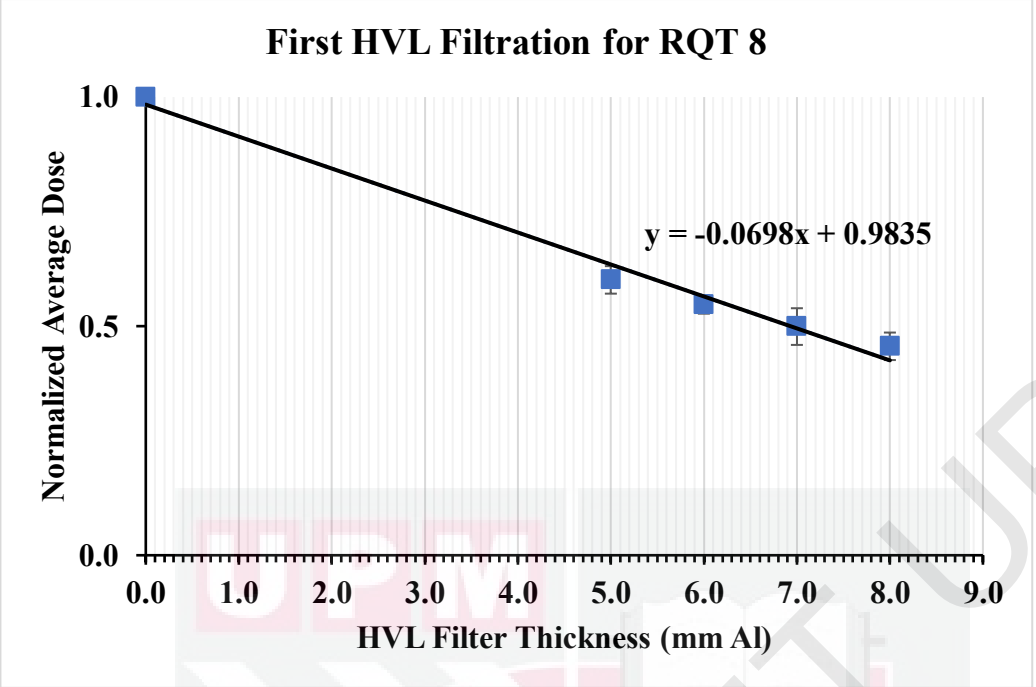

Figure 4.1: Measured first HVL filtration (mm Al) for RQT 8

4.1.2 RQT 9 Additional Filtration Determination

Similarly, the determination of additional filtration for characterisation of radiation quality RQT 9 (120 kV) started by slotting in RQR-added filters with 4.0 mm Al thickness and RQT-added filter of 0.2 mm Cu thickness in front of the X-ray tube as shown in Table 4.2. The average dose recorded without the HVL filter was 17.1 mGy, as shown in column 5 of Table 4.2. Half of the average dose of 17.1 mGy was 8.55 mGy. HVL filters of different thicknesses were added to achieve an average dose as close to half of the original dose without an HVL filter. The nominal first HVL filtration for RQT 9 was 8.4 mm Al in reference to the theoretical value of IAEA (2007). As such, the thickness of HVL filters was added around this value. For the second exposure, an HVL filter of 7.0 mm Al thickness was slotted in front of the collimator, and the average dose of five readings was recorded as 9.3 mGy. This step was repeated by adding in subsequent 8, 9- and 10-mm Al thickness and average dose

readings of 8.6, 7.9- and 7.3-mGy were achieved, respectively. A linear graph of the normalised average dose against the aluminium thickness was then produced, as shown in Figure 4.2. Finally, a measured first HVL filtration was acquired from the interception of the linear graph at its half value of normalised average dose represented by the dotted line in Figure 4.2, together with the calculation of the x-value in the linear equation provided through the graph. The calculated first HVL filtration of RQT 9 was 8.3 mm Al, as shown in column 7 of Table 4.2 below. This amounted to a decrease of 1.2 % difference when compared to the theoretical value of 8.4 mm Al as recommended by IAEA (2007). This new value change with respect to the value established in IAEA was less than a 3% difference. The establishment of RQT 9 radiation quality at Nuklear Malaysia for the year 2020 was deemed successful, with no change of added filtration RQR (mm Al) and RQT (mm Cu) thickness.

Table 4.2: Determination of additional filtration for characterisation of radiation quality RQT 9

Radiation Quality	X-ray Tube Voltage (kV)	Added Filtration RQR (mm Al) + RQT (mm Cu)	HVL Filter (mm Al)	Average Dose (mGy)	First HVL Filtration (mm Al)		Diff (%)
					Theory	Measured	
RQT 9	120	4.0 + 0.2	0	17.1	8.4	8.3	1.2
			7.0	9.3			
			8.0	8.6			
			9.0	7.9			
			10.0	7.3			

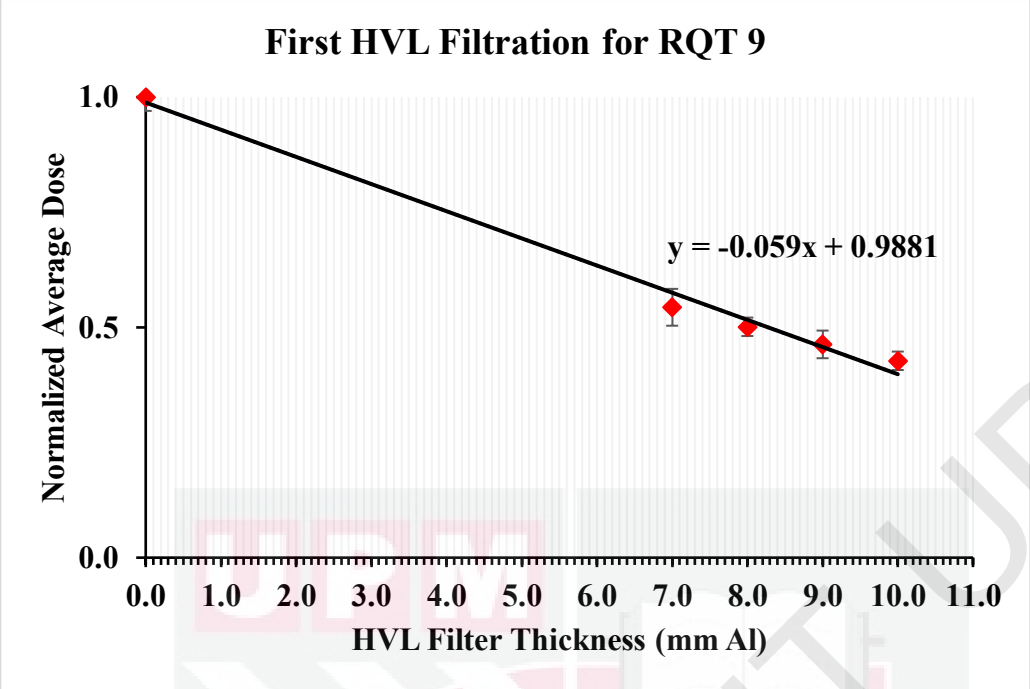

Figure 4.2: Measured first HVL filtration (mm Al) for RQT 9

4.1.3 RQT 10 Additional Filtration Determination

As referred to in Table 4.3, RQR-added filters with 4.8 mm Al thickness and RQT-added filters of 0.2 mm Cu thickness were initially slotted in front of the X-ray tube to determine RQT 10 characterisation before exposing it to 150 kV. The average dose recorded without the HVL filter was 27.4 mGy, and half of the average dose was calculated as 13.7 mGy. The reference (theory) value for RQT 10 first HVL filtration was 10.1 mm Al (IAEA, 2007). As such, the thickness of HVL filters was added around this value. For the second exposure, an HVL filter of 9.0 mm Al thickness was slotted in front of the collimator, and the average dose of five readings was recorded as 14.0 mGy. This step was repeated by adding 10, 11- and 12-mm Al thickness and average dose readings of 13.2, 12.4- and 11.6-mGy were achieved, respectively. Figure 4.3 shows a linear graph of the normalised average dose against the Al thickness. Finally, the first measured HVL filtration was acquired from the

interception of the linear graph at its half value of normalised average doses represented by the dotted line in Figure 4.3, together with the calculation of the x-value. The caluclated (measured) first HVL filtration of RQT 10 was 9.9 mm Al, as shown in Table 4.3. This amounted to a decrease of 2.0% difference when compared to the 10.1 mm Al IAEA reference value (IAEA, 2007). Similar to RQT 9, this new value changed with respect to the prior value established in the IAEA, had less than a 3% difference. The establishment of RQT 10 radiation quality at Nuklear for the year 2020 was deemed successful, with no change of added filtration RQR (mm Al) and RQT (mm Cu) thickness.

Table 4.3: Determination of additional filtration for characterisation of radiation quality RQT 10

Radiation Quality	X-ray Tube Voltage (kV)	Added Filtration RQR (mm Al) + RQT (mm Cu)	HVL Filter (mm Al)	Average Dose (mGy)	First HVL Filtration (mm Al)		Diff (%)
					Theory	Measured	
RQT 10	150	4.8 + 0.2	0	27.4	10.1	9.9	2.0
			9.0	14.0			
			10.0	13.2			
			11.0	12.4			
			12.0	11.6			

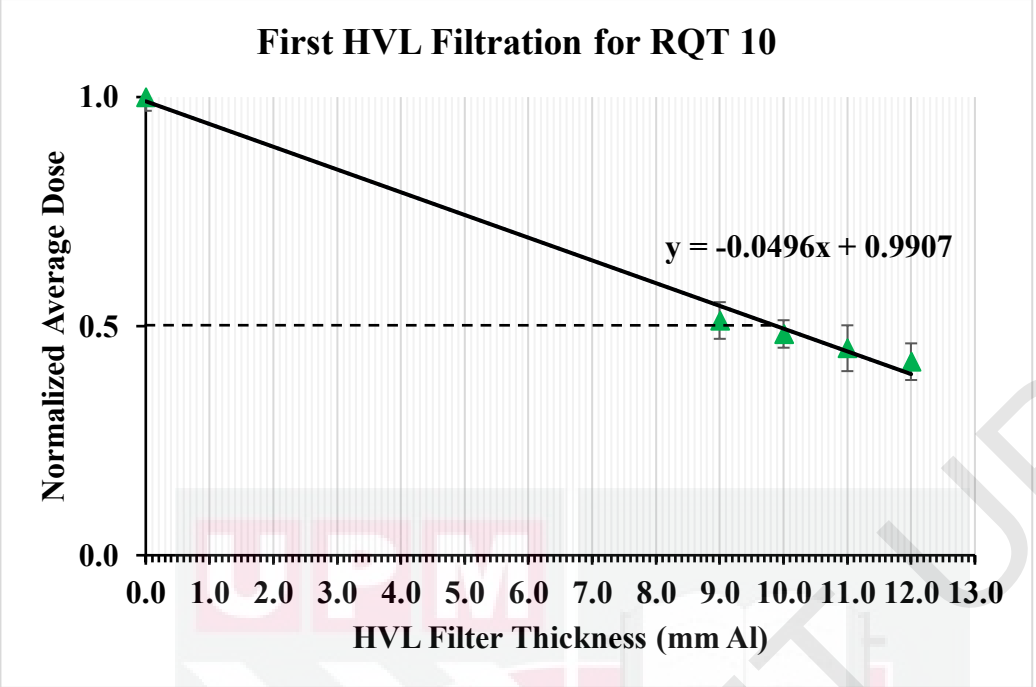

Figure 4.3: Measured first HVL filtration (mm Al) for RQT 10

4.1.4 Establishment of RQT Radiation Quality

In reference to Table 4.4, the finalised total added filtration of RQR (mm Al), added RQT (mm Cu) and measured value for the first HVL filtration were depicted. The results demonstrated that all three measured RQTs' first HVL filtrations (mm Al) complied with the tolerance limits of ± 3% as recommended by the TRS 457 (IAEA, 2007). Yearly monitoring on the first HVL filtration of the beams should be performed to verify that possible changes with respect to prior values were within the limit, thus maintaining the accuracy of standard radiation qualities for calibrating diagnostic dosimeters for CT applications in Malaysia. In summary, the periodic establishment of RQT radiation quality at Nuklear Malaysia for the year 2020 was accomplished. Subsequent dosimeter screening, basic characterisation irradiations, and absorbed dose determination were implemented for this study using these established RQT radiation qualities at Nuklear Malaysia.

Table 4.4: Establishment of radiation quality series RQT at Malaysian Nuclear Agency for the year 2020

Radiation Quality	X-ray Tube Voltage (kV)	Added Filtration RQR (mm Al)	Added Filtration RQT (mm Cu)	Total Filtration RQR (mm Al) + RQT (mm Cu)	First HVL Filtration (mm Al)		
					Theory	Measured	Diff (%)
RQT 8	100	3.7	0.2	3.7 + 0.2	6.9	6.9	0
RQT 9	120	4.0	0.2	4.0 + 0.2	8.4	8.3	1.2
RQT 10	150	4.8	0.2	4.8 + 0.2	10.1	9.9	2.0

4.2 Dosimeter Screening

Screening of dosimeters was carried out to ensure they produced more uniform signal responses prior to the start of the dosimetric study. The screening process generated three subgroups categorised as lower, middle, and upper. The middle group represented a batch of dosimeters that produced readings between -5% and +5%, while the lower group indicated a batch that produced signals smaller than -5% from the mean signal. Last but not least, the dosimeters that showed signals greater than 5% over their mean signal were grouped and designated as the upper group. Table 4.5 contains detailed information about the dosimeter screening results, and Figures 4.4 to 4.10 display scatter plots of the screening results for each type of fibre, TLD-100 chip, and OSLD nanoDot. The shaded regions on the scatter plots represented the middle group of the dosimeters that gave the average signals for the entire batch. It can be seen from Table 4.5 that the coefficient of variation (CV), defined as the percentage ratio of the standard deviation to the mean thermoluminescence (TL) response of all dosimeters in the middle group, was less than 4%. In comparison, the dosimeter responses' variabilities in the lower and upper groups were mainly around

5% to 6%, respectively. For the newly fabricated optical fibres, these CVs reflected the relative homogeneous dopant concentrations within these groups.

As demonstrated in Figure 4.4 for 2.3 mol% Ge-FF, a total of 61 out of 240 flat fibres were distributed within the middle group with 3.09% CV. For the lower and upper groups, the number of optical fibres was 95 and 84 fibres, respectively. It could be seen in the figure that the individual fibre in the lower and upper groups was dispersed more widely, with 5.47% and 6.25% CV. Figure 4.5 meanwhile illustrated a distribution of 2.3 mol% Ge-CF after the screening process. A total of 76 out of 240 cylindrical fibres were closely scattered within the middle group with 2.86% CV. For the lower and upper groups, the number of optical fibres was 86 and 78 fibres each. It could also be seen in the figure that the individual fibre in the lower and upper groups was spread further apart with 5.18% and 6.77% CV, respectively. Following the screening process of 6.0 mol% Ge-FF, a total of 68 out of 240 flat fibres were distributed within the middle group with 2.80% CV. This was the lowest CV when compared against all investigated fabricated fibres. For lower and upper groups, the number of optical fibres was similar which was 86 fibres. It could be seen in the figure that some of the individual fibre in the lower and upper groups were distributed outside the shaded area with 5.14% and 5.48 % CV, respectively. For 6.0 mol% Ge-CF, the total number of flat fibres was slightly lesser than the other fabricated fibres with 230 fibres. However, the number of optical fibres within this middle group was the highest, with 83 fibres after the screening process, as displayed in Figure 4.7. The CV for the middle group was recorded as 2.89%. For lower and upper groups, the number of optical fibres was 79 and 68 fibres, with their CVs among the lowest for fabricated fibres, which were 5.04% and 4.04%, respectively.

For commercial fibre, TLD-100 chip and OSLD nanoDot, their distributions are exhibited in Figures 4.8, 4.9 and 4.10 with a total number of 90 fibres, 99 chips and 49 nanoDots respectively. The number of dosimeters in the middle groups for commercial fibre, TLD-100 chip and OSLD nanoDot was 40 (3.04% CV), 32 (2.21% CV) and 43 (2.12% CV) while the number of dosimeters in the lower groups was 26 (6.08% CV), 33 (5.87% CV) and 4 (2.19% CV). Finally, the number of dosimeters in the upper groups was 24 (5.61% CV), 34 (2.65% CV) and 2 (0.67% CV) for commercial fibre, TLD-100 chip and OSLD nanoDot, respectively.

Table 4.55: Distribution of dosimeters in designated groups after the screening process

Types of Dosimeters	Average Signal	Total Number of Dosimeters	Number of Dosimeters			Coefficient of Variation CV (%)		
			Lower	Middle	Upper	Lower	Middle	Upper
2.3 mol% Ge-FF	51.00 nC	240	95	61	84	5.47	3.09	6.25
2.3 mol% Ge-CF	54.18 nC	240	86	76	78	5.18	2.86	6.77
6 mol% Ge-FF	15.25 nC	240	86	68	86	5.14	2.80	5.48
6 mol% Ge-CF	59.04 nC	230	79	83	68	5.04	2.89	4.04
Commercial Fibre	10.83 nC	90	26	40	24	6.08	3.04	5.61
TLD-100 chip	192.90 nC	99	33	32	34	5.87	2.21	2.65
OSLD nanoDot	124364 count	49	4	43	2	2.19	2.12	0.67

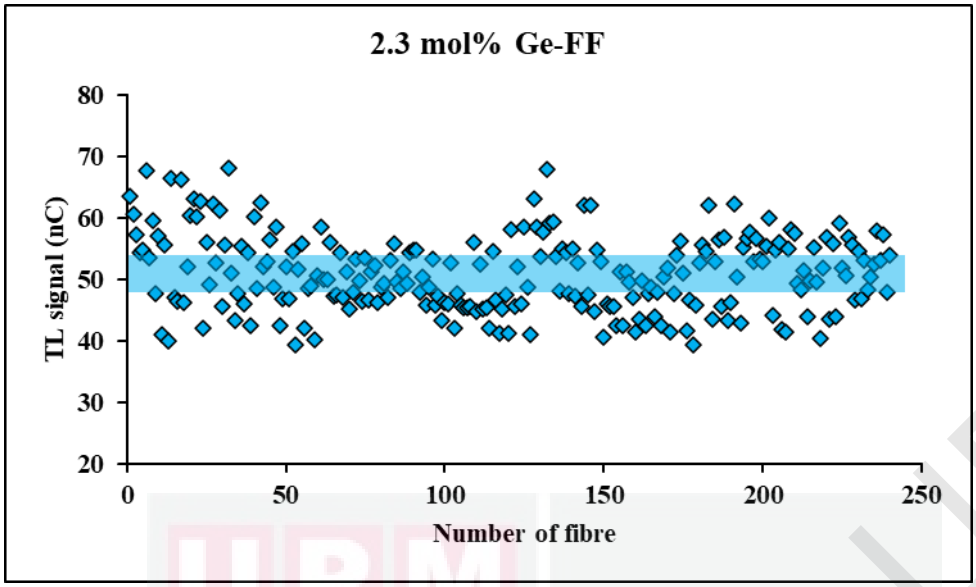

Figure 4.4: Distribution of 2.3 mol% Ge-FF after the screening process. The shaded area represents the middle group

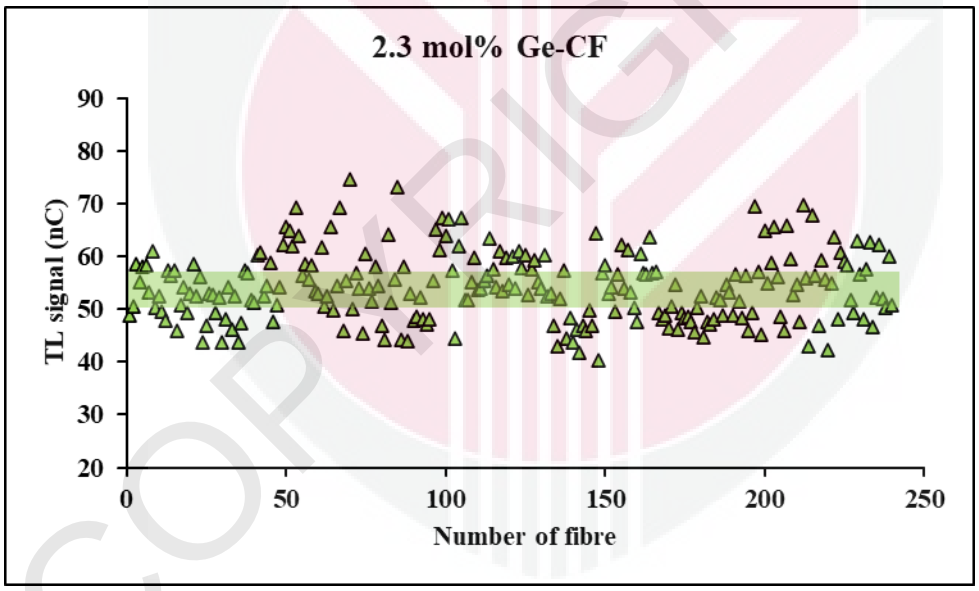

Figure 4.5: Distribution of 2.3 mol% Ge-CF after the screening process. The shaded area represents the middle group

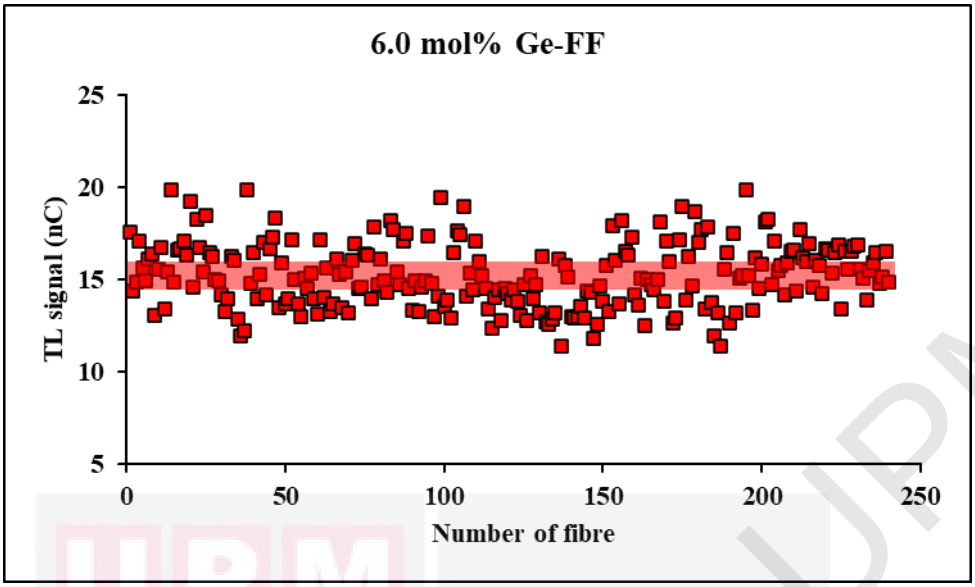

Figure 4.6: Distribution of 6.0 mol% Ge-FF after the screening process. The shaded area represents the middle group

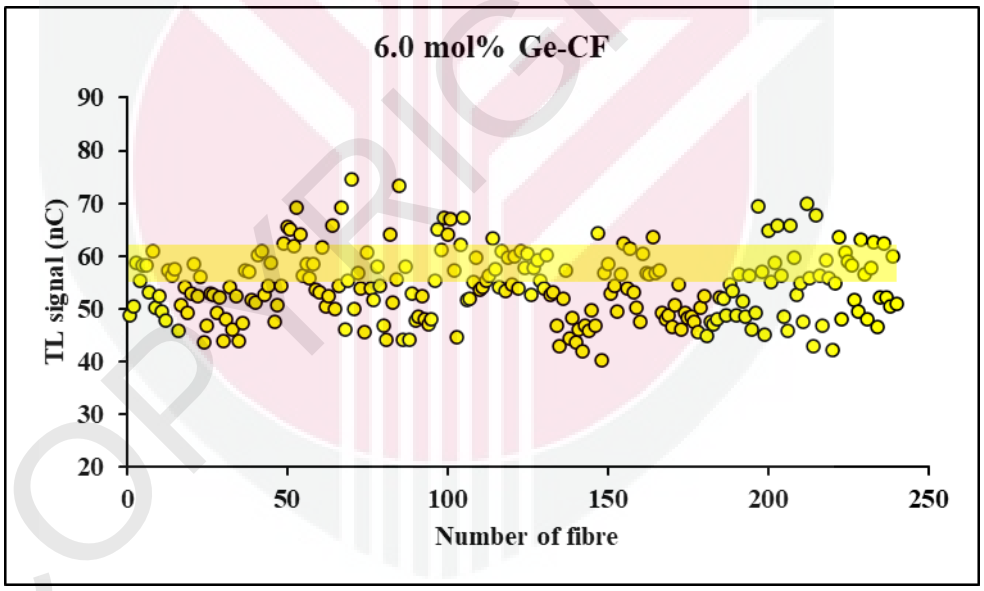

Figure 4.7: Distribution of 6.0 mol% Ge-CF after the screening process. The shaded area represents the middle group

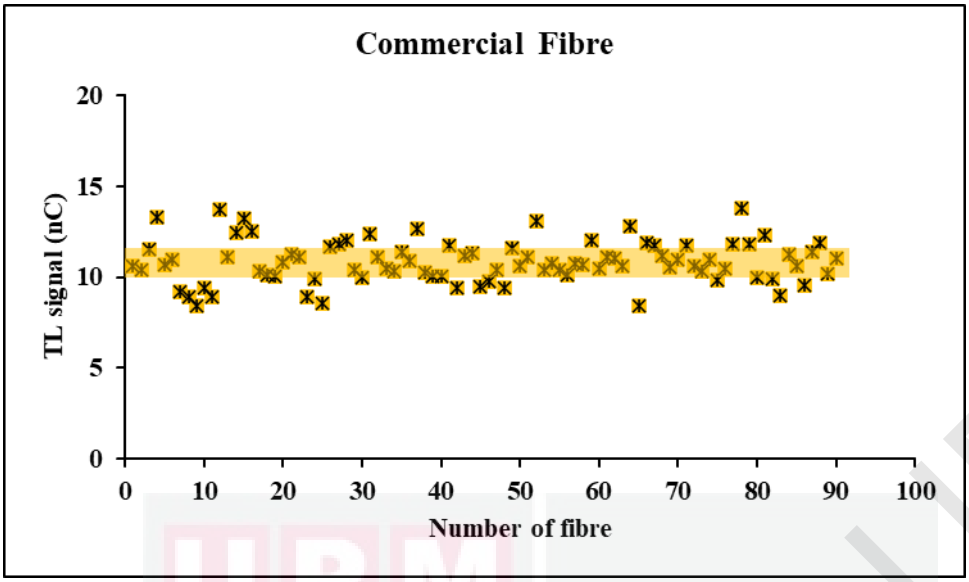

Figure 4.8: Distribution of commercial fibre after the screening process. The shaded area represents the middle group

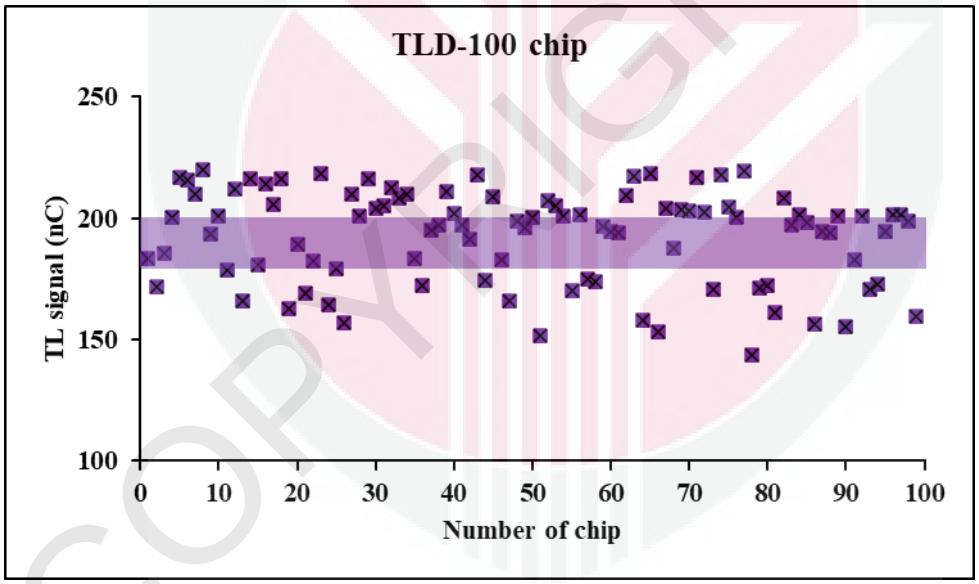

Figure 4.9: Distribution of TLD-100 chips after the screening process. The shaded area represents the middle group

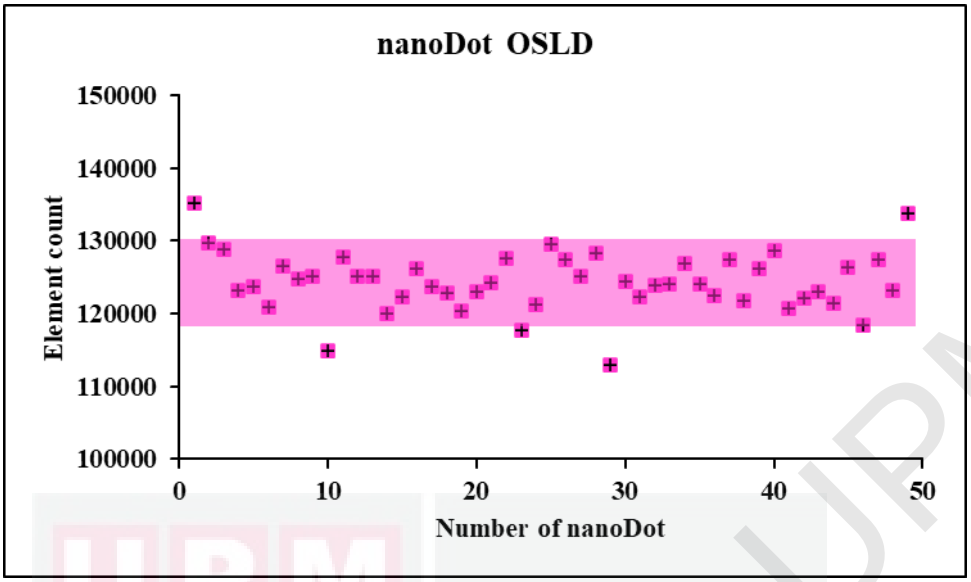

Figure 4.10: Distribution of OSL nanoDots after the screening process. The shaded area represents the middle group

The lower sensitivity batch was used for higher dose measurements while the higher sensitivity batch was used for lower dose measurements in later characterisation and clinical studies due to the limited number of dosimeters. In other words, all dosimeters in the lower, middle and upper groups were used for subsequent studies. To minimise disparity in the dosimeter response throughout the dose range, the dosimeters in the upper group were assigned for lower dose measurements due to their increased sensitivity in minimum dose detection. The lower group of dosimeters, which had lower sensitivity, was subsequently assigned for higher dose measurements. That being said, these three groups were still within ±5% of the mean dosimeter response. The individual correction factor was also done to determine the uncertainty, as detailed in the subsequent sections. In particular, the approach of raw signal conversion to absorbed dosage through the application of individual correction factors depends on this screening procedure to group the dosimeters.

4.3 Scanning Electron Microscope (SEM) with Energy Dispersive X-ray Analysis (EDX) of Fabricated Fibres

The optical fibres were sent to Quasi-S Technology Sdn after the screening process. Bhd, Universiti Kebangsaan Malaysia (UKM) for scanning electron microscopy with energy-dispersive X-ray spectroscopy (SEM/EDX) analysis prior to the commencement of the dosimetry study in order to map the elemental distribution and germanium (Ge) concentration in the cores as well as measure the cross-sectional dimension of the recently manufactured optical fibres. The fibres that had the highest yields following exposure to the RQT beam quality source were chosen for SEM/EDX examination. This is important to ensure that the existence of Ge in the fibres can be most easily detected during EDX analysis (Mohd Noor, 2012). The optical fibres' cross-sectional surface was scanned, and a point mapping technique was utilized for element identification on the core area.

4.3.1 Scanning Electron Microscope (SEM) Analysis

As can be seen from their mostly circular and flat geometries, Figures 4.11 and 4.12 demonstrate SEM images of two different types of cylindrical fibres (CF), while Figures 4.13 and 4.14 display images of flat fibres. The Ge is seen to have been deposited in the optical fibre's centre core based on the scanned images. The brighter zone represented the Ge-enriched region, and the darker zone represented the silica material. The Ge-doped region appears as a circular ring for cylindrical fibres, but for flat fibres (FF), the core appears as a thin strip. According to Figure 4.11 (a), which shows cross-sectional views of 2.3 mol% Ge-CF, the core has a diameter of 125 µm while the cladding, or exterior diameter of the entire fibre, is measured at 475 µm as shown in Figure 4.11 (b). The same is true for the cross-sectional views of the 6 mol%

Ge-CF, with a core diameter of 96.4 µm and a cladding diameter of 613 µm, in Figure 4.12. To get the core volumes for flat fibres, the dimensions of the core are determined as the product of their lengths and widths. Figure 4.13 shows the cross-sectional image of 2.3 mol% Ge-FF with (a) a core length of 307 µm, (b) a core width of 22 µm while (c) demonstrates a cladding dimension of 603 µm and a cladding width of 379 µm. Figure 4.14 shows the cross-sectional image of 6 mol% Ge-FF with (a) a core length of 462 µm, (b) a core width of 3.86 µm while (c) demonstrates a cladding dimension of 627 µm and a cladding width of 171 µm. In order to compare the dosimetric responses of the fibres and other dosimeters in subsequent basic characterisation and clinical studies, the volume of their active elements is priorly calculated, which in the case of optical fibres are the Ge-doped cores. The largest core volume is identified in 2.3 mol% Ge-CF with 7.36×10^{-5} µm^3, followed by 6 mol% Ge-CF (4.38×10^{-5} µm^3), 2.3 mol% Ge-FF (4.05×10^{-5} µm^3) and the smallest in 6 mol% Ge-FF with a core volume of 1.07×10^{-5} µm^3.

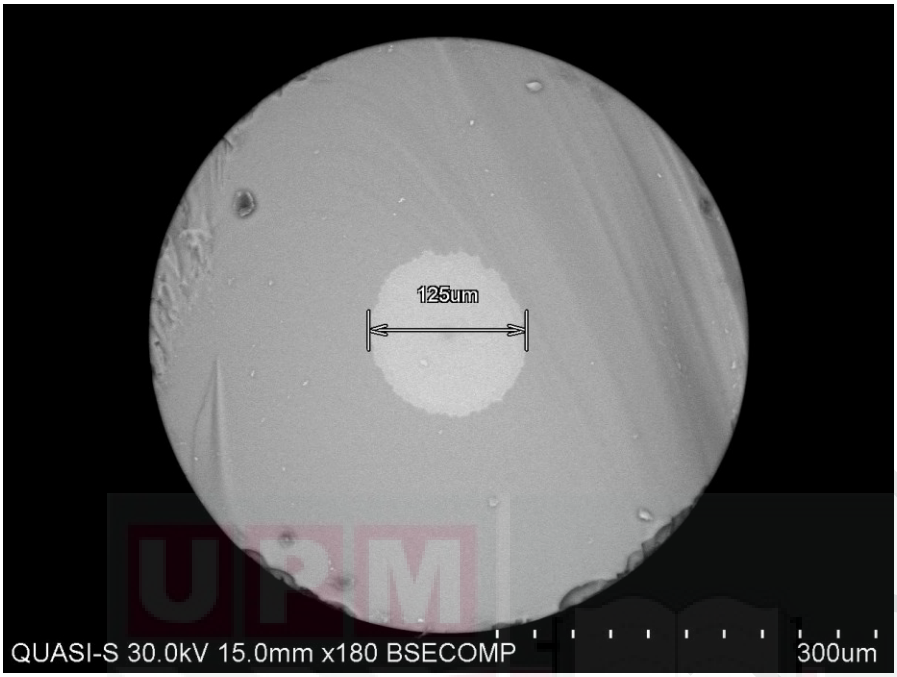

(a)

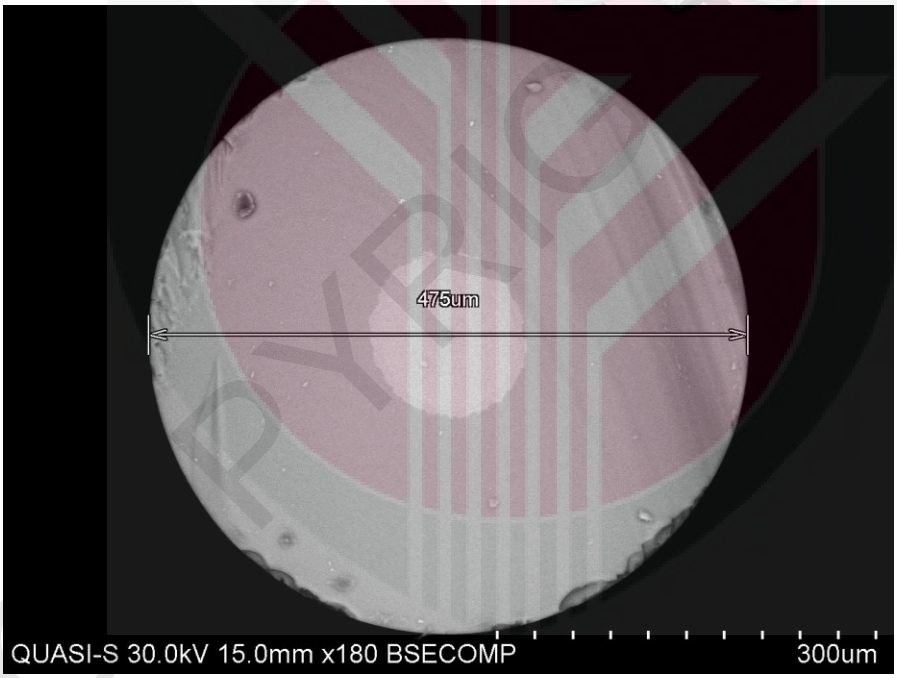

(b)

Figure 4.11: (a) Cross-sectional image of 2.3 mol% Ge-CF with a core dimension of 125 µm and (b) cladding dimension of 475 µm

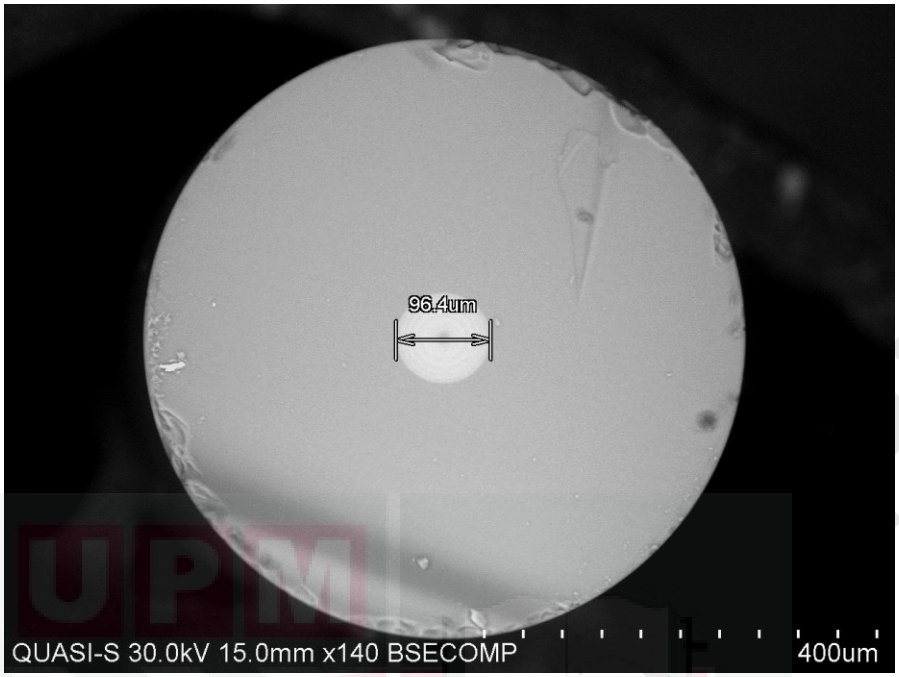

(a)

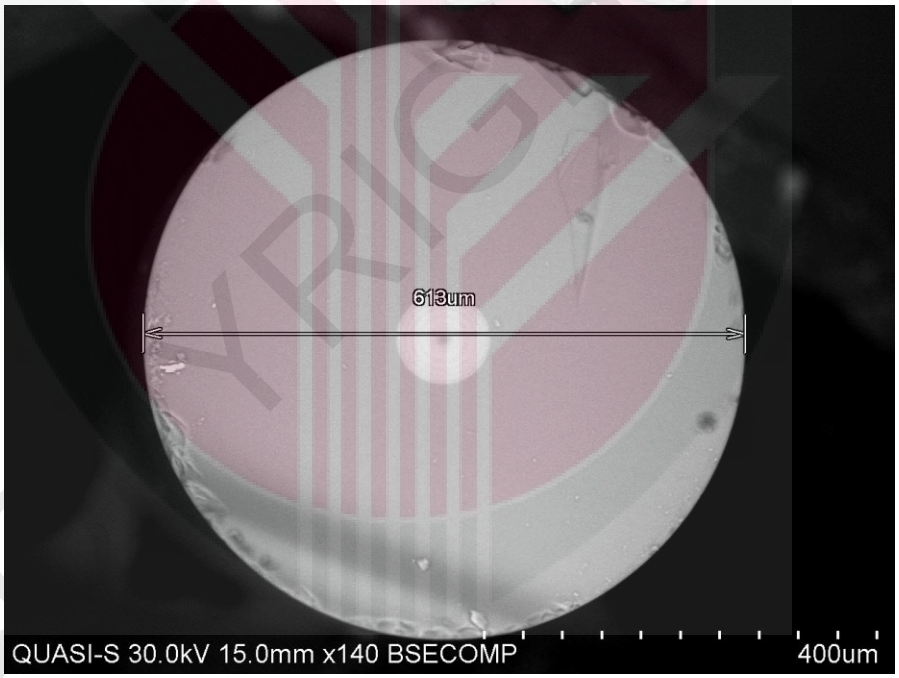

(b)

Figure 4.12: (a) Cross-sectional image of 6 mol% Ge-CF with the core dimension of 96.4 µm and (b) cladding dimension of 613 µm

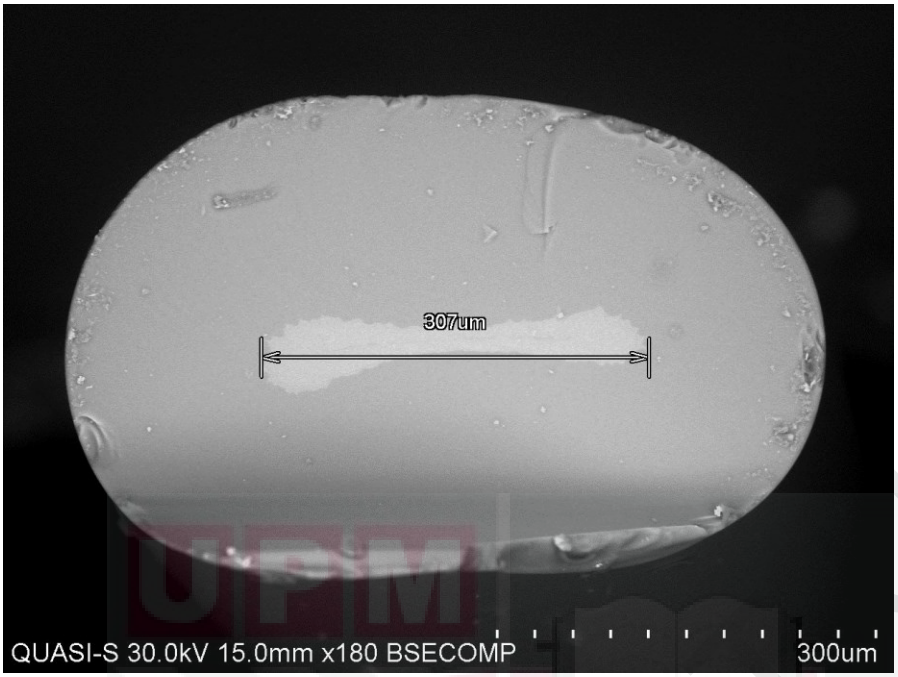

(a)

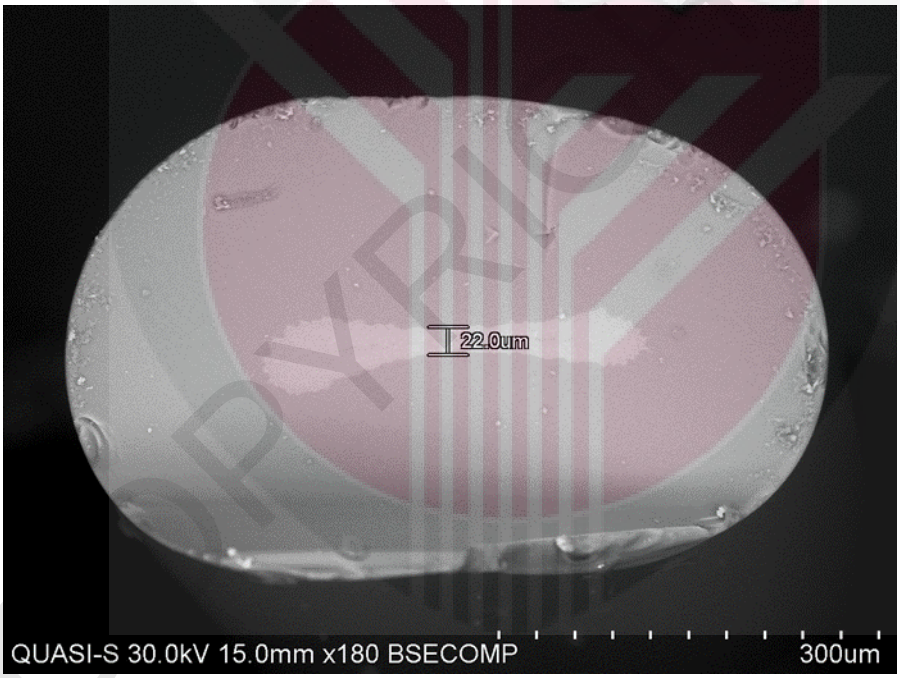

(b)

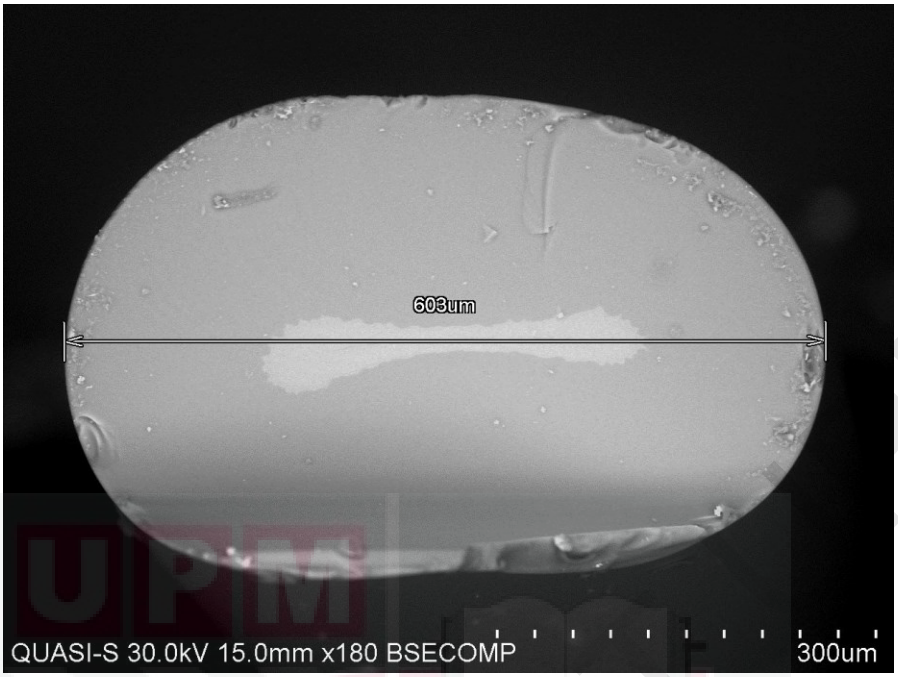

(c)

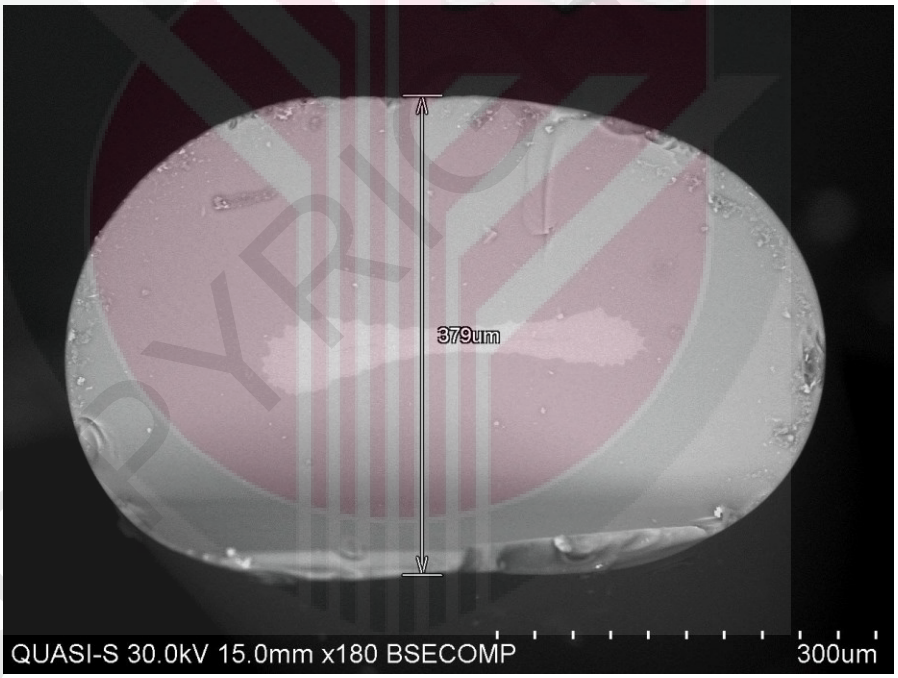

(d)

Figure 4.13: (a - b) Cross-sectional image of 2.3 mol% Ge-FF with the core dimension of 307 x 22 µm^2 and (c - d) cladding dimension of 603 x 379 µm^2

(a)

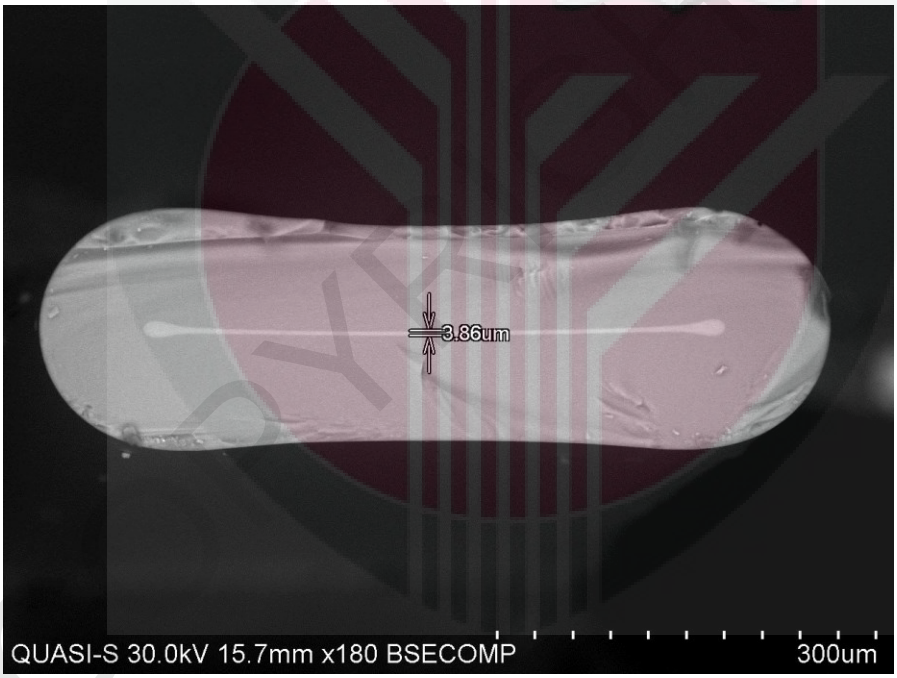

(b)

(c)

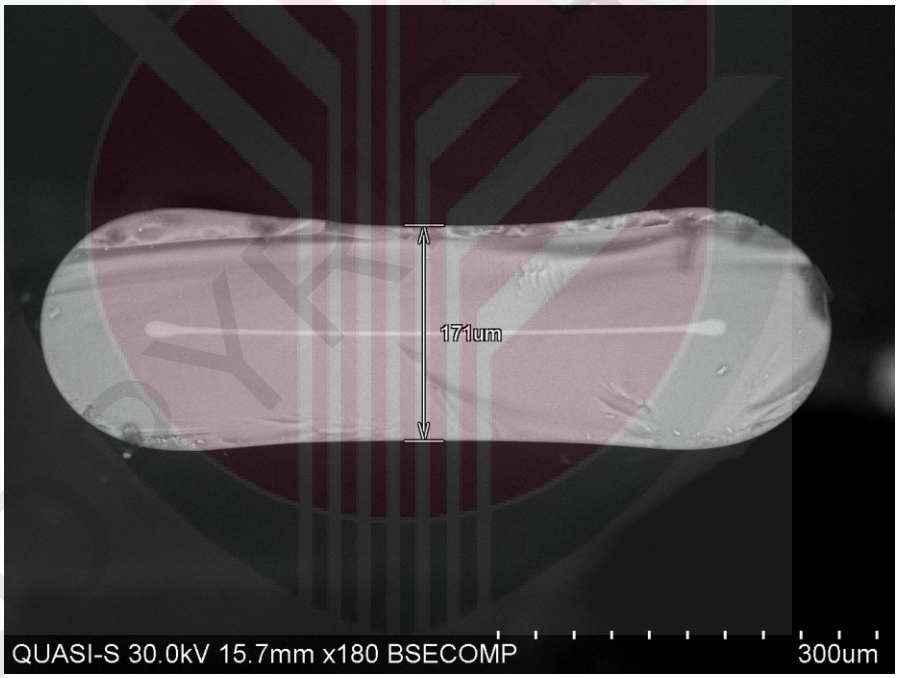

(d)

Figure 4.14: (a - b) Cross-sectional image of 6 mol% Ge-FF with the core dimension of 462 x 3.86 µm^2 and (c - d) cladding dimension of 627 x 171 µm^2

4.3.2 Energy Dispersive X-ray (EDX) Analysis

A useful technique for qualitative and quantitative element analysis is Energy Dispersive X-ray (EDX) analysis, which maps the elemental distribution and determines the chemical makeup of numerous materials. The EDX examination is carried out to show the X-ray fluorescence emissions of silica (Si), oxygen (O), and germanium (Ge) elements. Figure 4.15 shows the element distribution for 2.3 mol% Ge-CF with the cladding mainly dominated by Si represented in yellow (a) and the Ge represented as red (b) at the central region or core of the fibre. Similarly for 6 mol% Ge-CF with the cladding in yellow (c) and the core as red (d) representing Ge. Figure 4.16 also shows a similar element distribution albeit in flat-shaped optical fibre with (a) Si and (b) Ge for 2.3 mol% Ge-FF. Flat fibre showed a clearly defined flat dimension and a bulging zone on both ends. It appears plausible that the bulging areas at the flat fibres' margins formed when they had reached the limit of their capacity to collapse inward under tension. As mentioned in Section 3.6, EDX analysis for 6 mol% Ge-FF was done in multiple spots due to its smaller dimension in showing the elemental distribution. Figure 4.16 (c-d) shows the presence of Si at both ends together with Ge in (e-f). The summarised EDX spectrum represented in Figure 4.17 indicated the existence of a Ge peak in cylindrical and flat Ge-doped optical fibres in addition to the predominant presence of Si and O peaks in accordance with the keV energy. It is shown that for (a) cylindrical fibres, 1 to 1.5 keV energy is required for the visibility of the Ge peak. An additional Ge peak is also evident at 10 keV. Meanwhile for (b) flat fibres, the Ge peak is observable at 1 to 1.5 keV.

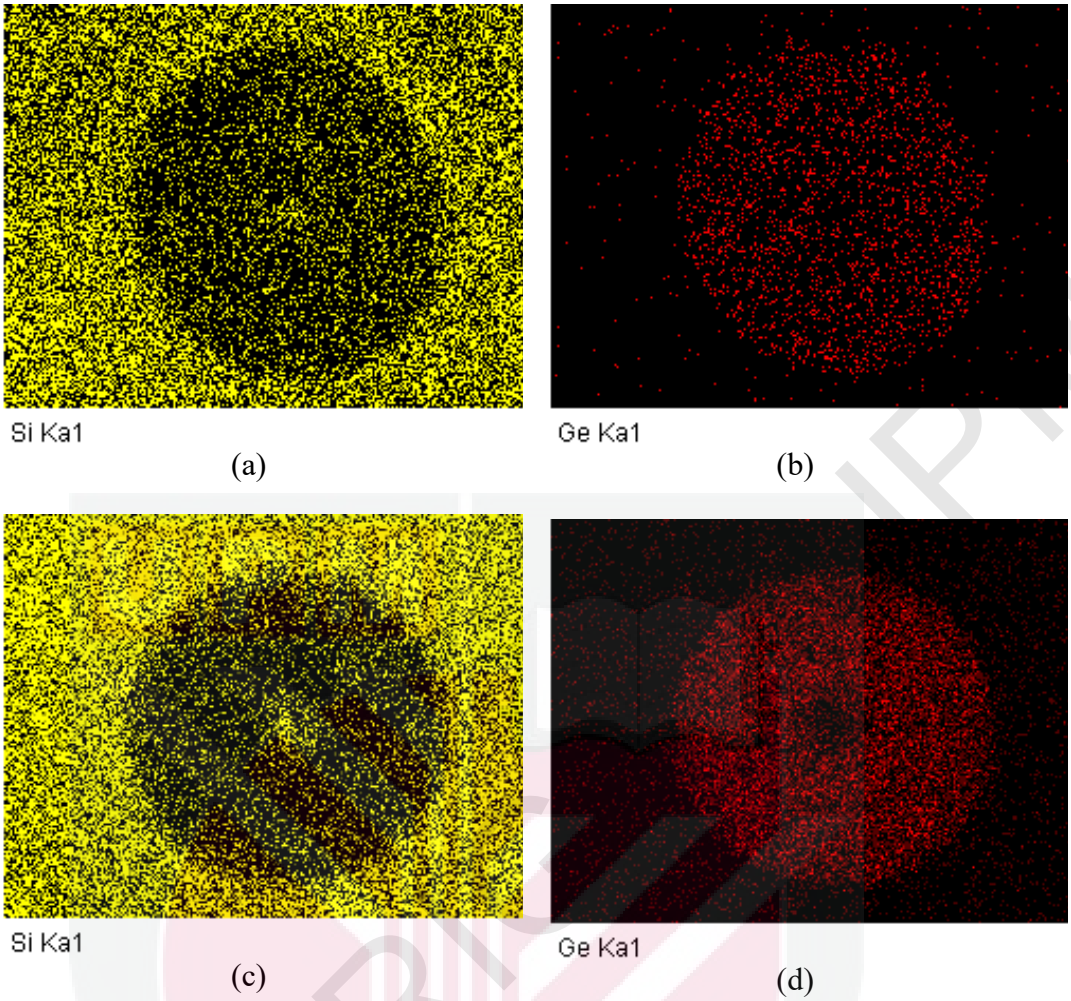

Figure 4.15: EDX analysis showing the elemental distribution of (a) silica, (b) germanium for 2.3 mol% Ge-CF with (c) Si and (d) Ge for 6 mol% Ge-CF

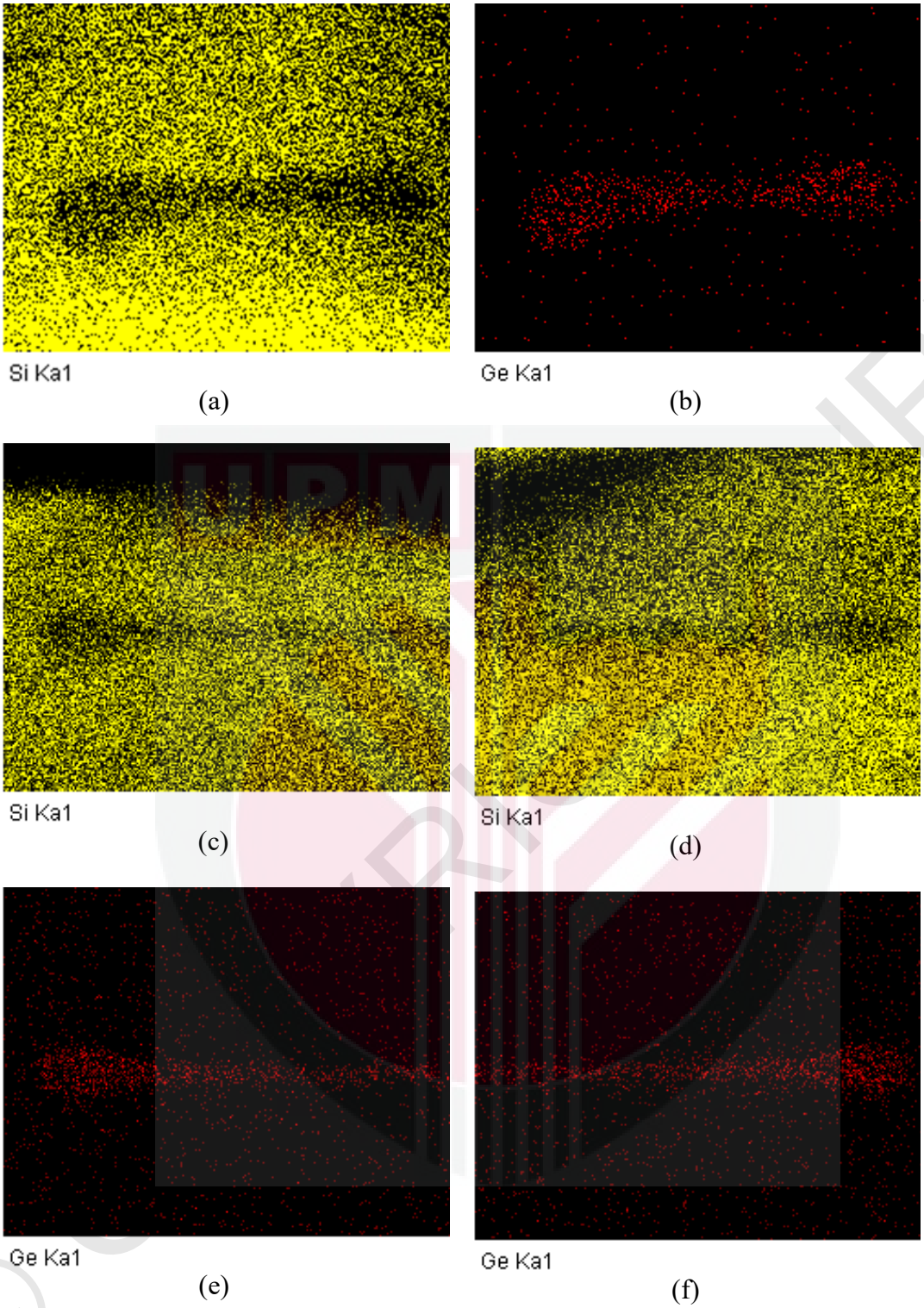

Figure 4.16: EDX analysis showing the elemental distribution of (a) silica, (b) germanium for 2.3 mol% Ge-FF with (c-d) Si and (e-f) Ge for 6 mol% Ge-FF

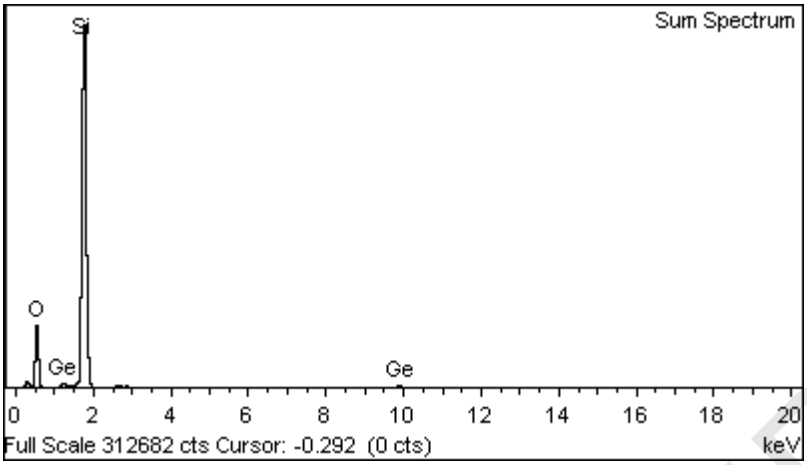

(a)

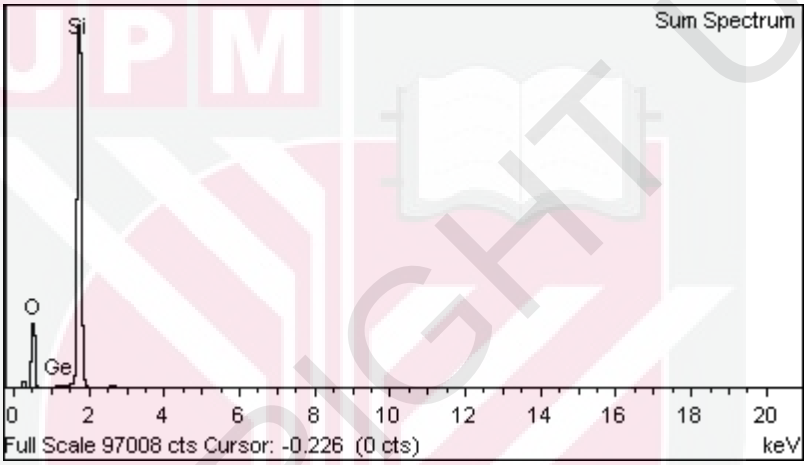

(b)

Figure 4.17: Summarised EDX spectrum showing the elemental peaks of Si, O and Ge in (a) cylindrical and (b) flat fabricated optical fibres

Table 4.6: Elemental compositions of fabricated optical fibres from EDX analysis

Element	Weight %			
	2.3 mol% Ge-CF	6 mol% Ge-CF	2.3 mol% Ge-FF	6 mol% Ge-FF
O	53.24	52.54	56.17	54.33
Si	45.34	44.82	43.45	45.15
Ge	1.42	2.65	0.38	0.52

Table 4.6 shows the summary of the weight fraction contributions of the elements identified in the fabricated optical fibres. It shows that the fibres produced from Ge-doped preforms have average concentrations of 2.65 wt%, 1.42 wt%, 0.52 wt% and

0.38 wt% for 6 mol% Ge-CF, 2.3 mol% Ge-CF, 6 mol% Ge-FF and 2.3 mol% Ge-FF respectively. Previous work conducted by Begum et al. (2015) has demonstrated that, whereas too little extrinsic dopant results in relatively poor radiation sensitivity, too much of the same dopant can result in luminescence self-absorption (also known as concentration quenching). It should be noted that Ge concentration has been shown to be higher in cylindrical fibres than in flat fibres. The use of high temperatures (> 2000 °C) in MCVD processes and the collapse of the hollow preform to form the flat fibre, which caused the diffusion of Ge between the edge of the fibre core and the inner surface of the cladding, may contribute to a lower Ge dopant concentration in flat fibre (Sani et al., 2014).

4.4 Basic Dosimetric Characteristics of Optical Fibres, TLD-100 and nanoDots

Basic dosimetric characteristics of fabricated Ge-doped optical fibres, TLD-100 chips and OSLD nanoDots to photon energy range for CT dosimetry were investigated, focusing on dose linearity, RQT beam quality, dose reproducibility, dose sensitivity, minimum detectable dose and fading.

4.4.1 Dose Linearity

Linearity or dose-response is defined as the functional dependence of the intensity of the measured signal upon the absorbed dose. An ideal radiation dosimeter response should be directly proportional to the radiation dose to ensure the new dosimeter has a linear dose-response over a wide range of doses. For the study of TL (for optical fibre and TLD-100 chip) and count signal (nanoDot) versus dose, each RQT radiation quality with designated tube potential was studied. These were RQT 8 (100 kV), RQT

9 (120 kV) and RQT 10 (150 kV). The doses selected were the typical CT doses received by paediatric patients (Jibiri & Adewale, 2014) for the subsequent application in the later part of the study. The selected doses ranged from 2 mGy to 40 mGy (2-, 4-, 6-, 8-, 10-, 15-, 20-, 25-, 30-, 35- and 40 mGy). The dose linearity for all dosimeters in each RQT beam quality is illustrated in Figures 4.18 to 4.21. Each dose point represents the mean of 10 fibres per capsule, three TLD-100 chips and two OSLD nanoDots with the data normalised to sample volume. The readings for each dose measurement are averaged and the standard deviation (SD) is calculated to finally arrive at the standard uncertainty of the measurement reproducibility. These uncertainties are represented as error bars in all subsequent figures. The lines are least-squares straight line fits to the data. All dosimeters have a correlation of determination (R^2) of > 0.99, and all are observed to show good dose responses and linearity irrespective of different beam quality. Also apparent is that the TL yields are superior for the fibres, most notably for the 2.3 mol% Ge-FF, followed by 6 mol% Ge-FF, 6 mol% Ge-CF, commercial fibre, 2.3 mol% Ge-CF and finally, TLD-100 chip. For nanoDot OSLD, the responses have to be illustrated on a separate graph due to the use of element count to represent the signal yield as opposed to the TL response, as shown in Figure 4.21. Each RQT beam quality is represented on the same graph. It can be seen that nanoDot is also linear to the dose increment with a good correlation of determination (R^2) of > 0.99 across different X-ray energies. However, it can be seen that the signal response decreased as the energy increased from 100 kV (RQT 8) to 150 kV (RQT 10). This phenomenon will be further discussed in the subsequent section of the basic characterisation study of RQT beam quality.

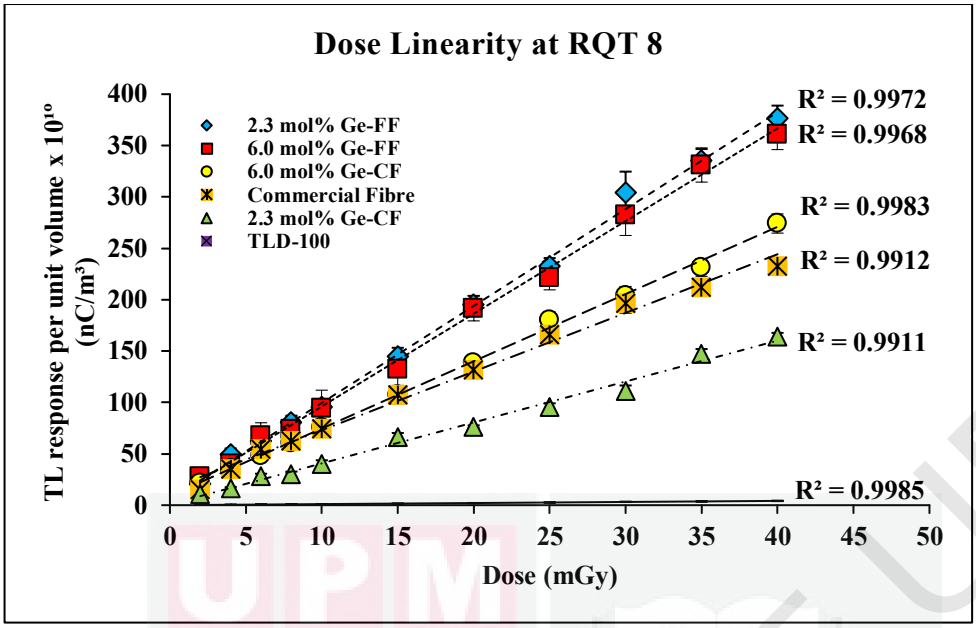

Figure 4.18: Dose linearity for TL dosimeters subjected to RQT 8 (100 kV) beam quality

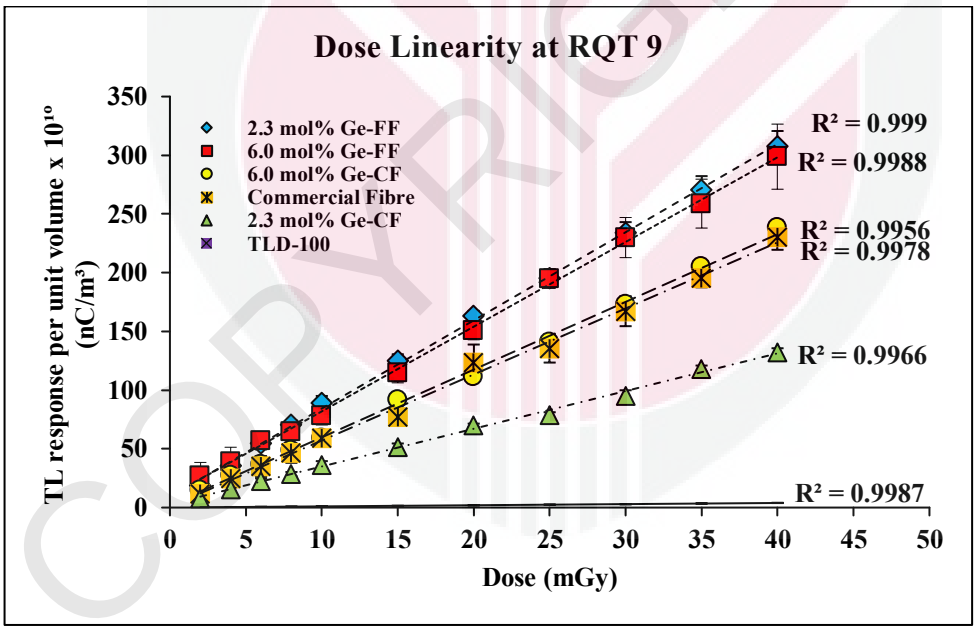

Figure 4.19: Dose linearity for TL dosimeters subjected to RQT 9 (120 kV) beam quality

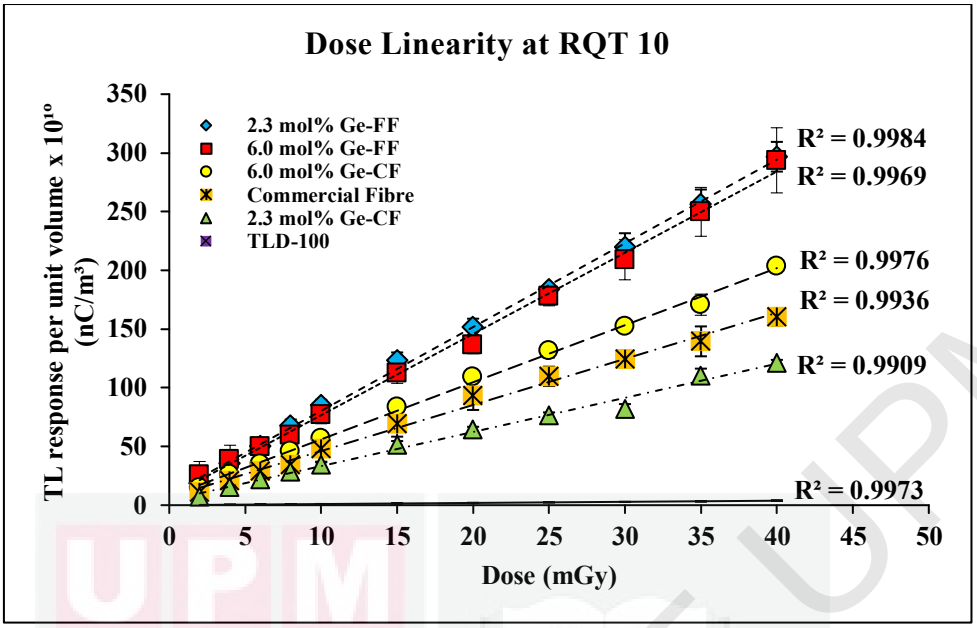

Figure 4.20: Dose linearity for TL dosimeters subjected to RQT 10 (150 kV) beam quality

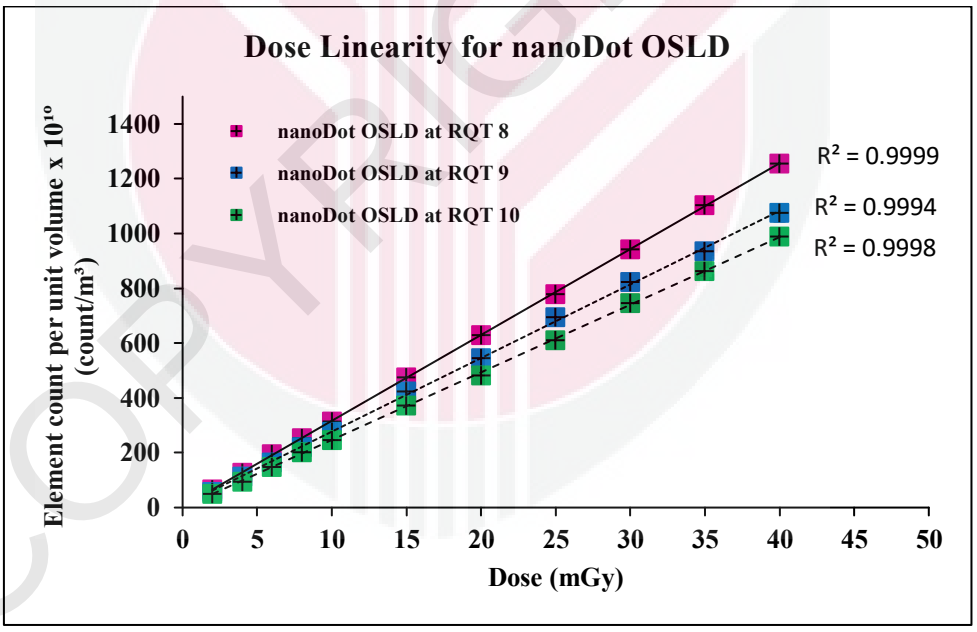

Figure 4.21: Dose linearity for nanoDot OSLD subjected to RQT 8, 9 and 10 beam qualities

4.4.2 RQT Beam Quality

The energy response or beam quality is the variation of the detected TL output for a fixed dose as a function of the energy of the absorbed radiation (Hashim, 2010). As the dosimetry systems are calibrated at a specified radiation beam quality and used over a much wider energy range, the variation of the response of a dosimetry system with radiation quality (energy dependence) requires correction. Ideally, the energy response should be flat (the system calibration should be independent of energy over a specific range of radiation qualities). In reality, energy correction must be included in determining the dosimetric quantity for most measurement situations. For the study of each RQT beam quality, varied kilovoltage of RQT 8 (100 kV), RQT 9 (120 kV) and RQT 10 (150 kV) were investigated for a fixed dose of 30 mGy.

Figure 4.22 shows results for all dosimeters exposed to a fixed dose of 30 mGy for RQT 8, RQT 9 and RQT 10 spectra. While for the three spectra, all investigated dosimeters agree approximately in terms of relative response, the absolute response across RQT 8, RQT 9 and RQT 10 spectra are not in agreement. The responses are most significant for the fibres, the greatest being for 2.3 mol% Ge-FF, followed by 6 mol% Ge-FF, 6 mol% Ge-CF, the commercial fibre and 2.3 mol% Ge-CF, while the TLD-100 chip shows the most minuscule TL yield. The energy response trends for all dosimeters show clear photoelectric dependence, decreasing with an increase in kV as expected. For the 2.3 mol% Ge-FF, the reduction in response from 100 to 120 kV is 22.9% and 27.6% when irradiated at 150 kV. Similarly, for the 6 mol% Ge-FF, an 18.5% drop in response is observed from 100 to 120 kV and 25.9% when irradiated at 150 kV. 6 mol% Ge-CF, the equivalent response reductions are 15.2% and 25.3%. The same reduction patterns are observed from 100 kV to 120 kV for commercial fibre and

2.3 mol% Ge-CF with 14.8% and 14.4%, respectively, and 36.4% and 26% when irradiated at 150 kV. While favourable in terms of sensitivity compared to the TLD-100 chip, using the fibres for CT dose assessments would require the appropriate response corrections to be built into the evaluations. The same is also true in using the TLD-100 chip for the same purpose, albeit to a much lesser degree, with the change in reduction recorded as 12.9% and 13.8% from 100 kV to 120 kV and when irradiated at 150 kV. For nanoDot OSLD, an element count is observed for three different dose levels of 20, 30 and 40 mGy for each RQT beam quality. It can be seen in Figure 4.23 that for a fixed kV value, the response increases with dose. However, the signal response decreases with increasing X-ray potential from 100 to 150 kV, with the dose maintained. At a fixed dose of 30 mGy, the reduction in response for nanoDot from 100 to 120 kV is 12.6% and 21% when irradiated at 150 kV.

Energy dependence is caused by the higher beam penetration for 150 kV photon beams compared to 120 kV and 100 kV, as well as the photoelectric dependence, particularly of optical fibres due to their atomic number (Z_{eff}) of approximately 14 (Begum et al., 2015). Of all the dosimeters, the TLD-100 chip seemed to use the least energy. This condition arises from the fact that the TLD-100 chip, whose effective atomic number is near to the tissue equivalent of 8.3 (Hranitzky et al., 2006), does not exhibit a considerable pair production interaction at high Z_{eff} compared to other dosimeters, which would indicate a stronger photon energy dependence.

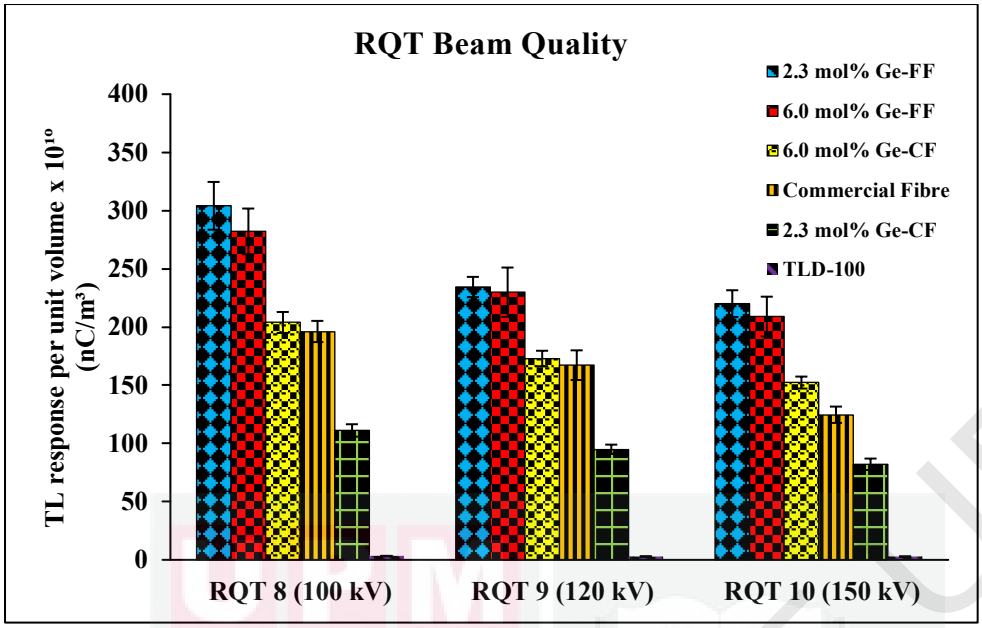

Figure 4.22: RQT beam qualities for TL-based dosimeters irradiated to a dose of 30 mGy using X-ray potentials of 100, 120 and 150 kV

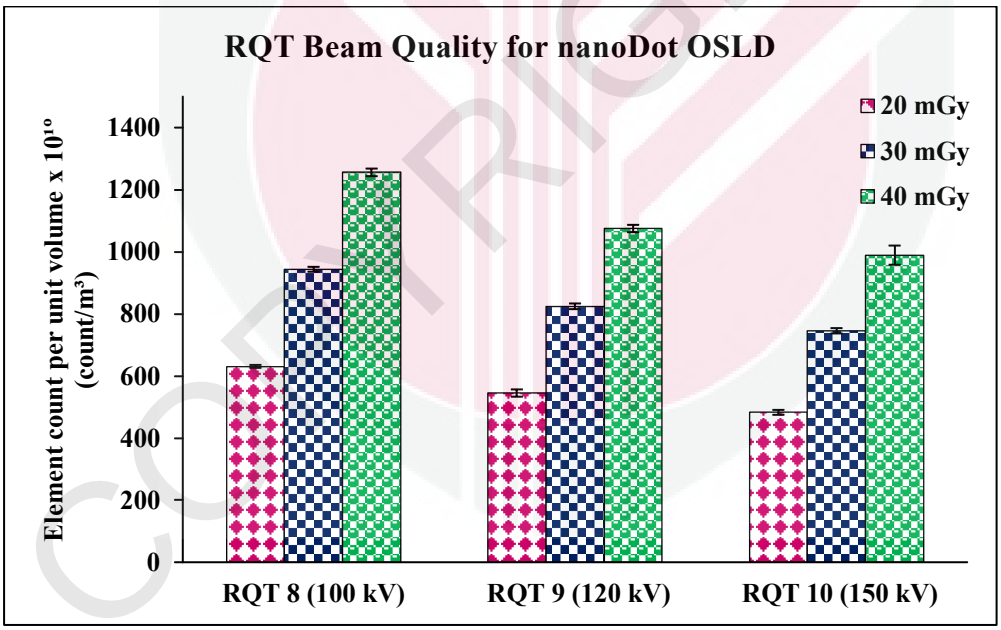

Figure 4.23: RQT 8, RQT 9 and RQT 10 beam qualities for nanodot OSLD irradiated to doses of 20, 30 and 40 mGy

4.4.3 Dose Reproducibility

The precision of dosimetry measurements specifies the reproducibility of the measurements under similar conditions and can be estimated from the data obtained in repeated measurements. High precision is associated with a small standard deviation (SD) of the distribution of the measurement results. Ideally, dosimeters should be reproducible. The reproducibility of each material to a certain dose level can be determined by calculating the SD coefficient of variation (CV) of a repeated set of measurements under the same exposure and reading condition (Hashim, 2010). To investigate dose reproducibility, the dosimeters were irradiated with a reproducible dose of 20 mGy, 30 mGy, and 40 mGy at a fixed RQT 8 beam quality. After re-annealing on each occasion, these irradiations were repeated using the same set of dosimeters. The dosimeters' SD and CV for each irradiation were then calculated. Table 4.7 shows that the CV from reproducibility analysis of all types of dosimeters irradiated with various doses under a fixed 100 kV energy (RQT 8) was less than 5%, except for the commercial fibre, which demonstrated a CV of less than 8%. The fabricated optical fibres have demonstrated reproducibility of better than 4% of the mean, surpassing the performance of TLD-100 chips. At the same time, OSLD nanoDots possessed the lowest CV due to their large number in terms of the signal response in element count as opposed to TL dosimeters, which yield their signals in the nanoCoulomb (nC) unit. From low-dose diagnostics (Ramli et al., 2015), medium-dose photon irradiation (Ghomeishi et al., 2015), to high-dose gamma irradiation (Noor et al., 2014), the reproducibility of Ge-doped optical fibres revealed a high precision value for repeated measurement with the lowest CV at 0.5% in a wide dose range.

Table 4.7 also showed the increment of the dosimeter average signal relative to the three different doses at a fixed 100 kV. For the 2.3 mol% Ge-FF, the increment in response from 20 to 30 mGy was 48.6% and 24.4% when irradiated at 40 mGy. Similarly for the 2.3 mol% Ge-CF, a 54.6% increase in response was observed from 20 to 30 mGy and 25.8% when irradiated at 40 mGy. For 6 mol% Ge-FF, the equivalent response increments were 54.9% and 16.4%. The same increment patterns were observed for 20 to 30 mGy for 6 mol% Ge-CF and commercial fibre, 64.1% and 46.7% respectively. 35.9% and 45.3% were observed when they were irradiated at 40 mGy. The same was also true for the TLD-100 chip, with the percentage change recorded as 53% and 30.5% from 20 mGy to 30 mGy and when irradiated 40 mGy. For nanoDot OSLD, an element count was observed, and it could also be seen that the response increased with dose for a fixed kV value. The increment in response for nanoDot from 20 to 30 mGy was 49.6% and 33.1% when irradiated at 40 mGy.

Table 4.7: Dose reproducibility for all investigated dosimeters at RQT 8

Types of Dosimeters	Dose (mGy)	Average Signal	Response Increment (%)	SD	CV (%)
2.3 mol% Ge-FF	20	51.0	n/a	1.3	2.6
	30	75.8	48.6	2.4	3.2
	40	94.3	24.4	3.6	3.8
2.3 mol% Ge-CF	20	57.5	n/a	0.7	1.2
	30	88.9	54.6	2.4	2.6
	40	111.8	25.8	1.5	1.3
6 mol% Ge-FF	20	19.3	n/a	0.5	2.5
	30	29.9	54.9	0.6	1.9
	40	34.8	16.4	1.5	4.2
6 mol% Ge-CF	20	54.3	n/a	0.5	0.9
	30	89.1	64.1	1.9	2.1
	40	121.1	35.9	1.8	1.5
Commercial Fibre	20	12.2	n/a	0.8	6.8
	30	17.9	46.7	1.0	5.7
	40	26.0	45.3	2.0	7.6
TLD-100 chip	20	190.8	n/a	9.0	4.7
	30	292.0	53.0	15.7	5.4
	40	381.2	30.5	20.2	5.3
OSLD nanoDot	20	37167.5	n/a	278.2	0.7
	30	55594.9	49.6	461.5	0.8
	40	73982.0	33.1	720.5	1.0

NA: Not applicable
Note: Average signal for OSLD nanoDot is in Count as opposed to other TL dosimeters which is in nC

4.4.4 Dose Sensitivity

In TL-based dosimetry, sensitivity is defined as TL yield per unit dose per unit mass of the material. It is a significant dosimetric characteristic that exhibits material response against any particular dose range. The activators or defect types and concentrations within the TL material will generally influence the sensitivity of a specific dosimeter. The lower limit of useful sensitivity is based on the characteristics of the TL material and the TLD reader applied during dose readout. This comprises several factors, such as the light detection and heating process. The relative sensitivity may be quantified by differentiating the TL signal from the newly fabricated fibres

against the TL signal from standardised TLD-100. High energy conversion will probably happen efficiently if the doping material has an optimum concentration for both hole and electron traps and luminescence centres (Hashim, 2010). Free electrons are produced once the optical fibre is exposed to radiation and will be trapped in the material. Lattice defects or impurities generate these traps (Noor et al., 2014). For fabricated Ge-doped optical fibres, the glow peak arises primarily from the signal in the core as opposed to the whole fibre with the cladding. Thus, for this study, the sensitivity was normalised to the unit volume of the fibre core instead of the entire fibre mass.

As mentioned above, the present study's TL sensitivity is expressed as the TL yield (measured in nC) per unit volume of dosimeter and per unit dose (m^{-3}. mGy^{-1}). Each fibre type's average readings of 10 fibres per capsule were calculated at each dose interval to eliminate any outliers. The same goes for TLD-100 chips, where three mean readings were taken. As shown in Table 4.8, the average sensitivities for all dosimeters were calculated based on 11 different dose readings from 2 mGy to 40 mGy. In detail, the TL response per unit absorbed dose from the highest to lowest sensitivities are observed in 6 mol% Ge-FF, 2.3 mol% Ge-FF, commercial fibre, 6 mol% Ge-CF, 2.3 mol% Ge-CF, and TLD-100 chip with 8.75, 8.43, 7.39, 5.87, 3.57, and 0.10 nC/m^3. mGy respectively. By using Equation 3.2 to get the percentage change between the investigated dosimeters and the TLD-100 chip, it was found that 6 mol% and 2.3 mol% Ge-FF showed the highest TL sensitivities, which were 87 and 83 times more than that of TLD-100. This is followed by commercial fibres, 6 mol% and 2.3 mol% Ge-CF, with 73, 58, and 35 times more sensitivity than the TLD-100 chip, respectively. Figure 4.24 shows both types of fabricated and commercial fibres exhibit superior

sensitivities against TLD-100. It visually represents the optical fibre sensitivities against the TLD-100 across the dose range from 2 to 40 mGy. 6 mol% Ge-FF was positioned the highest on the graph to denote the highest sensitivity, followed by 2.3 mol% Ge-FF, commercial fibre, 6 mol% Ge-CF, 2.3 mol% Ge-CF and at the bottom of the graph with the lowest sensitivity, TLD-100 chip. Although TLD-100 had the least sensitivity, the standard deviation (SD) difference across the dose ranges for TLD-100 was found to be the most consistent when compared against the other optical fibres, in particular 6 mol% Ge-FF. The error bars could also be seen with a greater spread around the mean for 6 mol% Ge-FF as opposed to the TLD-100 chip.

A study by Alyahyawi et al. (2017) depicted the sensitivity of Germanium co-doped with Boron (Ge-B) optical fibre to be 39 times more than that of TLD-100 in diagnostic energies for general medical imaging applications. Another study by Alyahyawi et al. (2018) also demonstrated superior sensitivity of the Ge-B-doped FF for both dental and mammography dose ranges, up to 4 times more than that of TLD-100. The TL yield of the fabricated fibres by Rozaila et al. (2016) irradiated using X-ray energy in diagnostic imaging is 9 and 7 times that of TLD-100. In summary, Ge-doped fabricated fibre, especially 6 mol% and 2.3 mol% Ge-FF, may be rendered an appropriate new dosimetry material for medical imaging applications in the dose ranges investigated as high sensitivity will generate signals even at very low radiation doses.

Variances in sensitivity may happen depending on the shapes of the optical fibres, the types of dopants, the sample preparation and the type of radiation energy used (Hashim, 2010). It could be seen that flat fibres (FF) demonstrated greater sensitivity

than cylindrical fibres (CF). By collapsing down the optical fibres during the MCVD and fibre-pulling process, it has been shown that considerable enhancement in TL yield could be obtained with the fused inner walls generating defects beyond that existing in the cylindrical fibres due to the increased amount of electron traps. As referred to in Bradley et al. (2015), the mass-normalized TL yield of the FF has been shown to be improved when compared to that of CF. The outcome of such studies can also be linked with the results of previous investigations in which the focus has been on extrinsically doped tailor-made silica fibres. Compared to other dopants, the TL yield has been shown to be increased when doped by Germanium (Ge) (Mahdiraji et al., 2015) and more significantly for Ge-doped optical fibres collapsed into FF (Bradley et al., 2015). Besides the type, concentrations of dopants and additional defects induced during the drawing-down process, the ionising radiation type and energy also play a role (Hashim, 2010), with the current research focusing on RQT beam quality compared to low-dose dental and mammography dose ranges. Lastly, the sample preparation will also affect the TL yield due to the probability of dirt contamination on the sample's surface.

Discrepancies in sensitivity may also happen even if the dosimeters are being produced in similar groups. Several reasons that resulted in these disparities are the length differences between dosimeters and the material mass (Hashim, 2010). In other words, there is always the probability that different samples may produce different sensitivities, although they come from a similar batch. The main reason screening is done before any irradiation is to eliminate outliers that will give rise to different sensitivities across the dose range. Nevertheless, the sensitivity could disperse for up to ±10% between each dose interval (Hashim, 2010). This study calculates average

standard deviations for each dosimeter reading within 2 mGy to 40 mGy dose ranges. TLD-100 chip has the lowest sensitivity difference across the dose ranges, with a 0.01% difference, as seen in Table 4.8. 2.3 mol% and 6 mol% Ge-CF show 0.26% and 0.53% sensitivity changes across the dose regions, followed by 2.3 mol% Ge-FF, commercial fibre and 6 mol% Ge-FF with 0.62%, 1.30% and 1.56% differences in sensitivity respectively.

Table 4.8: Dose sensitivities for investigated dosimeter

Dosimeters	2.3 mol% Ge-FF	2.3 mol% Ge-CF	Commercial Fibre	6 mol% Ge-FF	6 mol% Ge-CF	TLD-100
Sensitivity x 10^{10} (nC/m^3. mGy)	8.43	3.57	7.39	8.75	5.87	0.10
Sensitivity when compared against TLD-100	83x	35x	73x	87x	58x	n/a
Standard Deviation	0.62	0.26	1.30	1.56	0.53	0.01

NA: Not applicable

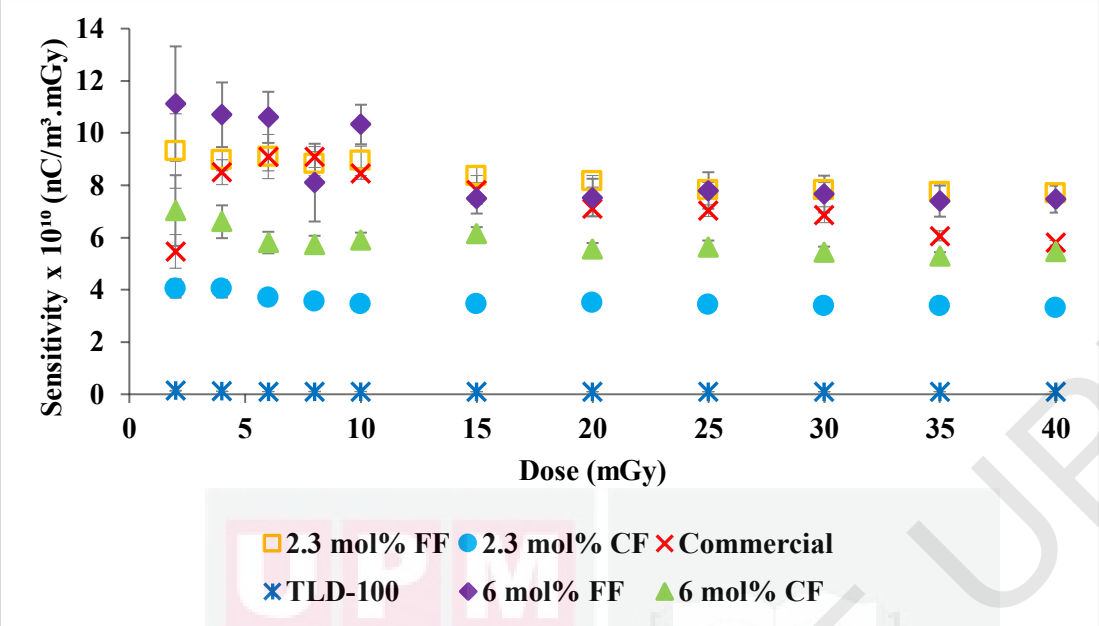

Figure 4.24: Dose sensitivities for investigated dosimeters

4.4.5 Minimum Detectable Dose (MDD)

Identifying the minimum dose boundary for a particular dosimeter is crucial in low-dose applications since several types of research have shown that the signal produced from an irradiated TLD-100 is more or less similar to the background reading. The essential aspects in successfully achieving a low detection limit depend on both dosimeter material with high TL sensitivity and the type of TLD reader used (Hashim, 2010). A comparison of the minimum detectable dose (MDD) for different fibre types is presented in Table 4.9. The results show that 2.3 mol% Ge-CF can identify doses down to 0.29 mGy, rendering a superior lower dose detection competency than 2.3 mol% Ge-FF and commercial fibre with 0.68 mGy and 0.88 mGy MDD. 1.02 and 1.30 mGy MDDs are also observed for 6 mol% Ge-doped FF and CF. In other words, the fabricated and commercial fibres can detect dose levels down to the least delivered dose of 2 mGy used in this study. One study by Noor et al. (2014) investigated MDD for 6, 8 and 10 mol% Ge-doped optical fibres, which were exposed to X-ray doses

ranging from 0.5 Gy up to 10 Gy. The outcomes showed that the 6 mol% Ge-doped cylindrical fibres with a diameter of 604 mm could identify doses down to 27 mGy, providing a superior MDD competency as opposed to the 8 and 10 mol% Ge-doped optical fibres, respectively. A study by Alyahyawi et al. (2017) also presented a superior MDD capability for Ge-B-doped FF and Ge-doped disc down to 0.1 μGy and 1.0 μGy, respectively. In summary, the fabricated fibres in the current study have been proven to have superior low-dose identification, from low doses to comparatively higher dose ranges in CT dosimetry.

Table 4.9: Minimum detectable dose between fabricated and commercial fibres

Fibres	Reciprocal of Slope	Mean Background Reading (nC)	Standard Deviation of Background Reading	Minimum Detectable Dose (mGy)
2.3 mol% Ge-FF	0.133	3.81	0.64	0.68
2.3 mol% Ge-CF	0.304	0.44	0.26	0.29
Commercial fibre	0.173	3.62	0.74	0.88
6 mol% Ge-FF	0.141	4.528	1.339	1.02
2.3 mol% Ge-CF	0.189	3.901	1.483	1.30

4.4.6 Fading

Figures 4.25 and 4.26 show the gradual post-irradiation fading characteristic for all investigated dosimeters when stored in the lighttight box at room temperature after irradiation. The fading characteristic was obtained by reading the TL signal up to 10 days post-irradiation. All the data were normalised to 1st day post-irradiation and plotted as a function of time post-irradiation. A maximum signal loss of 33% was observed for 6 mol% Ge-FF, followed by both the commercial fibre and 2.3 mol%

Ge-CF with 24% signal decrement after 10 days post-irradiation. 2.3 mol% Ge-FF and 6 mol% Ge-CF faded 23% and 22%, respectively, from the original signal, as in Figure 4.26. NanoDots and TLD-100 chips encountered the least TL signal loss of 10% and 7%, respectively. The high fading rate of optical fibres compared to TLD-100 chips and nanoDots is related to the presence of many shallow traps within the fibres.

This situation results from defects brought about by the doping of Ge in the core region (Ghomeishi et al., 2015; Mahdiraji et al., 2015), which makes the spontaneous fading process occur prominently in the optical fibre compared to other dosimeters (Moradi et al., 2017). According to Sani et al. (2014), a new strain-generation of defects, or strain defect, that occurred during the collapsing of the internal surfaces of FF also affects the TL signal production. The additional traps increase the number of shallow traps, causing the surrounding temperatures to encourage the release of trapped electrons and increasing the rate at which FF fades. When the acquisition of the TL signal from the irradiated dosimeter is delayed for a set amount of time, the fading process, which also heavily depends on the number of electrons trapped in various trapping levels, can significantly reduce the TL signal of the dosimeter (Hashim, 2010). In addition, exposure to heat (thermal fading) and light (optical fading) can cause spontaneous fading (Noor et al., 2012) and result in inaccurate measurement of the absorbed dose. However, the actual TL signal can still be determined by correctly using the fading correction factor.

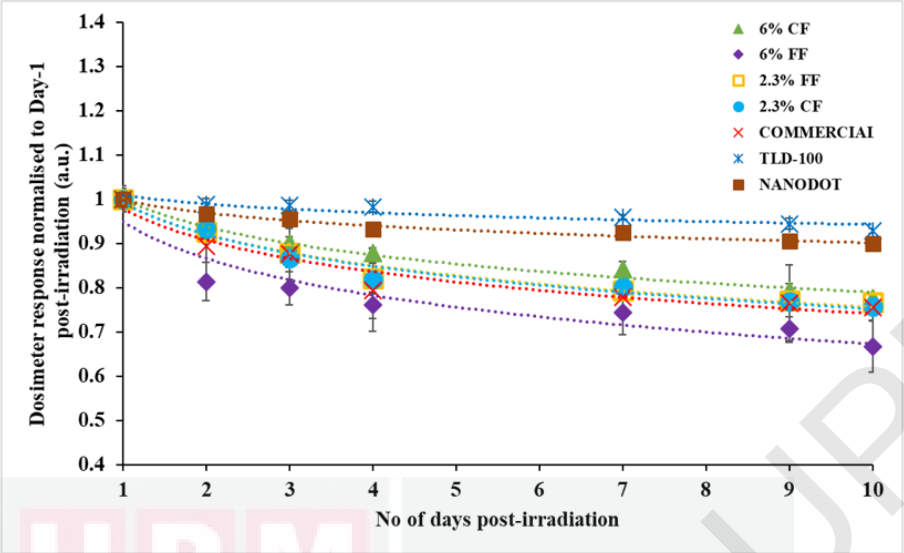

Figure 4.25: Dosimeter response normalised to Day-1 post-irradiation

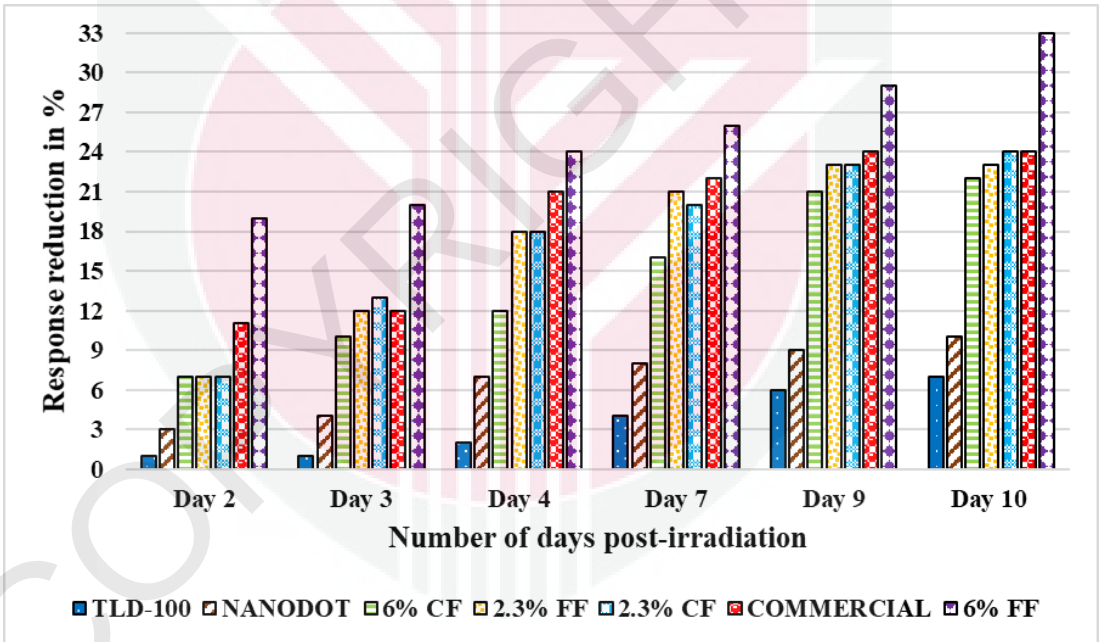

Figure 4.26: Response reduction in percentage (%)

The basic dosimetric characteristics of fabricated Ge-doped optical fibres have been established. These preliminary investigations revealed that all of the fibres could yield excellent fit to linear dose-response for every RQT beam quality with a minimal energy dependency, reproducibility of less than 5% and moderate TL fading, which

offer a viable dosimetry system subsequent usage in CT clinical studies and future implementations. The findings also indicated that all of the dosimeters, particularly the fabricated optical fibres, required correction factors for energy dependence and fading, which should be carried out using the absorbed dose methodology for the Ge-doped optical fibres dosimetry system developed by Noor et al. (2014) to convert the signal response of nC and counts to an absolute absorbed dose of mGy and mSv.

4.5 Glow Curve Analysis for Fabricated Optical Fibre

The glow curve of a TL material best characterises the material response, particularly for newly fabricated dosimeters. The relative amplitude of the peaks illustrates approximately the relative population of the electrons among the range of traps. The peak height and area under the glow curve can be used to measure the absorbed dose in the TL medium.

4.5.1 Shapes of TL Glow Curves

As the TLD reader temperature rises, the TL intensity increases until the population of trapped electrons in the metastable state is sufficiently depleted. At this point, the TL intensity decreases with a further increase in temperature. This will produce the characteristic of the TL glow curve, which consists of the luminescence peaks in a plot of luminescence intensity versus temperature, as was illustrated schematically by WinREMs software (Alawiah et al., 2015). The area under the curve also represents the radiation energy deposited (Hashim, 2010). The glow curve or light intensity yield as a function of temperature was recorded using different preheat settings. As shown in Figure 4.27, a typical pattern of the glow curve obtained from fabricated optical fibre irradiated at 120 kV (RQT 9) and 30 mGy demonstrated a broad peak

characteristic of amorphous media. The broad TL distribution observed across the range of temperatures is by the spread of electron trap levels in the silica, reflecting the structure and properties of amorphous media. Figure 4.28 demonstrates the combined TL glow curves normalised to core volumes, with 2.3 mol% Ge-FF showing the highest TL response.

Figures 4.27 and 4.28 show that aside from 6.0 mol% Ge-FF, which is broadly double-peaked, other fibres exhibited broad single-peak glow curves. In other words, the fabricated Ge-CF and 2.3 mol % Ge-FF are composed of a single peak located centrally within the channel range. For the fabricated 6.0 mol% Ge-FF, the TL glow curve manifests as a double-peaked distribution. These glow curve patterns are in agreement with other studies by Fadzil et al. (2018), Ghomeishi et al. (2015) and Hassan et al. (2019), which assumed the collapsing of the fibre walls during fabrication. 6.0 mol% Ge-FF, which has the smallest core volumes as compared to other fabricated fibres, has generated considerable strain defect, which, in consequence, generates additional trapping centres that can modify the TL yield. In other words, the double-peaked condition implies that the flat fibres probably have two trapping systems with different recombination energies, and electron re-trapping may occur (Ghomeishi et al., 2015).

The primary physical factor determining the stability of the TL material for the dosimeter is the temperature at which the peak of the glow curve occurs (Hashim, 2010). The maximum temperature of the glow curve refers to the point of the highest peak height. According to Moscovitch and Horowitz (2006), the glow curve's maximum TL intensity is highly dependent on the dose, and the maximum TL

intensity of the glow curve refers to the point of the highest peak height. Based on average ramping temperature data in Figure 4.27, it is observed that the temperature at maximum TL intensity of the glow curves subjected to 30 mGy at 120 kV is 267 ºC for 6 mol% Ge-CF, 276 ºC (2.3 mol% Ge-FF) and 289 ºC (2.3 mol% Ge-CF). This result is comparable to the maximum temperature in the previous study conducted by Alawiah et al. (2015), Fadzil et al. (2018) and Hashim (2010). Further detailed inspection of the glow curves formation of double-peaked FF unveils that the second glow peak is slightly higher than the first peak. This contrasts with a study by Fadzil et al. (2018) and Ghomeishi et al. (2015), where the first peak is dominant compared to the second glow peak. This is probably because they studied the radiotherapy range, which uses higher photon energy.

The first glow peak (from Channel 1 to 100) is denoted as a low-temperature peak (LTP), while the second peak is denoted as a high-temperature peak (HTP), represented by Channel 101 to 200. Based on Figure 4.27, the LTP is observed with maximum TL intensity at the average temperature range of 215 ºC. Meanwhile, for the HTP, the maximum peak height is observed at a ramping temperature of 366 ºC. This result is comparable with the average maximum temperature as conducted previously by Fadzil et al. (2018), even though their first glow peak is higher than the second peak, as mentioned earlier. These considerably high glow peak temperatures indicate deep-seated electron traps, which will render the fabricated fibre a stable element, which is one of the essential characteristics of the fading factor for any dosimeter.

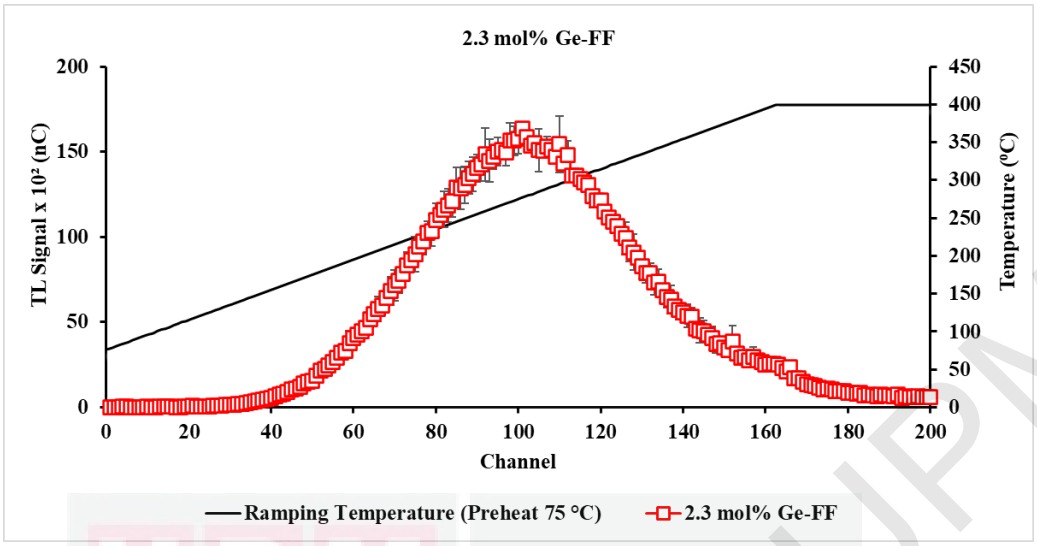

(a)

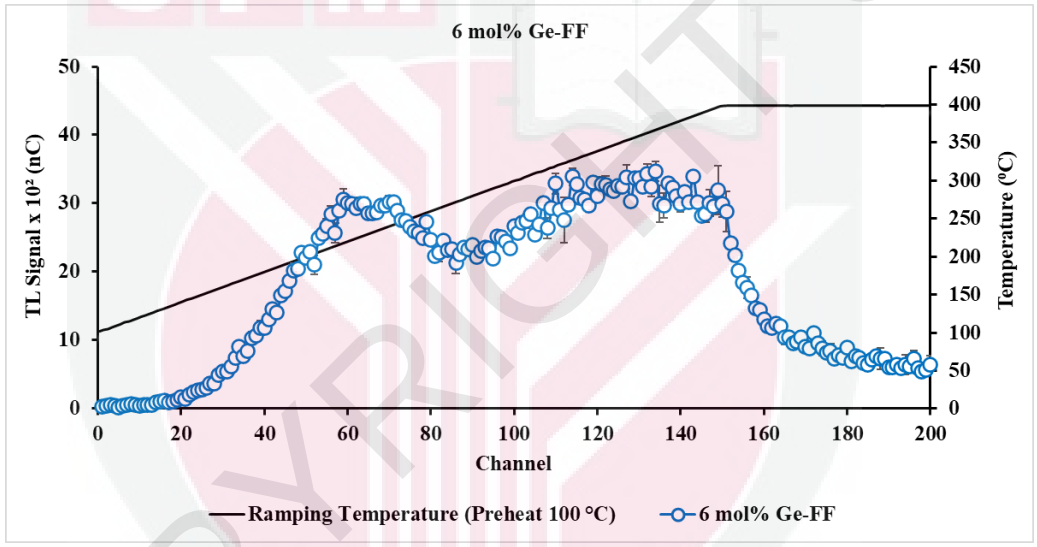

(b)

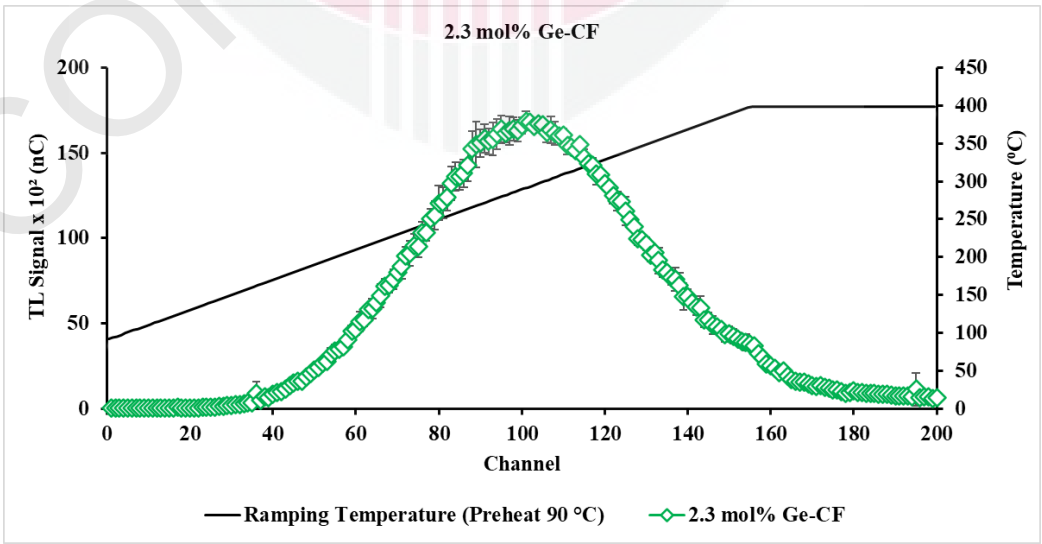

(c)

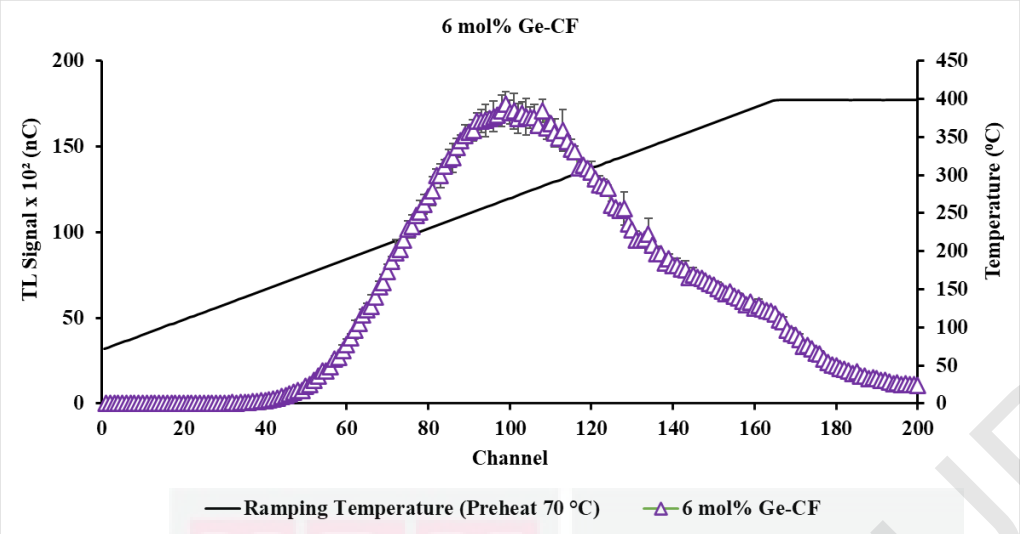

(d)

Figure 4.27: TL glow curves of Ge-doped (a) 2.3 mol% FF, (b) 6 mol% FF, (c) 2.3 mol% CF and (d) 6 mol% CF, irradiated with RQT 9 (120 kV) photon beam and a dose of 30 mGy

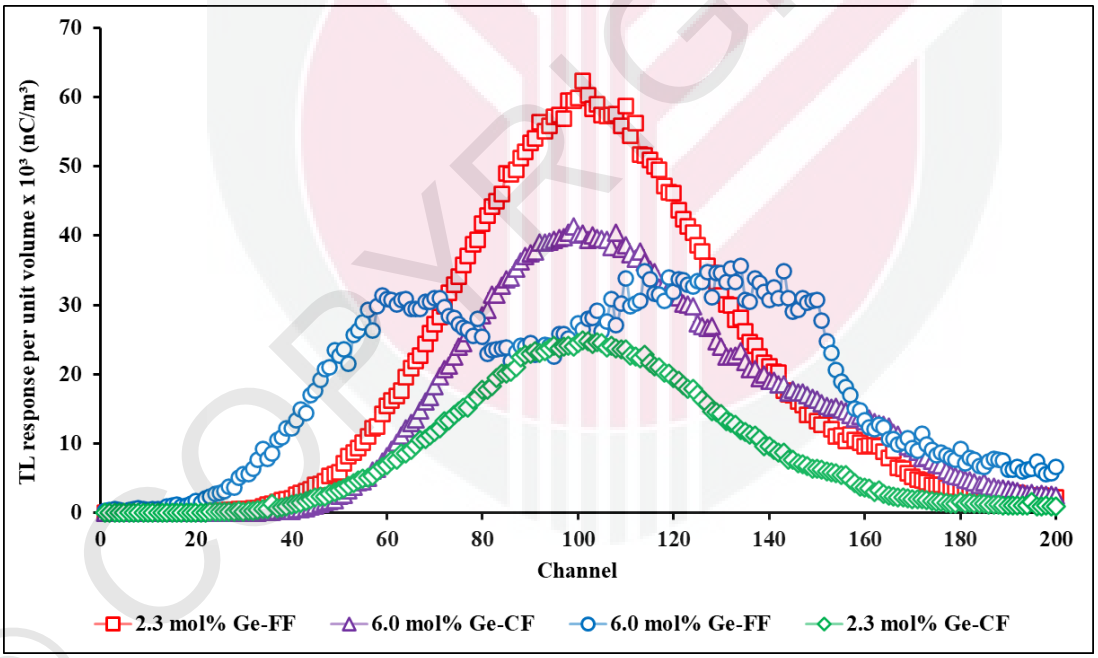

Figure 4.28: Combined TL glow curves normalised to core volumes

4.5.2 TL Glow Curves Subjected to Different Doses and Energies

The effects of TL glow curves formation on fabricated Ge-FF and Ge-CF irradiated with constant energy RQT 9 (120 kV) photon beam and three different radiation doses of 20, 30 and 40 mGy are shown in Figure 4.29. The height of the maximum TL glow curves can be seen increasing progressively with radiation dose within the investigated range. Also observed is that the general structure of TL glow curves for all samples remains unchanged over that increment in dose range. In each type of fabricated Ge-doped optical fibre, the maximum in the TL glow curve peak occurs at approximately the same temperature across the investigated radiation dose range. This result is also found to be comparable with TL glow curves subjected to different doses and energies by Alawiah et al. (2015), Fadzil et al. (2018) and Hassan et al. (2019). The increment of the height of the glow curve directly increases the glow curve area as well, which indicates the number of free electrons transiting from the electron traps to luminescence centres. The fact that the glow peak area and the peak height are highly dependent on the dose is supported by the observations of Moscovitch and Horowitz (2006). They have stated that the average distance between the trap centre and luminescence centre entities decreases as the dose increases. Recombination increases due to the higher probability of charge carrier transition between these entities without interception by the competitive process of non-luminescence.

Meanwhile, in Figure 4.30, TL glow curves of fabricated fibres irradiated with a 30 mGy dose and three different energies of RQT 8 (100 kV), RQT 9 (120 kV), and RQT 10 (150 kV) show that the TL response or peak height decreases with increasing energy, showing clear photoelectric dependence of the optical fibre. In such cases, the

energy correction factor must be considered when converting the TL signals into absorbed doses.

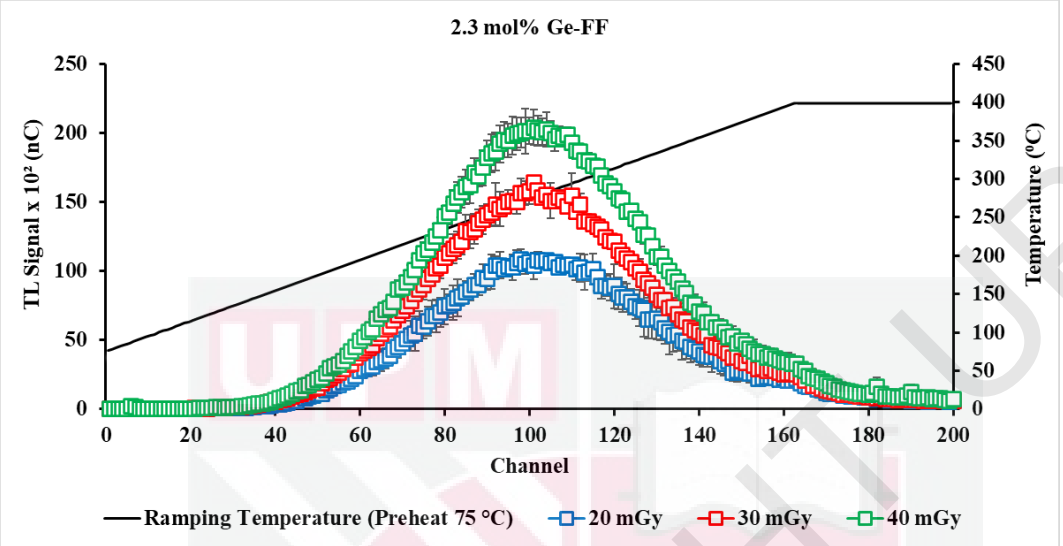

(a)

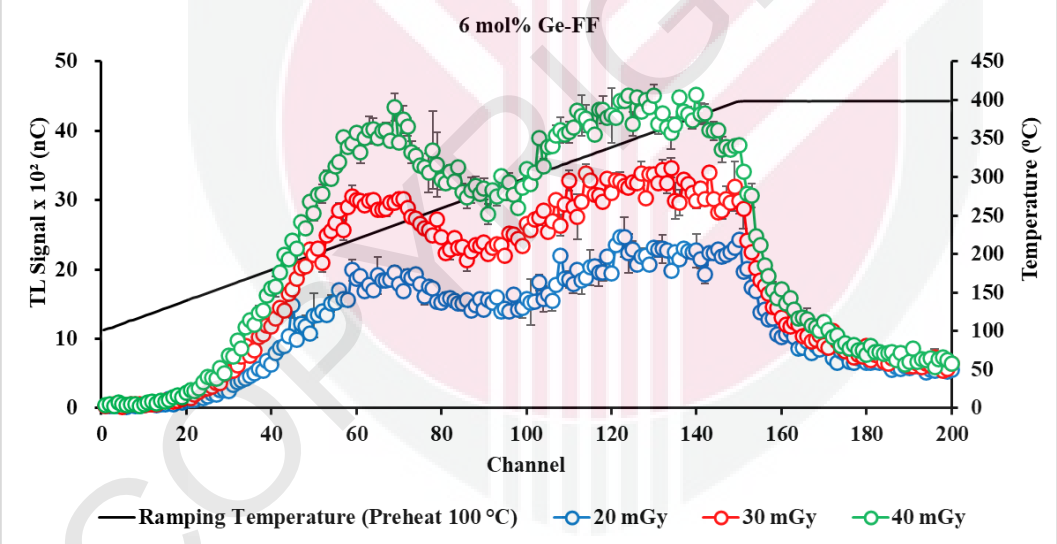

(b)

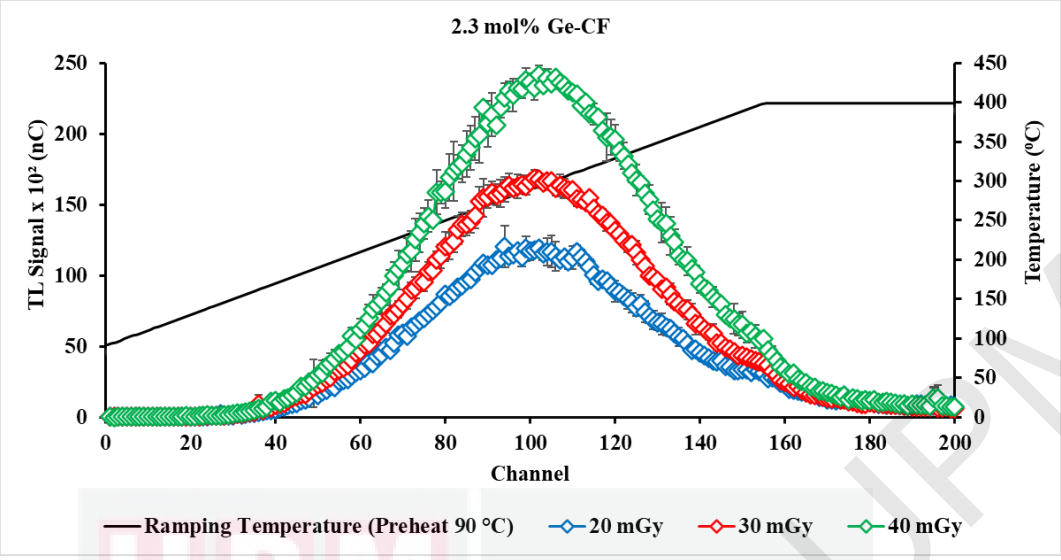

(c)

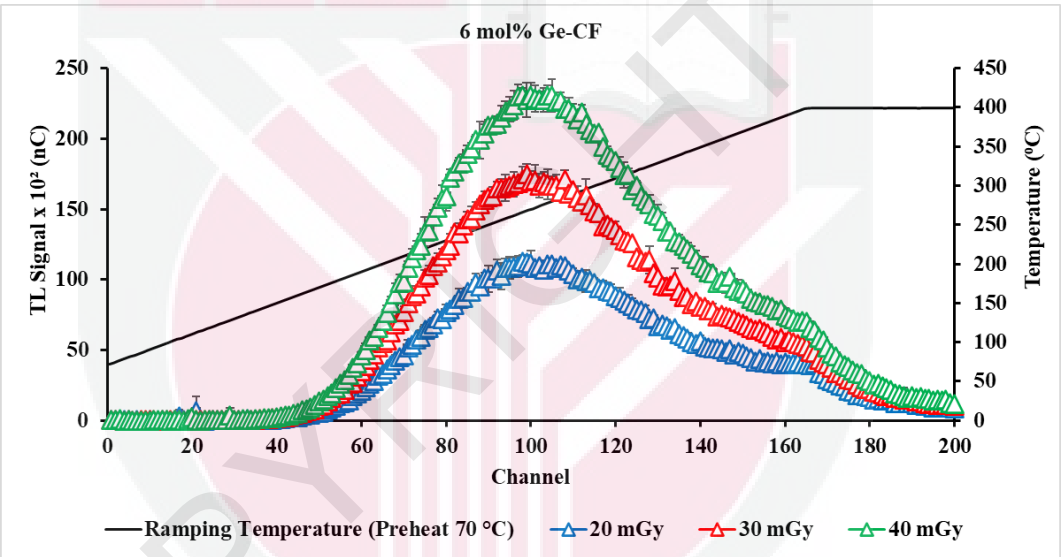

(d)

Figure 4.29: TL glow curves of Ge-doped (a) 2.3 mol% FF, (b) 6 mol% FF, (c) 2.3 mol% CF and (d) 6 mol% CF, irradiated with RQT 9 (120 kV) photon beam and three different radiation doses of 20, 30 and 40 mGy

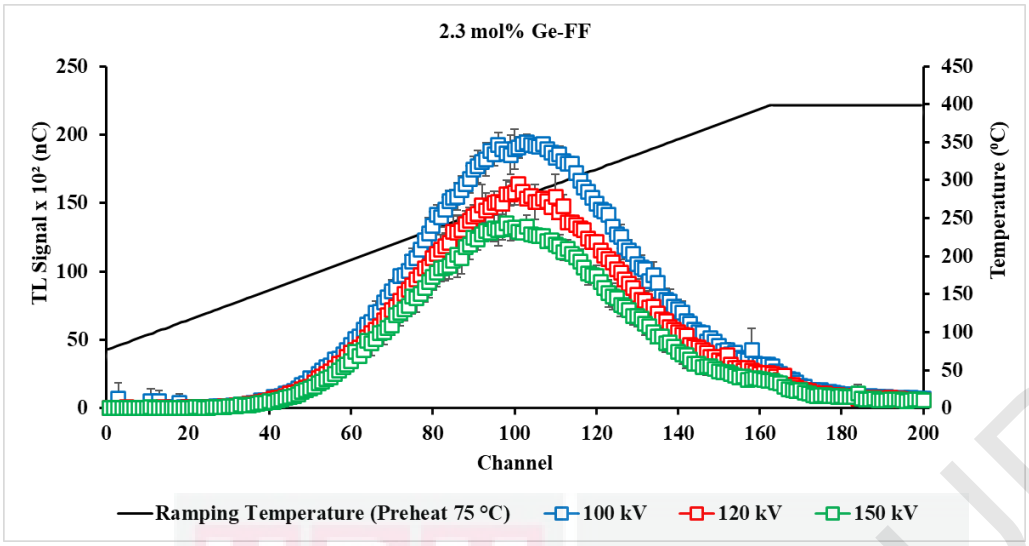

(a)

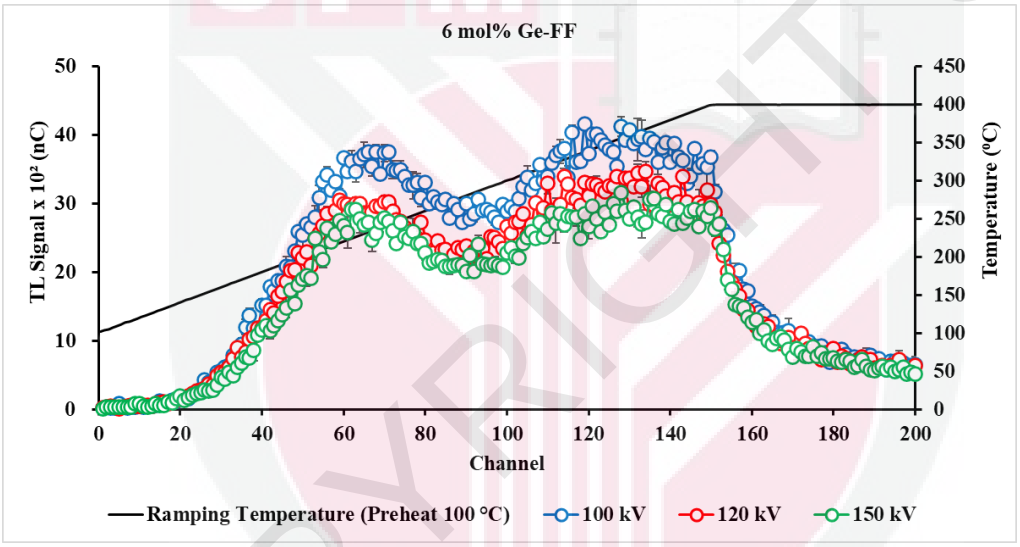

(b)

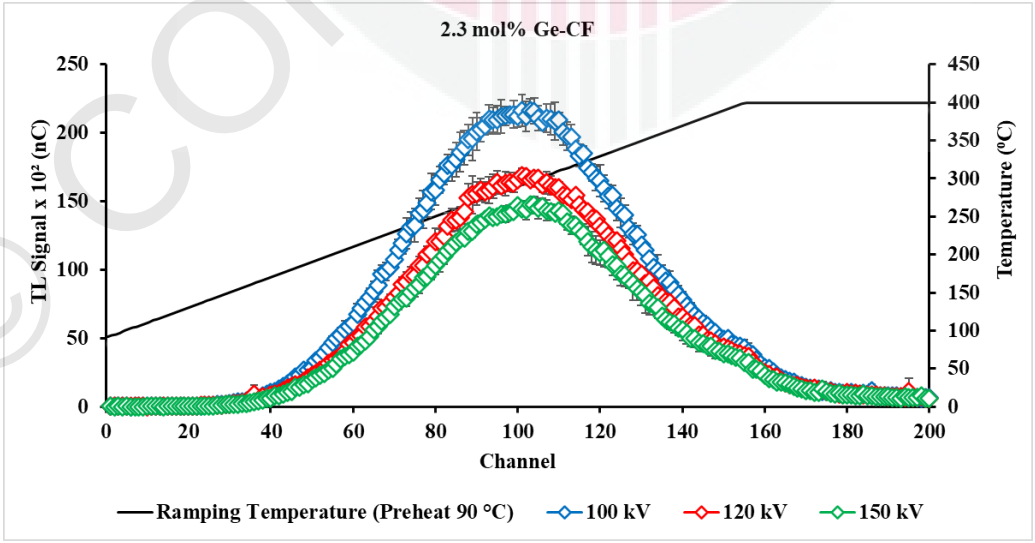

(c)

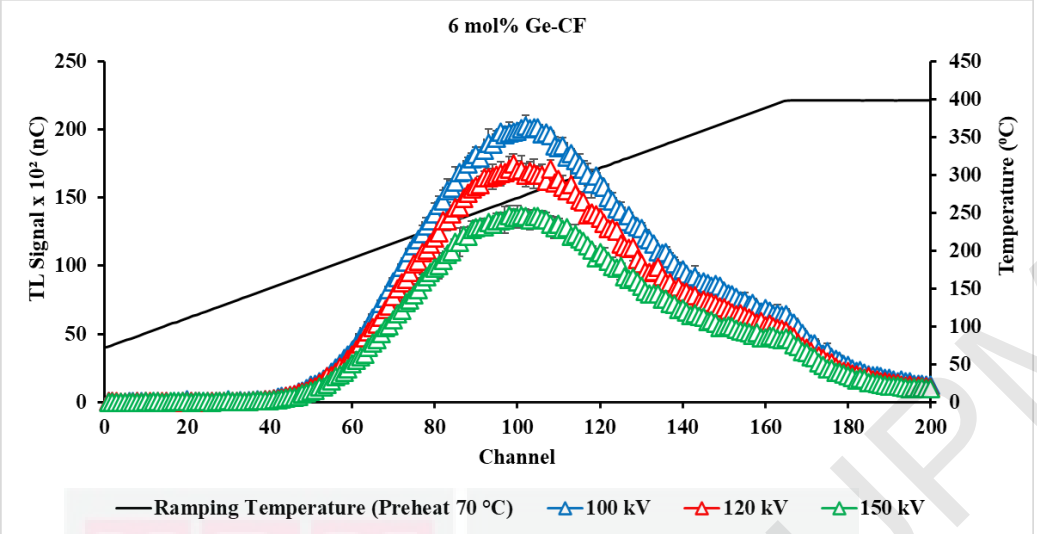

(d)

Figure 4.30: TL glow curves of Ge-doped (a) 2.3 mol% FF, (b) 6 mol% FF, (c) 2.3 mol% CF and (d) 6 mol% CF, irradiated with 30 mGy dose and three different energies of RQT 8 (100 kV), RQT 9 (120 kV) and RQT 10 (150 kV)

4.5.3 Deconvoluted TL Glow Curves

The glow curve response and kinetic parameters of glow peaks were obtained using WinGCF computerised deconvolution that assumed first-order kinetics for each peak composing the glow curve. Fabricated fibre's deconvoluted TL glow curves consist of at least five individual glow peaks (Alawiah et al., 2015). The figure of merit (FOM) obtained in this work was between 2.4% and 4.9%. All kinetic parameters of each peak, such as maximum temperature (T_{max}), activation energy (E_a) and peak integral (PI), were determined by the deconvolution of glow curves. In Figure 4.31, the resulting glow peaks were denoted in ascending order of temperature as peak 1 (P-1), peak 2 (P-2), peak 3 (P-3), peak 4 (P-4) and peak 5 (P-5). P-1 can be considered as the contribution of the electrons released from the lowest temperature trap, whereas the electrons released from the highest temperature trap contribute to the formation of P-5 (Lam, 2019).

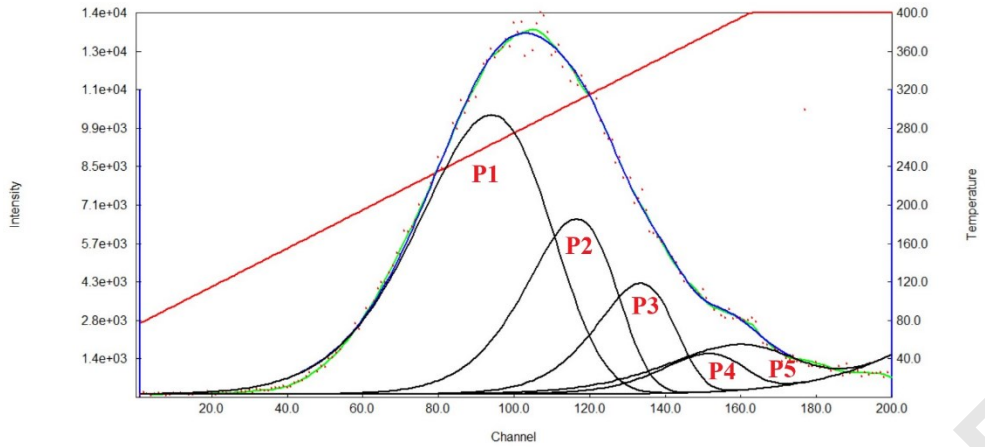

(a)

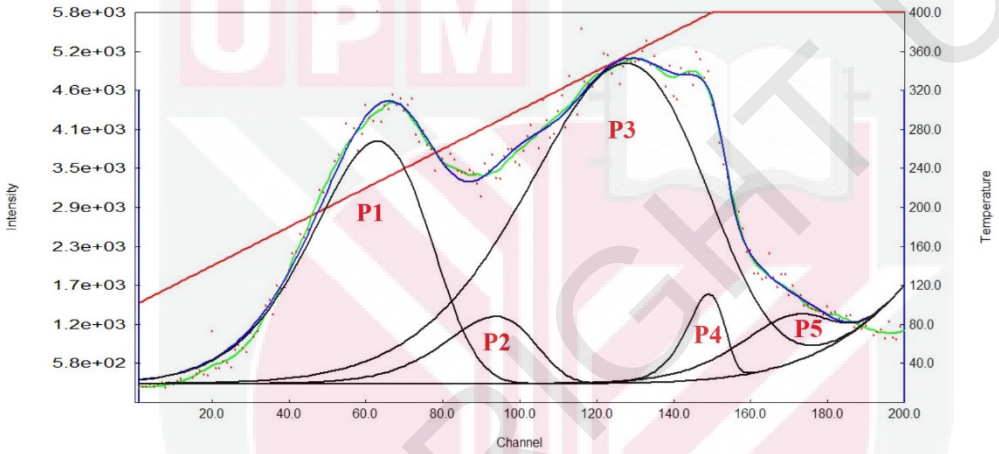

(b)

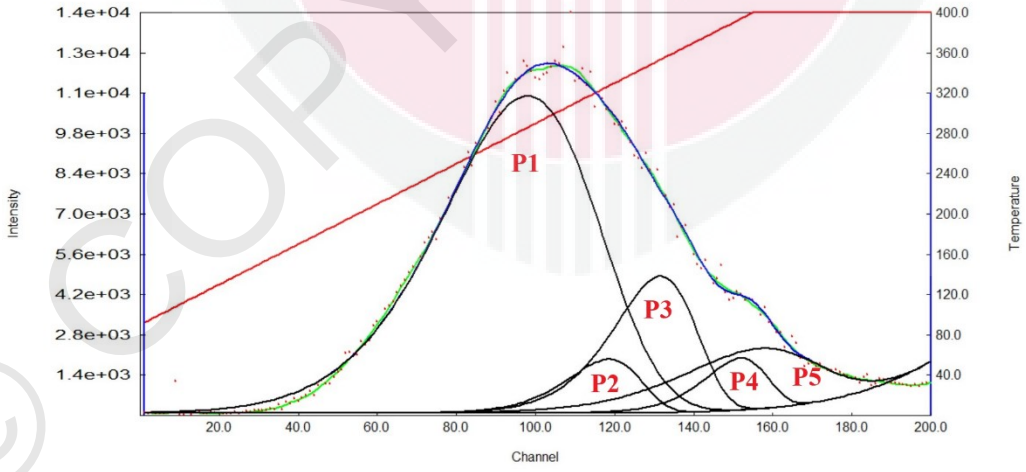

(c)

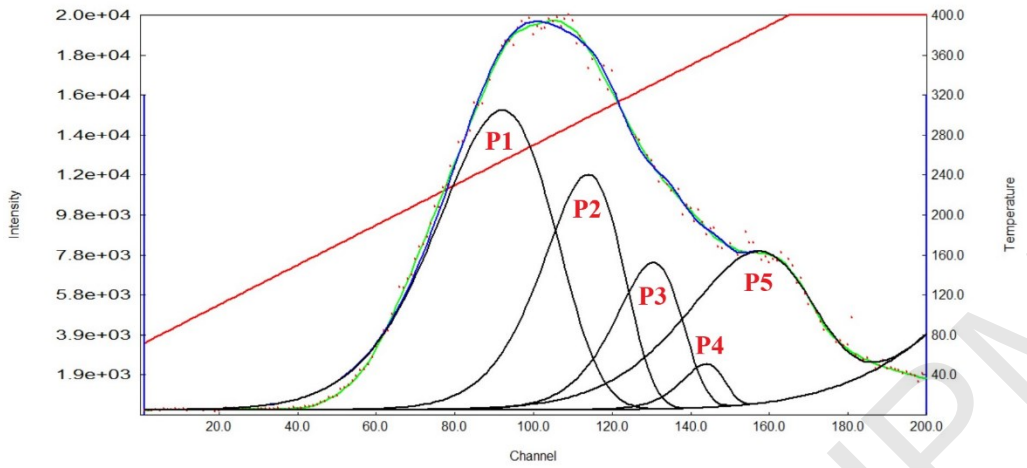

(d)

Figure 4.31: Deconvoluted TL glow curves of Ge-doped (a) 2.3 mol% FF, (b) 6 mol% FF, (c) 2.3 mol% CF and (d) 6 mol% CF consisting of five individual peaks (P1 to P5)

4.5.4 Peak Integral (PI)

The peak integral (PI), associated with the peak area, indicates the number of free electrons that transit from the traps to the luminescence centre, which is influenced by the defect centres or impurities within the material (Alawiah et al., 2015). Figure 4.32 shows the PI of individual deconvoluted glow curves for each RQT 8, 9 and 10 at 30 mGy. For single peaked 2.3 mol% FF, 2.3 mol% CF and 6 mol% CF, peak 1 has the highest PI value across all beam qualities. This means that peak 1, associated with a lower temperature region, is the dominant peak for the CT photon studied. As expected in low-energy photons, most free electrons are trapped in the shallower traps. A lower temperature is needed to release these electrons to the recombination centre which directly manifests the dominant TL yield into peak 1 individual glow curve.

As mentioned previously, 6 mol% FF consists of a double-peaked instead of one, and the second peak at a higher temperature region is slightly taller than the preceding peak. Peak 3, peak 4 and peak 5 of the deconvoluted glow curve are entirely within

the second peak, and as demonstrated in Figure 4.32, it can be seen that peak 3 has the highest PI value across all beam qualities. This means that peak 3, associated with a higher temperature region, is the dominant peak for 6 mol% FF. This indicates that most of the free electrons are trapped in a much deeper trap, and a higher temperature is needed to release these electrons to the recombination centre to release the TL yield. The differences between peak integral trends in CF and FF can be explained by the presence of additional defects (Bradley et al., 2017; Mahdiraji et al., 2015) in FF, which are caused by internal surface fused of FF during the application of vacuum pressure throughout the fabrication process. This is an interesting fact to note, as higher peak temperatures are associated with a less fading effect, which needs to be considered in the advantage of the potential use of 6 mol% FF for low photon radiation.

The lowest PI value for all fabricated fibre, regardless of the single or double-peaked, is demonstrated by peak 4, which indicates the smallest area under the individual curve occupied by the electrons for all energy ranges. The possibility of electrons re-trapping at deeper traps increases as the number of defect centres increases, thus giving rise to more possibilities for the luminescence process occurring at the later stage of the TL acquisition process. This also indicates the possibility of strong electron re-trapping, thus causing a delay in luminescence emission at peak 5 (Bradley et al., 2017; Mahdiraji et al., 2015).

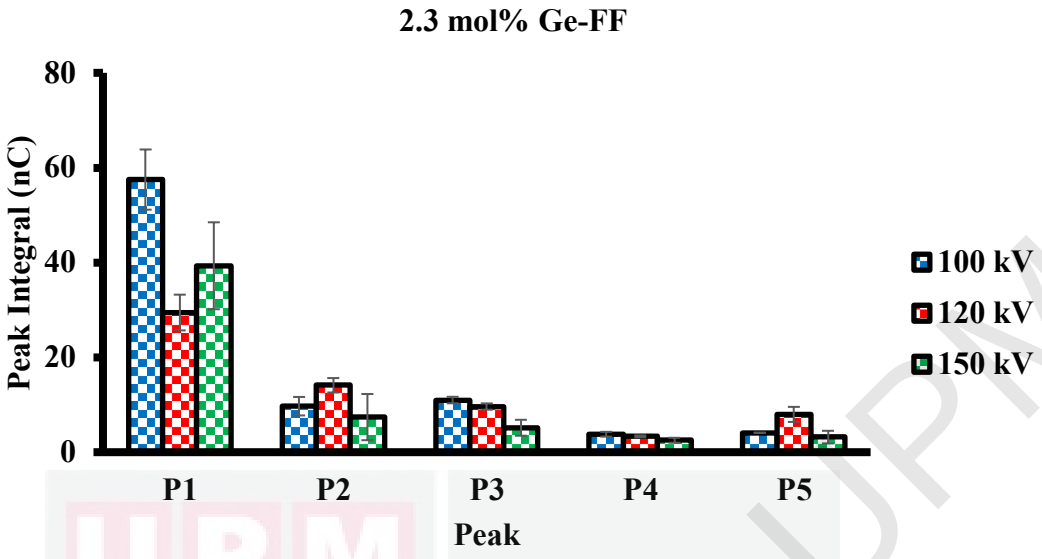

(a)

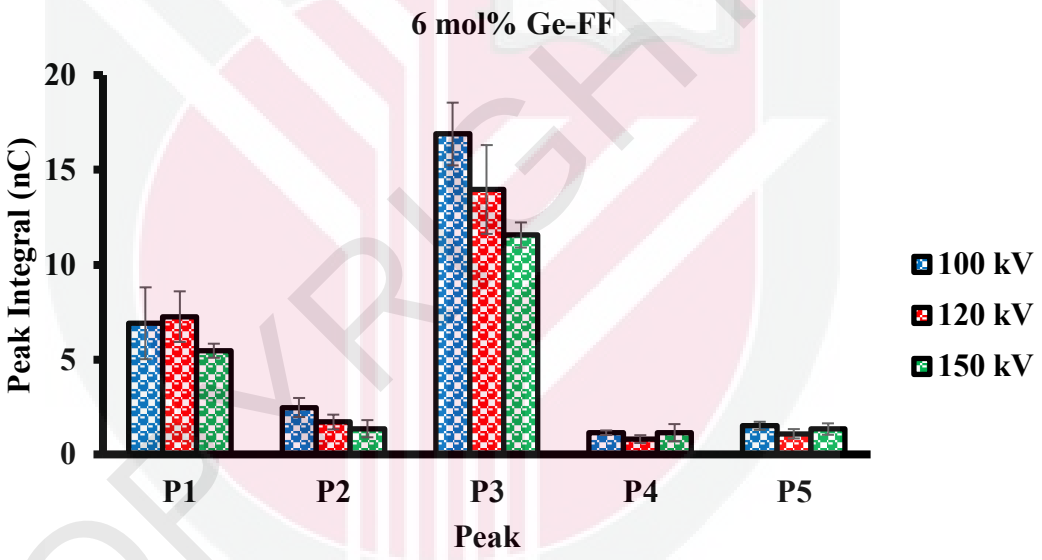

(b)

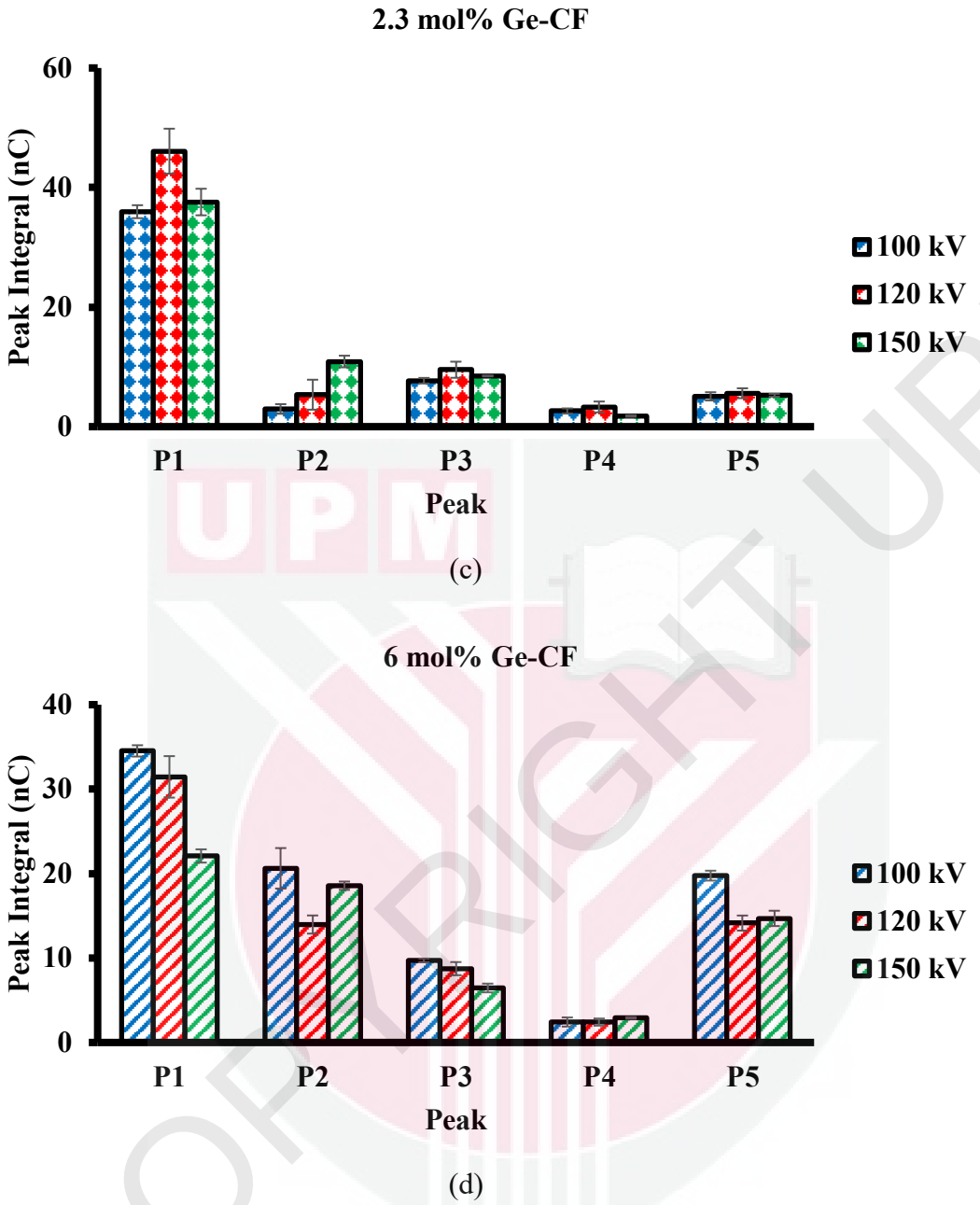

Figure 4.32: Peak integral (PI) of Ge-doped (a) 2.3 mol% FF, (b) 6 mol% FF, (c) 2.3 mol% CF and (d) 6 mol% CF for RQT 8, 9 and 10

4.5.5 Maximum Temperature (T_{max})

The maximum temperature T_{max} of the glow peaks (P1 to P5) pattern was consistent throughout the energy range used for all fibre types in this study, as shown in Figure 4.33. As each beam quality gives the same location of T_{max}, every individual

deconvoluted peak (P1 to P5) has been shown to require a constant temperature to provide the TL intensity. This study is similar to Alawiah et al. (2015) and Fadzil et al. (2018). The temperature pattern can also be seen previously; even as the dose and energy are increased, the glow curves only increase in height under the same temperature ramp. The differences in the T_{max} are influenced only by the fibre type. As mentioned previously, peak 1, which is the dominant peak for all single-peaked glow curves, has T_{max} recorded in the range of 195.88 to 200.09 ºC for 2.3 mol% FF, 202.32 to 209.04 ºC (2.3 mol% CF) and 182.12 to 190.04 ºC (2.3 mol% CF). For double-peaked 6 mol% FF, in which P3 is indicated as the dominant peak, a much higher T_{max} is recorded at the 256.11 to 262.03 ºC range. Maximum temperature ranges are also consistent with other studies (Alawiah et al., 2015; Fadzil et al., 2018).

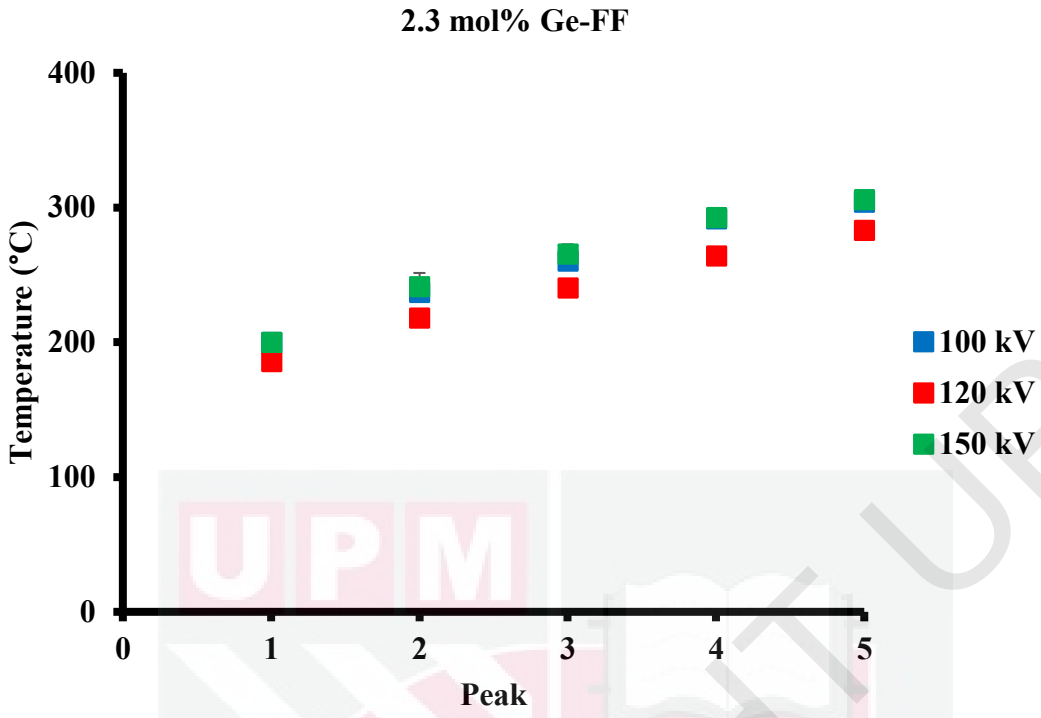

(a)

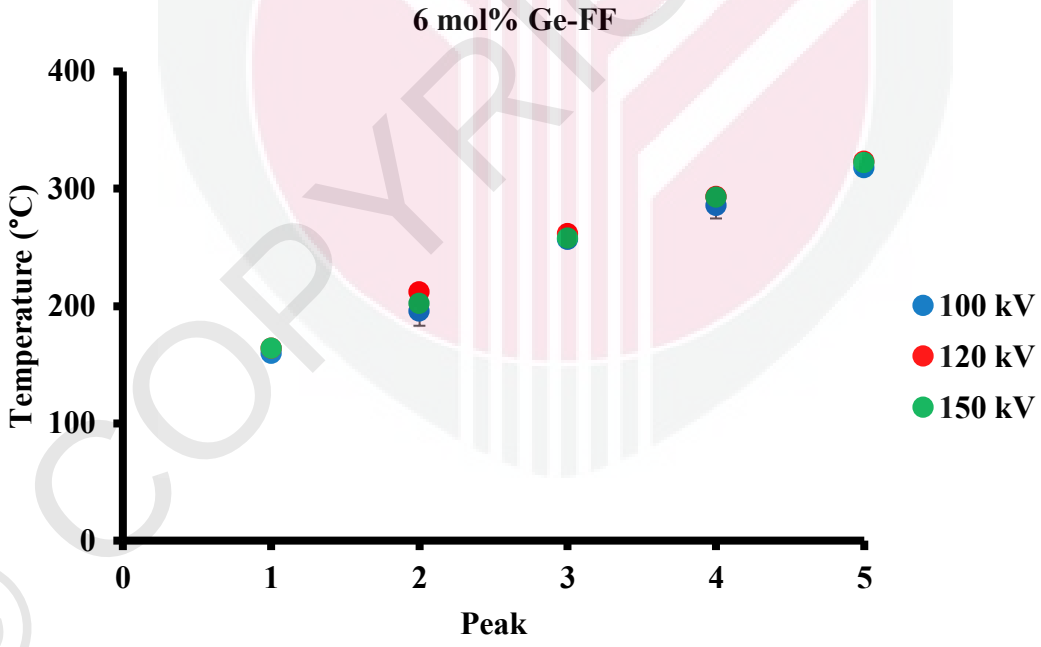

(b)

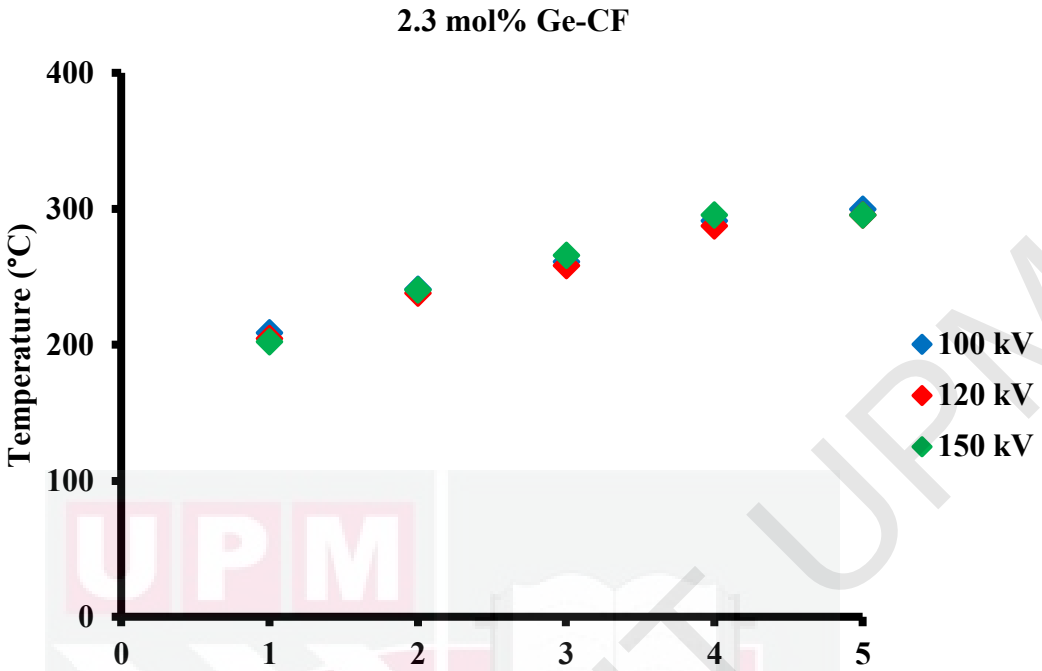

(c)

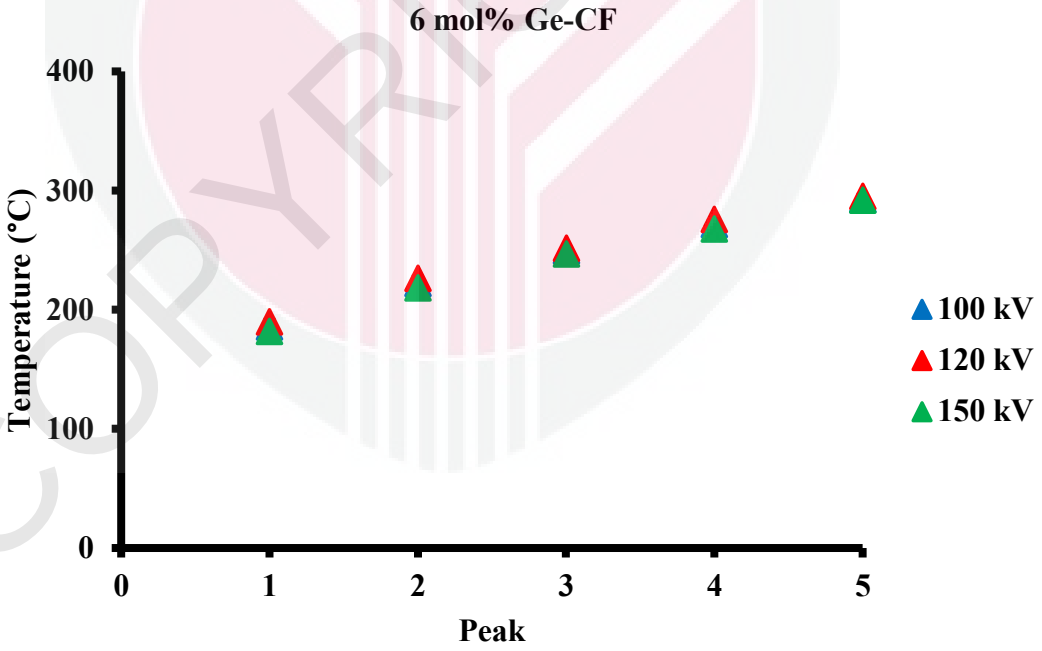

(d)

Figure 4.33: Maximum temperature (T_{max}) of Ge-doped (a) 2.3 mol% FF, (b) 6 mol% FF, (c) 2.3 mol% CF and (d) 6 mol% CF for RQT 8, 9 and 10

4.5.6 Activation Energy (E_a)

Activation energy (E_a) refers to the energy needed to excite the electron from the valence band to the conduction band (Horowitz et al., 2008). The E_a is also known as the energy depth of the trap, according to Attix (2008). As referred to in Figure 4.34, for a single peaked glow curve, the dominant peak 1 with the lowest T_{max}, as mentioned previously, has the lowest E_a (0.63 to 0.76 eV), while peak 4 with the smallest PI has the highest E_a (1.9 – 3.32 eV) across all beam qualities. These results further proved that the dominant electrons in peak 1 were occupied at low energy traps. In contrast, for peak 4, only a few high-energy electrons are trapped at the deeper energy levels, hence the minimum number of PI. As mentioned previously, these results indicate the possibility of strong electron re-trapping at peak 5, thus causing a delay in luminescence emission and widening the emission over a broad high-temperature range (Bradley et al., 2017; Mahdiraji et al., 2015). For double peaked 6 mol% FF, the dominant peak 3 has the lowest E_a (0.68 to 0.72 eV); most of the low photon energy is trapped at the lowest energy depth trap, contributing to increased PI at peak 3.

To summarise the data in the previous paragraph, it is to be noted that most of the electrons generated from diagnostic CT photon irradiation were trapped in shallow traps compared to deep traps. These shallow traps require low E_a to release the trapped electrons. Large quantities of electrons trapped in the shallow traps were manifested by the dominant contribution of peak 1 (single peak) and peak 3 (double peak) in the formation of a glow curve for these fabricated fibres, which differs from TLD-100 that has a dominant dosimetry peak at peak 5 with a higher E_a value of 2.0 eV (Horowitz et al., 2008). Thus, this condition caused a higher fading rate in the fabricated fibres

than TLD-100. The fading correction factor must be considered in calculating the absorbed dose methodology, as detailed in Noor et al. (2014).

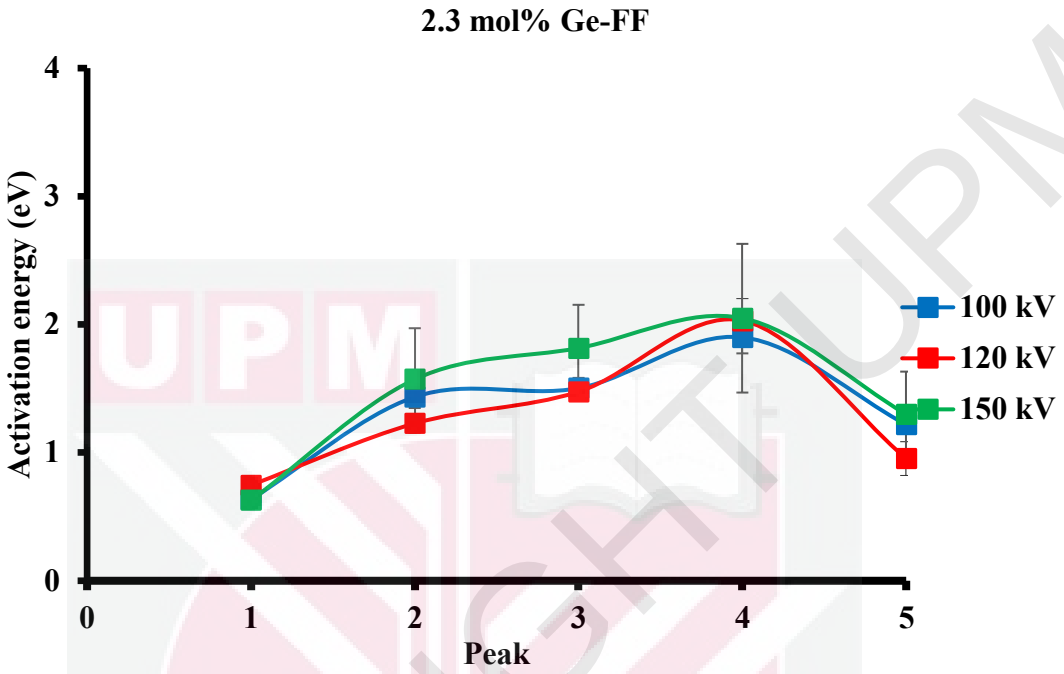

(a)

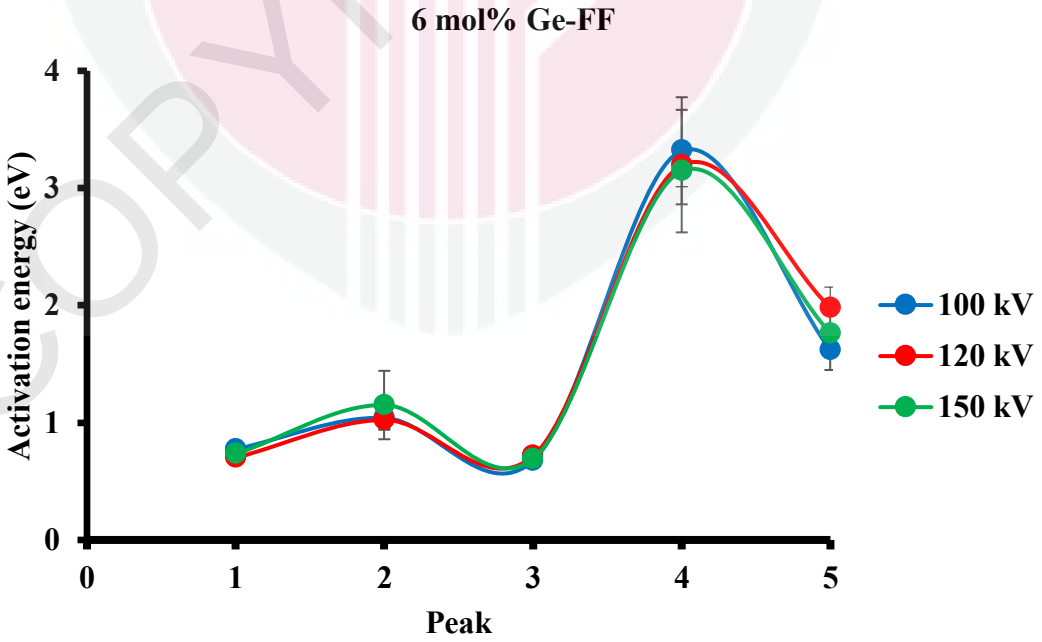

(b)

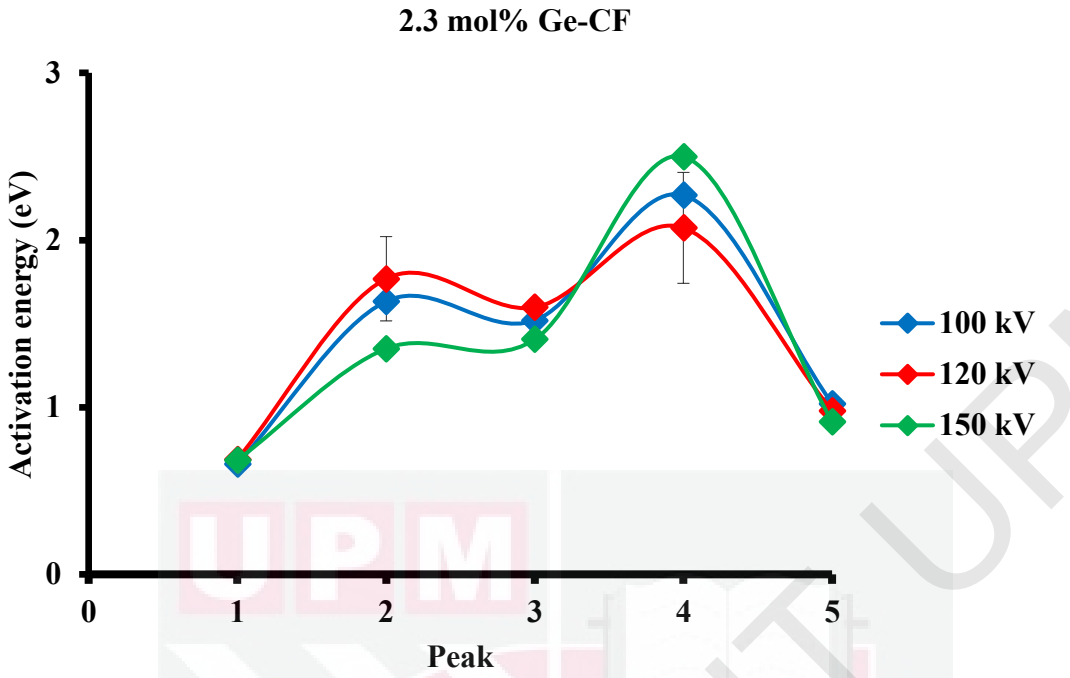

(c)

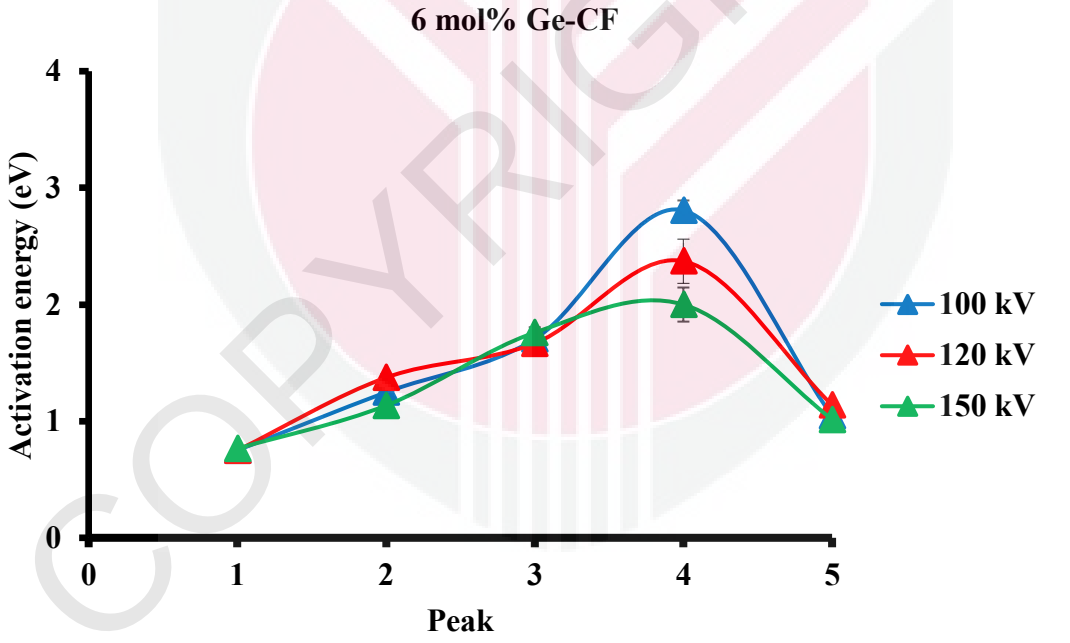

(d)

Figure 4.34: Activation energy (E_a) of Ge-doped (a) 2.3 mol% FF, (b) 6 mol% FF, (c) 2.3 mol% CF and (d) 6 mol% CF for RQT 8, 9 and 10

4.6 Calibration Curves of the Investigated Dosimeters

As a relative dosimeter, the Ge-doped fabricated optical fibres, TLD-100 chips and OSLD nanoDots must be calibrated against absolute dosimetry systems such as a calibrated ion chamber before they are used (IAEA, 2007). In this study, the investigated dosimeters were calibrated against a 0.6 cc PTW Unidos ionisation chamber. The ionisation chamber was cross-calibrated against another standard ionisation chamber at the Secondary Standard Dosimetry Laboratory (SSDL), Malaysian Nuclear Agency. The latter has been calibrated with the reference standard ionisation chamber in terms of RQT beam quality at the IAEA Dosimetry Laboratory according to procedures described in the IAEA TRS-457. Only a calibration curve for RQT 8 (100 kV) was established for this dosimetry study since it was the primary kV used in the comparative dosimetry verification study, as described in previous sections. The selected doses were similar to the dose linearity study, which was in the range of 2 mGy to 40 mGy (2-, 4-, 6-, 8-, 10-, 15-, 20-, 25-, 30-, 35- and 40 mGy). The calibration curve was established by graphing the dosimeter response against the measured dose. The TL signal-absorbed dose calibration curves for optical fibres, TLD-100 chip and count signal-absorbed dose for OSLD nanodot are presented in Figure 4.35. There is a significant positive correlation between TL and count signals against the absorbed dose for all investigated dosimeters, with a coefficient of determination at 0.98% to 0.99% for RQT 8 beam quality.

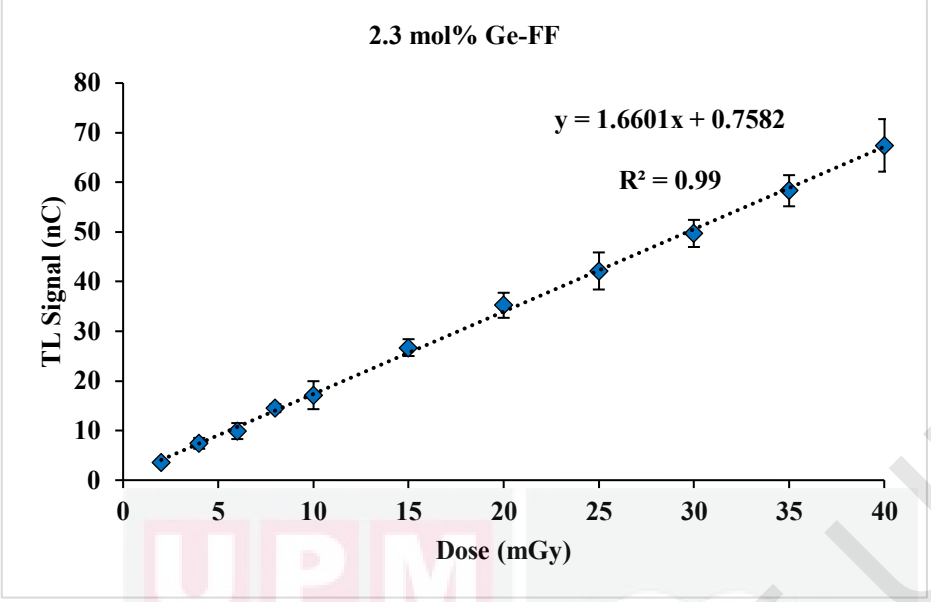

(a)

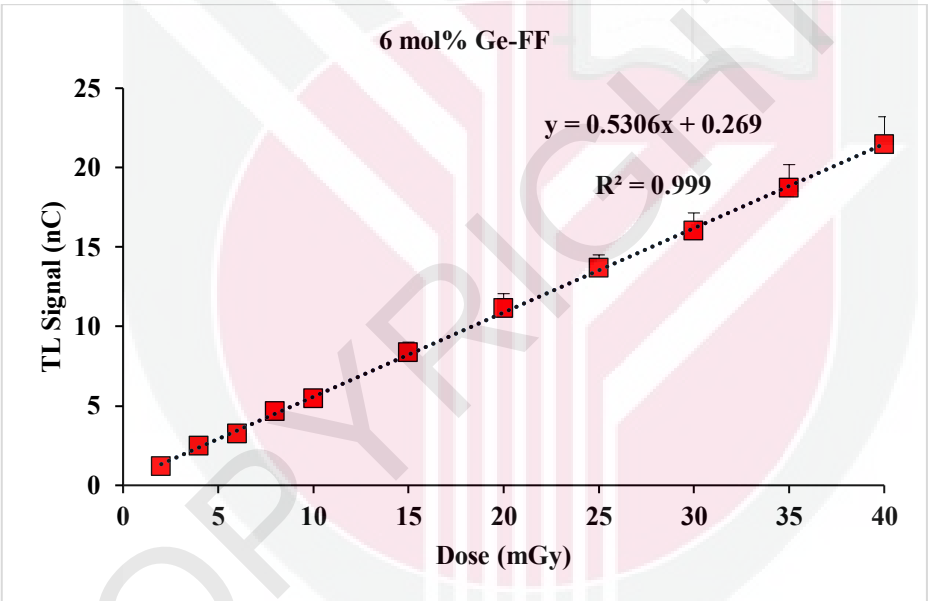

(b)

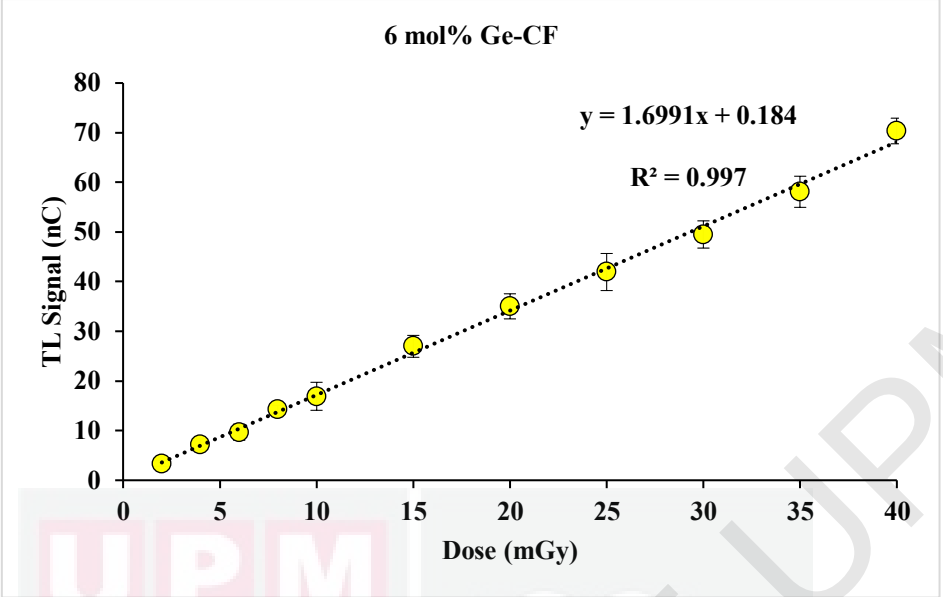

(c)

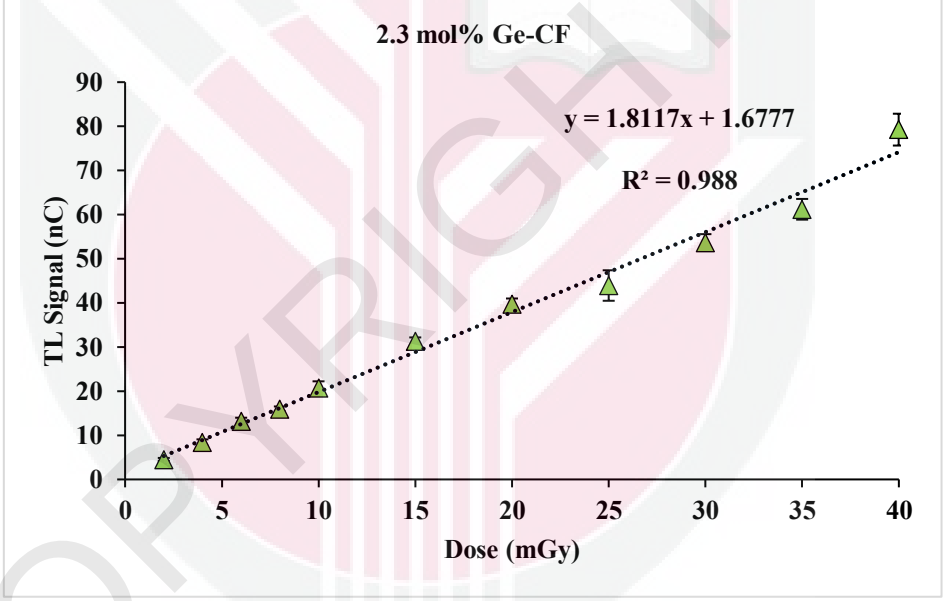

(d)

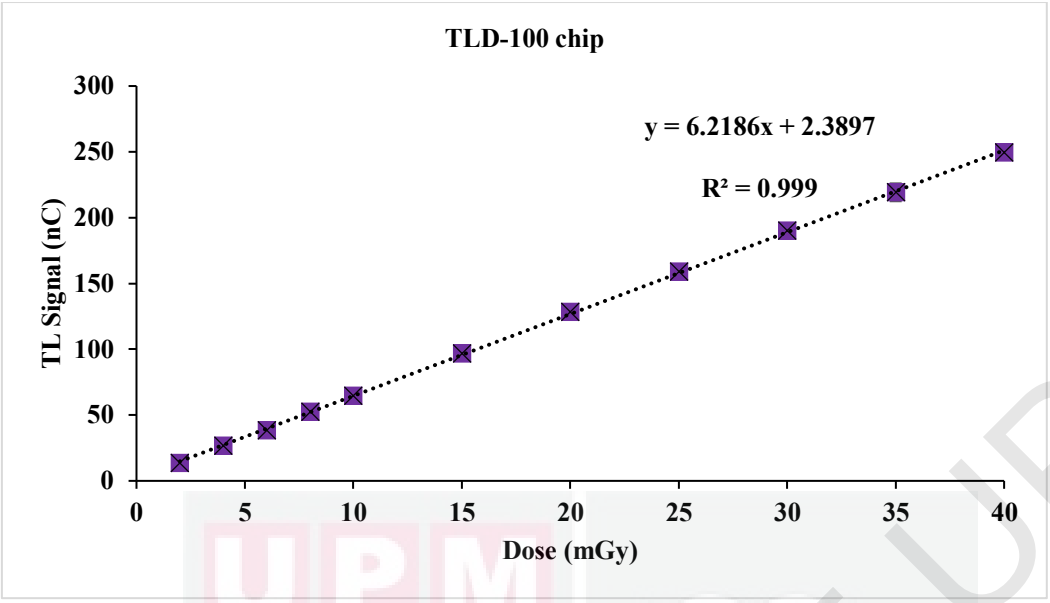

(e)

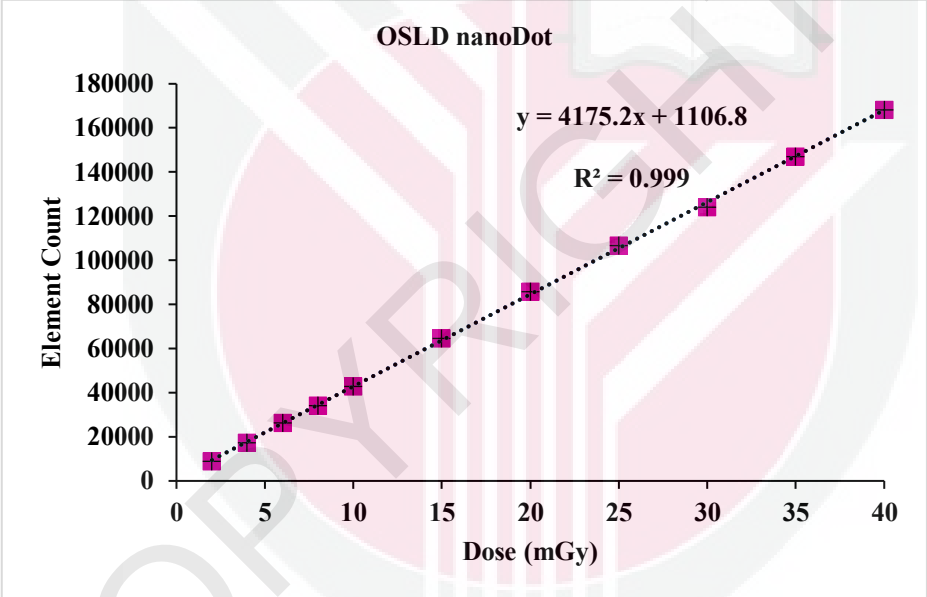

(f)

Figure 4.35: Calibration curve for (a) 2.3 mol% Ge-FF, (b) 6 mol% Ge-FF, (c) 6 mol% Ge-CF, (d) 2.3 mol% Ge-CF, (d) TLD-100 chip and (f) OSLD nanoDot

4.7 CIRS ATOM® Dosimetry Verification Paediatric Phantom Irradiation

Computed tomography (CT) provides cross-sectional images and aids in a detailed examination of anatomy and diagnosis of pathology. CT examinations have increased globally by about 700 - 800%, with more than 10% of CT scans done in the pediatric

group due to advancements in CT technology (Naranje et al., 2022). With the expanding use of CT in children and the increasing attention to the potential risk from CT radiation to this population, there has been growing interest in better managing paediatric patient dose at CT examinations (Goske et al., 2008). One of the first steps to facilitate this patient management is to estimate and measure patient dose. However, efforts to report CT dose and to assess radiation risk have mainly relied on CT dose index (CTDI) and dose length product (DLP) determined in standard-sized cylindric phantoms and their conversion coefficients to effective dose derived for patients of standard ages (Huda et al., 2008). It is best to mention that patient doses acquired with CT dosimetry software have also yet to be independently verified with any radiation dose measurements (Huda et al., 2008).

This part of the study involves an investigation of organ doses to the brain, eyes and thyroids and entrance skin doses of the eyes and thyroids from head computed tomography, with a subsequent investigation of organ doses to the lungs and thyroids and entrance skin dose to thyroid from chest computed tomography examination. The scans were done within the exposure factor range of paediatric patients below two years old.

As mentioned in Chapter 1, it was hypothesised that the newly fabricated germanium-doped optical fibres would show similar or better dosimetric properties than TLD-100 chips and OSLD nanoDots in terms of the basic characterisations and clinical studies. Also, to determine which of the fabricated fibres showed the best performance for the dosimetry application in future clinical settings

4.7.1 Head Computed Tomography Scan

4.7.1.1 Brain Organ Dose

Figure 4.36 shows the brain scan for each slab, which corresponds to the methodology detailed in Section 3.9.1. In contrast, Figure 4.37 shows the average brain organ dose for all slabs measured by the investigated dosimeters during a phantom head scan. The average brain organ dose recorded by the TLD-100 chip was recorded as 25.16 mGy, followed by 25.29 mGy for 2.3 mol% Ge-CF, 25.61 mGy for 6 mol% Ge-CF, 25.71 mGy for 6 mol% Ge-FF, and finally a 25.83 mGy for 2.3 mol% Ge-FF. Table 4.10 shows the percentage difference for each investigated dosimeter against the gold standard TLD-100 chip with 2.3 mol% Ge-CF showing the least percentage difference of 0.52%, followed by 1.77% for 6 mol% Ge-CF, 2.16% for 6 mol% Ge-FF, and a percentage difference of 2.63% for 2.3 mol% Ge-FF. In summary, all dosimeters showed a less than 3% percentage difference. A one-way between-groups analysis of variance (ANOVA) was used to compare the sample's response between different types of dosimeters towards absorbed dose measurement of the brain. Inspection of the skewness, kurtosis and Shapiro-Wilk statistics indicated that the normality assumption was supported for each type of investigated dosimeter. There was no significant difference ($p = 0.346$) between the absorbed dose measured by all investigated dosimeters. The ANOVA table is attached in Appendix A1.

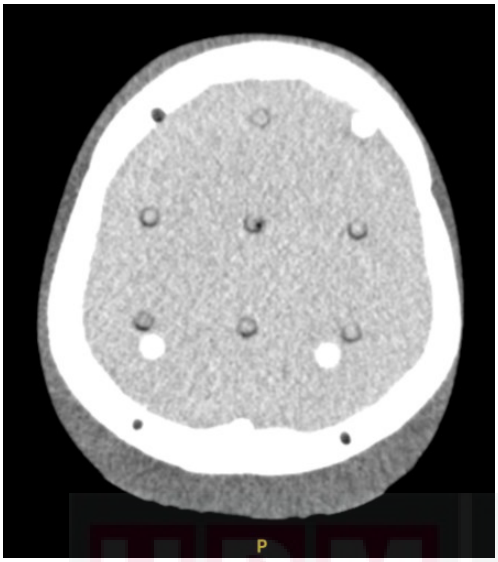

Slab 2

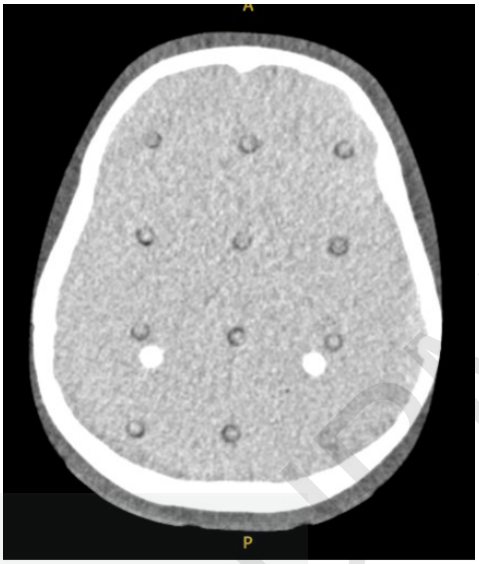

Slab 3

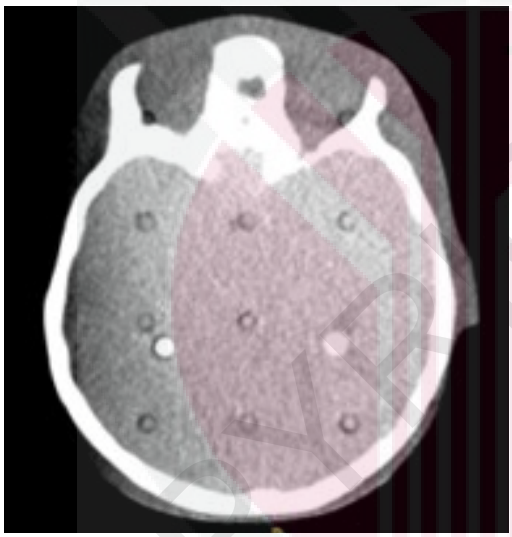

Slab 4

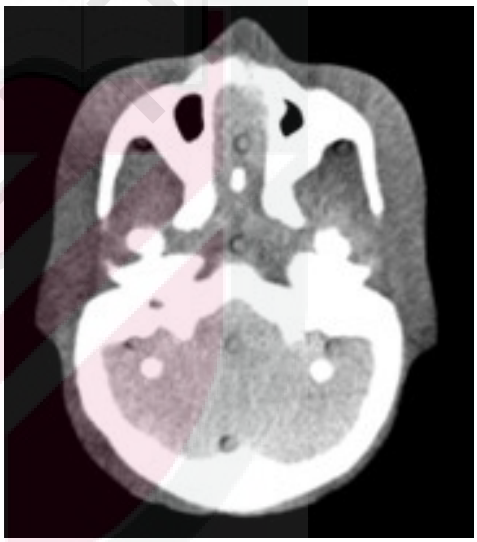

Slab 5

Figure 4.36: Images of a brain scan of CIRS ATOM® dosimetry paediatric 1-year-old phantom

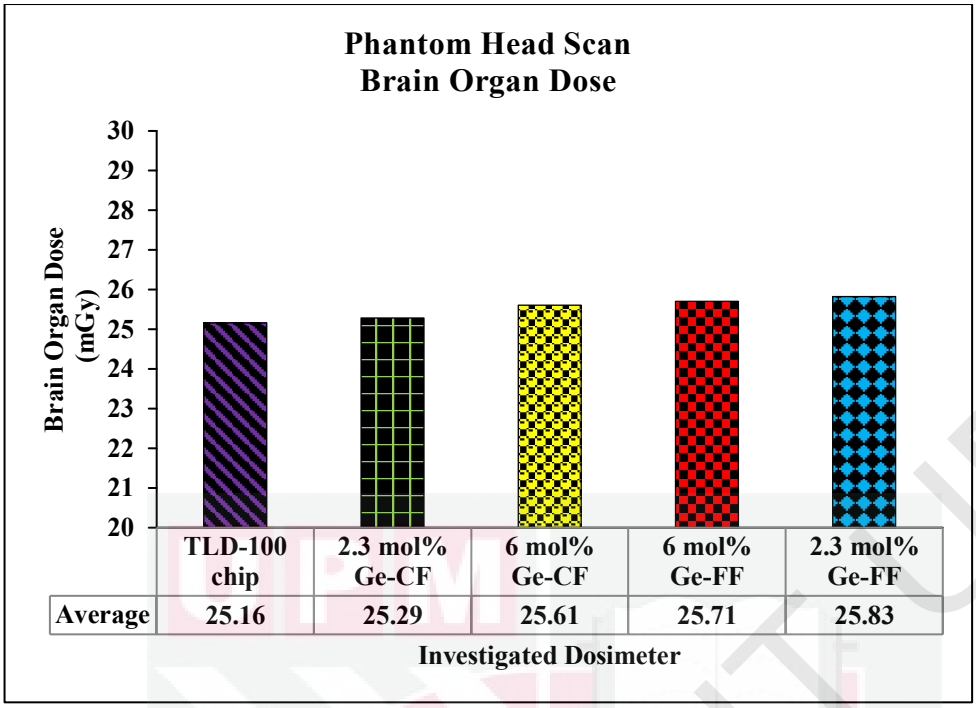

Figure 4.37: Brain organ dose for phantom head scan

Table 4.10: Percentage difference of fabricated optical fibres against TLD-100 for brain organ dose

Investigated Dosimeter	Percentage Difference Against TLD-100
2.3 mol% Ge-CF	0.52%
6 mol% Ge-CF	1.77%
6 mol% Ge-FF	2.16%
2.3 mol% Ge-FF	2.63%

In hospitals across Asia, including Malaysia, 12.2% of paediatric CT exams were conducted, according to an IAEA study on CT frequency (Vassileva et al., 2012). About 75% of all paediatric CT exams were CT brain scans. Another 2012 study by Pearce et al. (2012) found that the risk of leukaemia was higher from CT brain examinations for younger patients than for older children. Paediatric patients in the United Kingdom who were exposed to CT brain radiation dosage of 50 mGy or higher were 2.8 times more predisposed to future risk of brain malignancy.

Brady et al. (2011) employed TLDs to measure the doses to the brain in an anthropomorphic phantom of a 10-year-old child for a CT brain scan. The brain received an average absorbed radiation of 33.6 mGy. In another study by Feng et al. (2010), a 5-year-old paediatric phantom was used to evaluate radiosensitive organs during head CT, and the brain received 17.9 mGy. A study by Kiani and Chaparian (2023) evaluated organ doses from paediatric brain CT scans using the ImpactDose software based on Monte Carlo simulations. The highest mean organ dose in brain CT scan was related to the brain, with 22.1 mGy for patients under one year old and 31.4 mGy for those between 2 to 5 years of age. Their results showed a direct and significant correlation between brain organ doses and the age of patients as the average absorbed doses of these organs increased with the increasing age of patients. This pattern was also observed in the study of De Basea et al. (2018) using their National Cancer Institute Computed Tomography (NCICT) dosimetry software. Brain doses progressively increased with age, with head examinations providing a range of median doses from 23.6 mGy in 0 to 4-year-old children.

These differences in organ doses in this study compared to other investigations can be related to differences in the type of scanner (model and manufacturer) and scan parameters (kVp, mA, rotation time, pitch, slice thickness, etc.). In addition, differences in organ dose measurements between direct dosimetry verification on phantom and the type of software used to estimate patient organ doses can be another reason for these differences. However, it could be noted that the dose measured by the TLD-100 chip and fabricated optical fibres were in the range of other studies. Based on the statistical analysis, the findings suggested no significant difference between the absorbed dose measured by all investigated dosimeters. Thus, the fabricated Ge-doped

optical fibres have been shown to have great potential to be used as an alternative dosimeter in paediatric phantom dose measurement.

4.7.1.2 Eye Organ Dose

Figure 4.38 shows the phantom head scan for eye organ dose measurement. In this particular slice (slab 4), the placement of the dosimeter, in this case, TLD-100 chip, within the left and right eyes of the phantom is identified by the red circles. Figure 4.39 shows the bar chart representing the average eye organ dose measured by all investigated dosimeters during a phantom head scan. The eye organ dose recorded by the TLD-100 chip was recorded as 28.92 mGy, followed by 28.94 mGy for 2.3 mol% Ge-CF, 29.29 mGy for 6 mol% Ge-CF, 29.39 mGy for 6 mol% Ge-FF and 29.69 mGy for 2.3 mol% Ge-FF. Table 4.11 shows the percentage difference for each investigated dosimeter against the gold standard TLD-100 chip with 2.3 mol% Ge-CF showing the least percentage difference of 0.07%, followed by 1.27% for 6 mol% Ge-CF and a percentage difference of 1.61% and 2.63% for 6 mol% Ge-FF and 2.3 mol% Ge-FF respectively. In summary, all dosimeters showed a less than 3% percentage difference. A one-way between-groups analysis of variance (ANOVA) was used to compare the response of the sample between different types of dosimeters towards eye organ dose during phantom head scan. Inspection of the skewness, kurtosis and Shapiro-Wilk statistics indicated that the assumption of normality was supported for each type of investigated dosimeter. There was no significant difference ($p = 0.209$) between the absorbed dose measured by all investigated dosimeters. The ANOVA table is attached in Appendix A1.

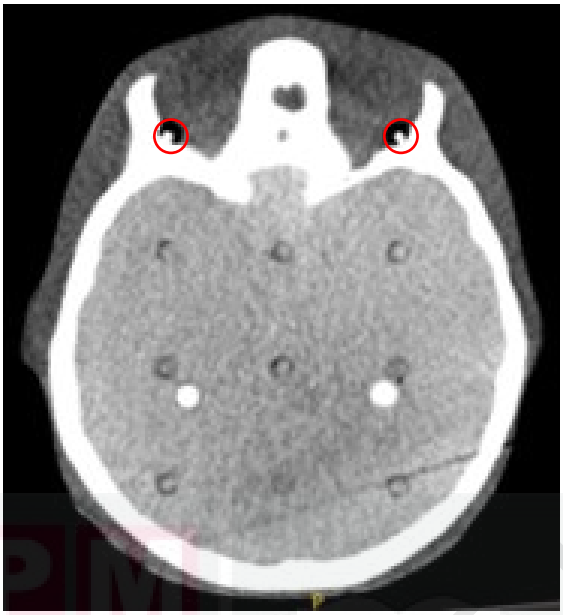

Figure 4.38: Placement of TLD-100 chips (red circles) within the eye dosimetry holes for eye organ dose measurement

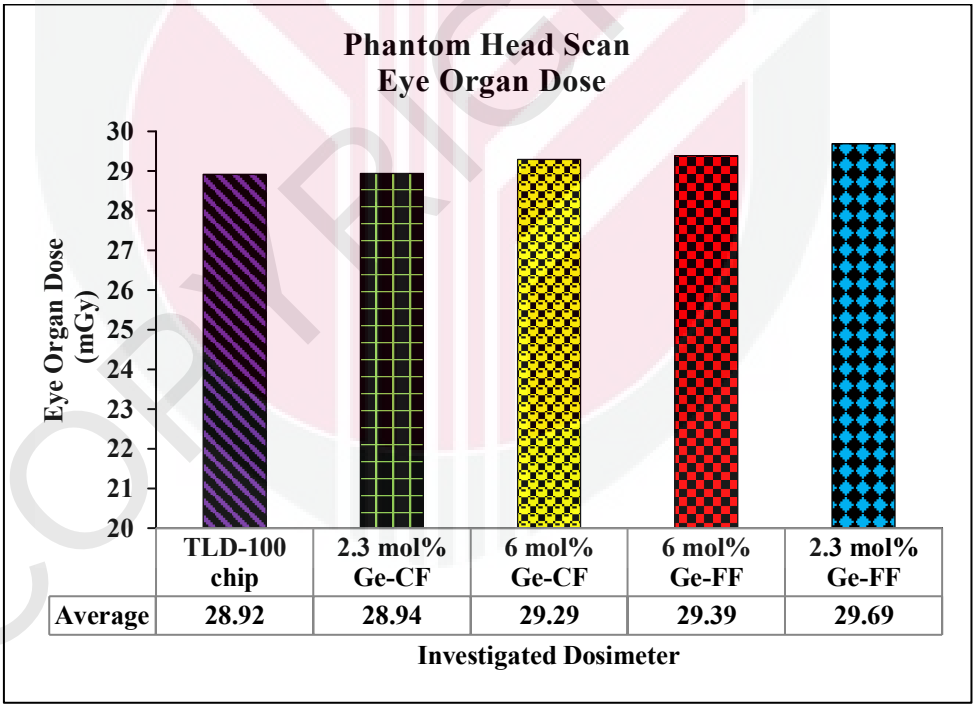

Figure 4.39: Eye organ dose for a phantom head scan

Table 4.11: Percentage difference of fabricated optical fibres against TLD-100 for eye organ dose

Investigated Dosimeter	Percentage Difference Against TLD-100
2.3 mol% Ge-CF	0.07%
6 mol% Ge-CF	1.27%
6 mol% Ge-FF	1.61%
2.3 mol% Ge-FF	2.63%

By the late 1980s and early 1990s, the majority of reported lens dose estimations were below 100 mGy (Nishizawa et al., 1991) as compared to the studies published in the late 1970s and early 1980s which indicated lens doses of up to 350 mGy (Lund & Halaburt, 1982). The dose reduction was highly related to the advancement of modern CT scanners. Depending on the device and technique, the radiation exposure to the eye during a CT of the brain is around 50 mGy. The lens of the eye is highly radiosensitive; doses as little as 0.5 to 2 Gray (Gy) can result in observable opacities, while exposures as high as 4 Gy may result in secondary cataract formation and visual impairment. Children's eyes are particularly radiosensitive, with cataracts developing from less than half of this radiation. As such, eye dosimetry study in phantom or patients undergoing CT procedures is one of the dose descriptors for determining the level of radiation exposure, knowing fully well that ocular exposure during the CT scan could potentially induce cancer and cataracts (Jibiri & Adewale, 2014).

Brady et al. (2011) employed TLDs to measure the doses to the lens in an anthropomorphic phantom of a 10-year-old child for a CT brain scan. Although it was still well below the deterministic threshold of around 1.5 Gy for cataracts (Valentin, 2007), the lens dosage of 19.3 mGy was recorded for the 2011 study. In another study by Feng et al. (2010), a 5-year-old paediatric phantom was used to evaluate

radiosensitive organs during head CT. The lens received a considerably high organ dose of roughly 25.9 mGy. Fearon et al. (2011) using two pediatric anthropomorphic phantoms and TLDs found that the dose to the eye lens was 24.4 mGy for neonates and 21.6 mGy for the 12-year-old phantom. Another study based on Monte Carlo simulation techniques showed that the lens dose was 34.5 mGy for a 5-year-old anthropomorphic phantom (McDermott et al., 2009).

As mentioned previously, these differences in organ doses can be related to differences in the type of scanner and scan parameters together with the differences in organ dose measurements between direct dosimetry verification on different age phantom. However, it could be noted that the dose measured by the TLD-100 chip and fabricated optical fibres were in the range of other studies and based on the statistical analysis, the findings suggested that there was no significant difference between the absorbed dose measured by all investigated dosimeters. Thus, the fabricated Ge-doped optical fibres have been shown to have great potential to be used as an alternative dosimeter in phantom dose measurement.

4.7.1.3 Thyroid Organ Dose

Along with the brain and eye lens, which are exposed directly during head CT, there is another radio-sensitive organ that is not directly exposed, which receives a lesser radiation dose via scatter radiation but is linked to relatively significant lifetime attributable risk which is the thyroid (Kiani & Chaparian, 2023). Figure 4.40 shows the bar chart to represent the average thyroid organ dose as measured by all investigated dosimeters during a phantom head scan due to scattered radiation. As the thyroid was not within the collimation field during the phantom head scan, no image

was recorded. The average thyroid organ dose recorded by the TLD-100 chip from scattered radiation of the phantom head scan was recorded as 1.85 mGy, followed by 1.89 mGy for both 2.3 mol% Ge-CF and 6 mol% Ge-CF, 1.90 mGy for 6 mol% Ge-FF and 1.94 mGy for 2.3 mol% Ge-FF. Table 4.12 shows the percentage difference for each investigated dosimeter against gold standard TLD-100 chip with 2.3 mol% Ge-FF showing the largest difference of 4.75% while both 2.3 mol% Ge-CF and 6 mol% Ge-CF recorded the least percentage difference of 2.14%, followed by 2.67% for 6 mol% Ge-FF. In summary, all fabricated Ge-doped optical fibres showed a percentage difference of less than 5%. A one-way between-groups analysis of variance (ANOVA) was used to compare the response of the sample between different types of dosimeters towards thyroid organ dose during phantom head scan. Inspection of the skewness, kurtosis and Shapiro-Wilk statistics indicated that the assumption of normality was supported for each type of investigated dosimeter. There was no significant difference ($p = 0.999$) between the absorbed dose measured by all investigated dosimeters. The ANOVA table is attached in Appendix A1.

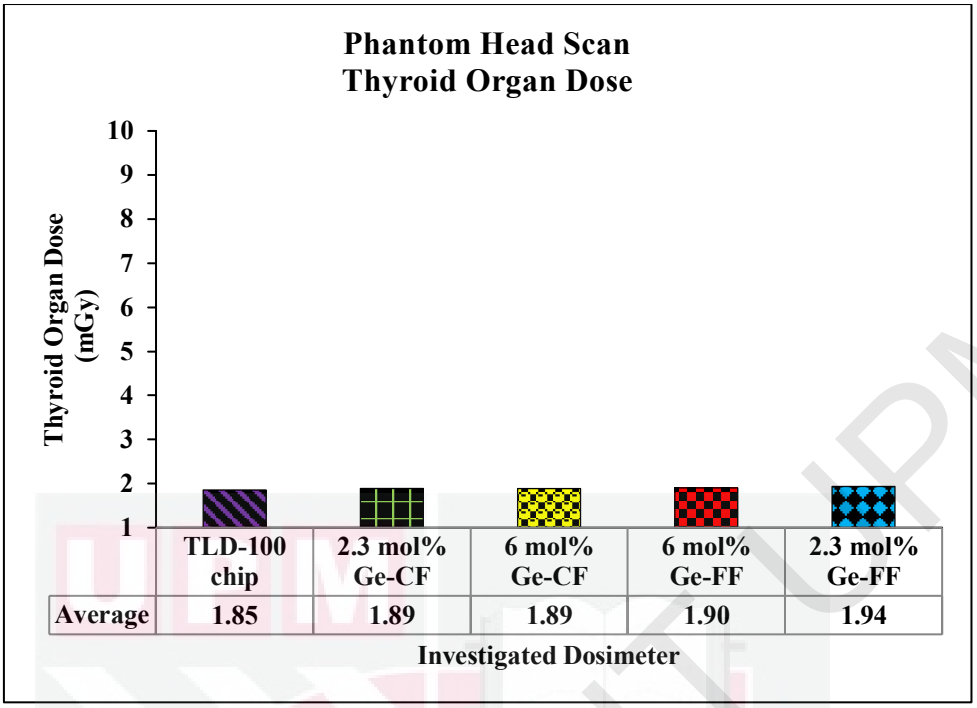

Figure 4.40: Thyroid organ dose for a phantom head scan

Table 4.12: Percentage difference of fabricated optical fibres against TLD-100 for thyroid organ dose

Investigated Dosimeter	Percentage Difference Against TLD-100
2.3 mol% Ge-CF	2.14%
6 mol% Ge-CF	2.14%
6 mol% Ge-FF	2.67%
2.3 mol% Ge-FF	4.75%

The thyroid has been identified as an organ with relatively low sensitivity to ionising radiation as cell damage may occur at a low dose, although it may take decades or a lifetime for malignancies to manifest in children younger than 12 years old. In other words, thyroid cancer is categorised as a stochastic radiation impact, and it is extremely uncommon to develop in children, with an annual incidence of fewer than one case per million in most developed nations (Sinnott et al., 2010). However, the

thyroid that receives 50 to 100 mGy of radiation dosage during CT of the head and neck, has been linked to a higher risk of thyroid cancer in children (Ghaznavi, 2020).

Brady et al. (2011) employed TLDs to measure the doses to the thyroid in an anthropomorphic phantom of a 10-year-old child for a CT brain scan. 1.67 mGy of scattered radiation was observed at the thyroid. In another study by Feng et al. (2010), a 5-year-old paediatric phantom was used to evaluate radiosensitive organs during head CT. A 2.5 mGy thyroid dosage was also recorded. In a Monte Carlo simulation study conducted by Mazonakis et al. (2006), the scattered dose to the thyroid from brain CT scans was found to be 2.3, 2.8, 2.1, 2.2 and 2.1 mGy for pediatric phantoms of 0, 1, 5, 10 and 15 years old, respectively. Additionally, Su et al. (2014) using the ImPACT Patient Dosimetry Calculator estimated that the range of scattered radiation dose to the thyroid for pediatric patients who underwent head CT examinations was 1.10 to 2.45 mGy. Kiani and Chaparian (2023) also evaluated organ doses from paediatric brain CT scans by using the ImpactDose software based on Monte Carlo simulations. While the highest mean organ dose in brain CT scan was related to the brain with results showing a direct and significant correlation between brain organ dose and the age of patients, the mean organ dose for thyroid, which is among the most radiosensitive organs in childhood, was highest among the most sensitive group as they reported a thyroid organ dose of 1.8 mGy for patients under one year of age. In other words, their study reported significant inverse correlation was observed between the organ dose of thyroid with the age of patients. Hence the importance of thyroid dosimetry study for younger patients.

These differences in organ doses in this study compared to other investigations can be related to differences in the type of scanner and scan parameters together with differences in organ dose measurements between direct dosimetry verification on phantom and the type of software used to estimate patient organ doses. However, it could be noted that the dose measured by the TLD-100 chip and fabricated optical fibres were in the range of other studies and based on the statistical analysis, the findings suggested that there was no significant difference between the absorbed dose measured by all investigated dosimeters. Thus, the fabricated Ge-doped optical fibres have been shown to have great potential to be used as an alternative dosimeter in phantom dose measurement.

4.7.1.4 Eye Entrance Skin Dose

Figure 4.41 shows the phantom head scan for eye entrance skin dose measurement. It can be seen in this particular slice (slab 4), the placement of the dosimeter in this case optical fibre, on the skin surface anterior to both the right and left eyes as identified by the red circles. Figure 4.42 shows the bar chart to represent the average eye entrance skin dose as measured by all investigated dosimeters during a phantom head scan. It was to be noted that nanoDot measurement was included as it was feasible to measure the dose for entrance skin measurement as compared to organ doses due to the limitation of the phantom with the absence of nanoDot dosimetry holes for organ dose measurement. The eye entrance skin dose recorded by the TLD-100 chip was recorded as 29.49 mGy, followed by 29.52 mGy for 2.3 mol% Ge-CF, 29.56 mGy for mol% Ge-CF, 29.61 mGy for nanoDot, 29.73 mGy for 6 mol% Ge-FF and 29.85 mGy for 2.3 mol% Ge-FF. Table 4.13 shows the percentage difference for each investigated dosimeter against the gold standard TLD-100 chip with all dosimeters showing a

percentage difference of less than 1% except for 2.3 mol% Ge-FF with 1.21%. NanoDot also showed a percentage difference of 0.41% when compared to the TLD-100 chip. A one-way between-groups analysis of variance (ANOVA) was used to compare the response of the sample between different types of dosimeters towards eye entrance skin dose during phantom head scan. Inspection of the skewness, kurtosis and Shapiro-Wilk statistics indicated that the assumption of normality was supported for each type of investigated dosimeter. There was no significant difference ($p = 0.582$) between the entrance skin doses measured by all investigated dosimeters. The ANOVA table is attached in Appendix A2.

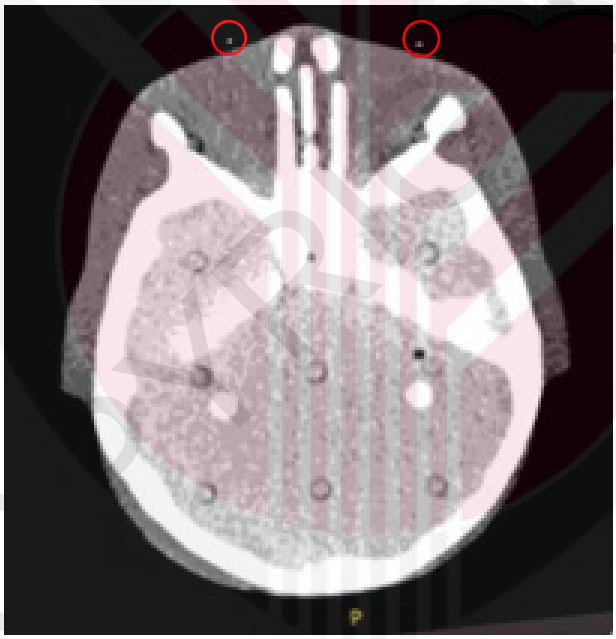

Figure 4.41: Placement of optical fibres (red circles) for the measurement of eye entrance skin dose

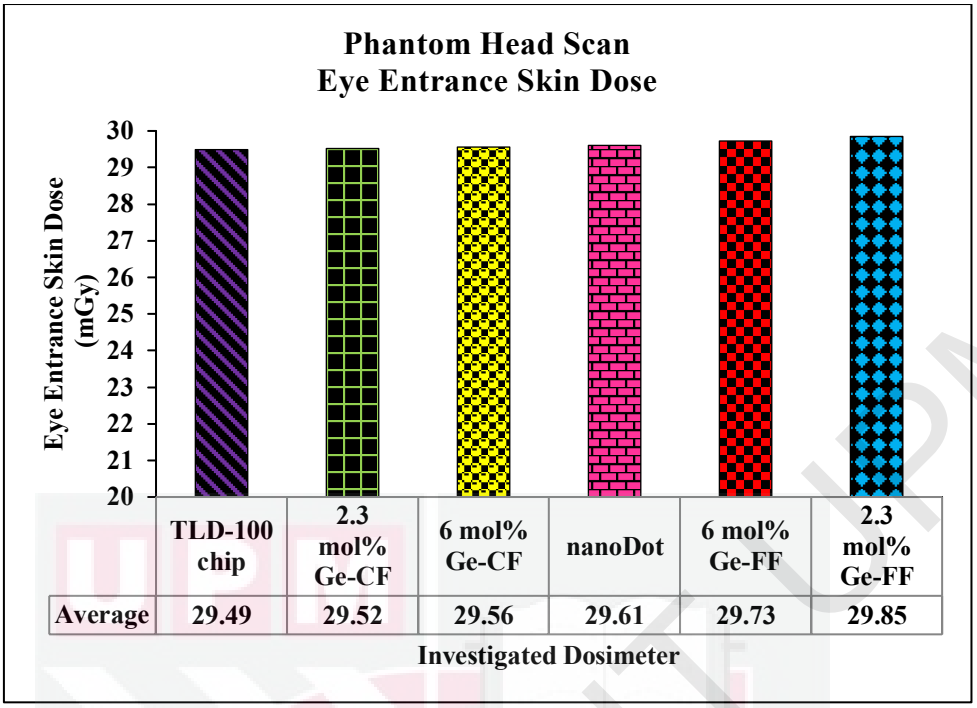

Figure 4.42: Eye entrance skin dose for a phantom head scan

Table 4.13: Percentage difference of investigated dosimeter against TLD-100 for eye entrance skin dose

Investigated Dosimeter	Percentage Difference Against TLD-100 (%)
2.3 mol% Ge-CF	0.10
6 mol% Ge-CF	0.24
nanoDot	0.41
6 mol% Ge-FF	0.81
2.3 mol% Ge-FF	1.21

In a real clinical patient study, several study groups were found to investigate the skin doses by using TLDs. TLD-100 chips were placed in the centre of each eye and since the eye lens is located at a depth of about 2–4 mm (Ploussi et al., 2017), the entrance skin dose can be considered to be a reliable estimation of the absorbed dose to the eye lens. Abdulhamid et al. (2022) for example examined a total of 17 paediatric patients ranging in age from 6 months to 17 years old between three different hospitals.

According to measurements made from the TLD signals, the mean dose to the lens of the eyes was 5.87 mGy. This value was lower than those recorded in Iran by Toossi et al. (2018) in CT brain procedures of 15 paediatric patients between the ages of 1.5 and 15 years old in five different hospitals which recorded lens dosages of 16.05 mGy. A study by Ploussi et al. (2017) recorded eye entrance skin doses in three patients from the age of 0 to 2 years old and six patients from the age of 2 to 5 years old to be 10.5 mGy and 29.9 mGy respectively while Jibiri and Adewale (2014) study in a Nigerian hospital on five patients aged 1.5 to 18 years old was recorded as 31.14 mGy. The greatest dose was observed by Stathopoulos et al. (2016) when examining paediatric children who underwent head CT scans in Athens, ranging in age from newborns to 15 years old. On the eye lens, the mean surface dosage was 37.01 mGy. The CT procedures, the acquisition method, and the patient's age between different hospitals contributed to the dose variation. In summary, the average eye entrance skin dose by using a 1-year-old phantom in this study was similar to the majority of the previously mentioned studies. The fabricated Ge-doped optical fibres have been shown to have great potential to be used as an alternative dosimeter in entrance skin dose measurement.

4.7.1.5 Thyroid Entrance Skin Dose

Figure 4.43 shows the bar chart to represent thyroid entrance skin dose as measured by all investigated dosimeters during a phantom head scan due to scattered radiation. As the thyroid was not within the collimation field during the phantom head scan, no image was recorded. The thyroid entrance skin dose recorded by the TLD-100 chip from scattered radiation of the phantom head scan was recorded as 1.89 mGy, followed by 1.91 mGy for 2.3 mol% Ge-CF, 1.94 mGy for 6 mol% Ge-CF, 1.95% for

nanoDot, as well as 1.97 mGy for both 6 mol% and 2.3 mol% Ge-FF. Table 4.14 shows the percentage difference for each investigated dosimeter against the gold standard TLD-100 chip with both 6 mol% and 2.3 mol% Ge-FF showing the largest difference of 4.15%. NanoDot had a percentage difference of 3.13% while 6 mol% Ge-CF documented a 2.61% with the least percentage difference of 1.05% recorded by 2.3 mol% Ge-CF. A one-way between-groups analysis of variance (ANOVA) was used to compare the response of the sample between different types of dosimeters towards thyroid entrance skin dose during phantom head scan. Inspection of the skewness, kurtosis and Shapiro-Wilk statistics indicated that the assumption of normality was supported for each type of investigated dosimeter. There was no significant difference ($p = 1.000$) between the entrance skin doses measured by all investigated dosimeters. The ANOVA table is attached in Appendix A2.

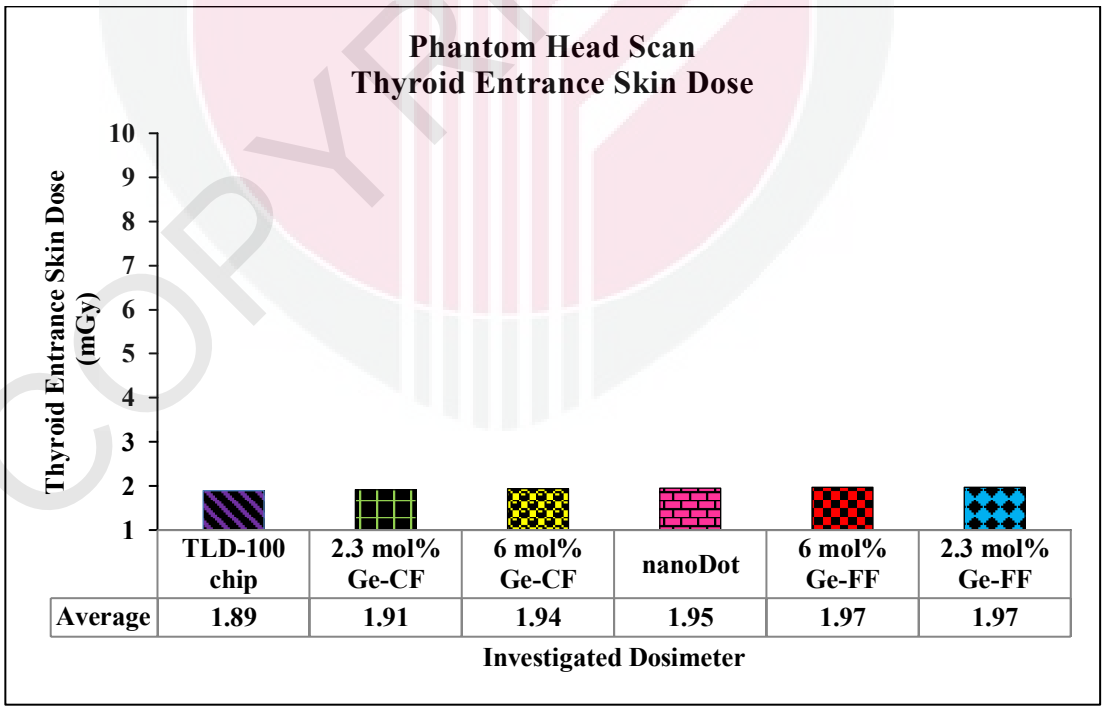

Figure 4.43: Thyroid entrance skin dose for a phantom head scan

Table 4.14: Percentage difference of investigated dosimeter against TLD-100 for thyroid entrance skin dose

Investigated Dosimeter	Percentage Difference Against TLD-100
2.3 mol% Ge-CF	1.05%
6 mol% Ge-CF	2.61%
nanoDot	3.13%
6 mol% Ge-FF	4.15%
2.3 mol% Ge-FF	4.15%

Concerning the thyroid, which is a superficial organ, the maximum variation between surface and thyroid dose was approximately 10% in pediatric patients (Al-Senan & Hatab, 2011). Therefore, the surface dose is a good estimator for the thyroid dose in children. In a real clinical patient study, several study groups were found to investigate the skin doses by using TLDs overlying the thyroid gland to measure the scatter radiation at this region. Abdulhamid et al. (2022) for example examined a total of 17 paediatric patients ranging in age from 6 months to 17 years old between three different hospitals. According to measurements made from the TLD signals, the mean dose to the thyroid was 3.42 mGy. This value was lower than those recorded in Iran by Toossi et al. (2018) in CT brain procedures of 15 paediatric patients between the ages of 1.5 and 15 years old in five different hospitals which was 5.89 mGy. A study by Stathopoulos et al. (2016) on paediatric children who underwent head CT scans in Athens, ranging in age from newborns to 15 years old recorded an entrance skin dose of 1.95 mGy while a study by Ploussi et al. (2017) recorded thyroid skin doses in three patients from the age of 0 to 2 years old and six patients from the age of 2 to 5 years old to be 1.7 mGy and 2.4 mGy respectively. The results revealed small variations in radiation dose since the thyroid is outside the scanning range for brain CT

examinations. The CT procedures, the acquisition method, and the patient's age between different hospitals also contributed to the dose variation.

4.7.2 Chest Computed Tomography Scan

4.7.2.1 Lung Organ Dose

Figure 4.44 shows the lung scan for each slab in CIRS ATOM® dosimetry paediatric 1-year-old phantom while Figure 4.45 shows the average lung organ dose as measured by all investigated dosimeters during a phantom chest scan. The lung organ dose recorded by the TLD-100 chip was recorded as 3.83 mGy, followed by 3.85 mGy for 2.3 mol% Ge-CF, 3.88 mGy for 6 mol% Ge-CF, and 3.92 mGy for both 6 mol% and 2.3 mol% Ge-FF. Table 4.15 shows the percentage difference for each investigated dosimeter against the gold standard TLD-100 chip with both 6 mol% and 2.3 mol% Ge-FF showing the largest difference of 2.32%. 6 mol% Ge-CF documented a 1.30% with the least percentage difference of 0.52% recorded by 2.3 mol% Ge-CF. A one-way between-groups analysis of variance (ANOVA) was used to compare the response of the sample between different types of dosimeters towards absorbed dose measurement of the lung in a phantom chest scan. Inspection of the skewness, kurtosis and Shapiro-Wilk statistics indicated that the assumption of normality was supported for each type of investigated dosimeter. There was no significant difference ($p = 0.998$) between the organ doses measured by all investigated dosimeters. The ANOVA table is attached in Appendix A3.

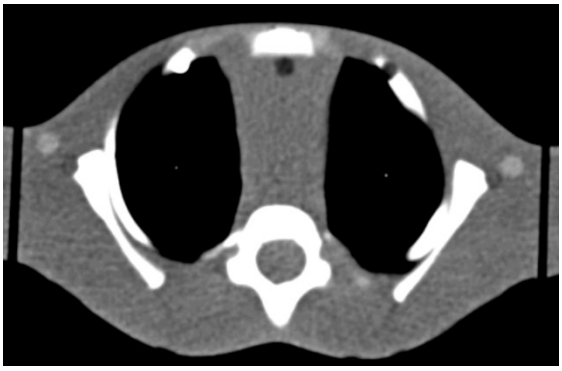

Slab 9

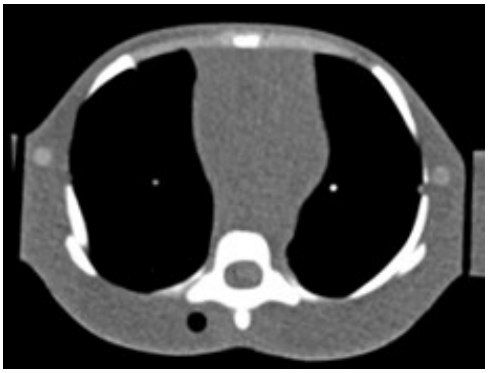

Slab 10

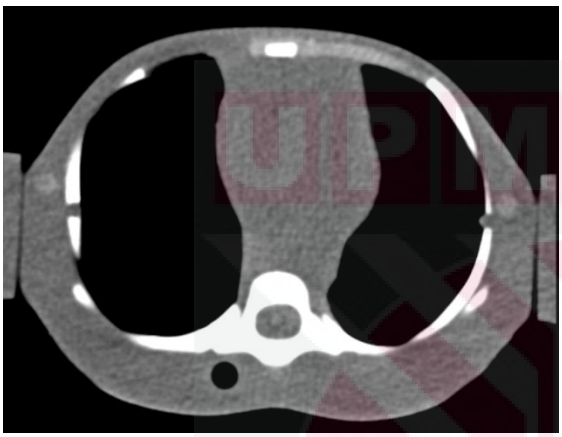

Slab 11

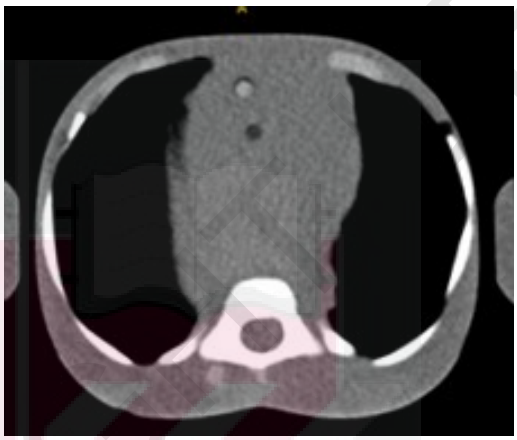

Slab 12

Figure 4.44: Images of a lung scan of CIRS ATOM® dosimetry paediatric 1-year-old phantom

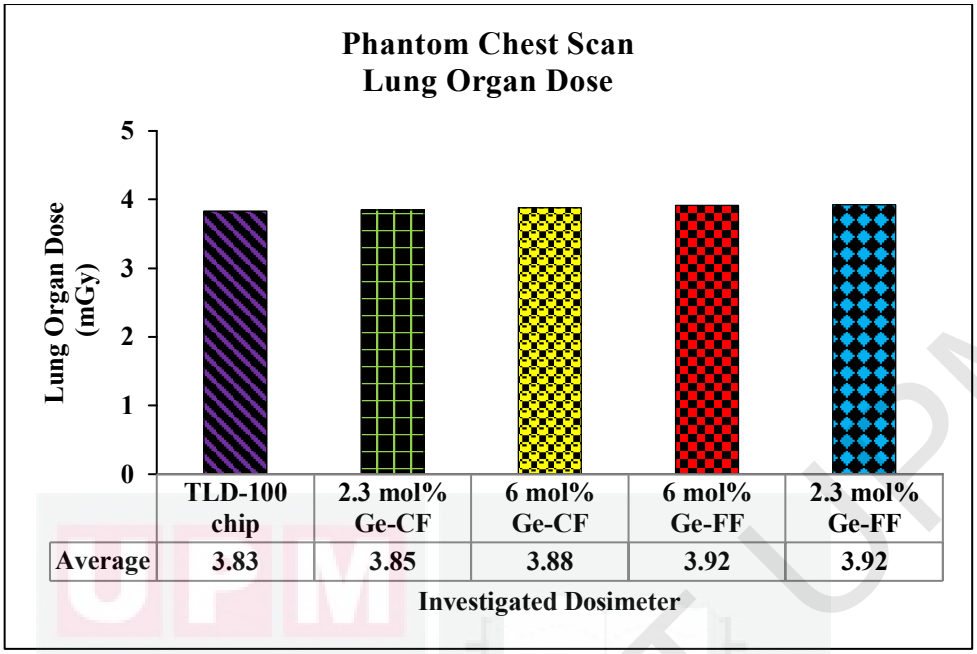

Figure 4.45: Lung organ dose on a phantom chest scan

Table 4.15: Percentage difference of fabricated optical fibre against TLD-100 for lung organ dose

Investigated Dosimeter	Percentage Difference Against TLD-100
2.3 mol% Ge-CF	0.52%
6 mol% Ge-CF	1.30%
6 mol% Ge-FF	2.32%
2.3 mol% Ge-FF	2.32%

A study by Giansante et al. (2019) evaluated organ doses for chest computed tomography procedures with TL dosimeters by using a 5-year-old pediatric anthropomorphic phantom and 120 kV exposure factor. Similar to the present study, TLD-100 chips were positioned inside the phantoms according to the lung distributions. Due to the usage of higher technical factors and larger phantom size, the lung organ dose was noticeably higher than the present study with a 5.13 mGy dose reading. Brady et al. (2011) employed TLDs to calculate the organ-absorbed doses for

a CT chest scan on an anthropomorphic phantom of a 10-year-old. 9.9 mGy was recorded in the lung. A 5-year-old paediatric phantom was utilised in another investigation by Feng et al. (2010) to measure radiosensitive organs during thorax CT and an organ dose of 5.41 mGy was recorded for the lung. These differences in organ doses can be related to differences in the type of scanner and scan parameters together with the differences in organ dose measurements between direct dosimetry verification on different age phantom. However, it could be noted that the dose measured by the TLD-100 chip and fabricated optical fibres were in the logical range of other studies and based on the statistical analysis, the findings suggested that there was no significant difference between the absorbed dose measured by all investigated dosimeters. Thus, the fabricated Ge-doped optical fibres have been shown to have great potential to be used as an alternative dosimeter in phantom dose measurement.

4.7.2.2 Thyroid Organ Dose

Figure 4.46 shows the thyroid region of the phantom which was within the collimation field during the chest scan for lung organ dose measurement. The thyroid is the radiosensitive organ which is greatly affected due to scattered radiation from the lung scan. It can be seen in this particular slice (slab 8), that the placement of optical fibre within the thyroid dosimetry hole of the phantom as identified by the red circle. Figure 4.47 shows the bar chart to represent the average thyroid organ dose as measured by all investigated dosimeters during a phantom chest scan. The thyroid organ dose recorded by the TLD-100 chip was recorded as 2.05 mGy, followed by 2.06 mGy for 2.3 mol% Ge-CF, 2.11 mGy for 6 mol% Ge-CF, 2.13 mGy for 6 mol% Ge-FF and 2.15 mGy for 2.3 mol% Ge-FF. Table 4.16 shows the percentage difference for each investigated dosimeter against gold standard TLD-100 chip with 2.3 mol% showing

the least percentage difference of 0.49% followed by 2.88% for 6 mol% Ge-CF, 3.83% for 6 mol% Ge-FF and 4.76% difference for 2.3 mol% Ge-FF. All dosimeters showed a percentage difference of less than 5%. A one-way between-groups analysis of variance (ANOVA) was used to compare the response of the sample between different types of dosimeters towards absorbed dose measurement of the thyroid in a phantom chest scan. Inspection of the skewness, kurtosis and Shapiro-Wilk statistics indicated that the assumption of normality was supported for each type of investigated dosimeter. There was no significant difference ($p = 0.992$) between the organ doses measured by all investigated dosimeters. The ANOVA table is attached in Appendix A3.

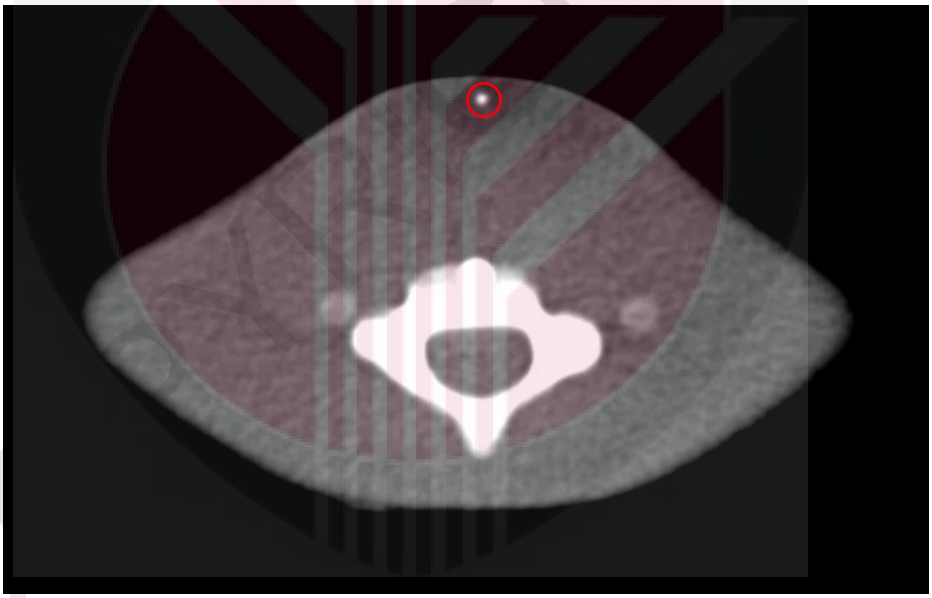

Figure 4.46: Placement of optical fibres (red circle) within thyroid dosimetry hole in slab 8 for thyroid organ dose measurement

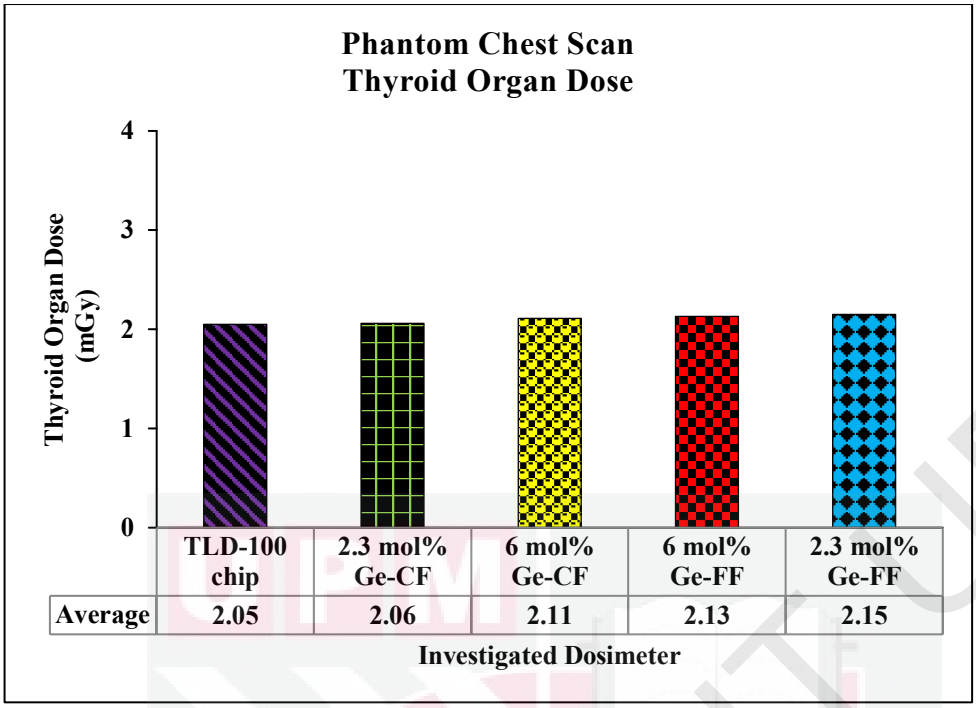

Figure 4.47: Thyroid organ dose on a phantom chest scan

Table 4.16: Percentage difference of fabricated optical fibre against TLD-100 for thyroid organ dose

Investigated Dosimeter	Percentage Difference Against TLD-100
2.3 mol% Ge-CF	0.49%
6 mol% Ge-CF	2.88%
6 mol% Ge-FF	3.83%
2.3 mol% Ge-FF	4.76%

A study by Giansante et al. (2019) evaluated organ doses for chest computed tomography procedures with TL dosimeters by using a 5-year-old pediatric anthropomorphic phantom and 120 kV exposure factor. Similar to the present study, TLD-100 chips were positioned inside the phantoms according to the thyroid distributions. Due to the usage of higher technical factors and larger phantom size, the thyroid organ dose was noticeably higher than the present study with a 4.05 mGy dose reading. Brady et al. (2011) employed TLDs to calculate the organ-absorbed doses for

a CT chest scan on an anthropomorphic phantom of a 10-year-old. The thyroid received the highest average absorbed radiation within the region of interest which was 10.9 mGy. A 5-year-old paediatric phantom was utilised in another investigation by Feng et al. (2010) to measure radiosensitive organs during thorax CT and an organ dose of around 3.40 mGy was recorded for the thyroid. These differences in organ doses can be related to differences in the type of scanner and scan parameters together with the differences in organ dose measurements between direct dosimetry verification on different age phantom.

4.7.2.3 Thyroid Entrance Skin Dose

Figure 4.48 shows the placement of optical fibre on the anterior surface of the thyroid dosimetry hole to represent entrance skin dose measurement during a chest scan as identified by the red circle while Figure 4.49 shows the bar chart to represent average thyroid entrance skin dose as measured by all investigated dosimeters during a phantom chest scan. It was also to be noted that nanoDot measurement was included as it was feasible to measure the dose for entrance skin measurement as compared to organ doses due to the limitation of the phantom with the absence of nanoDot dosimetry holes for organ dose measurements. The thyroid entrance skin dose recorded by both TLD-100 chip and 2.3 mol% Ge-CF was recorded as 2.18 mGy, followed by 2.19 mGy for both 6 mol% Ge-CF and nanoDot, 2.20 mGy for 6 mol% Ge-FF and 2.21 mGy for 2.3 mol% Ge-FF. Table 4.17 shows the percentage difference for each investigated dosimeter against gold standard TLD-100 chip with 2.3 mol% Ge-CF showing no difference and all other dosimeters except for 2.3 mol% Ge-FF showing a percentage difference of less than 1%. The largest difference recorded by 2.3 mol% Ge-FF showed a small percentage difference of 1.37%. A one-way between-

groups analysis of variance (ANOVA) was used to compare the response of the sample between different types of dosimeters towards entrance skin dose measurement of the thyroid in a phantom chest scan. Inspection of the skewness, kurtosis and Shapiro-Wilk statistics indicated that the assumption of normality was supported for each type of investigated dosimeter. There was no significant difference ($p = 1.000$) between the entrance skin doses measured by all investigated dosimeters. The ANOVA table is attached in Appendix A3.

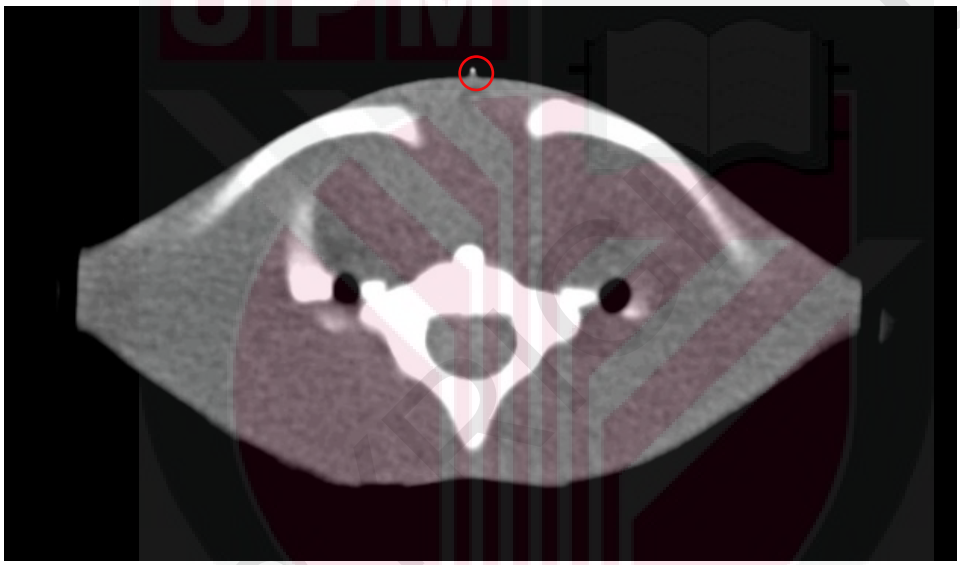

Figure 4.48: Placement of optical fibres (red circle) for the measurement of thyroid entrance skin dose

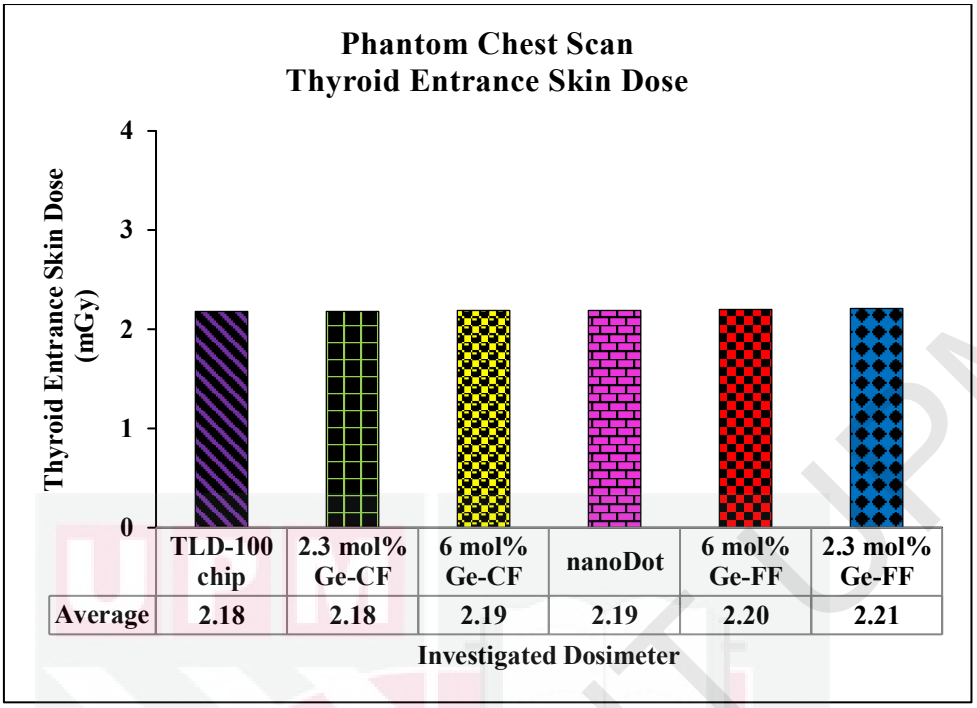

Figure 4.49: Thyroid entrance skin dose for phantom chest scan

Table 4.17: Percentage difference of investigated dosimeter against TLD-100 for thyroid entrance skin dose

Investigated Dosimeter	Percentage Difference Against TLD-100 (%)
2.3 mol% Ge-CF	0
6 mol% Ge-CF	0.46
nanoDot	0.46
6 mol% Ge-FF	0.91
2.3 mol% Ge-FF	1.37

Scanning paediatric patients is discovered to be challenging in a real clinical investigation due to various ethical issues. One study by Ramač et al. (2013) was able to assess and compare entrance skin doses by utilising the common CT methodology for adult thorax. The average thyroid dose, as determined by TLD-100 measurements on 60 participants, was found to be 4.68 mGy. Despite the many challenges of recruiting paediatric patients for dosimetry study, patient-specific dosimetry is still

essential for paediatric patients. A reliable dosimeter that offers an accurate and efficient way to evaluate skin dose is therefore required (Stathopoulos et al., 2016). One of the strongest metrics to distinguish individual radiation burden is the dose exposure on each superficial organ (Tian et al., 2014). Therefore, the surface dose is a good estimator for the thyroid dose in children.

4.8 Dosimetry Verification in Real Clinical Setting: CT Pulmonary Angiogram (CTPA)

Pulmonary embolism (PE) is a considerable cause of mortality. Computed tomography pulmonary angiography (CTPA) is the primary imaging modality for visualising the pulmonary arteries and diagnosing PE. However, the strong ionising radiation doses given off by CT raise the risk of mortality and the incidence of cancer induction. Few studies have addressed the radiation dose related to CTPA, in contrast to the extensively researched dosimetry studies of computed tomography coronary angiography (Heyer et al., 2007). The assessment of cancer risk based on an individual's effective dose can result in an underestimation for children of both genders by a factor of 1.5 to 4 and an overestimation for adult patients by a factor of 2.5 and 10, respectively. This is because radiation risks and sensitivities for different tissues vary with gender and age at exposure (Balonov & Shrimpton, 2012).

In the present study, children under two (2) years old who already consented to CTPA examinations that came to the Radiology Department, Hospital Serdang were approached to participate in this study, subject to their caregivers' approvals. A total of 15 patients who satisfied the inclusion criteria were able to be included in this dosimetry study between October 2021 and March 2022. Table 4.18 summarises the

gender, age, total DLP recorded from the dose report as shown in Figure 4.50 and anteroposterior (AP) and lateral thorax dimensions measured after the scan images were acquired as shown in one of the examples in Figure 4.51.

From Table 4.18, it can be summarised the patients were categorized into eight male and seven female patients. Per inclusion criteria, all patients were at or under two years of age with the youngest being 28 days old. The DLP range was recorded between 17 to 38 mGycm and AP and lateral thorax dimensions were in accordance with the patient's body habitus with some of the younger patients exhibiting bigger thorax dimensions than the older ones. In general, AP thorax dimension for paediatric patients under two years of age was recorded within the range of 7.07 cm to 13.35 cm while lateral thorax dimension was logged within the range of 9.98 cm to 18.90 cm.

Table 4.18: Summary of subjects included in clinical study

No	Gender	Age	Total DLP (mGycm)	AP Thorax Dimension (cm)	Lateral Thorax Dimension (cm)
1	Female	28 day	17	8.98	10.07
2	Male	1 month	18	9.04	10.81
3	Female	9 month	19	10.87	12.72
4	Female	5 month	19	8.69	11.25
5	Male	1 year	20	10.58	14.68
6	Male	6 week	21	7.07	9.98
7	Female	2 year	21	12.00	15.07
8	Male	3 month	25	10.48	13.48
9	Male	9 month	30	11.38	16.73
10	Female	4 month	31	11.55	16.89
11	Male	2 year	31	11.27	15.91
12	Male	11 month	33	9.16	12.02
13	Female	2 year	35	11.37	15.15
14	Female	2 year	36	12.69	18.25
15	Male	2 year	38	13.35	18.90

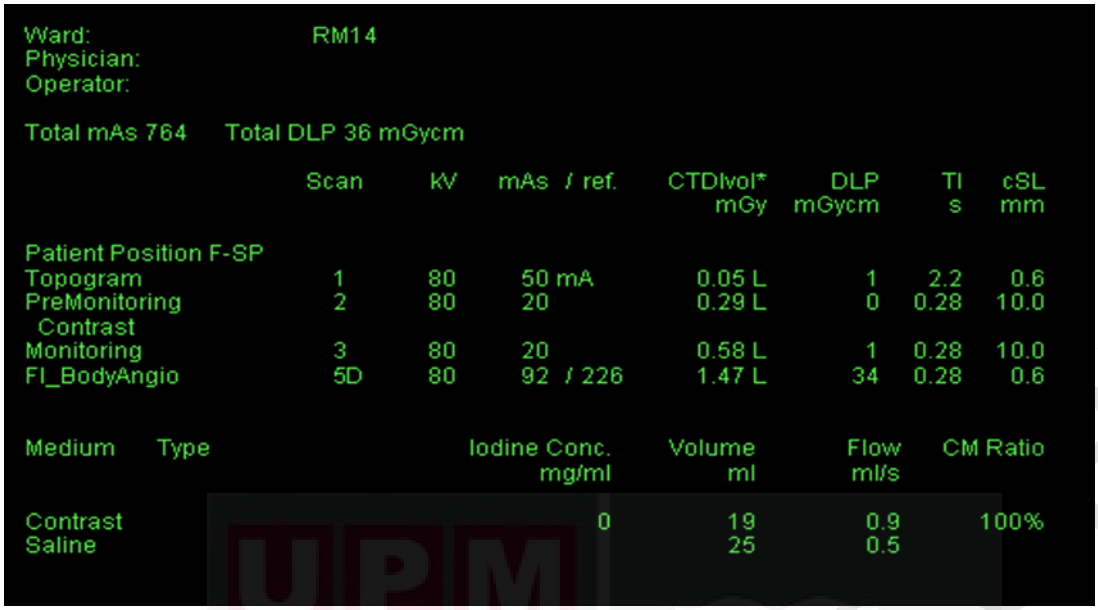

Ward: RM14
Physician:
Operator:

Total mAs 764 Total DLP 36 mGycm

	Scan	kV	mAs / ref.	CTDIvol* mGy	DLP mGycm	TI s	cSL mm
Patient Position F-SP							
Topogram	1	80	50 mA	0.05 L	1	2.2	0.6
PreMonitoring	2	80	20	0.29 L	0	0.28	10.0
Contrast Monitoring	3	80	20	0.58 L	1	0.28	10.0
FI_BodyAngio	5D	80	92 / 226	1.47 L	34	0.28	0.6

Medium	Type	Iodine Conc. mg/ml	Volume ml	Flow ml/s	CM Ratio
Contrast		0	19	0.9	100%
Saline			25	0.5	

Figure 4.50: Example of a dose report

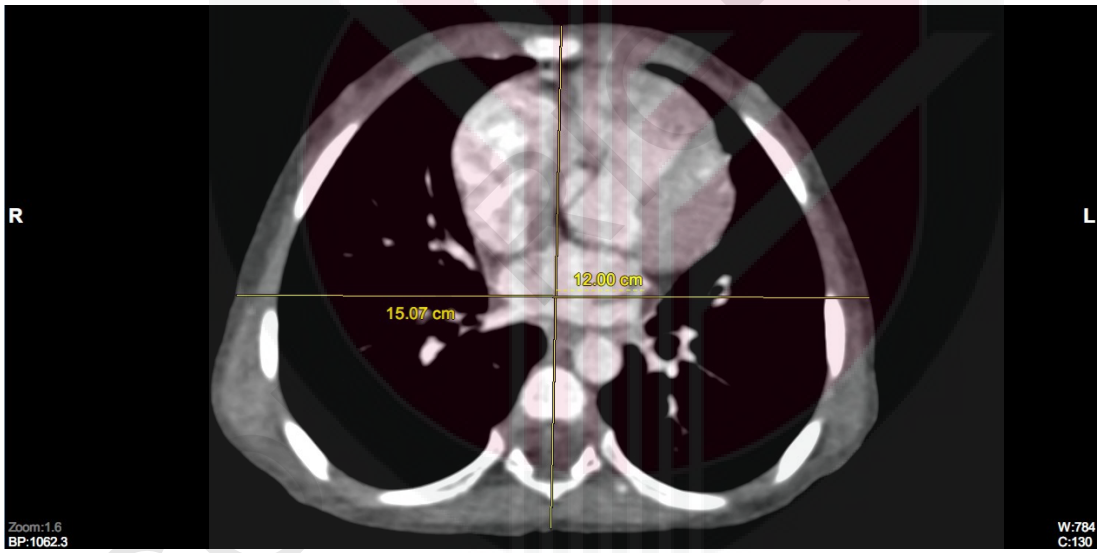

Figure 4.51: Anteroposterior (AP) and lateral thorax dimensions

Figure 4.52 shows the placement of the investigated dosimeters anterior to the thyroid region for the measurement of entrance skin dose during CTPA examination as identified by the red rectangle. It can be seen on the image as the high radio-opaque contrast of small dots representing the encapsulated optical fibres and TLD-100 chips and a lower density line adjacent to the dot representing the nanoDot OSLD. Figure

4.53 shows a contrast-enhanced (windowing) image to better visualize the investigated dosimeters within the capsules and the nanoDot OSLD during the measurement of thyroid entrance skin dose of CTPA examination as identified by the red rectangle.

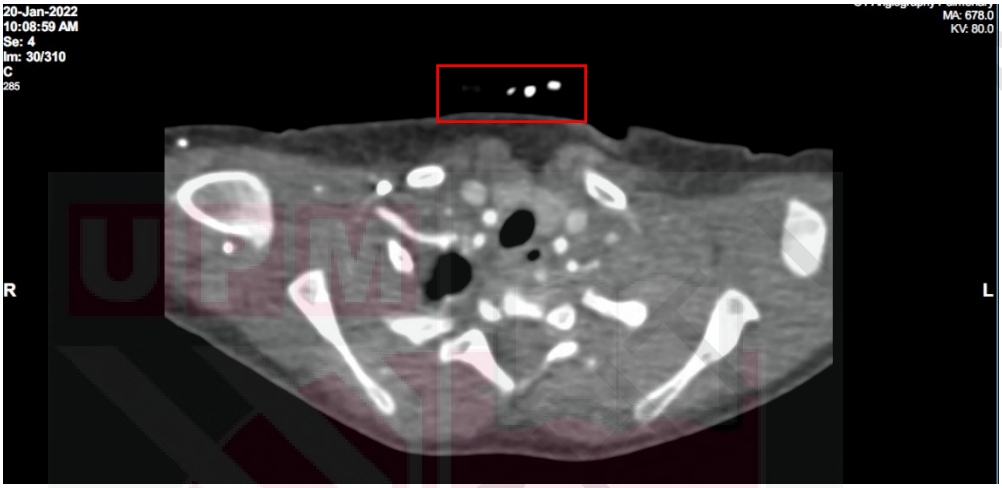

Figure 4.52: Placement of investigated dosimeters (red rectangle) anterior to the thyroid region for the measurement of entrance skin dose during CTPA examination

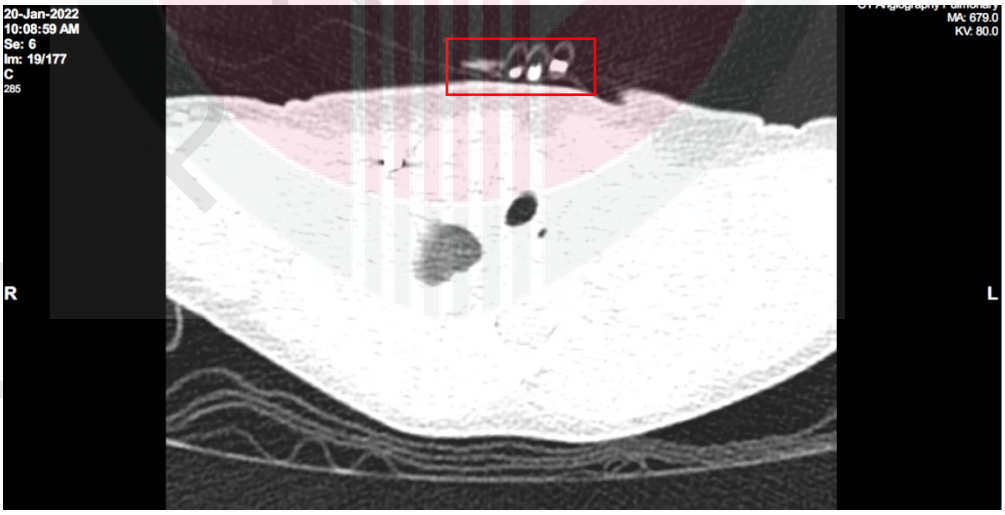

Figure 4.53: Contrast-enhanced image to better visualize the investigated dosimeters (red rectangle) for entrance skin dose measurement

Figure 4.54 shows the bar chart to represent the average thyroid entrance skin dose as measured by all investigated dosimeters during a CTPA examination. It has been shown that the higher the DLP value, the higher the dose received and measured on the patient. The dose range recorded by the TLD-100 chip across all patients was between 2.04 to 4.85 mGy while the range recorded by 2.3 mol% Ge-CF was 2.09 to 4.90 mGy, followed by 2.11 to 4.97 mGy for 6 mol% Ge-CF, 2.11 to 5.04 mGy for nanoDot, 2.12 to 5.07 mGy for 6 mol% Ge-FF and lastly 2.14 to 5.09 mGy for 2.3 mol% Ge-FF. Table 4.19 also shows the percentage difference for each investigated dosimeter against gold standard TLD-100 chip with all dosimeters showing a percentage difference of less than 5%. The smallest difference was recorded by 2.3 mol% Ge-CF ranging from 0.84% to 2.42% while 2.3 mol% Ge-FF recorded the largest percentage difference ranging from 4.58% to 4.95% against the TLD-100 chip. It is also to be noted that nanoDot OSLD recorded a range of 2.64% to 4.39% percentage difference when compared to the TLD-100 chip. For 6 mol% Ge-CF and Ge-FF, a percentage range of 2.12% to 3.37% and 3.01% to 4.63% was recorded respectively. In addition, a one-way between-group analysis of variance (ANOVA) was used to compare the response of the sample between all of these investigated dosimeters towards entrance skin dose measurement of the thyroid in the CTPA examination. Inspection of the skewness, kurtosis and Shapiro-Wilk statistics indicated that the assumption of normality was supported for each type of investigated dosimeter. Based on the statistical analysis, the findings suggest that there was no significant difference ($p > 0.05$) between the absorbed dose measured by all investigated dosimeters. Thus, the fabricated Ge-doped optical fibres have been shown to have great potential to be used as an alternative dosimeter in phantom dose measurement. The ANOVA table is attached in Appendix A4 – A8.

Limited information is available regarding the current practice of paediatric CTPA procedures in Malaysia. In one CTPA study by Karim et al. (2019), TLD chips were implanted into slabs of an adult phantom. The thyroid gland received the highest dose, 16.94 mGy, followed by the skin and breast, each receiving 12.95 mGy and 12.61 mGy. In another CTPA study by utilizing the ImpactDose programme, Karimizarchi and Chaparian (2017) calculated the organ doses for 152 adult patients with a mean age of 52. The dosage distributions in various-sized phantoms were simulated in accordance with the patient's age and compared to thermoluminescent dosimeter measurements. Organs that were directly exposed to radiation, such as the lung, received doses of 5.98 mGy, while the thyroid, which was in proximity to the scan range, received a dosage of 2.00 mGy.

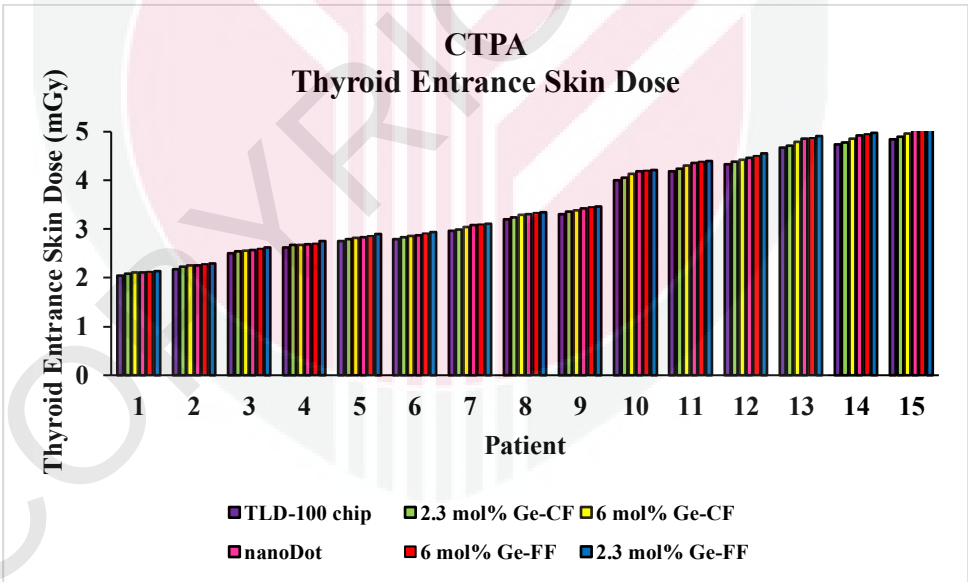

Figure 4.54: Thyroid entrance skin dose for patients undergoing CTPA

Table 4.19: Percentage difference for investigated dosimeter against TLD-100

Patient	TLD-100 chip (mGy)	2.3 mol% Ge-CF (mGy)	6 mol% Ge-CF (mGy)	nanoDot OSLD (mGy)	6 mol% Ge-FF (mGy)	2.3 mol% Ge-FF (mGy)	ANOVA
1	2.04	2.09	2.11	2.11	2.12	2.14	0.999
% diff	n/a	2.42	3.37	3.37	3.85	4.78	
2	2.18	2.23	2.25	2.26	2.28	2.29	0.999
% diff	n/a	2.27	3.16	3.60	4.48	4.92	
3	2.50	2.55	2.56	2.57	2.60	2.62	0.996
% diff	n/a	1.98	2.37	2.76	3.92	4.69	
4	2.62	2.67	2.68	2.69	2.70	2.75	0.995
% diff	n/a	1.89	2.26	2.64	3.01	4.84	
5	2.76	2.80	2.82	2.84	2.86	2.90	0.999
% diff	n/a	1.44	2.15	2.86	3.56	4.95	
6	2.80	2.84	2.86	2.88	2.91	2.94	0.999
% diff	n/a	1.42	2.12	2.82	3.85	4.88	
7	2.96	2.99	3.04	3.09	3.10	3.11	0.991
% diff	n/a	1.01	2.67	4.30	4.62	4.94	
8	3.20	3.24	3.30	3.31	3.33	3.35	0.693
% diff	n/a	1.24	3.08	3.38	3.98	4.58	
9	3.31	3.36	3.39	3.42	3.45	3.47	0.960
% diff	n/a	1.50	2.39	3.27	4.14	4.72	
10	4.01	4.06	4.13	4.19	4.20	4.21	0.963
% diff	n/a	1.24	2.95	4.39	4.63	4.87	
11	4.19	4.24	4.30	4.36	4.38	4.40	0.969
% diff	n/a	1.19	2.59	3.98	4.43	4.89	
12	4.33	4.38	4.43	4.47	4.50	4.55	0.871
% diff	n/a	1.15	2.28	3.18	3.85	4.95	
13	4.68	4.72	4.79	4.86	4.87	4.91	0.932
% diff	n/a	0.85	2.32	3.77	3.98	4.80	
14	4.74	4.78	4.86	4.93	4.95	4.98	0.777
% diff	n/a	0.84	2.50	3.93	4.33	4.94	
15	4.85	4.90	4.97	5.04	5.07	5.09	0.987
% diff	n/a	1.03	2.44	3.84	4.44	4.83	

NA: Not applicable

4.9 Uncertainty Analysis

In this section, the measurement errors of the average reading of the dosimeters, calibration coefficient, individual correction factor, beam quality and fading analysis are discussed, followed by the combined and expanded uncertainties at the end of this chapter.

4.9.1 Uncertainty of an Average Reading

The uncertainty of the average reading of the dosimeters was determined by analysing TL and element count signals from all capsules of screened fabricated Ge-optical fibres and TLD-100 chips together with the individual OSLD nanoDots. The histograms in Figure 4.55 to 4.60 revealed the number of capsules used during screening against the relative TL responses of 6.0 mol% Ge-doped FF, 2.3 mol% Ge-doped FF, 2.3 mol% Ge-doped CF and 6.0 mol% Ge-doped CF, TLD-100 chips and OSLD nanoDot. 230 to 240 optical fibres were grouped into 23 to 24 capsules, with 10 fibres per capsule. The average TL response for the whole fibre batch was calculated and the reference capsule with the closest TL response to the mean reading was selected. Average background radiation in the clinical setting for this study was measured between 2.3 to 2.5 nC. Relative TL response or mean distribution, therefore, was the dose received for each capsule divided by the dose received from the reference capsule (D_i^{th}/D_{ref}). The distribution of the mean was 1.01 for 6.0 mol% Ge-doped FF, 2.3 mol% Ge-CF, and 6.0 mol% Ge-doped CF respectively while 2.3 mol% Ge-FF demonstrated a mean distribution of 1.02. With the exception of 6.0 mol% Ge-CF which showed a 0.10 standard deviation, all fabricated optical fibres demonstrated a similar 0.12 standard deviation.

For TLD-100, 99 chips were used and grouped into three chips per capsule, accumulating 33 capsules to represent the whole batch, while 49 nanoDots OSLD were used to represent individual nanoDots. Each nanoDot was read five times to get an average individual reading. The distribution of the means for TLD-100 chips and nanoDots OSLD were recorded as 1.01 and 1.00, with a standard deviation of 0.11 and 0.03 respectively. These findings were observed to provide good agreement with

the given dose as the mean TL response was relatively 1.00, showing a recorded dose close to the reference value. These findings also supported the homogeneity of fabricated Ge-doped optical fibres and the other dosimeters based on a 95% confidence level of sensitivity. Hence, all capsules and nanoDots were able to be used in subsequent phantom and clinical measurements. Finally, the type A uncertainty for the mean TL reading ($u(R_i)$) calculated from Equation 3.18 for the investigated dosimeters was found to be 0.16% for 6.0 mol% Ge-doped FF, 2.3 mol% Ge-doped FF and 2.3 mol% Ge-doped CF, while 6.0 mol% Ge-doped CF recorded an uncertainty of 0.14% respectively. The uncertainties 0.19% and 0.03% were calculated for TLD-100 chips and nanoDot OSLD showed the highest and lowest values of the average reading uncertainties when all the investigated dosimeters were compared. In other words, this value of uncertainty generated from the newly fabricated optical fibres was found to be within the range of uncertainty produced by reference dosimeters of TLD-100 chips and nanoDot OSLD which were deemed acceptable. Table 4.20 summarises the mean distribution, standard deviation and type A uncertainty for all investigated dosimeters.

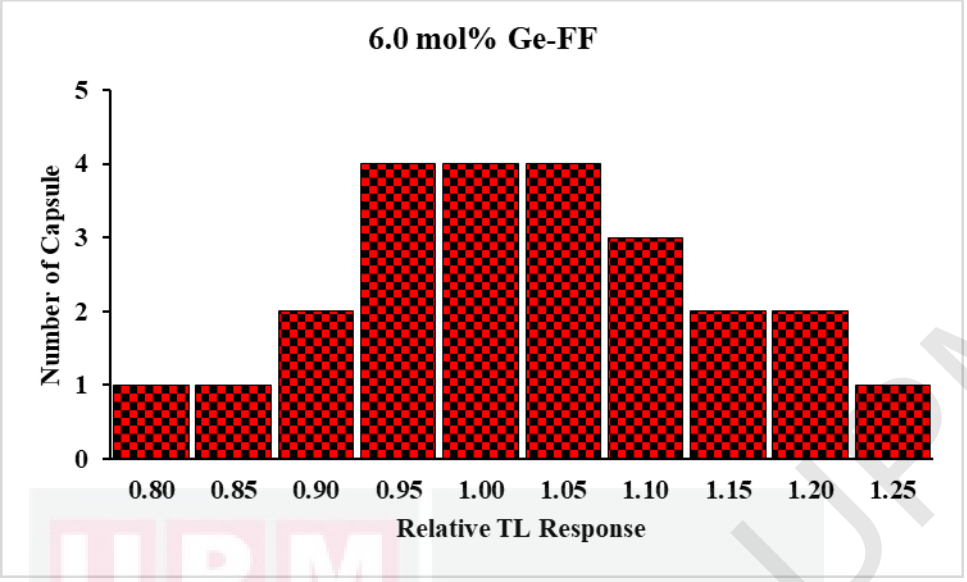

Figure 4.55: Frequency distribution of the relative TL response for 6.0 mol% Ge-FF

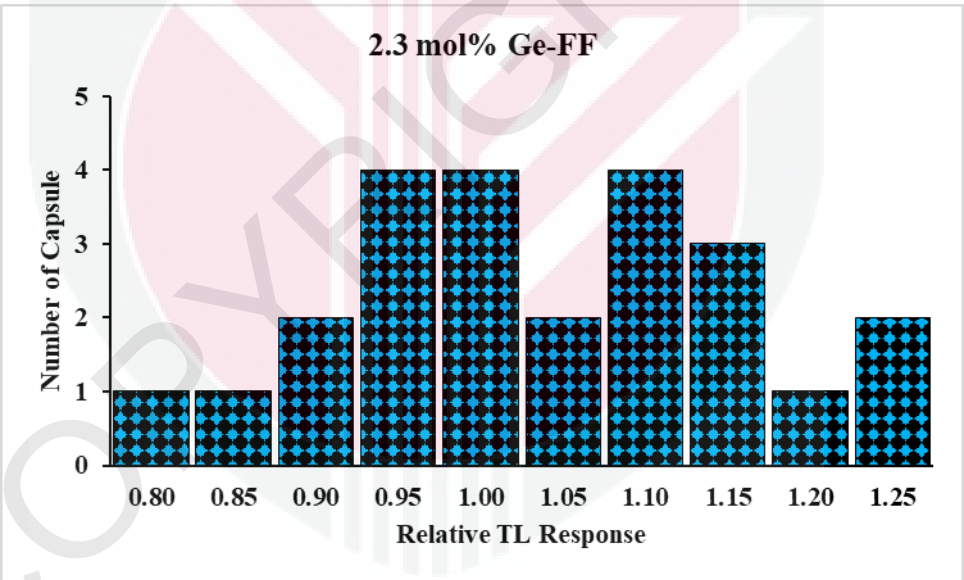

Figure 4.56: Frequency distribution of the relative TL response for 2.3 mol% Ge-FF

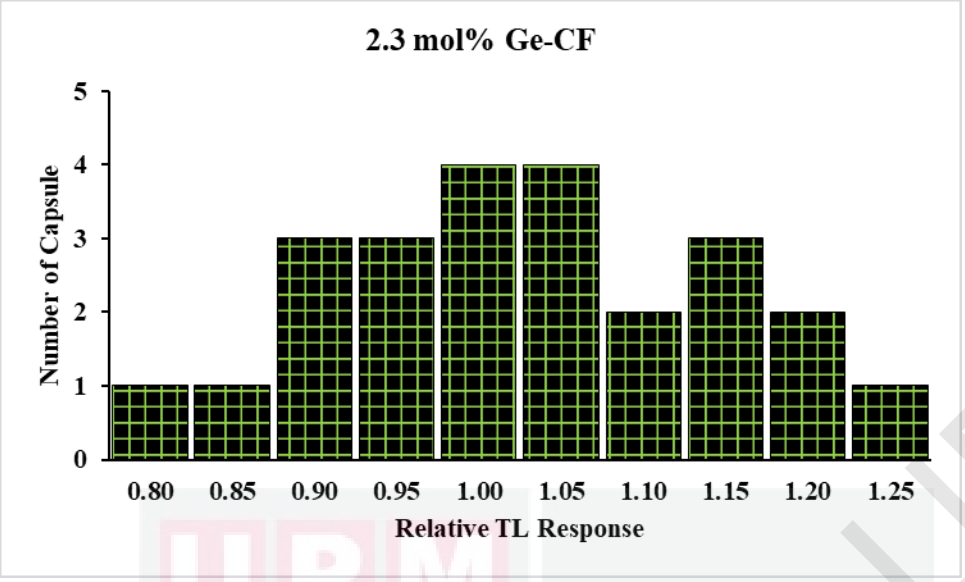

Figure 4.57: Frequency distribution of the relative TL response for 2.3 mol% Ge-CF

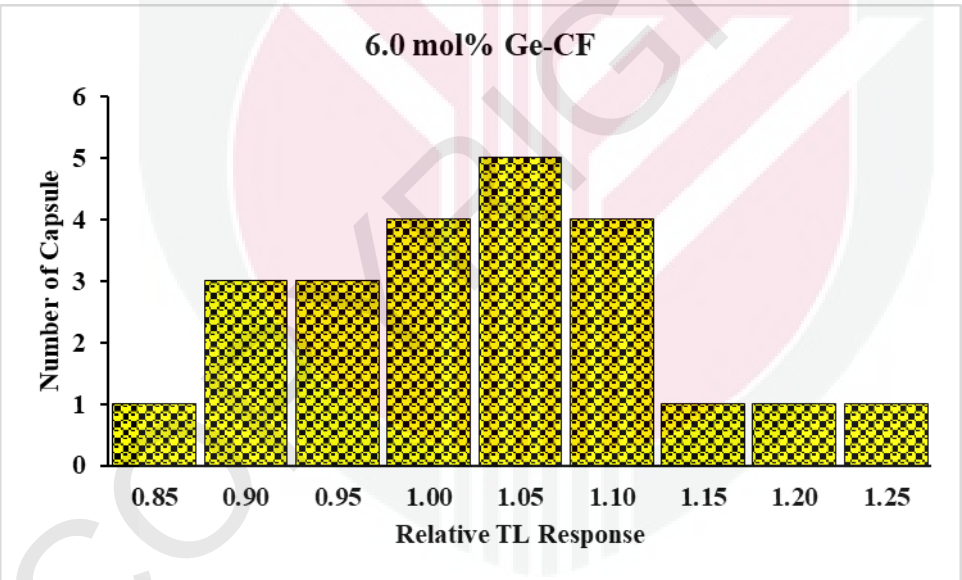

Figure 4.58: Frequency distribution of the relative TL response for 6.0 mol% Ge-CF

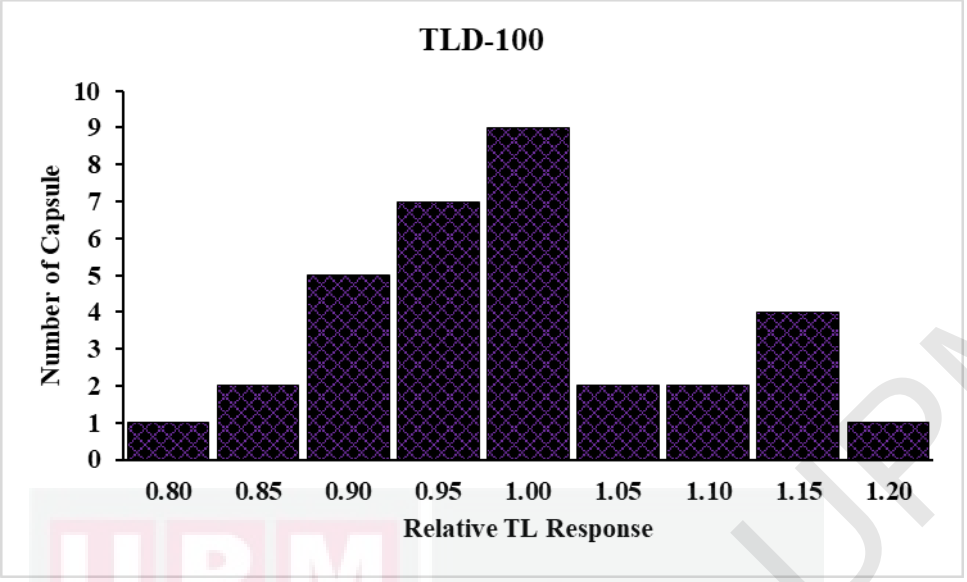

Figure 4.59: Frequency distribution of the relative TL response for TLD-100 chips

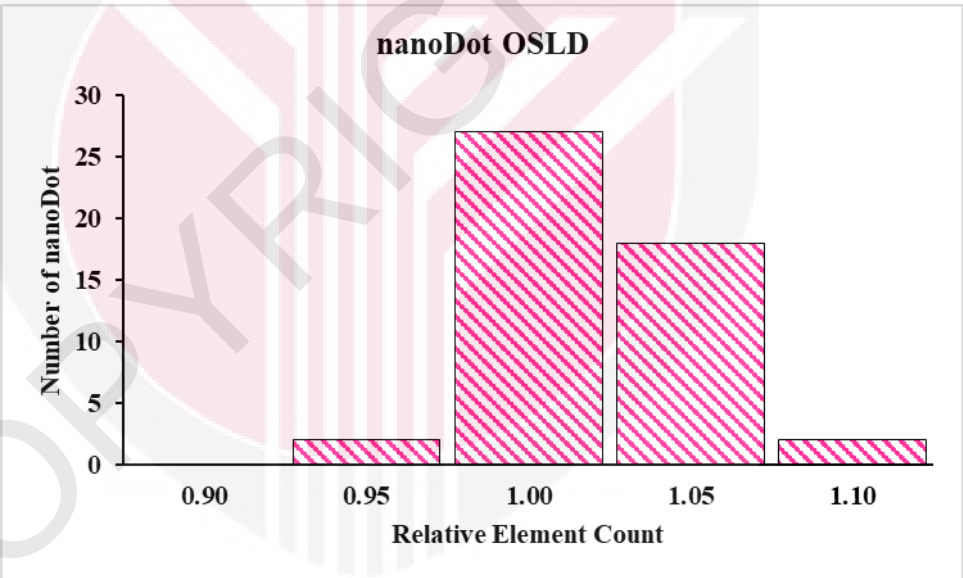

Figure 4.60: Frequency distribution of the relative element count for nanoDot OSLD

Table 4.20: Uncertainty of average reading for all dosimeters, $u(R_i)$

Dosimeter	Mean Distribution	Standard Deviation	Type A Uncertainty
6.0 mol% Ge-FF	1.01	0.12	0.16%
2.3 mol% Ge-FF	1.02	0.12	0.16%
2.3 mol% Ge-CF	1.01	0.12	0.16%
6.0 mol% Ge-CF	1.01	0.10	0.14%
TLD-100 chip	1.01	0.11	0.19%
nanoDot OSLD	1.00	0.03	0.03%

4.9.2 Uncertainty of the Calibration Coefficient

The uncertainty of the calibration coefficient of fabricated Ge-doped optical fibres, TLD-100 chips and nanoDots was contributed by several factors, including uncertainty in the readings of optical fibres and TLD-100 chips within a capsule or repeated readings per nanoDot $u(R_i)$ and uncertainty during the determination of absorbed dose by the ionization chamber $u(D_{IC})$ as shown in Equation 3.19. These uncertainties were accounted for in the combined uncertainty of absorbed dose measurement by all investigated dosimeters.

The uncertainty from the mean reading of fabricated Ge-doped optical fibres, TLD-100 chips and nanoDots was explained in detail in subsection 3.13.1. The expanded uncertainty of the calibration coefficient (CF) in terms of air kerma (N_k) for the ionisation chamber stated in the calibration certificate issued by the SSDL is 1.30%, with a coverage factor of k = 2 to provide a 95% confidence level. This is considered a Type B uncertainty as the data is extracted from the calibration report. For a coverage factor of k = 1, the uncertainty for the calibration coefficient for the ionisation chamber is 0.65%. Type A uncertainty for calibration coefficient N_k is not usually done by the end-user and therefore is not calculated. For type A uncertainty for mean reading from

the ionisation chamber and barometer for temperature and pressure, it is found to be 0.24%, 0.35% and 0.007% respectively.

Meanwhile, the evaluations of Type B uncertainties related to the ionisation chamber and barometer for temperature and pressure are based on the information given by the manufacturer's specifications and general properties of the instrument, particularly the resolution. During the measurement of temperature in the calibration process of the fabricated Ge-doped optical fibres, TLD-100 chips and nanoDots, the resolution of the barometer for temperature is denoted as 0.1ºC with the reference temperature of 20ºC. Meanwhile, the resolution of the barometer for pressure is recorded as 0.1 hPa with a reference pressure of 1013.25 hPa. By assuming a rectangular distribution, the combined uncertainty that arose from a type B component of measured temperature and pressure by the barometer was 0.14%.

The combined uncertainty in the 6.0 mol% Ge-doped FF, 2.3 mol% Ge-doped FF, 2.3 mol% Ge-doped CF, 6.0 mol% Ge-doped CF, TLD-100 chips and OSLD nanoDot was determined at 0.87%, 0.87%, 0.87%, 0.86%, 0.88% and 0.84% respectively. Overall components involved in the determination of uncertainty in the calibration coefficient of the investigated dosimeters are presented in detail in Table 4.21.

Table 4.21: Summary of combined individual uncertainties in the calibration coefficient factor of all dosimeters

Quantity	Type A (%)	Type B (%)	Combine A & B (%)
Uncertainty of dose given by ionisation chamber $u(D_{IC})$			
Mean reading $u(M_{RAW})$	0.24		0.24
Calibration coefficient $u(N_K)$		0.65	0.65
Temperature $u(K_T)$	0.35	0.14	0.37
Pressure $u(K_P)$	0.007	0.14	0.03
Total	0.36	0.69	0.84
Uncertainty of dosimeter reading reproducibility $u(R_i)$			
6 mol% Ge-FF $u(R_{6FF})$	0.16		0.16
2.3 mol% Ge-FF $u(R_{2.3FF})$	0.16		0.16
2.3 mol% Ge-CF $u(R_{2.3CF})$	0.16		0.16
6 mol% Ge-CF $u(R_{6CF})$	0.14		0.14
TLD-100 Chip $u(R_{TLD})$	0.19		0.19
nanoDot OSLD $u(R_{OSL})$	0.03		0.03
The total uncertainty of calibration coefficient factor in dosimeter $u(N_i)$			
6 mol% Ge-FF $u(N_{6FF})$			0.87
2.3 mol% Ge-FF $u(N_{2.3FF})$			0.87
2.3 mol% Ge-CF $u(N_{2.3CF})$			0.87
6 mol% Ge-CF $u(N_{6CF})$			0.86
TLD-100 Chip $u(N_{TLD})$			0.88
nanoDot OSLD $u(N_{OSL})$			0.84

4.9.3 Uncertainty in an Individual Correction Factor

Uncertainty in the individual correction factors was determined by plotting the histogram of the relative standard deviation of the individual capsule correction factors for 6 mol% Ge-FF, 2.3 mol% Ge-FF, 2.3 mol% Ge-CF, 6 mol% Ge-CF, TLD-100 chips and individual OSLD nanoDot respectively as shown in Figures 4.61 to 4.66. Uncertainty in this correction factor was a major contribution to the combined uncertainty in the determination of dose from the investigated dosimeters as referred to in Equation 3.20. The mean of the relative standard deviation of the histogram, together with the maximum and minimum values for all dosimeters were summarised in Table 4.22.

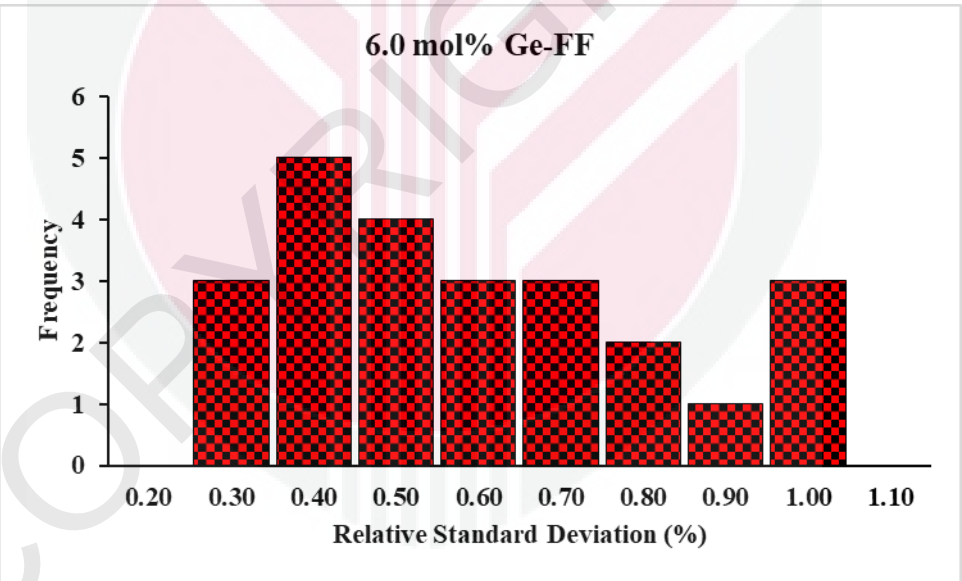

Figure 4.61: Frequency distribution of the relative standard deviation of individual correction factors of 6.0 mol% Ge-FF

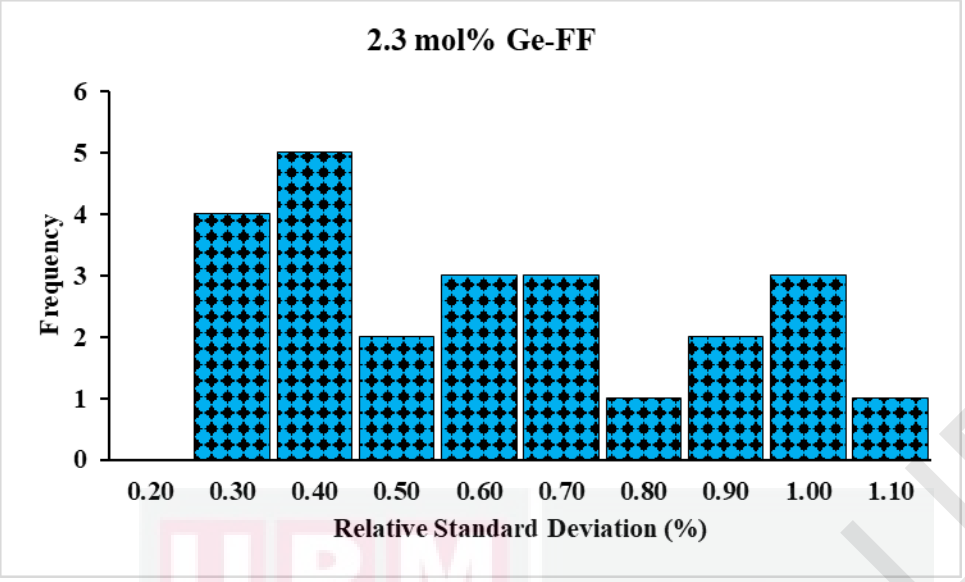

Figure 4.62: Frequency distribution of the relative standard deviation of individual correction factors of 2.3 mol% Ge-FF

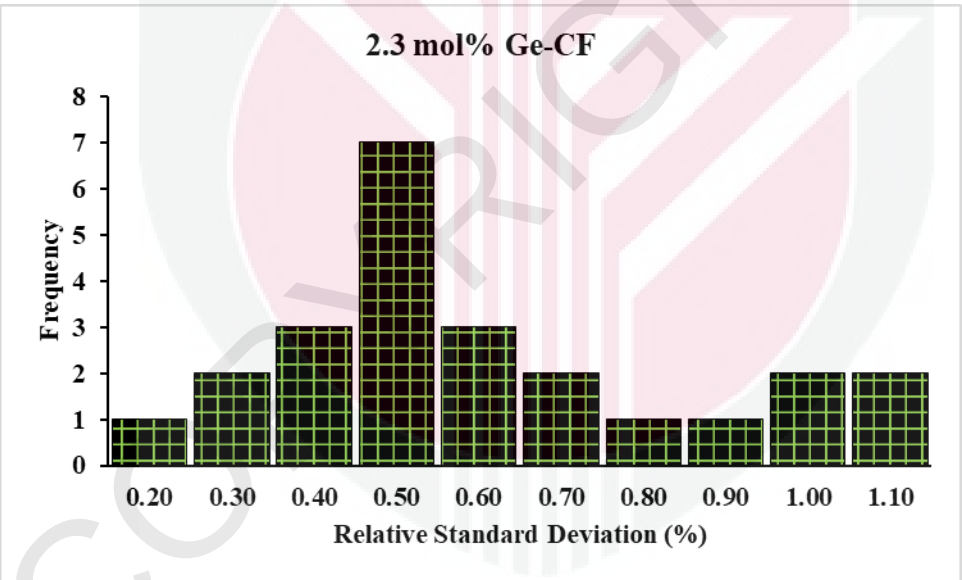

Figure 4.63: Frequency distribution of the relative standard deviation of individual correction factors 2.3 mol% Ge-CF

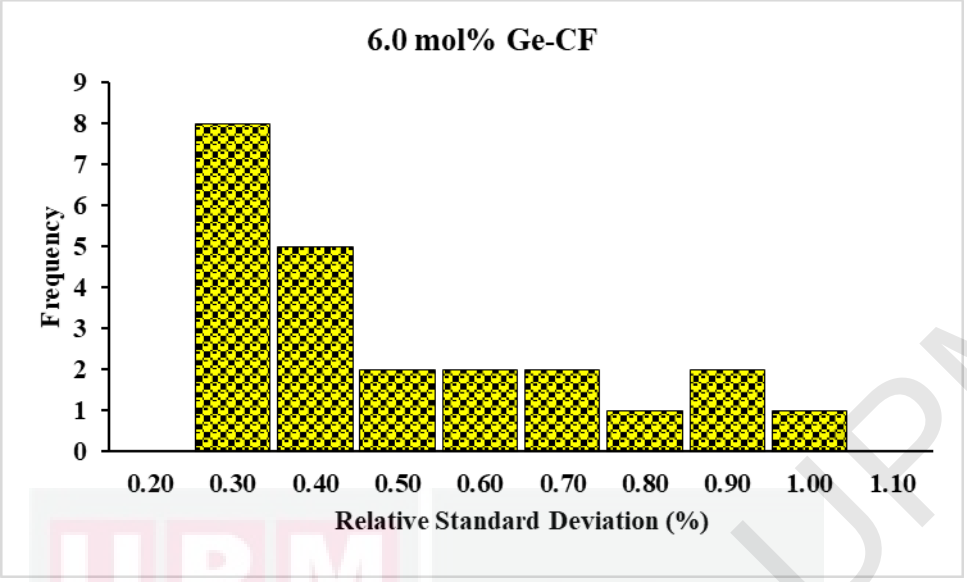

Figure 4.64: Frequency distribution of the relative standard deviation of individual correction factors of 6.0 mol% Ge-CF

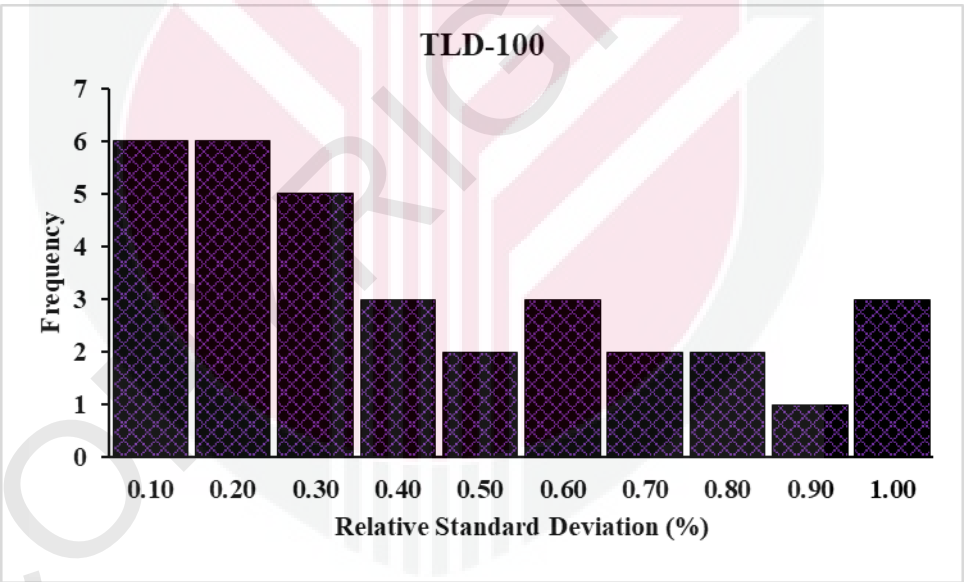

Figure 4.65: Frequency distribution of the relative standard deviation of individual correction factors of TLD-100 chips

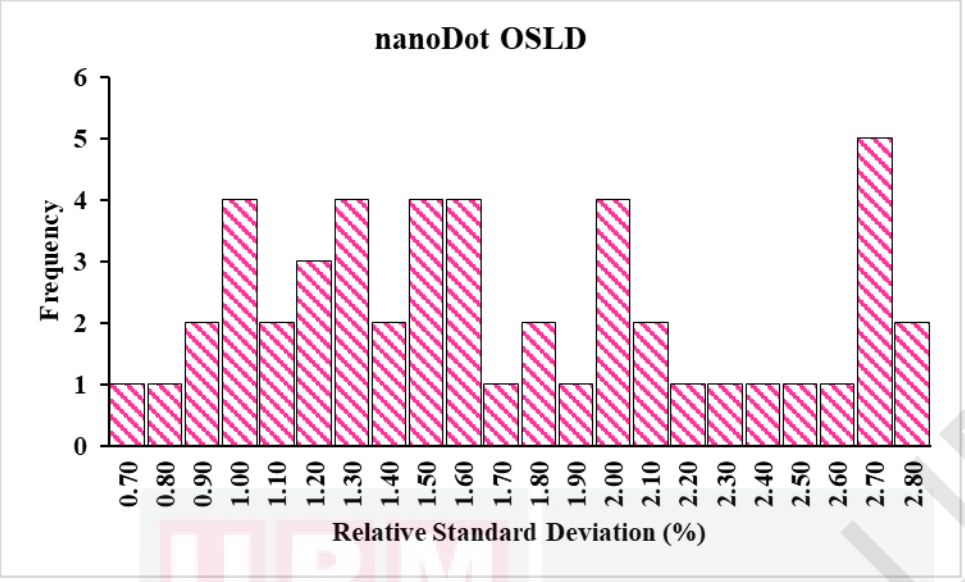

Figure 4.66: Frequency distribution of the relative standard deviation of individual correction factors of nanoDot OSLD

Table 4.22: Relative standard deviation value based on the histogram

Dosimeter	Minimum Value	Maximum Value	Mean of Relative Standard Deviation
6.0 mol% Ge-FF	0.28%	1.05%	0.59%
2.3 mol% Ge-FF	0.26%	1.07%	0.62%
2.3 mol% Ge-CF	0.23%	1.12%	0.61%
6.0 mol% Ge-CF	0.27%	1.02%	0.51%
TLD-100 chip	0.05%	1.04%	0.42%
nanoDot OSLD	0.72%	2.83%	1.72%

4.9.4 Uncertainty of the Beam Quality

A linear fitting function for the energy or beam quality correction factor was illustrated in Figure 4.67. According to Equation 3.21, the calculated uncertainty for 6.0 mol% Ge-FF, 2.3 mol% Ge-FF, 2.3 mol% Ge-CF, 6.0 mol% Ge-CF, TLD-100 chip and nanoDot was 2.8%, 1.5%, 0.5%, 0.3%. 0.3% and 1.2% respectively. The response of each beam quality of RQT 8 (100 kV), RQT 9 (120 kV) and RQT 10 (150 kV) was normalised to the response for RQT 8 beam quality as it was used in the phantom

study. The equations of a straight line for each dosimeter were generated in order to calculate the energy correction factor for 80 kV used in clinical study as shown in Table 4.23.

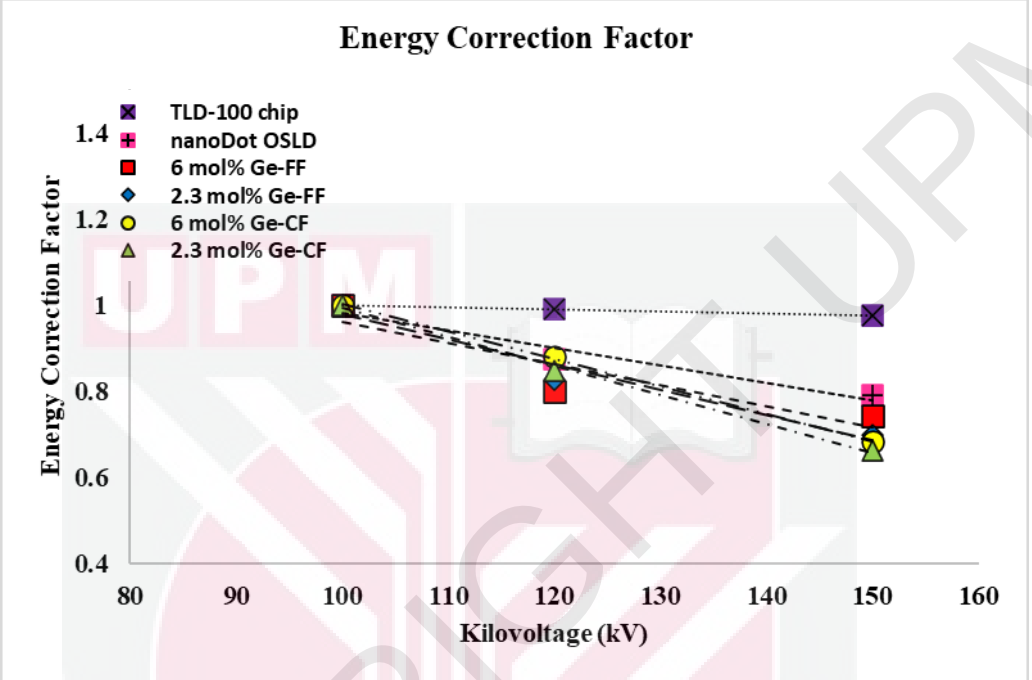

Figure 4.67: Linear fit to energy correction factor for investigated dosimeters

Table 4.23: Equation of straight line and energy correction factor at 80 kV for investigated dosimeter

Dosimeter	Equation of Straight Line	Energy Correction Factor at 80 kV
TLD-100 chip	y = -0.0005x + 1.0453	1.00
nanoDot OSLD	y = -0.0041x + 1.3919	1.06
6.0 mol% Ge-FF	y = -0.0049x + 1.4524	1.06
2.3 mol% Ge-FF	y = -0.0059x + 1.5674	1.10
2.3 mol% Ge-CF	y = -0.0067x + 1.6649	1.11
6.0 mol% Ge-CF	y = -0.0064x +1.6391	1.13

4.9.5 Uncertainty in the Fading Correction Factor

Figure 4.68 demonstrated the single exponential decay fading functions for 6.0 mol% Ge-FF, 2.3 mol% Ge-FF, 2.3 mol% Ge-CF, 6.0 mol% Ge-CF, TLD-100 chip and nanoDot OSLD. The equations for the nonlinear fitting function of the graph are demonstrated in Table 4.24. The values for $u(yo)$, $u(d)$and $u(k)$ as shown in Table 4.25 were the uncertainties in the coefficient yo, d and k obtained from nonlinear regression analysis which were extracted from the analysis using GraphPad Prism software. The uncertainties due to signal loss for all dosimeters were subsequently determined using Equation 3.22.

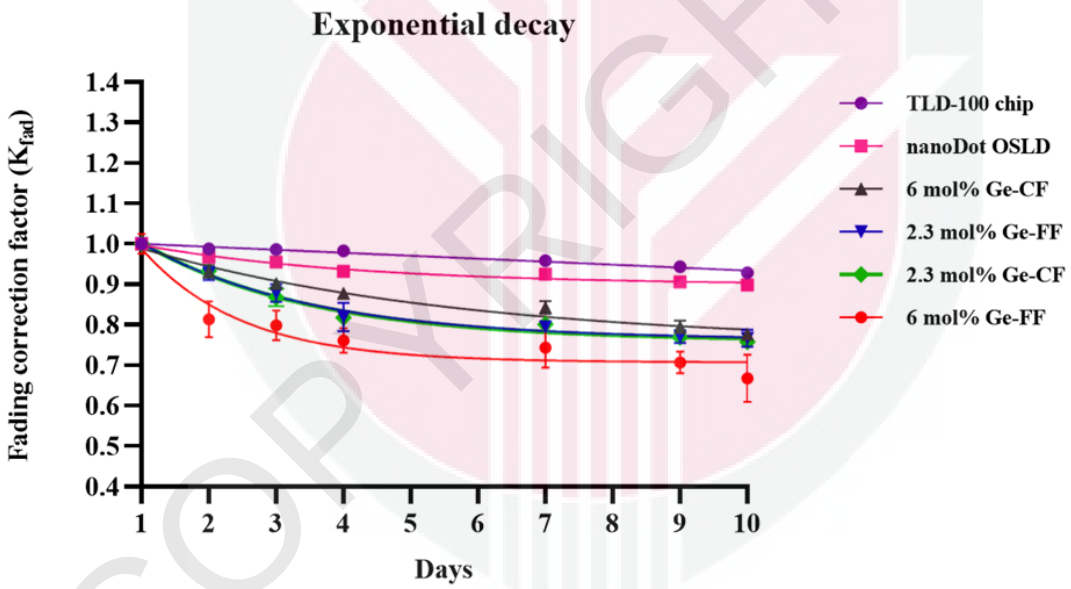

Figure 4.68: Exponential decay for all investigated dosimeters up to 10 days post-irradiation

Table 4.24: Equation for nonlinear fitting function

Dosimeter	Equation of Single Exponential Decay Fit
TLD-100 chip	$y = 0.109e^{-0.2433x} + 0.899$
nanoDot OSLD	$y = 0.135e^{-0.3090x} + 0.899$
6 mol% Ge-CF	$y = 0.292e^{-0.2074x} + 0.752$
2.3 mol% Ge-FF	$y = 0.356e^{-0.3973x} + 0.763$
2.3 mol% Ge-CF	$y = 0.363e^{-0.3998x} + 0.760$
6 mol% Ge-FF	$y = 0.553e^{-0.6746x} + 0.707$

Table 4.25: Fading uncertainties for all investigated dosimeters

Coefficient Uncertainty	TLD-100 chip	nanoDot OSLD	6 mol% Ge-CF	2.3 mol% Ge-FF	2.3 mol% Ge-CF	6 mol% Ge-FF
$u(y_o)$	0.006	0.016	0.029	0.027	0.036	0.146
u(d)	0.009	0.009	0.039	0.009	0.013	0.021
u(k)	0.068	0.086	0.078	0.053	0.071	0.209
Fading Uncertainty $u(K_{FAD})$	0.01	0.01	0.06	0.03	0.04	0.13

4.9.6 Combined and Expanded Uncertainty

The total uncertainties for all investigated dosimeters are summarised in Tables 4.26 to 4.31 respectively. The combined uncertainty in the determination of absorbed dose by 6 mol% Ge-FF, 2.3 mol% Ge-FF, 2.3 mol% Ge-CF, 6 mol% Ge-CF, TLD-100 chip and OSLD nanoDot was found at 2.96%, 1.83%, 1.19%, 0.64%. 1.48% and 2.27% respectively based on Equation 3.23. The major contributor to combined uncertainty in fabricated Ge-doped optical fibre systems was the uncertainty of individual capsules and beam quality correction factors. The finding on this combined uncertainty especially in fabricated Ge-doped optical fibres was mainly affected by the screening process which was conducted to separate and group the fabricated Ge-doped optical fibres into three different TL signal sensitivity without segregating the outliers that

showed variation less or more than 5%. This approach was taken due to the limited amount of fabricated Ge-doped optical fibres produced to fulfil the need for this research. Finally, the expanded uncertainties were 5.92%, 3.67%, 2.38%, 1.27%. 2.97% and 4.54% for 6 mol% Ge-FF, 2.3 mol% Ge-FF, 2.3 mol% Ge-CF, 6 mol% Ge-CF, TLD-100 chip and OSLD nanoDot respectively after multiplication by a coverage factor k = 2 as shown in Equation 3.24. This uncertainty provided a level of confidence of approximately 95%.

Table 4.26: Combined and expanded uncertainties for measurement of absorbed dose using 6 mol% Ge-FF

Uncertainties	Type A (%)	Type B (%)	Combined A, B (%)
Reading, $u(R_{6FF})$	0.16		0.16
Calibration Coefficient, $u(N_{6FF})$	0.39	0.69	0.87
Individual Correction, $u(K_{6FF})$	0.59		0.59
Beam Quality Correction, $u(K_{RQT8})$	2.76		2.76
Fading Correction, $u(K_{FAD})$	0.13		0.13
Combined Uncertainty, $U_C(D_{6FF})$			2.96
Expanded Uncertainty, $U_P(D_{6FF})$			5.92

Table 4.27: Combined and expanded uncertainties for measurement of absorbed dose using 2.3 mol% Ge-FF

Uncertainties	Type A (%)	Type B (%)	Combined A, B (%)
Reading, $u(R_{2.3FF})$	0.16		0.16
Calibration Coefficient, $u(N_{2.3FF})$	0.39	0.69	0.87
Individual Correction, $u(K_{2.3FF})$	0.62		0.62
Beam Quality Correction, $u(K_{RQT8})$	1.48		1.48
Fading Correction, $u(K_{FAD})$	0.03		0.03
Combined Uncertainty, $U_C(D_{2.3FF})$			1.83
Expanded Uncertainty, $U_P(D_{2.3FF})$			3.67

Table 4.28: Combined and expanded uncertainties for measurement of absorbed dose using 2.3 mol% Ge-CF

Uncertainties	Type A (%)	Type B (%)	Combined A, B (%)
Reading, $u(R_{2.3CF})$	0.16		0.16
Calibration Coefficient, $u(N_{2.3CF})$	0.39	0.69	0.87
Individual Correction, $u(K_{2.3CF})$	0.61		0.61
Beam Quality Correction, $u(K_{RQT8})$	0.51		0.51
Fading Correction, $u(K_{FAD})$	0.04		0.04
Combined Uncertainty, $U_C(D_{2.3CF})$			1.19
Expanded Uncertainty, $U_P(D_{2.3CF})$			2.38

Table 4.29: Combined and expanded uncertainties for measurement of absorbed dose using 6 mol% Ge-CF

Uncertainties	Type A (%)	Type B (%)	Combined A, B (%)
Reading, $u(R_{6CF})$	0.14		0.14
Calibration Coefficient, $u(N_{6CF})$	0.38	0.69	0.14
Individual Correction, $u(K_{6CF})$	0.51		0.51
Beam Quality Correction, $u(K_{RQT8})$	0.32		0.32
Fading Correction, $u(K_{FAD})$	0.06		0.06
Combined Uncertainty, $U_C(D_{6CF})$			0.64
Expanded Uncertainty, $U_P(D_{6CF})$			1.27

Table 4.30: Combined and expanded uncertainties for measurement of absorbed dose using TLD-100 chip

Uncertainties	Type A (%)	Type B (%)	Combined A, B (%)
Reading, $u(R_{TLD})$	0.19		0.19
Calibration Coefficient, $u(N_{TLD})$	0.40	0.69	0.88
Individual Correction, $u(K_{TLD})$	0.42		0.42
Beam Quality Correction, $u(K_{RQT8})$	0.33		0.33
Fading Correction, $u(K_{FAD})$	0.01		1.05
Combined Uncertainty, $U_C(D_{TLD})$			1.48
Expanded Uncertainty, $U_P(D_{TLD})$			2.97

Table 4.31: Combined and expanded uncertainties for measurement of absorbed dose using OSLD nanoDot

Uncertainties	Type A (%)	Type B (%)	Combined A, B (%)
Reading, $u(R_{OSL})$	0.03		0.03
Calibration Coefficient, $u(N_{OSL})$	0.36	0.69	0.84
Individual Correction, $u(K_{OSL})$	1.72		1.72
Beam Quality Correction, $u(K_{RQT8})$	1.22		1.22
Fading Correction, $u(K_{FAD})$	0.01		0.01
Combined Uncertainty, $U_C(D_{OSL})$			2.27
Expanded Uncertainty, $U_P(D_{OSL})$			4.54

CHAPTER 5

CONCLUSION, LIMITATIONS AND RECOMMENDATIONS

5.1 Conclusion

A detailed investigation of the basic dosimetric characteristics of fabricated Ge-doped optical fibres found that 2.3 mol% Ge-FF, 6 mol% Ge-FF, 6 mol% Ge-CF, and 2.3 mol% Ge-CF satisfy numerous TL characteristics such as dose linearity, RQT beam quality, dose reproducibility, dose sensitivity, minimum detectable dose, and fading.

For the first specific objective, the TL signals of all fibres are found to be linear for doses ranging from 2 to 40 mGy for all RQT beam quality of 100 kV (RQT 8), 120 kV (RQT 9), and 150 kV (RQT 10). Also apparent is that the TL responses per unit volumes are superior for the fibres compared to the TLD-100 chip. However, in the RQT beam quality study, it can be seen that the signal response decreased as the energy increased from 100 kV to 150 kV. The energy response trends for all dosimeters show clear photoelectric dependence, decreasing with an increase in kV. While favourable in terms of sensitivity compared to TLD-100 chips, the use of the fibres for CT dose assessments would require the appropriate response corrections to be built into the evaluations. The fabricated optical fibres also have demonstrated reproducibility of better than 4% of the mean, surpassing the performance of the TLD-100 chip while OSLD nanoDots possessed the lowest CV. In terms of dose sensitivity of optical fibre, from the highest to lowest sensitivities are observed in 6 mol% Ge-FF, 2.3 mol% Ge-FF, 6 mol% Ge-CF and 2.3 mol% Ge-CF respectively with 6 mol% and 2.3 mol% Ge-FF showing 87 and 84 times more sensitivity than that of TLD-100 chip. The fabricated optical fibres are also able to detect dose levels down to the least

delivered dose of 2 mGy used in this study with superior lower dose detection competency of 2.3 mol% Ge-CF to identify doses down to 0.29 mGy. Finally, a higher fading rate of optical fibres as compared to TLD-100 chip and nanoDots after 10 days post-irradiation is observed due to the presence of a large number of shallow traps within the fibres. This indicates a requirement for a fading correction factor during the conversion of the signal response of nC and to an absolute absorbed dose of mGy.

In terms of the second specific objective which is to study the kinetic parameters of fabricated Ge-doped optical fibres using the glow curve analysis, including the maximum peak temperature (T_{max}), peak integral (PI) and activation energy (E_a) in the CT radiation dosimetry, it is found that aside from 6.0 mol% Ge-FF which is broadly double-peaked, other fibres exhibited broad single-peak glow curves. This is due to the collapsing of the fibre walls during the fabrication of 6.0 mol% Ge-FF which has the smallest core volumes, has generated considerable strain defect. The maximum temperature T_{max} of the glow peaks pattern is found to be consistent throughout RQT 8, 9 and 10 beam qualities for all fibre types. However, most of the electrons generated from diagnostic CT photon irradiation are trapped in shallow traps compared to deep traps. These shallow traps require low E_a in order to release the trapped electrons. Large quantities of electrons trapped in the shallow traps are manifested by the dominant contribution of peak 1 (single peak) and peak 3 (double peak) in the formation of a glow curve for these fabricated fibres. Thus, this condition caused a higher fading rate in the fabricated fibres than TLD-100 chip. This supports the earlier statement that the fading correction factor must be considered when calculating the absorbed dose methodology.

For the third specific objective, absorbed dose methodology, calibration coefficient and correction factors for Ge-doped optical fibres for CT dosimetry are successfully established based on the equation developed by Noor et al. (2014). According to the basic dosimetry characterisations, the TL response of fabricated Ge-doped optical fibres is found to be dependent on the beam quality and fading. Thus, beam quality (K_{RQT}) and fading correction factors K_{FAD} are included in the absorbed dose measurement formula. Furthermore, an individual fibre capsule (K_{SI}), TLD-100 chips (K_{TLD}) and OSLD nanoDots (K_{OSL}) are also incorporated to measure the actual dose delivered to the dosimeters. Finally, the expanded uncertainties are 5.92%, 3.67%, 2.38%, 1.27%. 2.97% and 4.54% for 6 mol% Ge-FF, 2.3 mol% Ge-FF, 2.3 mol% Ge-CF, 6 mol% Ge-CF, TLD-100 chip and OSLD nanoDot respectively after multiplication by a coverage factor k = 2. This uncertainty provided a level of confidence of approximately 95%.

For the fourth specific objective in comparing the response between fabricated optical fibres, TLD-100 chips and OSLD nanoDots on CIRS ATOM® dosimetry verification paediatric phantom irradiation, it is found that the percentage difference of the investigated dosimeter reading against TLD-100 is mostly less than 3%. In detail, the brain and eye organ doses during phantom head scans recorded by the TLD-100 chip are recorded as 25.16 mGy and 28.92 mGy, respectively. Meanwhile, the thyroid organ dose is recorded as 1.85 mGy with a percentage difference of 2.3 mol% Ge-FF, showing the largest difference of 4.75%. For entrance skin dose measurement of the eyes and thyroid during the phantom head scan, the TLD-100 chip recorded a reading of 29.49 mGy and 1.89 mGy respectively with each investigated dosimeter showing a percentage difference of less than 2% for eyes measurements while for thyroid

measurements, both 6 mol% Ge-FF and 2.3 mol% Ge-FF showed the largest difference of 4.15%.

For the study of chest computed tomography scan on CIRS ATOM® dosimetry paediatric 1-year-old phantom, the lung organ dose recorded by TLD-100 chip is recorded as 3.83 mGy, with all fabricated Ge-doped optical fibres showed a percentage difference of less than 3%. Similarly, the thyroid organ dose is recorded as 2.05 mGy with less than a 5% difference when compared between all investigated dosimeters. The thyroid entrance skin dose during phantom chest scan measured by both TLD-100 chip and 2.3 mol% Ge-CF is recorded as 2.18 mGy while other dosimeters showed a percentage difference of less than 2%.

Finally, the last objective of the study is to verify and compare the responses of the investigated dosimeters in a real clinical setting for paediatric patients undergoing CT pulmonary angiogram (CTPA). 15 patients who satisfied the inclusion criteria of being under two (2) years old and already consented to CTPA at the Radiology Department, Hospital Serdang were able to be recruited. The dose range recorded by the TLD-100 chip for entrance skin dose measurements of the thyroid is between 2.04 to 4.85 mGy, with all dosimeters showing a percentage difference of less than 5%. The smallest difference was recorded by 2.3 mol% Ge-CF, ranging from 0.84% to 2.42%, while 2.3 mol% Ge-FF recorded the largest percentage difference, ranging from 4.58% to 4.95% against the TLD-100 chip.

Overall, the findings of the current study have accomplished all the specific objectives stated in this thesis with the aim to establish the dosimetric properties of fabricated

Germanium-doped optical fibres irradiated using X-ray photons at energies applied in computed tomography or RQT beam quality. The advanced characteristics in terms of the kinetic parameters of fabricated Ge-doped optical fibres have also been successfully investigated prior to establishing absorbed dose methodology with uncertainty analysis. The response and comparison of the optical fibres with gold standards for absorbed and entrance skin dose measurements on CIRS ATOM® dosimetry verification paediatric phantom during head and lung computed tomography scans are also successfully accomplished. The majority of the percentage difference of investigated dosimeters is less than 3% when compared against TLD-100 chips. The dosimetry verification in a real clinical setting for entrance skin dose measurement of the thyroids in paediatric patients undergoing Computed Tomography Pulmonary Angiogram (CTPA) examinations is also achieved with a percentage difference of less than 5%. In conclusion, all four fabricated Ge-doped optical fibres, namely 6 mol% Ge-FF, 2.3 mol% Ge-FF, 2.3 mol% Ge-CF and 6 mol% Ge-CF, are feasible to be potential novel dosimeters in CT dosimetry RQT beam quality.

5.2 Limitations of the Study

The generalisability of these results is subject to certain limitations. One of them is the limited number of Ge-doped optical fibre samples being fabricated for dosimetry characterisation and subsequent assessment. In this study, the fabricated Ge-doped optical fibres are manufactured using a modified chemical vapour deposition technique, where both fabrication and pulling processes take place in other institutions which contributed to limited access and availability. As a result, small numbers of fabricated Ge-doped optical fibres are produced with approximately 250 pieces of the fabricated Ge-doped optical fibre samples used for sensitivity screening prior to any

irradiation tests. Instead of eliminating the outliers that have sensitivity less and more than ±5% from the TL mean reading, each of the samples is grouped according to the three different sensitivity levels. Thus, the whole batches of the fabricated Ge-doped optical fibre samples are used to accommodate the dosimetry characterisation study, phantom and clinical study measurements. The large deviation in the group of the optical fibres has led to the high individual capsule correction factor, thus contributing to the large combined uncertainty for measurement of absorbed dose by fabricated Ge-doped optical fibres.

Another source of limitation in this study is the shortage of paediatric patients who are able to be recruited for the investigation of the fabricated optical fibres in a real clinical setting for entrance skin dose measurement of the thyroids undergoing CTPA examinations due to COVID-19 restrictions. During the lockdown, UPM and Hospital Serdang were not accessible for the continuation of the data collection. The phantom and clinical data collection are mainly done after the lockdown is lifted in phase, with a queuing system for the usage of study equipment and services as many people are equally affected and delayed. As such, this directly affects the number of subjects for clinical study and the duration of the study in general.

5.3 Recommendations for Future Works

The findings from this research provide several insights for future research. Even though various studies have investigated these tailor-made Ge-doped optical fibres in the field of radiotherapy, the outcomes from this research will hopefully add novel insights into the dosimetric response of these fabricated silica glasses in computed tomography RQT beam quality. As such, this present study may act as a reference for future scientists to follow up for more detailed research on the basic and advanced dosimetric characterisation response of these fibres in CT radiation dosimetry. In addition, the conversion of the initial signal produced by the fibre in nanocoulombs (nC) to milligray (mGy) through the establishment of absorbed dose methodology is the pivotal and final methodology to closing the loop of any fundamental dosimetry study.

Finally, the independent verification to measure the organ and entrance skin doses to the radiosensitive lens and thyroid via paediatric phantom CT scan and CTPA examinations on real patients is unprecedented. Thus, it is hoped that the novel fabricated Ge-doped optical fibre in the present study can also be investigated for other radiosensitive organs such as gonads and bone marrow for both paediatric and adult phantom as well on real patients. Desirably, in the long run, the implementation of evidence-based tools for radiation detection and dose measurement for clinical diagnosis can serve a beneficial purpose and long-lasting benefit in patient care and resource utilization.

REFERENCES

Aamry, A., Alsufayan, M., Aldossari, H., Alonazi, B., & Sulieman, A. (2020). Assessment of imaging protocol and patient radiation exposure in pediatric computed tomography angiography. *Radiation Physics and Chemistry*, *172*, 1–6.

Abdulhamid, M., Ibrahim, U., Zira, J. D., Yusuf, S. D., & Abdulhamid, A. (2022). Assessment of head CT protocol to reduce the radiation dose in eye lens in some selected hospital in Kaduna State, Nigeria. *Applied Radiation and Isotopes*, *190*, 1–6.

Addanki, S., Amiri, I. S., & Yupapin, P. (2018). Review of optical fibers-introduction and applications in fiber lasers. *Results in Physics*, *10*, 743–750.

Ahmad Fadzil, M. S. (2020). *Use of fabricated germanium-doped optical fibres for radiotherapy postal dose audit of megavoltage photon beams under non-reference conditions in selected Malaysian radiotherapy facilities*. Universiti Putra Malaysia.

Al-Senan, R. M., & Hatab, M. R. (2011). Characteristics of an OSLD in the diagnostic energy range. *Medical Physics*, *38*(7), 4396–4405.

Alawiah, A., Alina, M. S., Bauk, S., Abdul-Rashid, H. A., Gieszczyk, W., Noramaliza, M. N., Mahdiraji, G. A., Tamchek, N., Zulkifli, M. I., & Bradley, D. A. (2015). The thermoluminescence characteristics and the glow curves of Thulium doped silica fiber exposed to 10 MV photon and 21 MeV electron radiation. *Applied Radiation and Isotopes*, *98*, 80–86.

Alkhorayef, M. (2020). Survey of paediatric imaging exposure from computed tomography examinations. *Radiation Physics and Chemistry*, *167*, 1–4.

Almujally, A., Tamam, N., Sulieman, A., Tai, D. T., Omer, H., Abuhadi, N., Salah, H., Mattar, E., Khandaker, M. U., & Bradley, D. (2022). Evaluation of paediatric computed tomography imaging for brain, and abdomen procedures. *Radiation Physics and Chemistry*, *200*, 1–5.

Alvarez, P., Kry, S. F., Stingo, F., & Followill, D. (2017). TLD and OSLD dosimetry systems for remote audits of radiotherapy external beam calibration. *Radiation Measurements*, *106*, 412–415.

Alyahyawi, A., Jupp, T., Alkhorayef, M., & Bradley, D. A. (2018). Tailor-made Ge-doped silica-glass for clinical diagnostic X-ray dosimetry. *Applied Radiation and Isotopes*, *138*, 45–49.

Alyahyawi, A., Rozaila, Z. S., Shafiqah, A. S. S., Sabtu, S. N., Alsubaie, A., Alanazi, A., Daar, E., Sani, S. F. A., & Bradley, D. A. (2017). Investigation of silica-based TL media for diagnostic X-ray dosimetry. *Radiation Physics and Chemistry*, *140*, 78–82.

Asni, H., Wagiran, H., Saripan, M. I., Ramli, A. T., & Yaakob, N. H. (2010). Thermoluminescence Energy Response of Germanium Doped Optical Fibre Using Monte Carlo N-Particle Code Simulation. *AIP Conference Proceedings*, *1250*(1), 420–423.

Attix, F. H. (2008). *Introduction to radiological physics and radiation dosimetry*. John Wiley and Sons.

Balonov, M. I., & Shrimpton, P. C. (2012). Effective dose and risks from medical x-ray procedures. *Annals of the ICRP*, *41*(3-4), 129-141.

Begum, M., Rahman, A. K. M. M., Abdul-Rashid, H. A., Yusoff, Z., Begum, M., Mat-Sharif, K. A., Amin, Y. M., & Bradley, D. A. (2015). Thermoluminescence characteristics of Ge-doped optical fibers with different dimensions for radiation dosimetry. *Applied Radiation and Isotopes*, *100*, 79–83.

Benabdesselam, M., Mady, F., Girard, S., Mebrouk, Y., Duchez, J. B., Gaillardin, M., & Paillet, P. (2013). Performance of Ge-doped optical fiber as a thermoluminescent dosimeter. *IEEE Transactions on Nuclear Science*, *60*(6), 4251–4256.

Berdon, W. E., & Slovis, T. L. (2002). Where we are since ALARA and the series of articles on CT dose in children and risk of long-term cancers: what has changed? *Pediatric Radiology*, *32*(10), 699–699.

Boone, J., Strauss, K., Cody, D., McCollough, C., McNitt-Gray, M., Toth, T., Goske, M., & Frush, D. (2011). Size-Specific Dose Estimates (SSDE) in Pediatric and Adult Body CT Examinations. Retrieved September 30, 2022, from https://www.aapm.org/pubs/reports/RPT_204.pdf

Bos, A. J. J. (2001). On the energy conversion in thermoluminescence dosimetry materials. *Radiation Measurements*, *33*(5), 737–744.

Bradley, D. A., Hugtenburg, R. P., Nisbet, A., Rahman, A. T. A., Issa, F., Noor, N. M., & Alalawi, A. (2012). Review of doped silica glass optical fibre: their TL properties and potential applications in radiation therapy dosimetry. *Applied Radiation and Isotopes*, *71*, 2–11.

Bradley, D. A., Khandaker, M. U., & Alanazi, A. (2020). Irradiated glass and thermoluminescence yield: Dosimetric utility reviewed. *Radiation Physics and Chemistry*, *170*, 1–5.

Bradley, D. A, Mahdiraji, G. A., Ghomeishi, M., Dermosesian, E., Adikan, F. R. M., Rashid, H. A. A., & Maah, M. J. (2015). Enhancing the radiation dose detection sensitivity of optical fibres. *Applied Radiation and Isotopes*, *100*, 43–49.

Bradley, D. A., Sani, S. F. A., Alalawi, A. I., Jafari, S. M., Noor, N. M., Azhar, A. R. H., Mahdiraji, G. A., Tamchek, N., Ghosh, S., & Paul, M. C. (2014). Development of tailor-made silica fibres for TL dosimetry. *Radiation Physics and Chemistry*, *104*, 3–9.

Bradley, D. A., Shafiqah, A. S. S., Rozaila, Z. S., Sabtu, S. N., Sani, S. F. A., Alanazi, A. H., Jafari, S. M., Mahdiraji, G. A., Adikan, F. R. M., & Maah, M. J. (2017). Developments in production of silica-based thermoluminescence dosimeters. *Radiation Physics and Chemistry*, *137*, 37–44.

Brady, Z., Cain, T. M., & Johnston, P. N. (2011). Differences in using the international commission on radiological protection's publications 60 and 103 for determining effective dose in paediatric CT examinations. *Radiation Measurements*, *46*(12), 2031–2034.

Brenner, D. J. (2012). Minimising medically unwarranted computed tomography scans. *Annals of the ICRP*, *41*(3–4), 161–169.

Brenner, D. J., Elliston, C. D., Hall, E. J., & Berdon, W. E. (2001). Estimated risks of radiation-induced fatal cancer from pediatric CT. *American Journal of Roentgenology*, *176*(2), 289–296.

Brenner, D. J., & Hall, E. J. (2007). Computed tomography—an increasing source of radiation exposure. *New England Journal of Medicine*, *357*(22), 2277–2284.

Brody, A. S., Frush, D. P., Huda, W., Brent, R. L., & Radiology, S. on. (2007). Radiation risk to children from computed tomography. *Pediatrics*, *120*(3), 677–682.

Bushberg, J. T., Seibert, J. A., Leidholdt, E. M., & Boone, J. M. (2020). *The essential physics of medical imaging*. Lippincott Williams and Wilkins.

Chapple, C. L., Willis, S., & Frame, J. (2001). Effective dose in paediatric computed tomography. *Physics in Medicine and Biology*, *47*(1), 107–115.

Deak, P. D., Smal, Y., & Kalender, W. A. (2010). Multisection CT protocols: sex-and age-specific conversion factors used to determine effective dose from dose-length product. *Radiology*, *257*(1), 158–166.

De Basea, M. B., Moriña, D., Figuerola, J., Barber, I., Muchart, J., Lee, C., & Cardis, E. (2018). Subtle excess in lifetime cancer risk related to CT scanning in Spanish young people. *Environment International*, *120*, 1–10.

Dewerd, L. A., & Wagner, L. K. (1999). Characteristics of radiation detectors for diagnostic radiology. *Applied Radiation and Isotopes*, *50*(1), 125–136.

Doll, G. L., Mensah, B. A., Mohseni, H., & Scharf, T. W. (2009). Chemical vapor deposition and atomic layer deposition of coatings for mechanical applications. *Journal of Thermal Spray Technology*, *19*(1–2), 510–516.

Dougeni, E., Chapple, C. L., Willis, J., & Panayiotakis, G. (2011). Assessment of effective dose in paediatric CT examinations. *Radiation Protection Dosimetry*, *147*(1–2), 147–150.

Dunn, L., Lye, J., Kenny, J., Lehmann, J., Williams, I., & Kron, T. (2013). Commissioning of optically stimulated luminescence dosimeters for use in

radiotherapy. *Radiation Measurements*, *51*, 31–39.

Fadzil, M. S. A., Tamchek, N., Ung, N. M., Ariffin, A., Abdullah, N., Bradley, D. A., & Noor, N. M. (2018). Assessment of thermoluminescence glow curves and kinetic parameters of fabricated Ge-doped flat fiber for radiotherapy application. *Jurnal Sains Nuklear Malaysia*, *30*(2), 1–14.

Faulkner, K., Broadhead, D. A., & Harrison, R. M. (1999). Patient dosimetry measurement methods. *Applied Radiation and Isotopes*, *50*(1), 113–123.

Fearon, T., Xie, H., Cheng, J. Y., Ning, H., Zhuge, Y., & Miller, R. W. (2011). Patient-specific CT dosimetry calculation: a feasibility study. *Journal of Applied Clinical Medical Physics*, *12*(4), 196-209.

Feng, S., Law, M. W., Huang, B., Ng, S., Li, Z., Meng, Q., & Khong, P. (2010). Radiation dose and cancer risk from pediatric CT examinations on 64-slice CT: a phantom study. *European Journal of Radiology*, *76*(2), 19–23.

Frush, D. P., & Yoshizumi, T. (2006). Conventional and CT angiography in children: Dosimetry and dose comparisons. *Pediatric Radiology*, *36*(2), 154–158.

Furetta, C., Prokic, M., Salamon, R., Prokic, V., & Kitis, G. (2001). Dosimetric characteristics of tissue equivalent thermoluminescent solid TL detectors based on lithium borate. *Nuclear Instruments and Methods in Physics Research, Section A: Accelerators, Spectrometers, Detectors and Associated Equipment*, *456*(3), 411–417.

Geleijns, J., Joemai, R. M. S., Cros, M., Hernandez-Giron, I., Calzado, A., Dewey, M., & Salvado, M. (2015). A Monte Carlo simulation for the estimation of patient dose in rest and stress cardiac computed tomography with a 320-detector row CT scanner. *Physica Medica*, *31*(8), 1029–1034.

Ghaznavi, H. (2020). Thyroid cancer risk in patients undergoing 64 slice brain and paranasal sinuses computed tomography. *Frontiers in Biomedical Technologies*, *7*(2), 100–104.

Ghomeishi, M., Mahdiraji, G. A., Adikan, F. R. M., Ung, N. M., & Bradley, D. A. (2015). Sensitive fibre-based thermoluminescence detectors for high resolution in-vivo dosimetry. *Scientific Reports*, *5*(1), 1–10.

Giansante, L., Martins, J. C., Nersissian, D. Y., Kiers, K. C., Kay, F. U., Sawamura, M. V., & Costa, P. R. (2019). Organ doses evaluation for chest computed tomography procedures with TL dosimeters: comparison with Monte Carlo simulations. *Journal of Applied Clinical Medical Physics*, *20*(1), 308-320.

Goske, M. J., Applegate, K. E., Boylan, J., Butler, P. F., Callahan, M. J., Coley, B. D., Farley, S., Frush, D. P., Hernanz-Schulman, M., Jaramillo, D., Johnson, N. D., Kaste, S. C., Morrison, G., Strauss, K. J., & Tuggle, N. (2008). The 'Image Gently' campaign: increasing CT radiation dose awareness through a national education and awareness program. *Pediatric Radiology*, *38*(3), 265–269.

Hall, E. J. (2002). Lessons we have learned from our children: cancer risks from diagnostic radiology. *Pediatric Radiology*, *32*, 700–706.

Hall, E. J., & Giaccia, A. J. (2006). *Radiobiology for the radiologist*. Lippincott Williams & Wilkins.

Harun, H. H., Abdul Karim, M. K., Abbas, Z., Abdul Rahman, M. A., Sabarudin, A., & Ng, K. H. (2020). Association of radiation doses and cancer risks from CT pulmonary angiography examinations in relation to body diameter. *Diagnostics*, *10*(9), 1–9.

Hashim, S. (2010). *The thermoluminescence response of doped silicon dioxide optical fibres to ionizing radiation*. Universiti Teknologi Malaysia.

Hashim, S., Saripan, M. I., Rahman, A. T. A., Yaakob, N. H., Bradley, D. A., & Alzimami, K. (2013). Effective atomic number of Ge-doped and Al-doped optical fibers for radiation dosimetry purposes. *IEEE Transactions on Nuclear Science*, *60*(2), 555–559.

Hassan, M. F., Rahman, W., Tominaga, T., Geso, M., Akasaka, H., Bradley, D. A., & Noor, N. M. (2019). Ge-doped silica fibre for proton beam dosimetry. *Radiation Physics and Chemistry*, *165*, 1–7.

Hennelly, K. E., Baskin, M. N., Monuteuax, M. C., Hudgins, J., Kua, E., Commeree, A., Kimia, R., Lee, E. Y., Kimia, A., & Neuman, M. I. (2016). Detection of pulmonary embolism in high-risk children. *The Journal of Pediatrics*, *178*, 214–218.

Heyer, C. M., Mohr, P. S., Lemburg, S. P., Peters, S. A., & Nicolas, V. (2007). Image quality and radiation exposure at pulmonary CT angiography with 100-or 120-kVp protocol: prospective randomized study. *Radiology*, *245*(2), 577-583.

Horowitz, Y., Horowitz, A., Oster, L., Marino, S., Datz, H., & Margaliot, M. (2008). Investigation of the ionisation density dependence of the glow curve characteristics of LiF : Mg, Ti (TLD-100). *Radiation protection dosimetry*, *131*(4), 406-413.

Hranitzky, C., Stadtmann, H., & Olko, P. (2006). Determination of LiF: Mg, Ti and LiF: Mg, Cu, P TL efficiency for X-rays and their application to Monte Carlo simulations of dosemeter response. *Radiation Protection Dosimetry*, *119,* 483-486.

Huang, B., Law, M. W., Mak, H. K., Kwok, S. P., & Khong, P. (2009). Pediatric 64-MDCT coronary angiography with ECG-modulated tube current: radiation dose and cancer risk. *American Journal of Roentgenology*, *193*(2), 539–544.

Huda, W., Ogden, K. M., & Khorasani, M. R. (2008). Converting dose-length product to effective dose at CT. *Radiology*, *248*(3), 995–1003.

IAEA. (2007). *Dosimetry in diagnostic radiology : an international code of practice (TRS-457)*.

IAEA. (2008). *Measurement uncertainty: A practical guide for secondary standards dosimetry laboratories*. Technical Document Series No. 1585.

ICRP. (2007). The 2007 recommendations of the international commission on radiological protection. ICRP Publication 103.

ICRU. (1992). *Phantoms and computational models in therapy, diagnosis and protection. ICRU Report 48*.

Iglesias, M. L., Schmidt, A., Ghuzlan, A. Al, Lacroix, L., de Vathaire, F., Chevillard, S., & Schlumberger, M. (2017). Radiation exposure and thyroid cancer: A review. *Archives of Endocrinology and Metabolism*, *61*(2), 180–187.

Izewska, J., Hultqvist, M., & Bera, P. (2008). Analysis of uncertainties in the IAEA/WHO TLD postal dose audit system. *Radiation Measurements*, *43*(2–6), 959–963.

Jibiri, N. N., & Adewale, A. A. (2014). Estimation of radiation dose to the lens of eyes of patients undergoing cranial computed tomography in a teaching Hospital in Osun state, Nigeria. *International Journal of Radiation Research*, *12*(1), 53–60.

Jursinic, P. A. (2007). Characterization of optically stimulated luminescent dosimeters, OSLDs, for clinical dosimetric measurements. *Medical Physics*, *34*(12), 4594–4604.

Karim, M. K. A., Sabarudin, A., Muhammad, N. A., & Ng, K. H. (2019). A comparative study of radiation doses between phantom and patients via CT angiography of the intra-/extra-cranial, pulmonary, and abdominal/pelvic arteries. *Radiological Physics and Technology*, *12*, 374–381.

Karimizarchi, H., & Chaparian, A. (2017). Estimating risk of exposure induced cancer death in patients undergoing computed tomography pulmonary angiography. *Radioprotection, 5*2(2), 81-6.

Kiani, M., & Chaparian, A. (2023). Evaluation of image quality, organ doses, effective dose, and cancer risk from pediatric brain CT scans. *European Journal of Radiology*, *158*, 1–7.

Kim, J., Gosnell, J. E., & Roman, S. A. (2020). Geographic influences in the global rise of thyroid cancer. *Nature Reviews Endocrinology*, *16*(1), 17–29.

Kry, S. F., Price, M., Followill, D., Mourtada, F., & Salehpour, M. (2007). The use of LiF (TLD-100) as an out-of-field dosimeter. *Journal of Applied Clinical Medical Physics*, *8*(4), 169–175.

Kubo, T. (2019). Vendor free basics of radiation dose reduction techniques for CT. *European Journal of Radiology*, *110*, 14–21.

Lam, S. E. (2019). *Dosimetric characteristics of fabricated Ge-doped silica optical fibres for small field radiation dosimetry in radiotherapy.* Universiti Putra

Malaysia.

Lam, S. E., Bradley, D. A., Mahmud, R., Pawanchek, M., Rashid, H. A. A., & Noor, N. M. (2019). Dosimetric characteristics of fabricated Ge-doped silica optical fibre for small-field dosimetry. *Results in Physics*, *12*, 816–826.

Landauer, Inc. (2019). *NanoDot™ personal dosimeter - Product specification file.* Landauer, Inc, USA.

Lee, C., Kim, K. P., Long, D. J., & Bolch, W. E. (2012). Organ doses for reference pediatric and adolescent patients undergoing computed tomography estimated by Monte Carlo simulation. *Medical Physics*, *39*(4), 2129–2146.

Lee, E. Y., Kritsaneepaiboon, S., Zurakowski, D., Arellano, C. M. R., Strauss, K. J., & Boiselle, P. M. (2009). Beyond the pulmonary arteries: alternative diagnoses in children with MDCT pulmonary angiography negative for pulmonary embolism. *American Journal of Roentgenology*, *193*(3), 888–894.

Lund, E., & Halaburt, H. (1982). Irradiation dose to the lens of the eye during CT of the head. *Neuroradiology*, *22*, 181-184.

Mahdiraji, G. A., Ghomeishi, M., Dermosesian, E., Hashim, S., Ung, N. M., Adikan, F. R. M., & Bradley, D. A. (2015). Optical fiber based dosimeter sensor: beyond TLD-100 limits. *Sensors and Actuators A: Physical*, *222*, 48–57.

Mathews, J. D., Forsythe, A. V., Brady, Z., Butler, M. W., Goergen, S. K., Byrnes, G. B., Giles, G. G., Wallace, A. B., Anderson, P. R., Guiver, T. A., McGale, P., Cain, T. M., Dowty, J. G., Bickerstaffe, A. C., & Darby, S. C. (2013). Cancer risk in 680 000 people exposed to computed tomography scans in childhood or adolescence: Data linkage study of 11 million Australians. *BMJ*, *346*, 1–18.

Mazonakis, M., Tzedakis, A., Damilakis, J., Varveris, H., Kachris, S., & Gourtsoyiannis, N. (2006). Scattered dose to thyroid from prophylactic cranial irradiation during childhood: a Monte Carlo study. *Physics in Medicine & Biology*, *51*(8), N139.

McCollough, C. H., Christner, J. A., & Kofler, J. M. (2010). How effective is effective dose as a predictor of radiation risk? *American Journal of Roentgenology*, *194*(4), 890–896.

McDermott, A., White, R. A., Mc-Nitt-Gray, M., Angel, E., & Cody, D. (2009). Pediatric organ dose measurements in axial and helical multislice CT. *Medical physics*, *36*(5), 1494-1499.

McKeever, S. W. S., Moscovitch, M., & Townsend, P. D. (1995). *Thermoluminescence dosimetry materials: properties and uses*. Nuclear Technology Publishing.

Miglioretti, D. L., Johnson, E., Williams, A., Greenlee, R. T., Weinmann, S., Solberg, L. I., Feigelson, H. S., Roblin, D., Flynn, M. J., & Vanneman, N. (2013). The use of computed tomography in pediatrics and the associated radiation

exposure and estimated cancer risk. *JAMA Pediatrics*, *167*(8), 700–707.

Mohd Noor, N. (2012). *The use of Ge-doped optical fibres in external beam radiotherapy dosimetry.* University of Surrey.

Moore, B. M., Brady, S. L., Mirro, A. E., & Kaufman, R. A. (2014). Size-specific dose estimate (SSDE) provides a simple method to calculate organ dose for pediatric CT examinations. *Medical Physics*, *41*(7), 1–10.

Moradi, F., Mahdiraji, G. A., Dermosesian, E., Khandaker, M. U., Ung, N. M., Adikan, F. R. M., & Amin, Y. M. (2017). Influence of dose history on thermoluminescence response of Ge-doped silica optical fibre dosimeters. *Radiation Physics and Chemistry*, *134*, 62–70.

Moscovitch, M., & Horowitz, Y. (2006). Thermoluminescent materials for medical applications: LiF: Mg, Ti and LiF: Mg, Cu, P. *Radiation Measurements*, *41*, S71–S77.

Mrčela, I., Bokulić, T., Izewska, J., Budanec, M., Fröbe, A., & Kusić, Z. (2011). Optically stimulated luminescence in vivo dosimetry for radiotherapy: Physical characterization and clinical measurements in 60Co beams. *Physics in Medicine and Biology*, *56*(18), 6065–6082.

Musa, Y., Hashim, S., Karim, M. K. A., Bakar, K. A., Ang, W. C., & Salehhon, N. (2017). Response of optically stimulated luminescence dosimeters subjected to X-rays in diagnostic energy range. *Journal of Physics: Conference Series*, *851*(1), 1–6.

Naranje, P., Shera, T., Bhalla, A., Meena, P., Kabra, S., Gupta, A., & Kandasamy, D. (2022). Role of computed tomography angiography in the evaluation of haemoptysis in children: Decoding the abnormal vessels. *Indian Journal of Medical Research*, *155*(3), 356.

Nawi, S. N. B. M., Wahib, N. F. B., Zulkepely, N. N. B., Amin, Y. B. M., Min, U. N., Bradley, D. A., Nor, R. B. M., & Maah, M. J. (2015). The thermoluminescence response of Ge-doped flat fibers to gamma radiation. *Sensors*, *15*(8), 20557–20569.

Nishizawa, K., Maruyama, T., Takayama, M., Iwai, K., & Furuya, Y. (1995). Estimation of effective dose from CT examination. *Nihon Igaku Hoshasen Gakkai zasshi. Nippon Acta Radiologica*, *55*(11), 763-768.

Noor, N. M., Hussein, M., Kadni, T., Bradley, D. A., & Nisbet, A. (2014). Characterization of Ge-doped optical fibres for MV radiotherapy dosimetry. *Radiation Physics and Chemistry*, *98*, 33–41.

Noor, N. M., Shukor, N. A., Hussein, M., Nisbet, A., & Bradley, D. A. (2012). Comparison of the TL fading characteristics of Ge-doped optical fibres and LiF dosimeters. *Applied Radiation and Isotopes*, *70*(7), 1384–1387.

Pearce, M. S., Salotti, J. A., Little, M. P., McHugh, K., Lee, C., Kim, K. P., Howe, N. L., Ronckers, C. M., Rajaraman, P., & Craft, A. W. (2012). Radiation exposure from CT scans in childhood and subsequent risk of leukaemia and brain tumours: a retrospective cohort study. *The Lancet*, *380*(9840), 499–505.

Ploussi, A., Stathopoulos, I., Syrgiamiotis, V., Makri, T., Hatzigiorgi, C., Platoni, K., Carinou, E., & Efstathopoulos, E. P. (2017). Direct measurements of skin, eye lens and thyroid dose during pediatric brain ct examinations. *Radiation Protection Dosimetry*, *179*(3), 199–205.

Ponmalar, R., Manickam, R., Ganesh, K. M., Saminathan, S., Raman, A., & Godson, H. F. (2017). Dosimetric characterization of optically stimulated luminescence dosimeter with therapeutic photon beams for use in clinical radiotherapy measurements. *Journal of Cancer Research and Therapeutics*, *13*(2), 304–312.

Ramač, J. P., Knežević, Ž., Hebrang, A., Krišto, D. R., Vidjak, V., Slavica, M., & Ranogajec-Komor, M. (2013). Radiation dose reduction by using low dose CT protocol of thorax. *Radiation Measurements*, *55*, 46–50.

Ramli, N. N. H., Salleh, H., Mahdiraji, G. A., Zulkifli, M. I., Hashim, S., Bradley, D. A., & Noor, N. M. (2015). Characterization of amorphous thermoluminescence dosimeters for patient dose measurement in X-ray diagnostic procedures. *Radiation Physics and Chemistry*, *116*, 130–134.

Reft, C. S. (2009). The energy dependence and dose response of a commercial optically stimulated luminescent detector for kilovoltage photon, megavoltage photon, and electron, proton, and carbon beams. *Medical Physics*, *36*(5), 1690–1699.

Rozaila, Z. S., Alyahyawi, A., Khandaker, M. U., Amin, Y. M., Bradley, D. A., & Maah, M. J. (2016). Ge and B doped collapsed photonic crystal optical fibre, a potential TLD material for low dose measurements. *Radiation Physics and Chemistry*, *126*, 9–13.

Rozaila, Z. S., Khandaker, M. U., Abdul Sani, S. F., Sabtu, S. N., Amin, Y. M., Maah, M. J., & Bradley, D. A. (2017). Environmental monitoring through use of silica-based TLD. *Journal of Radiological Protection*, *37*(3), 761–779.

Sadeghi, M., Sina, S., & Faghihi, R. (2015). Investigation of LiF, Mg and Ti (TLD-100) reproducibility. *Journal of Biomedical Physics and Engineering*, *5*(4), 217–222.

Sani, S. A., Alalawi, A. I., AR, H. A., Mahdiraji, G. A., Tamchek, N., Nisbet, A., Maah, M., & Bradley, D. (2014). High sensitivity flat SiO_2 fibres for medical dosimetry. *Radiation Physics and Chemistry*, *104*, 134–138.

Sauter, A., Koehler, T., Brendel, B., Aichele, J., Neumann, J., Noël, P. B., Rummeny, E. J., & Muenzel, D. (2018). CT pulmonary angiography: dose reduction via a next generation iterative reconstruction algorithm. *Acta Radiologica*, *60*(4), 478–487.

Scarboro, S. B., Cody, D., Alvarez, P., Followill, D., Court, L., Stingo, F. C., Zhang, D., McNitt-Gray, M., & Kry, S. F. (2015). Characterization of the nanoDot OSLD dosimeter in CT. *Medical Physics*, *42*(4), 1797–1807.

Schmidt, B., Saltybaeva, N., Kolditz, D., & Kalender, W. A. (2013). Assessment of patient dose from CT localizer radiographs. *Medical Physics*, *40*(8), 1–8.

Seeram, E. (2015). *Computed tomography: physical principles, clinical applications, and quality control*. Elsevier.

Shrimpton, P. C., Jessen, K. A., Geleijns, J., Panzer, W., & Tosi, G. (1998). Reference doses in computed tomography. *Radiation Protection Dosimetry*, *80*(1–3), 55–59.

Sinnott, B., Ron, E., & Schneider, A. B. (2010). Exposing the thyroid to radiation: A review of its current extent, risks, and implications. *Endocrine Reviews*, *31*(5), 756–773.

Stathopoulos, I., Ploussi, A., Syrgiamiotis, V., Makri, T., Hatzigiorgi, C., Carinou, E., Sakellaropoulos, G., Panayiotakis, G. S., & Efstathopoulos, E. P. (2016). In vivo dosimetry for head CT examinations in paediatric patients. *Physica Medica*, *32*, 205–206.

Strauss, K. J., & Goske, M. J. (2011). Estimated pediatric radiation dose during CT. *Pediatric Radiology*, *41*, 472–482.

Su, Y. P., Niu, H. W., Chen, J. B., Fu, Y. H., Xiao, G. B., & Sun, Q. F. (2014). Radiation dose in the thyroid and the thyroid cancer risk attributable to CT scans for pediatric patients in one general hospital of China. *International journal of environmental research and public health*, *11*(3), 2793-2803.

Thacker, P. G., & Lee, E. Y. (2016). Advances in multidetector CT diagnosis of pediatric pulmonary thromboembolism. *Korean Journal of Radiology*, *17*(2), 198–208.

Thermo Electron Corporation. (2002). *Harshaw standard TTP recommendations - Technical notice - Publication number: DOSM-0-N-1202-001*. Thermo Electron Corporation, USA.

Tian, X., Li, X., Segars, W. P., Paulson, E. K., Frush, D. P., & Samei, E. (2014). Pediatric chest and abdominopelvic CT: organ dose estimation based on 42 patient models. *Radiology*, *270*(2), 535–547.

Tomashuk, A. L., Grekov, M. V, Vasiliev, S. A., & Svetukhin, V. V. (2014). Fiber-optic dosimeter based on radiation-induced attenuation in P-doped fiber: suppression of post-irradiation fading by using two working wavelengths in visible range. *Optics Express*, *22*(14), 16778–16783.

Toossi, M. T. B., Zare, H., Eslami, Z., Bayani Roodi, S., Daneshdoust, M., Saeed, Z., Sedighpour, M., Mohammadian, N., Hashemi, M., & Afsaneh, K. (2018). Assessment of radiation dose to the lens of the eye and thyroid of patients

undergoing head and neck computed tomography at five hospitals in Mashhad, Iran. *Iranian Journal of Medical Physics*, *15*(4), 226–230.

Valentin, J. (2007). *The 2007 recommendations of the international commission on radiological protection*. Elsevier Amsterdam.

Vassileva, J., Rehani, M. M., Al-Dhuhli, H., Al-Naemi, H. M., Al-Suwaidi, J. S., Appelgate, K., Arandjic, D., Bashier, E. H. O., Beganovic, A., & Benavente, T. (2012). IAEA survey of pediatric CT practice in 40 countries in Asia, Europe, Latin America, and Africa: Part 1, frequency and appropriateness. *American Journal of Roentgenology*, *198*(5), 1021–1031.

Yaakob, N. H., Wagiran, H., Hossain, M. I., Ramli, A. T., Bradley, D. A., Hashim, S., & Ali, H. (2011). Thermoluminescence response of Ge- and Al-doped optical fibers subjected to low-dose electron irradiation. *Journal of Nuclear Science and Technology*, *48*(7), 1115–1117.

Yusoff, A. L., Hugtenburg, R. P., & Bradley, D. A. (2005). Review of development of a silica-based thermoluminescence dosimeter. *Radiation Physics and Chemistry*, *74*(6), 459–481.

Zahaimi, N. A., Abdullah, M. H. R. O., Zin, H., Rahman, A. L. A., Hashim, S., Saripan, M. I., Paul, M. C., Bradley, D. A., & Rahman, A. T. A. (2014). Dopant concentration and thermoluminescence (TL) properties of tailor-made Ge-doped SiO2 fibres. *Radiation Physics and Chemistry*, *104*, 297–301.

Zakaria, Z., Aziz, M. Z. A., Ishak, N. H., Suppiah, S., Bradley, D. A., & Noor, N. M. (2020). Advanced thermoluminescence dosimetric characterization of fabricated Ge-Doped optical fibres (FGDOFs) for electron beams dosimetry. *Radiation Physics and Chemistry*, *166*, 1–7.

Zhang, D., Li, X., Gao, Y., Xu, X. G., & Liu, B. (2013). A method to acquire CT organ dose map using OSL dosimeters and ATOM anthropomorphic phantoms. *Medical Physics*, *40*(8), 1–9.

Zubair, H. T., Begum, M., Moradi, F., Rahman, A. K. M. M., Mahdiraji, G. A., Oresegun, A., Louay, G. T., Omar, N. Y. M., Khandaker, M. U., Adikan, F. R. M., Noor, N. M., Almugren, K. S., Almugren, K. S., Abdul-Rashid, H. A., & Bradley, D. A. (2020). Recent advances in silica glass optical fiber for dosimetry applications. *IEEE Photonics Journal*, *12*(3), 1–25.

APPENDICES

Appendix A1

Table A1a: Brain organ dose for phantom head scan

ANOVA

Brain Organ Dose

	Sum of Squares	df	Mean Square	F	Sig.
Between Groups	.963	4	.241	1.264	.346
Within Groups	1.904	10	.190		
Total	2.867	14			

Table A1b: Eye organ dose for phantom head scan

ANOVA

Eye Organ Dose

	Sum of Squares	df	Mean Square	F	Sig.
Between Groups	1.259	4	.315	1.783	.209
Within Groups	1.765	10	.177		
Total	3.024	14			

Table A1c: Thyroid organ dose for phantom head scan

ANOVA

Thyroid Organ Dose

	Sum of Squares	df	Mean Square	F	Sig.
Between Groups	.011	4	.003	.019	.999
Within Groups	1.422	10	.142		
Total	1.433	14			

Appendix A2

Table A2a: Eye entrance skin dose for phantom head scan

ANOVA

Eye Entrance Skin Dose

	Sum of Squares	df	Mean Square	F	Sig.
Between Groups	.284	5	.057	.781	.582
Within Groups	.874	12	.073		
Total	1.158	17			

Table A2b: Thyroid entrance skin dose for phantom head scan

ANOVA

Thyroid Entrance Skin Dose

	Sum of Squares	df	Mean Square	F	Sig.
Between Groups	.014	5	.003	.019	1.000
Within Groups	1.860	12	.155		
Total	1.874	17			

Appendix A3

Table A3a: Lung organ dose for phantom chest scan

ANOVA

Lung Organ Dose

	Sum of Squares	df	Mean Square	F	Sig.
Between Groups	.020	4	.005	.032	.998
Within Groups	1.563	10	.156		
Total	1.583	14			

Table A3b: Thyroid organ dose for phantom chest scan

ANOVA

Thyroid Organ Dose

	Sum of Squares	df	Mean Square	F	Sig.
Between Groups	.023	4	.006	.060	.992
Within Groups	.956	10	.096		
Total	.979	14			

Table A3c: Thyroid entrance skin dose for phantom chest scan

ANOVA

Thyroid Entrance Skin Dose

	Sum of Squares	df	Mean Square	F	Sig.
Between Groups	.002	5	.000	.002	1.000
Within Groups	3.003	12	.250		
Total	3.005	17			

Appendix A4

Table A4a: CTPA Patient 1

ANOVA

Thyroid Entrance Skin Dose (Patient 1)

	Sum of Squares	df	Mean Square	F	Sig.
Between Groups	.018	5	.004	.031	.999
Within Groups	1.403	12	.117		
Total	1.421	17			

Table A4b: CTPA Patient 2

ANOVA

Thyroid Entrance Skin Dose (Patient 2)

	Sum of Squares	df	Mean Square	F	Sig.
Between Groups	.024	5	.005	.030	.999
Within Groups	1.895	12	.158		
Total	1.919	17			

Table A4c: CTPA Patient 3

ANOVA

Thyroid Entrance Skin Dose (Patient 3)

	Sum of Squares	df	Mean Square	F	Sig.
Between Groups	.026	5	.005	.071	.996
Within Groups	.888	12	.074		
Total	.914	17			

Appendix A5

Table A5a: CTPA Patient 4

ANOVA

Thyroid Entrance Skin Dose (Patient 4)

	Sum of Squares	df	Mean Square	F	Sig.
Between Groups	.027	5	.005	.073	.995
Within Groups	.886	12	.074		
Total	.913	17			

Table A5b: CTPA Patient 5

ANOVA

Thyroid Entrance Skin Dose (Patient 5)

	Sum of Squares	df	Mean Square	F	Sig.
Between Groups	.035	5	.007	.034	.999
Within Groups	2.497	12	.208		
Total	2.533	17			

Table A5c: CTPA Patient 6

ANOVA

Thyroid Entrance Skin Dose (Patient 6)

	Sum of Squares	df	Mean Square	F	Sig.
Between Groups	.037	5	.007	.042	.999
Within Groups	2.154	12	.179		
Total	2.191	17			

Appendix A6

Table A6a: CTPA Patient 7

ANOVA

Thyroid Entrance Skin Dose (Patient 7)

	Sum of Squares	df	Mean Square	F	Sig.
Between Groups	.058	5	.012	.098	.991
Within Groups	1.427	12	.119		
Total	1.485	17			

Table A6b: CTPA Patient 8

ANOVA

Thyroid Entrance Skin Dose (Patient 8)

	Sum of Squares	df	Mean Square	F	Sig.
Between Groups	.049	5	.010	.612	.693
Within Groups	.192	12	.016		
Total	.240	17			

Table A6c: CTPA Patient 9

ANOVA

Thyroid Entrance Skin Dose (Patient 9)

	Sum of Squares	df	Mean Square	F	Sig.
Between Groups	.053	5	.011	.193	.960
Within Groups	.658	12	.055		
Total	.711	17			

Appendix A7

Table A7a: CTPA Patient 10

ANOVA

Thyroid Entrance Skin Dose (Patient 10)

	Sum of Squares	df	Mean Square	F	Sig.
Between Groups	.102	5	.020	.186	.963
Within Groups	1.324	12	.110		
Total	1.426	17			

Table A7b: CTPA Patient 11

ANOVA

Thyroid Entrance Skin Dose (Patient 11)

	Sum of Squares	df	Mean Square	F	Sig.
Between Groups	.105	5	.021	.170	.969
Within Groups	1.473	12	.123		
Total	1.578	17			

Table A7c: CTPA Patient 12

ANOVA

Thyroid Entrance Skin Dose (Patient 12)

	Sum of Squares	df	Mean Square	F	Sig.
Between Groups	.097	5	.019	.352	.871
Within Groups	.661	12	.055		
Total	.758	17			

Appendix A8

Table A8a: CTPA Patient 13

ANOVA

Thyroid Entrance Skin Dose (Patient 13)

	Sum of Squares	df	Mean Square	F	Sig.
Between Groups	.124	5	.025	.250	.932
Within Groups	1.191	12	.099		
Total	1.315	17			

Table A8b: CTPA Patient 14

ANOVA

Thyroid Entrance Skin Dose (Patient 14)

	Sum of Squares	df	Mean Square	F	Sig.
Between Groups	.141	5	.028	.490	.777
Within Groups	.692	12	.058		
Total	.833	17			

Table A8c: CTPA Patient 15

ANOVA

Thyroid Entrance Skin Dose (Patient 15)

	Sum of Squares	df	Mean Square	F	Sig.
Between Groups	.141	5	.028	.113	.987
Within Groups	2.994	12	.250		
Total	3.135	17			

Appendix B

Ionization Chamber Certificate of Calibration

KEMENTERIAN SAINS, TEKNOLOGI DAN INOVASI
MINISTRY OF SCIENCE, TECHNOLOGY AND INNOVATION

NUKLEAR MALAYSIA

STANDARDS MALAYSIA
MS ISO/IEC 17025
CALIBRATION
SAMM NO.275

CERTIFICATE OF CALIBRATION

DATE OF ISSUE: 05 July 2022 **CERTIFICATE NUMBER: SSDL/ 22073046**

Issued By : Makmal Standard Dosimetri Sekunder (SSDL)
Agensi Nuklear Malaysia
Kementerian Sains, Teknologi dan Inovasi
Bangi, 43000 Kajang, Selangor Darul Ehsan
Tel : 603-8911 2000 (ext: 1232/1096)
Faks : 603-8911 2163
Email: taufik@nuclearmalaysia.gov.my
http://www.nuclearmalaysia.gov.my

APPROVED SIGNATORIES

En. Mohd Taufik Dolah ☑
Ts. John Konsoh Sangau ☐

Name and Address of User : Makmal Fizik Perubatan,
Kumpulan Metrologi Sinaran,
Bahagian Keselamatan & Kesihatan Sinaran ,
Agensi Nuklear Malaysia,
Bangi, 43000 Kajang, SELANGOR

Electrometer Model / Serial No. : PTW Unidos T10005 / 50403
Ionization Chamber / Serial No. : TN 30010 / 2335
Instruments Condition When Returned : Calibrated and can be used in accordance with the instrument's function.

Reference Dosimeter:

Instrument:	Model / Serial No.:	Cal. Cert. No.:	Cal. Due Date :	Treacability:
Ionization Chamber	NE 2581 / 334 (0.6 cm^3)	SSDL/ 21030354	15 March 2023	IAEA, Vienna

Date Received:	Calibration Completed:	Calibration Due Date:
10 June 2022	05 July 2022	05 July 2023

(The user should be aware that any number of factors may cause this instrument to drift out of calibration before the specified calibration interval has expired)

Calibration Method :

This instrument was calibrated using the substitution methods: WI-CAL-008.

(Approved Signatory)

The expanded uncertainties are based on an estimated confidence probability of approximately 95% and have a coverage factor of k = 2 unless stated otherwise.

KEMENTERIAN SAINS, TEKNOLOGI DAN INOVASI
MINISTRY OF SCIENCE, TECHNOLOGY AND INNOVATION

NUKLEAR MALAYSIA

STANDARDS MALAYSIA
MS ISO/IEC 17025
CALIBRATION
SAMM NO.275

CERTIFICATE OF CALIBRATION

DATE OF ISSUE: 05 July 2022 **CERTIFICATE NUMBER: SSDL/ 22073046**

Calibration Results :

Table 1 : Calibration Coefficient (^{60}Co).

No.	Type of Calibration Coefficients	Calibration Coefficient (CF)	Uncertainty (%)	Standard Rate
1.	Absorbed Dose to Water ($N_{D,w}$)*	52.89 mGy/nC	1.41	20.2 mGy/min
2.	Air Kerma (N_K)	48.62 mGy/nC	1.30	22.8 mGy/min
3.	Exposure (N_X)	5.531 R/nC	1.42	2.6 R/min

***Build-up cap : Not use**
Voltage : + 300 Volts

Calibration coefficients are valid for use on standard ambient conditions with temperature = 20 °C and pressure = 101.325 kPa.

Note: The calibration results only apply for the instrument specified in this certificate.

Calibrated By : Zulkefly Mohamad

The expanded uncertainties are based on an estimated confidence probability of approximately 95% and have a coverage factor of k = 2 unless stated otherwise.

Appendix C

Digital Barometer Certificate of Calibration

MULTITECH CALIBRATION SERVICES SDN BHD
(Company No: 929584-D)
No. 48B, Jalan BRP 6/11, Section U20, Bukit Rahman Putra,
47000 Sungai Buloh, Selangor Darul Ehsan, Malaysia.
Tel: 603-6157 3033 / 6157 3055 Fax: 603-6157 3044
Email: multitech06@gmail.com Website: www.multitechcalibration.com

MS ISO/IEC 17025
CALIBRATION
SAMM NO.308

CERTIFICATE OF CALIBRATION

Date of Issue : 08 May 2021

Issue To : **AGENSI NUKLEAR MALAYSIA**
43000 Bangi, Kajang, Selangor

Teoh Kok Khiang
Approved Signatory

Certificate Number	: MAR0426
Calibration Sticker No.	: C 90936
Date of Calibration	: 08 May 2021
Requested Cal. Due Date	: 07 May 2022

* Recalibration date requested by customer.
* The user should be aware that any number of factors may cause this instrument to drift out of calibration before the specified calibration interval has expired.

Equipment Details

Instrument	: Digital Barometer
Manufacturer	: Extech
Model	: SD700
Serial Number	: Q673607
Factory Number	: MOSTI/NUKLEARMALAYSIA/BKS/H/12/24
Upon Receiving	: Good Condition
Upon Returning	: Calibrated

Environmental Condition		Min		Max	
Temperature	:	23	°C	23	°C
Relative Humidity	:	48	%R.H.	50	%R.H.

This Instrument has been Calibrated at **Multitech Calibration Services Sdn Bhd**

Work Instruction : In House Procedure WI200C / WI200S

Equipment Used	Certificate Number	Calibration Due Date	Traceable To
Standard Hygrometer	LAN0839	28 September 2021	NMIM
Humidity Chamber	LAN0143	08 June 2021	NMIM
Digital Test Gauge	LAP0890	12 July 2021	NMIM

MULTITECH CALIBRATION SERVICES SDN BHD
(Company No: 929584-D)
No. 48B, Jalan BRP 6/11, Section U20, Bukit Rahman Putra,
47000 Sungai Buloh, Selangor Darul Ehsan, Malaysia.
Tel: 603-6157 3033 / 6157 3055 Fax: 603-6157 3044
Email: multitech06@gmail.com Website: www.multitechcalibration.com

MS ISO/IEC 17025
CALIBRATION
SAMM NO.308

CERTIFICATE OF CALIBRATION

Date of Issue	: 08 May 2021	Temperature Range	: -20 ~ 80 °C
Certificate Number	: MAR0426	Temperature Resolution	: 0.1 °C
Instrument	: Digital Barometer	Humidity Range	: 5 ~ 95 % r.h.
Model	: SD700	Humidity Resolution	: 0.1 % r.h.
Serial Number	: Q673607		

CALIBRATION RESULTS

Calibration Range : 15 ~ 26 °C
Unit In : °C

Standards Reading	Unit Under Test Reading		
	After Adjustment	Before Adjustment	Correction
15.0	NIL	14.8	0.2
18.0	NIL	17.8	0.2
20.0	NIL	19.8	0.2
22.0	NIL	21.8	0.2
26.0	NIL	25.8	0.2

Measurement Uncertainty : ± 0.7 °C
Estimated at a confidence level of approximately 95% with a coverage factor of k = 2

Calibration Range : 40 ~ 90 % r.h.
Unit In : % r.h.

Standards Reading	Unit Under Test Reading		
	After Adjustment	Before Adjustment	Correction
40	NIL	42.2	-2.2
50	NIL	52.4	-2.4
60	NIL	62.3	-2.3
90	NIL	91.5	-1.5

Measurement Uncertainty : ± 2.0 % r.h.
Estimated at a confidence level of approximately 95% with a coverage factor of k = 2

True value = Unit Under Test Reading + Correction
All humidity range calibrated at Temperature 25 °C
The suitability of the instrument for its intended use should be determined based on the user's requirement.

Calibrated By
B.Logenthiran

MULTITECH CALIBRATION SERVICES SDN BHD
(Company No: 929584-D)
No. 48B, Jalan BRP 6/11, Section U20, Bukit Rahman Putra,
47000 Sungai Buloh, Selangor Darul Ehsan, Malaysia.
Tel: 603-6157 3033 / 6157 3055 Fax: 603-6157 3044
Email: multitech06@gmail.com Website: www.multitechcalibration.com

MS ISO/IEC 17025
CALIBRATION
SAMM NO.308

CERTIFICATE OF CALIBRATION

Certificate Number : MAR0426
Date of Issue : 08 May 2021
Instrument : Digital Barometer
Serial Number : Q673607

CALIBRATION RESULTS

Unit in : hPa

UUT Reading	Increasing				UUT Reading	Decreasing			
	Before Adjustment		After Adjustment			Before Adjustment		After Adjustment	
	Reference Reading	UUT Correction	Reference Reading	UUT Correction		Reference Reading	UUT Correction	Reference Reading	UUT Correction
900.0	900.6	0.6	-	-	900.0	900.6	0.6	-	-
940.0	940.6	0.6	-	-	940.0	940.6	0.6	-	-
970.0	970.7	0.7	-	-	970.0	970.7	0.7	-	-
1000.0	1000.8	0.8	-	-	1000.0	1000.8	0.8	-	-
1010.0	1010.8	0.8	-	-	1010.0	1010.8	0.8	-	-

Error of the instrument found after calibration = ± 0.073% of full scale.
Manufacturer specification = ± 0.100% of full scale.

The expanded uncertainty of measurement is ± 0.64 hPa, estimated at a confidence level of approximately 95 % with a coverage factor of k = 2.

Remarks : 1) True Value = Unit Under Test Reading + Correction
2) UUT = Unit Under Test.

Calibrated by
B.Logenthiran

LIST OF PUBLICATIONS

Journals

Rais, N. N. M., Bradley, D., Hashim, A., Isa, N. M., Osman, N. D., Ismail, I., Hassan, H., & Noor, N. M. (2019a). Dosimetric response of fabricated Ge-doped optical fibres in computed tomography RQT beam quality X-ray beams. *Journal of Radiological Protection,* 39(3), N8–N18.

Rais, N. N. M., Bradley, D., Hashim, A., Osman, N. D., & Noor, N. M. (2019b). Fabricated germanium-doped fibres for computed tomography dosimetry. *Applied Radiation and Isotopes*, *153*, 108810.

Rais, N. N. M., Bradley, D., Hashim, A., Isa, N. M., Osman, N. D., Ismail, I., Hassan, H., & Noor, N. M. (2021). Fabricated germanium-doped optical fibres for computed tomography dosimetry: Glow curve characteristics. *Radiation Physics and Chemistry*, *178*, 108935.

Rais, N., Noor, N., Hashim, A., Bradley, D., Osman, N., Ismail, I., & Hassan, H. (2022). Establishment of RQT beam quality (100 to 150 kV) for computed tomography applications. *Asian Journal of Medical Technology*, *2*(2), 1–14.

Conferences and Proceedings

Rais, N. N. M., Bradley, D., Hashim, A., Isa, N. M., Osman, N. D., Ismail, I., Hassan, H., & Noor, N. M. (2021). Fabricated germanium-doped optical fibres for computed tomography dosimetry: Glow curve characteristics. Presented in 2nd International Forum on Advances in Radiation Physics, Sunway University, Kuala Lumpur from 3rd to 4th December 2019.

Rais, N. N. M., Bradley, D., Hashim, A., Osman, N. D., & Noor, N. M. (2019b). Fabricated germanium-doped fibres for computed tomography dosimetry. Presented in 11th International Seminar on Medical Physics, Hotel Istana, Kuala Lumpur from 7th to 8th November 2019.

Rais, N. N. M., Bradley, D., Hashim, A., Isa, N. M., Osman, N. D., Ismail, I., Hassan, H., & Noor, N. M. (2019a). Dosimetric response of fabricated Ge-doped optical fibres in computed tomography RQT beam quality X-ray beams. Presented in 18th Asia-Oceania Congress of Medical Physics (AOCMP) in conjunction with the 16th South-East Asia Congress of Medical Physics (SEACOMP), Connexion Convention and Exhibition Centre, Bangsar South, Kuala Lumpur from 12th to 14th November 2018.